**THESE EN COTUTELLE**

Pour obtenir le titre de Docteur délivré par

**L'Université de Lorraine**

**École doctorale Energie Mécanique et Matériaux (EMMA)**

**&**

**L'Université Libanaise**

**École doctorale des sciences et technologie (EDST)**

**Spécialité: Chimie-Physique (Sciences des Matériaux)**

# Synthèse et caractérisation des nanoparticules intelligentes

Présentée et soutenue publiquement par

**Enaam JAMAL AL DINE**

**07 Juin 2017**

**Membre du Jury**

| | | |
|---|---|---|
| Sophie LANONE | DR (Inserm) | Rapporteur |
| Olivier SANDRE | DR (CNRS) | Rapporteur |
| Sophie DEMOUSTIER-CHAMPAGNE | Professeur (Université catholique de Louvain) | Examinateur |
| Florent MEYER | Professeur (Inserm) | Examinateur |
| Eric GAFFET | DR (CNRS) | Directeur de thèse |
| Joumana TOUFAILY | Professeur (Université Libanaise) | Directeur de thèse |
| Halima ALEM-MARCHAND | Maître de conférences (Université de Lorraine) | Co-directeur de thèse |
| Tayssir HAMIEH | Professeur (Université Libanaise) | Co-directeur de thèse |
| Thibault ROQUES-CARMES | Maître de conférences (Université de Lorraine) | Invité |
| Raphaël SCHNEIDER | Professeur (Université de Lorraine) | Invité |
| Fabrice NESSLANY | Chef du Service Toxicologie (Institut Pasteur de Lille) | Invité |

*To the memory*
*of my brother …*
*"Abdo"*

# ACKNOWLEDGEMENTS

**TABLE OF CONTENTS**

*Chapter 2: Efficient synthetic access to thermo-responsive core/shell nanoparticles*

*Chapter 3: Synthesis, characterization and cytotoxicity of ZnO@P(MEO$_2$MA$_X$-OEGMA$_{100-X}$) NPs*

*Chapter 4: Thermo-responsive magnetic Fe$_3$O$_4$@P(MEO$_2$MA$_X$-OEGMA$_{100-X}$) NPs and their applications as drug delivery systems*

# ABBREVIATIONS

| | |
|---|---|
| **ARGET** | Activator regenerated by electron transfer |
| **ATRP** | Atom transfer radical polymerization |
| **CM** | Culture medium/media |
| **CMPETMS** | ((Chloromethyl) phenylethyl)-trimethoxysilane |
| **DDS** | Drug delivery system |
| **DLS** | Dynamic light scattering |
| **DMF** | Dimethylformamide |
| **DMSO** | Dimethyl sulfoxide |
| **DOX** | Doxorubicin |
| **FT-IR** | Fourier transform infrared spectroscopy |
| **$H_D$** | Hydrodynamic diameter |
| **HR-TEM** | High-resolution transmission electron microscopy |
| **IONPs** | Iron oxide nanoparticles |
| **LCST** | Lower critical solution temperature |
| **$MEO_2MA$** | 2-(2-methoxyethoxy)ethyl methacrylate |
| **MNPs** | Magnetic nanoparticles |
| **$M_s$** | Saturation magnetization |
| **MTT** | 3-(4,5-Dimethylthiazol-2-Yl)-2,5-Diphenyltetrazolium bromide |
| **NPs** | Nanoparticles |
| **OA** | Oleic acid |
| **OEGMA** | Oligo(ethylene glycol) methacrylate |
| **PEG** | Polyethylene glycol |
| **PL** | Photoluminescence |
| **PNIPAM** | Poly(N-isopropylacrylamide) |
| **PS** | Polystyrene |
| **QDs** | Quantum dots |
| **SI-CRP** | Surface-initiated controlled radical polymerization |
| **SPIO** | Superparamagnetic iron oxide |
| **SRPs** | Stimuli responsive polymers |
| **TGA** | Thermogravimetric analysis |
| **TMAH** | Tetramethylammonium hydroxide |
| **TPMA** | (tris(2-pyridylmethyl) amine) |
| **TRPs** | Thermo-responsive polymers |
| **UCST** | Upper critical solution temperature |
| **UV-Vis** | Ultraviolet–visible spectroscopy |
| **XRD** | X-ray powder diffraction |

x

# *INTRODUCTION*

**From nanomaterials to Core/shell nanoparticles (NPs): Birth and Importance**

"It is all about technology!" This expression shortens the situation we are living nowadays. And as everything revolves around exploring the world from its smallest components, researchers have focused their attention on the "nanotechnology".

In 1959, the physicist Richard Feynman was the first to introduce the concept of nanotechnology and nanoscience long before these terms were used; "There"s Plenty of Room at the Bottom" [1]. He considered that scientists would be able to manipulate and control individual atoms and molecules. During the time between Feynman talk and the beginning of the 1980s nanotechnology got no great attention as the scientists didn"t have the right tools to investigate the materials at the nanoscale. Right after, with the development of highly resolved techniques, the age of nanotechnology was actually born since it was first possible to characterize objects at the nanometric scale [2].

Nanotechnology relies on the ability to design, manipulate, and manufacture materials at the nanoscale. These materials are called nanomaterials which have, by definition, one or more dimension in the nanometer scale (1-100 nm) range and subsequently show novel properties compared to their derived bulk materials [3]. Nanomaterials come in different shapes including rods, films, wires, particles, disks, cubes, tubes …. These small sized materials which could be natural or synthesized have attracted a wide attention in the past few years because of their promising applications in several important fields, e.g. in textiles, coatings, catalysis, electronics, biotechnology, health care, biomedical and pharmaceutical industries [4].

Nanoparticles (NPs), in particular, have gained much attention due to their unique physical, magnetic and electrical properties as they are effectively a bridge between bulk materials and atomic or molecular structures. The increase in the surface area to volume ratio in NPs leads to an increasing dominance of the surface atoms over those in its interior which affects their physical properties and therefore their reactivity as the interaction between other materials becomes stronger [5]. At this level, NPs were studied as single particles e.g. one material. Later then, in the late 1980s, researchers found that composite particles made of two or more materials with developing some new properties are more efficient than their corresponding single particles [6, 7]. More recently during the early 1990s, researchers synthesized concentric multilayer semiconductor NPs with the view to improving the property of such

semiconductor materials. Hence, subsequently the terminology "core/shell" was adopted [8-10].

Because of their improved multiple properties, core/shell NPs have easily invaded most of the fields, such as electronics, biomedical, pharmaceutical, optics, and catalysis. The ability to combine different materials with different distinctive properties and to tailor the surface of these NPs with different functionalities enables the researchers to study a wide variety of combinations to meet the diverse application requirements. In general, of these combinations, we have inorganic/inorganic, inorganic/organic, organic/inorganic, and organic/organic core/shell hybrids. We recall some examples: $Fe/SiO_2$ [11], CdSe/ZnS [12, 13], $Fe_2O_3$/Au [14], $Fe_3O_4$/PEG [15], Au/organosilica [16], $TiO_2$-$SiO_2$/PMMA [17], PS/ZnS [18] and hundreds more. Chaudhuri *et al.* have made a very interesting review on the core/shell NPs focusing on the development of their different aspects such as: the classes, properties, synthesis mechanisms, characterization techniques and applications [7].

There has been an increased interest in coating the surface of different inorganic NPs like silica, magnetic and semiconductors with organic shells like polymers for various studies on its optical, electronic, magnetic, mechanical and catalytic characters to increase their potential applications [19]. These kind of hybrids are called inorganic/organic core/shell NPs and they are widely used nowadays in many industrial applications mainly optoelectronics [20], development of photocatalytic systems [21-23] and biomedical applications in biosensing, as contrast agents in magnetic resonance imaging (MRI), for tissue engineering and for targeted drug and gene delivery [24-27]. These NPs combine the fascinating electronic, optical and magnetic properties of the core with the desired properties of the polymer such as solubility, chemical and biological stability, easy formability, biocompatibility and further functionalization possibilities [28]. In addition, the high surface area of the inorganic NPs is very important in terms of different important applications like in the biomedical field where the increase in the total surface area permits faster dissolution of the NPs in blood and higher and faster absorption in the human body [29]. Also, their surface chemistry readily lends them to functionalization with targeting proteins or chemical groups. However, their high surface-to-volume ratio often induces agglomeration and leads to the loss of their attractive properties. On the other hand, they are eliminated rapidly from the blood stream after being injected because they are recognized by macrophages from the mononuclear phagocyte system [30]. As a result, it is very important that the surface of inorganic NPs is modified to overcome

these problems. A polymer layer improves the dispersion stability of the NPs in organic or aqueous media and offers different end functionalities for post-synthetic modification. A neutral, biocompatible and hydrophilic polymer layer increases circulation life times and minimize premature clearance by macrophages [31]. Some polymers could serve as hosts for drug molecules enhancing their delivery in the body. In this case, responsive polymers could be a very good choice as this kind of polymer collapse on the NPs surface in response to a stimulus like temperature or pH causing the release of the drug [32].

Different techniques have been employed for the preparation of inorganic/polymer core/shell NPs; the first involves the reversible physisorption of the polymer chains onto the NPs surface via weak interactions (van den Waals forces, hydrogen bonds, etc.) and the second one is to covalently graft the polymer chains from the surface of the NPs (**Figure 1**) [33]. The second approach is preferable as the strong chemical bond between the inorganic NPs and the polymer chains ensure a durable modification. This can be achieved either by the "grafting to" method, in which previously prepared polymers are grafted onto the NPs surface using the affinity of the polymer end-group for the functionalities present on the NPs surface [34] or by growing the polymer chains from appropriately functionalized NPs surface known as the "grafting from" method. The latter is widely selected as it gives well-defined polymer chains with higher grafting density [35].
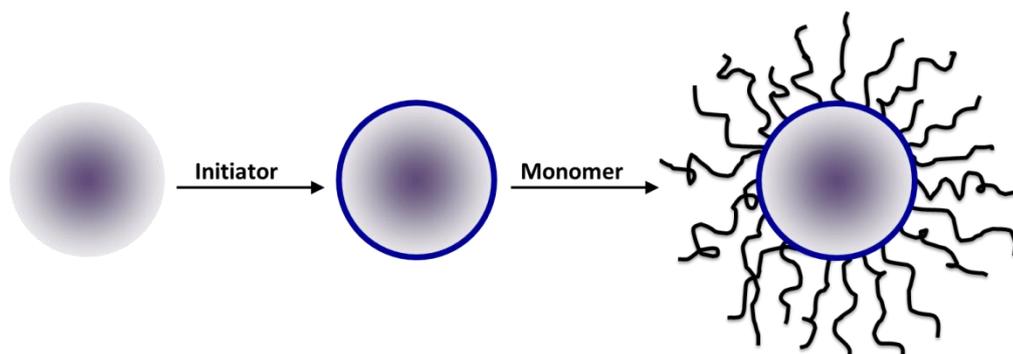


**Figure 1 Design of inorganic/organic core/shell NPs by covalent grafting polymer chains from the surface of the inorganic NPs.**

Controlled/ "living" radical polymerization (CRP) among different polymerization techniques like living anionic or cationic and ring-opening polymerization is preferred to grow the polymer from the surface of the NPs as it offers great potential for the preparation of well-defined core-shell NPs [36]. Reversible addition-fragmentation chain transfer polymerization (RAFT), nitroxide-mediated radical polymerization (NMP) and atom transfer radical

polymerization (ATRP) are CRP techniques. ATRP is very famous in this field; it allows the covalent attachment of polymers with well-defined grafting densities and controlled layer thicknesses [37]. The development of ATRP resulted in the activators regenerated by electron transfer (ARGET ATRP) process where the amount of the copper (Cu) catalyst used is reduced as Cu is considered to be toxic.

When engineering the smart NPs to biological applications, the size, surface charge, hydrophilicity, stability, biocompatibility and appropriate end functionality are important factors to be taken into consideration. Specifically for cancer treatment and drug delivery applications, two general characteristic of specific targeting and controllable release should be additionally possessed. Thus, designing a developed drug delivery system with these characteristics is a critical step to avoid damaging healthy cells and to improve cancer cure rates [31]. In this context, nanosize ZnO and IONPs/polymer core/shell NPs have appeared as very good tools to enhance a selective drug delivery to cancer cells [38]. The optical properties of the ZnO NPs and the magnetic properties of IONPs allow following these NPs in the body while the advantages of an appropriate polymer shell are many. On one hand, the drug embedded in the polymer chains is separated from the biological environment, further reducing coincidental interactions that may stimulate adverse mononuclear phagocyte system responses [31]. On the other hand with regard to controllable drug release, employing a responsive polymer shell which responds to different stimuli such as temperature, pH or light ensures a release at target sites (**Figure 2**). Polymers which are sensitive to temperature are called thermo-responsive polymers. They exhibit a transition temperature called lower critical solution temperature (LCST). Above this temperature the polymer chains collapse on the surface of the NPs. And as the temperature values in cancer cells are usually higher than those in blood or healthy cells, a polymer shell of LCST close to these values is able to release the drug only when in contact with the cancer cells. And as previously mentioned, a polymer shell improves the dispersion stability of the NPs in aqueous media and offers different end functionalities for post-synthetic modification.
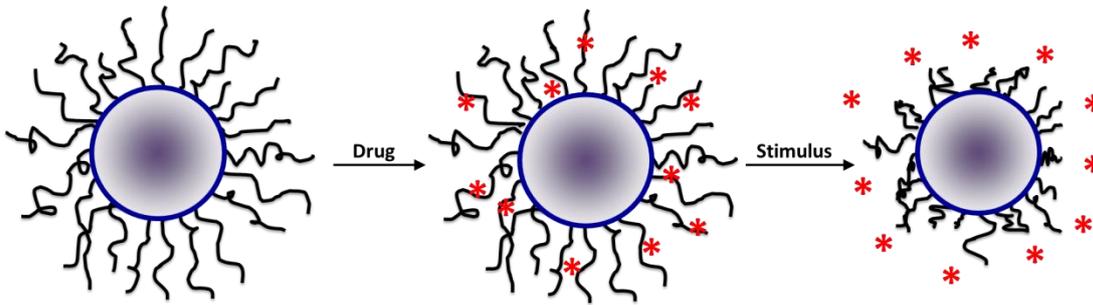
**Figure 2 Triggered drug release from responsive NPs.**

In this thesis, inorganic/organic core/shell NPs are designed by grafting two thermo-responsive polymers from the surface of ZnO and IONPs. Random copolymers of 2-(2-methoxyethoxy)ethyl methacrylate (MEO$_2$MA) and oligo(ethylene glycol) methacrylate (OEGMA) exhibit LCST in water, which can be finely tuned between 26 and 90 °C depending on the OEGMA content and its molecular mass. The LCST is almost dependent on the molar mass of the final copolymer, concentration, ionic strength and the grafting density [39, 40]. In addition, these copolymers are expected to be biocompatible, since the addition of oligo(ethylene oxide) units to responsive polymers was also shown to decrease cytotoxicity [41]. Copolymers with different ratios of OEGMA and MEO$_2$MA will be grafted from the surface of the NPs via surface initiated ARGET ATRP. The obtained NPs are then characterized by different techniques to investigate the morphology, thermal and optical properties and the ability to be further modified with folic acid.

## Thesis plan:

In this thesis, for the first time, a thermo-responsive copolymer composed of two biocompatible monomers was grafted from the surface of ZnO and Fe$_3$O$_4$ NPs by the surface initiated ARGET-ATRP in two modification steps. These NPs as biocompatible materials could serve as a drug delivery system by a simple modification with folic acid. IONPs, due to their easy separation from solutions, were tested for the release of doxorubicin (DOX). Following the release of the latter via UV-visible spectroscopy, the release was clear around and after crossing the LCST. Cytotoxicity tests were also performed in terms of using these NPs in vitro.

The first chapter will be the state of art about the application of ZnO and IONPs based core/shell NPs, their properties, synthesis and surface modification. Then we will present the

properties of the thermo-responsive copolymer grafted at the surface of the NPs, the grafting strategy and the polymerization method. In this part, a small title will include some of the work which has been dedicated to obtain these inorganic/organic NPs using the adopted polymerization technique which is ARGET ATRP. A last part of the chapter will present a brief description of the characterization techniques used to follow the synthesis process.

Chapter two will describe the general strategy to obtain the core/shell NPs composed of ZnO, $Fe_3O_4$ and $SiO_2$ cores grafted with $MEO_2MA_X$-$OEGMA_{100-X}$ copolymer and polystyrene in the case of $SiO_2$ NPs. The final NPs are characterized with different techniques to demonstrate the chemical attachment of the polymer to the surface of the NPs and to study the properties and the effect of the temperature responsive polymer layer on the NPs.

The third chapter will report the synthesis of the ZnO@P($MEO_2MA_X$-$OEGMA_{100-X}$) NPs with different X percentages and the behavior of these NPs in water and physiological media focusing on the samples with the temperature close to the physiological one. After, we will discuss the biological application of these NPs in terms of cytotoxicity tests.

Chapter four will discuss the biological application of $Fe_3O_4$@P($MEO_2MA_X$-$OEGMA_{100-X}$) NPs in terms of the drug release experiments and cytotoxicity tests. IONPs were similarly modified as ZnO NPs. The synthesis and characterization steps will be presented, with discussing also the behavior of these NPs in water and physiological media.

*Chapter 1: General Overview*

# 1. Inorganic/organic core/shell NPs

Core/shell NPs made from inorganic core and organic polymer shell represent a new class of materials that exhibit improved performance as the grafting of the inorganic core surface with organic compounds improve their dispersion stability in various liquid media and enhance their chemical functionality and biocompatibility for bio-applications [7]. Inorganic/organic core/shell NPs are often made by grafting synthetic polymers or a shell of any other high density organic material on inorganic particles or by adding modified NPs into polymer matrices and their further use as diagnostic tools.

## 1.1. Inorganic NPs

The inorganic core could be of metal (e.g. Au, Ag, and Fe), metalloid oxide (e.g. $SiO_2$), magnetic oxide (e.g. $Fe_2O_3$ and $Fe_3O_4$) or semiconductors called quantum dots (e.g. CdSe, CdTe, PbS, ZnO, $TiO_2$). In this thesis we will focus on the core/shell NPs obtained from an iron oxide or a quantum dot core. These two types of inorganic materials have attracted a great deal of attention due to the unique magnetic properties of the iron oxide, electrical/optical properties as well as photoluminescence of the semiconductors quantum dots and the ability for the two of being easily chemically modified for improved biocompatibility and dispersity.

### 1.1.1. ZnO QDs

Quantum dots (QDs) have received extensive attention during the past years owing to their advantages over the organic dyes and fluorescent proteins [42]. QDs are nanometer-sized crystals (2-10 nm in diameter) made of semiconductor materials. They are highly luminescent and are extremely resistant to photo bleaching. Moreover, they present a very broad absorption spectrum and a very narrow fluorescence emission spectrum in the visible and near infrared.

QDs exhibit novel optical and electronic properties due to the quantum confinement of excitons and phonons. The phenomenon of quantum confinement arises once the diameter of the particle is smaller than the Bohr radius. Quantum confinement generally results in widening of the band gap and it is the reason when the QDs are dispersed in a solution, the

solution of same material in term of chemical composition but with varied diameter, exhibit various colors upon the same excitation energy (**Figure 1.1.1**) [43].
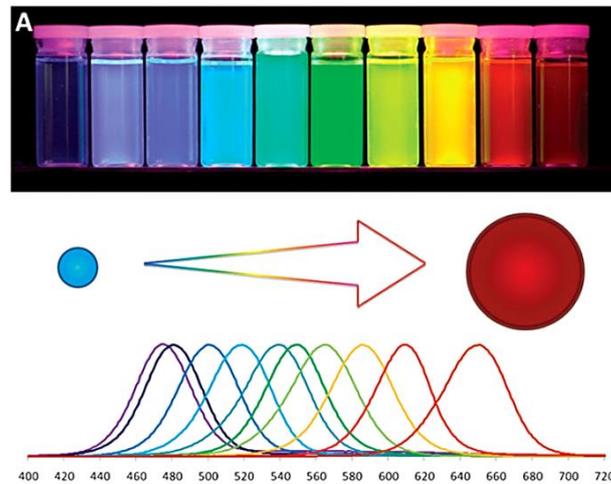


**Figure 1.1.1 Illustration of the change of fluorescence properties by changing the size of the QDs.**

QDs are often assembled from atoms from groups II-VI or III-V elements in the periodic table like CdSe, ZnS, ZnO, InSb and GaAs which are types of materials with the characteristic band gap. This band gap is defined as the energy difference between the valence and conduction bands and it is different for each type of bulk semiconductor material. The smaller size of a semiconductor QD, the larger is the band gap and thus, the fluorescence at a shorter wavelength is achieved.
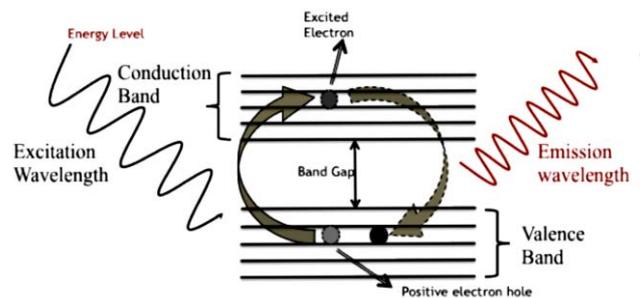


**Figure 1.1.2 Fluorescence emission as a result of QD excitation.**

When a QD is excited with light of specific energy (energy equal or greater than the band gap), the QD absorbs a photon resulting in the formation of an exciton (electron-hole pair). Then the electron falls back down across the band gap towards the valence band, via a radiative electron-hole recombination, generating fluorescence (**Figure 1.1.2**) and this

strongly depends on the size of the band gap, which can be altered by changing the size of the QD by changing the surface chemistry [44].

The strong size-dependence of QDs offers many advantages in use of their optical properties. Depending on the application, CdSe QDs of different sizes ranging from 2 to 8 nm emit photons across almost all the visible band. This unique property also attracts a lot of interest for applications of QDs in biological labeling and optical/electronic devices such as light emitting diodes and photovoltaic devices [45].

Nano-crystals of CdSe, CdTe, CdTe/CdSe and CdTe/ZnTe are reported as popular bio-labels in imaging and detection [46-48]. CdTe/ZnTe QDs can serve as excellent ultrasensitive probes for in vivo targeted bio-imaging. **Figure 1.1.3** shows an image of a mouse injected with three different sizes emitting CdTe/ZnTe QDs through subcutaneous and tail vein injections. The treated spots are highly luminescence where the synthesized QDs possessed a high quantum yield (52 %) [49].
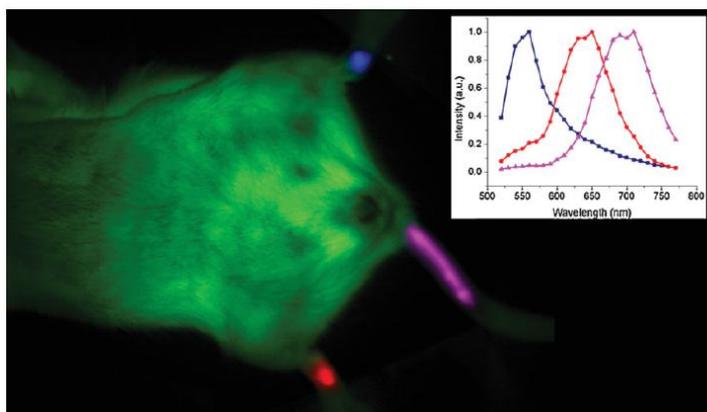


**Figure 1.1.3 Fluorescence images of mouse injected with three different sizes emitting CdTe/ZnTe QDs. PL spectra of the injected QDs are shown in the inset [49].**

However, the acute toxicity of Cadmium based core materials on biological systems due to the release of toxic heavy metal ions, and formation of reactive oxygen species (ROS) limited their uses for health care [50]. Therefore, the development of non-toxic alternatives is currently increasing for health care applications [51]. As a result, zinc oxide (ZnO) is one of the most excellent semiconductors with great potential for replacing the traditional Cd-related species applied in the optical and biological fields [52].

### 1.1.1.1. Physical and optical properties

ZnO is a well-known n-type, direct wide-band-gap II–VI semiconductor. Wurtzite (B4 phase), zinc blende (B3) and Rocksalt (B1) are the three crystallographic phases of ZnO [53]. At ambient conditions, wurtzite crystalline ZnO is the thermodynamically stable crystal structure. The structure exhibits a hexagonal structure with two lattice parameters, a = 0.3296 and c = 0.52065 nm in the ratio of c /o =1.602 and belongs to the space group of $C_{6V}^4$ or P6$_3$mc [54]. Each anion is surrounded by four cations at the corners of the tetrahedron, which shows the tetrahedral coordination and hence exhibits the sp$^3$ covalent-bonding (**Figure 1.1.4**).
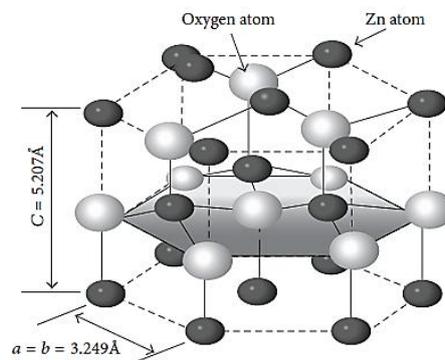


**Figure 1.1.4 Tetrahedral structure of ZnO.**

Much attention has been given to use ZnO for cell labeling applications because of their photoluminescence (PL) [51]. Wurtzite ZnO has normally two photoluminescent emission bands. One is centered in the UV region and the other is centered in the visible region. The origin of UV emission is well-known to be associated with the radiative electron-hole recombination, and because of their direct association with band gap, it is size dependent emission due to quantum confinement [55]. While for the visible emission, the origin and property of ZnO QDs have not been fully understood and it is believed that this emission is a result of many intrinsic defects such as oxygen vacancies, zinc interstitials, zinc vacancies, antisite oxygen, donor–acceptors pairs, and surface defects [56]. As discussed earlier, the wavelength of the fluorescent light is dependent on the size of the band gap. Bulk ZnO exhibits photoluminescence at about 495 nm excitation while this wavelength is decreased to 350 nm when ZnO is in the nanocrystalline form [57].

ZnO has unique properties compared to its counterparts such as the wide band gap of 3.37 eV, a large excitonic binding energy of 60 meV and a high thermal and mechanical stability at

room temperature. ZnO NPs also show piezo- and pyroelectric properties plus its hardness, rigidity, low toxicity, biocompatibility and biodegradability [57]. Therefore, because of its exceptional physical and chemical characteristics, the ZnO based NPs have shown great potential for use in UV laser devices, bio-imaging, drug delivery, sunscreens, photo-catalysis, chemical sensors, biosensors, solar cells and piezoelectric devices [58].

### 1.1.1.2. Synthesis

In general, NPs can be prepared by a variety of methods which are usually categorized in two main synthetic routes: the top down and the bottom up approaches. In the top down routes, the NPs are obtained from their bulk materials using different methods like lithography and laser ablation. While, in the bottom approach, the NPs are obtained from their basic building blocks (atoms or molecules) which react to generate the NPs of the desired shape and size [59].

As a versatile and multifunctional nanomaterial with very unique features, ZnO has attracted many researchers to develop a wide number of chemical and physical methods for its synthesis in different nanoscale as it provides one of the greatest assortments of varied particle structures among all known materials. Depending on the synthesis method we can obtain: particles, rods, belts, nanorings, needles, pellets, flowers, snowflakes, wires and other structures [60].

For NPs synthesis some examples are: vapor chemical deposition, precipitation in water solution, hydrothermal synthesis, electrochemical methods, sol-gel process, precipitation from microemulsions and mechanochemical processes [60]. Bio-routes have been also followed to obtain well-defined ZnO nanostructures using plant extracts and biotemplates, including macromolecules, bacteria, and bacteriophages [61]. A recent review reported these so-called green methods offering a good alternative choice over chemical and physical methods as they are environmentally friendly and of low-cost [62].

Chemical synthesis, found to be very simple, cost-effective, is one of the most important techniques which can be performed by using a range of precursors and different conditions like temperature, time, concentration of reactants, and other parameters. Variation of these parameters gives different structures and sizes of the produced NPs. Different chemical methods such as precipitation, hydrothermal and sol-gel were used for the synthesis of ZnO NPs [63]. Among these methods, the sol-gel is one of the most employed for the production

of ZnO NPs in view of the simplicity, low cost, reliability, repeatability, smaller particle size and morphological control, better homogeneity and purity. Moreover, the synthesis is conducted in relatively mild conditions of synthesis, which enable during the process the surface modification of ZnO with selected organic compounds [64]. NPs as small as 2.5 nm could be indeed obtained since 1985 by Koch *et al.* [65].

In sol-gel method, monomers are converted into a colloidal solution (*i.e.* sol) that acts as the precursor for an integrated network (*i.e.* gel) of either discrete particles or network polymers [66]. **Figure 1.1.5** illustrates the main stages of ZnO thin films (**Figure 1.1.5a**) and particles (**Figure 1.1.5b**) preparation by the sol-gel process. For example, for the film preparation, the precursor solution is first prepared and then the colloidal solution obtained is deposited on the substrate by one of two techniques (spin or dip-coating). After, the gel is dried and the xerogel films are obtained. The xerogel is the dried gel at ambient pressure. In the case of particles preparation, the colloidal solution undergoes condensation to a gel and then the evaporation of the solvent from the gel gives the xerogels. In the final step, the heat treatment in both cases is necessary to obtain well-ordered structures [67].
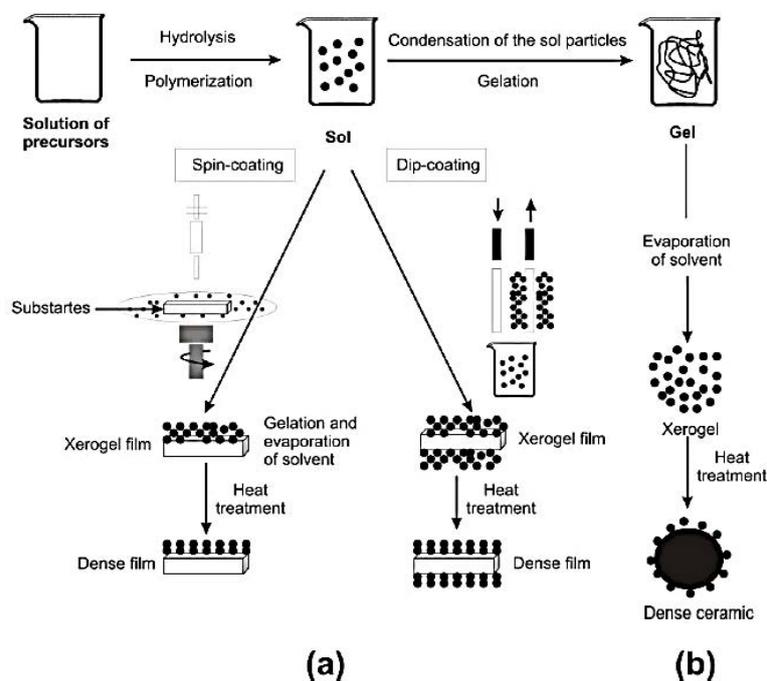


**Figure 1.1.5 Preparation routes of ZnO xerogels by sol-gel [68].**

The sol-gel method for the synthesis of ZnO NPs involves the alkaline hydrolysis of zinc salts in alcoholic or aqueous media. A slow and controlled hydrolysis generally leads to smaller

particle sizes [69]. The preparation usually undergoes different stages: solvation (preparation of the precursor solution), hydrolysis (sol), polymerization (gel) and transformation into ZnO (NPs) (**Figure 1.1.6**).
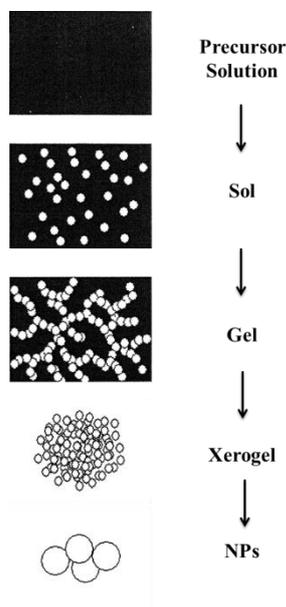


Figure 1.1.6 Schematic diagram of various steps involved in sol-gel process.

First, the precursor which is a zinc salt (zinc acetate, zinc nitrate, or zinc acetylacetonate) is dissolved in an alcohol like ethanol, methanol or isopropanol (**Equation 1**). As a second stage, a colloidal–gel of zinc hydroxide is formed through the addition of a base solution like potassium hydroxide (KOH), sodium hydroxide (NaOH), lithium hydroxide (LiOH) or tetramethyl ammonium hydroxide (TMAH) hydrolyzing the precursor, followed by polymerization of hydroxyl complex to form "Zn–O–Zn" bridges and finally transformed into ZnO (**Equation 2**).

$$Zn\,(OAc)_2 \rightarrow 2Zn^{2+} + 2(OAc)^- \tag{1}$$

$$Zn^{2+} + 2OH^- \rightarrow Zn(OH)_2 \rightarrow ZnO + H_2O \tag{2}$$

The choice of the solvent (size and activity) has obvious influence on the reacting progress and the final product [70]. Ethanol has smaller size and a more active OH⁻ and therefore it can react more easily to form a polymer precursor with a higher polymerization degree, which is required to convert sol into gel [71]. Bari *et al.* had observed that when TMAH was used as the solvent for zinc acetate to synthesis ZnO NPs via sol-gel, the particles were spherical in

shape (**Figure 1.1.7a**) and smaller (< 50 nm), while they were wire-shaped (**Figure 1.1.7b**) when NaOH was used [72].
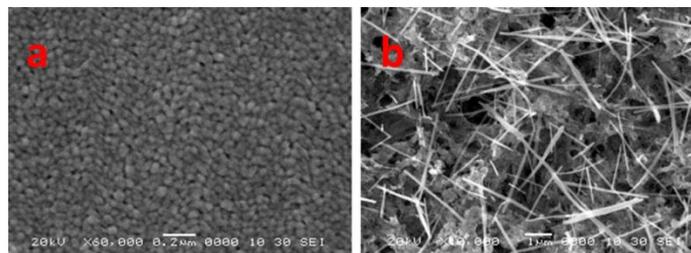


**Figure 1.1.7 SEM images of ZnO nanostructure using (a) LiOH and (b) NaOH solvents.**

The size of the synthesized ZnO QDs can be tuned by adjusting their synthesis time. ZnO QDs with tunable diameters were synthesized via sol-gel using self-made zinc-oleate complex as a precursor [73]. The synthesis time was varied from 5 min to 4 days obtaining NPs with diameters in a range of 2.2-7.8 nm. The results showed that the visible emission property of the ZnO QDs displays highly size-dependent behavior where with size decreasing, the visible emission peaks blue shifts to the positions with shorter wavelength. **Figure 1.1.8** shows the normalized PL spectra of the different size ZnO QDs dispersed in ethanol.
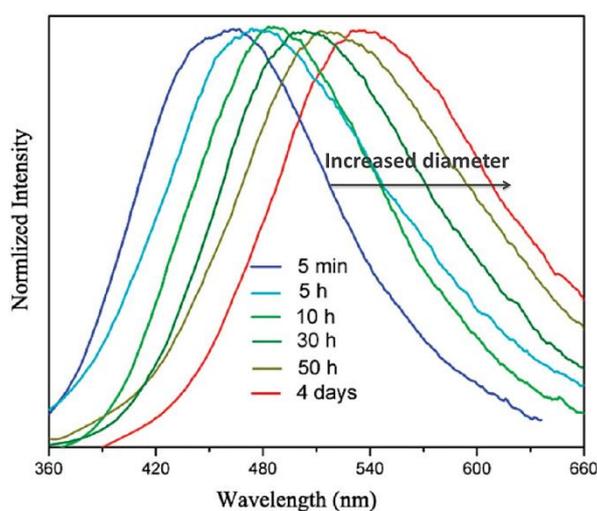


**Figure 1.1.8 Normalized PL emission spectra of ZnO NPs prepared at different time dispersed in ethanol [73].**

On the other hand, the annealing temperature is an important factor to control the morphology of the produced ZnO NPs. Jurablu *et al.* found that with increasing temperature the morphology of the particles changes to the spherical shape and the NPs were less agglomerated. The average diameter was obtained through transmission electron microscopy (TEM) analysis and found to be about 28 nm [74].

The size of the ZnO NPs can be also controlled by varying the concentration of the precursor, the ratio between the zinc precursor and the base, and the addition of ligands [75]. ZnO NPs were readily synthesized through sol-gel method using zinc acetate as a precursor and the average particle size was found to be 58.3 nm [76]. Self-assembled ZnO NPs with a smaller size of 4 nm were also prepared earlier by the dissolution of zinc acetate dehydrate in ethanol without the aid of special organic additives or face-specific organic molecules [77].

Solid state reaction method is another easy process to obtain crystalline ZnO NPs. In this one, ZnO NPs are prepared by mixing the precursors together at a specific temperature in one step. It is nontoxic, simple, low-cost and high-yield synthetic method, but it has some disadvantages like inhomogeneity, bigger crystallite and phase impurity [78]. A comparison was made by producing ZnO NPs using sol gel and solid state reaction method. It was found that when prepared under the same ambient conditions (temperature, pressure …) and keeping all the parameters same (precursors, molarity, solvent …); the NPs prepared via sol-gel route were highly crystalline and had smaller crystallite size ($\approx 24$ nm) as compared to the one prepared by solid state reaction method ($\approx 37$ nm) [68].

After the formation of ZnO NPs, their PL exhibits a continuous red-shift as it was seen that the size continues to grow even after the synthesis is stopped and its quantum yield (QY) decreases gradually [79]. Therefore, protective layers must be employed to the ZnO surface to inhibit further crystal growth and aggregation. Silanes, for examples, are used to coordinate with Zn atoms on the surface of ZnO QDs to hinder the formation of bulk ZnO. This method among the different methods will be mentioned in the next part.

### 1.1.1.3. Surface modification

In recent years, obtaining well defined structures of ZnO QDs is not the only concern of researchers because the surface functionalization of these particles is very important to use them in different application. ZnO QDs require enhanced properties which are a result of their surface functionalization. For example, when using the ZnO QDs in bio-imaging, it is necessary that these dots are able to conserve their fluorescence at one point and to easily disperse in aqueous media.

Consequently, the functionalization of ZnO QDs is of high importance for some purposes. On one hand is to stabilize the dots, especially in aqueous solution, because stability towards

water is strictly necessary for biological applications as the water molecules are able to degrade the ZnO QDs which lead to the loss of their photoluminescence properties [79]. On the other hand the grafting of specific functional groups onto ZnO surface for targeted analysis. On the third hand is to change or enhance ZnO luminescent properties by optimizing the surface structure of nanocrystals and minimizing the number of surface trap sites [43]. In order to stabilize ZnO QDs, various shells have been employed like silanes and polymers [80, 81]. In this context, during or after each ZnO QDs synthesis, a surface modification step is included [82-86]. Surface modification methods proposed by different groups are summarized in **Figure 1.1.9**. These methods are divided into inorganic ($SiO_2$, $Al_2O_3$), organic compounds (organic acids or silanes) and polymer layers (methacrylates) mentioning some of the resultant effects of each type of modification on the ZnO QDs.
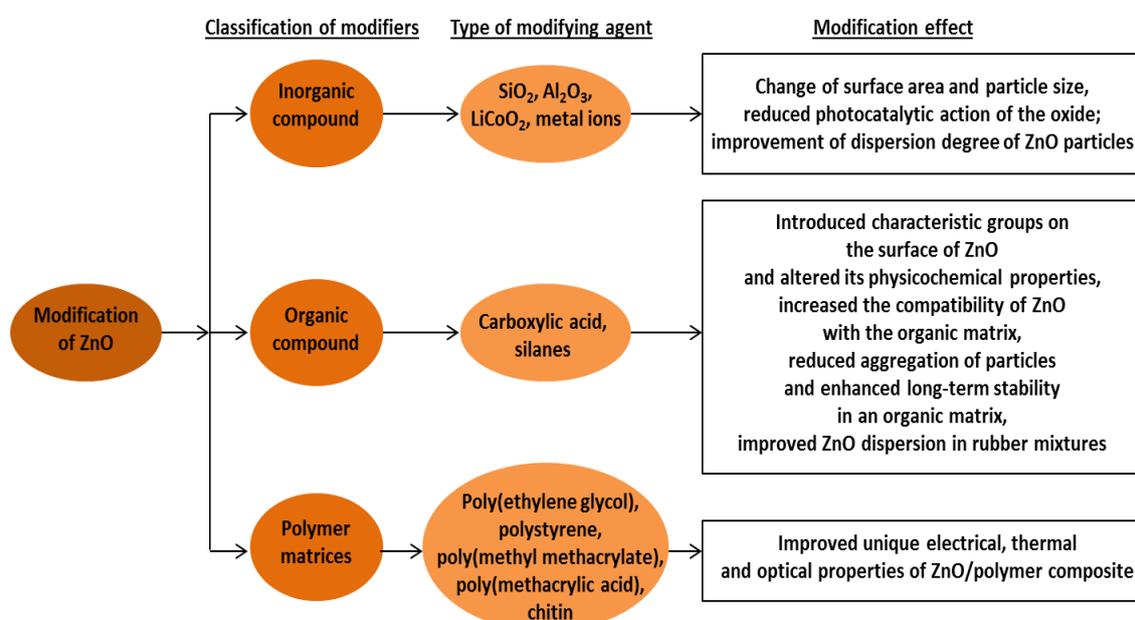


**Figure 1.1.9 Schematic diagram of the modification approaches of ZnO QDs [60].**

As we are interested in inorganic/organic core/shell QDs, we will describe the modification of ZnO QDs with organic molecules and mention some studies which reported the coating of ZnO QDs with organic acids, silanes and polymers.

Organic ligands, like oleic acid, are most of the time added as capping agents to stabilize the prepared QDs during the synthesis. Organic acids are used because carboxylates are known to strongly interact with metal oxides surfaces and allow controlling their size, shape, and dispersity [82]. In the work of Schejn *et al.* [86], carboxylate capped ZnO QDs were

synthesized using different ligands (oleic acid (OA), benzoic acid (BA), propionic acid (PA) and formic acid (FA)). The molecular structures of these ligands are schematically presented in **Figure 1.1.10**.
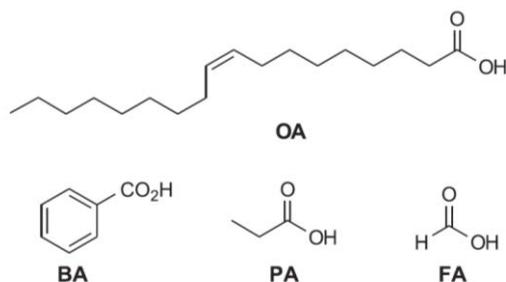


**Figure 1.1.10 Molecular structures of organic acids used in the work of Schejn *et al.* to modify ZnO QDs.**

The obtained ZnO NPs had diameters ranging between 3.6 to 5.2 nm and controlling some parameters like the reaction temperatures (20 or 35 °C), the propionate-capped ZnO NPs had optimal fluorescence quantum yields (QY) (up to 30 %) with narrow size distribution (4.2 $\pm$ 0.6 nm). **Figure 1.1.11** shows one TEM image with size distribution and diffraction pattern of propionate-capped ZnO NPs prepared at 35 °C.
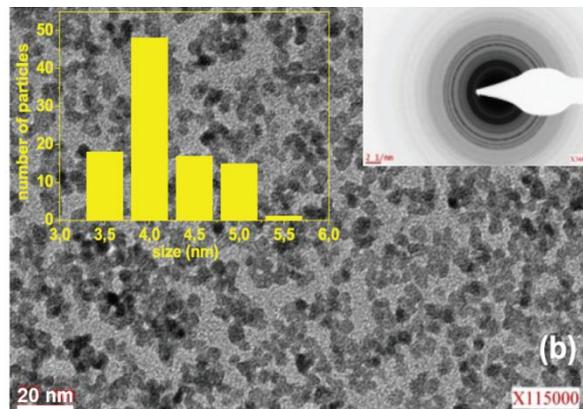


**Figure 1.1.11 TEM micrograph, size distribution and diffraction pattern of propionate-capped ZnO NPs prepared at 35 °C [86].**

Silane-based surface modifications of ZnO QDs have been also widely proposed forming a Si-O-Zn binding (**Figure 1.1.12**) [83, 87, 88]. This strategy has successfully been used for the stabilization of ZnO QDs in water. Trialkoxysilanes have a strong affinity with hydroxylated surfaces, forming covalent bonds with them, thereby creating a shielding barrier of cross-linked polysiloxanes that protects the nanocrystal at the core [89]. In addition to the stabilization and interaction ability, the attached silane molecules also have a very important

role of providing the NP surface with reactive groups like amine or halogen for further functionalization procedures.
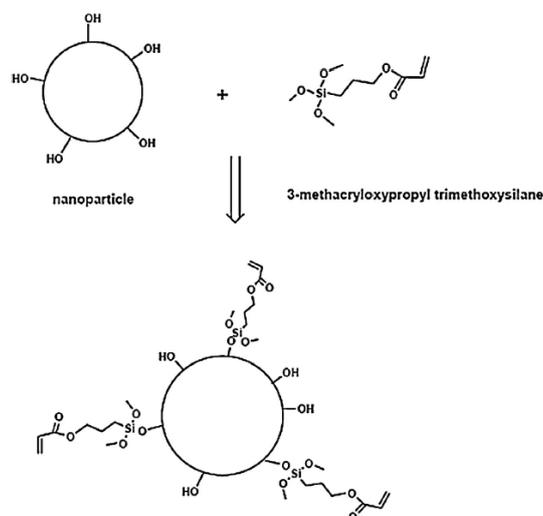


**Figure 1.1.12 Silane attachment to the surface of oxide NPs [87].**

A number of studies have been performed where silane molecules are attached to ZnO QDs surfaces. Aboulaich *et al.* have performed a study where three different poly(amino) silanes are chemically attached to ZnO QDs surfaces [89].
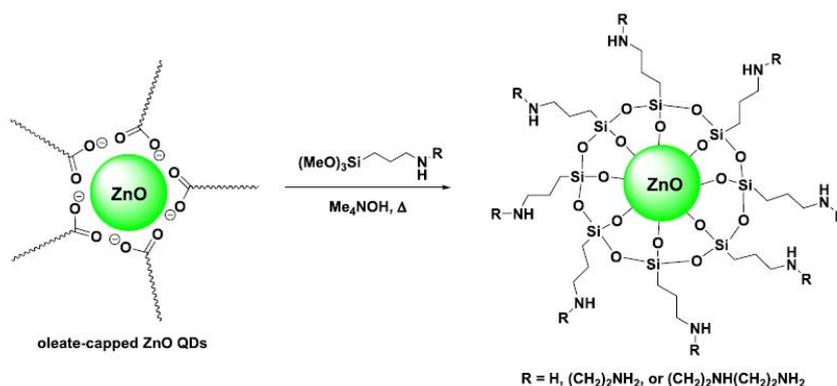


**Figure 1.1.13 Synthesis strategy of (poly)aminosilane-capped ZnO NPs [89].**

The aminosilanes were condensed using the same synthetic protocol where oleate-capped ZnO NPs were silanized in two step process. They were dispersed in toluene and then mixed with aminosilane. After, a solution of TMAH in ethanol was added with increasing the temperature to 85 °C. 15 min later, the suspension was cooled and the NPs were collected, washed and then redispersed again in toluene adding TMAH, increasing the temperature and keep on stirring for 30 min. The resulting aminosiloxane-capped ZnO NPs were collected and

washed with ethanol leading to a cross-linked shell that possesses outwardly directed amine groups (**Figure 1.1.13**). The NPs had an average diameter of about 4 nm and all PL excitation spectra recorded for an emission wavelength of 550 nm display a similar shape and present a strong absorption below 350 nm (**Figure 1.1.14**).
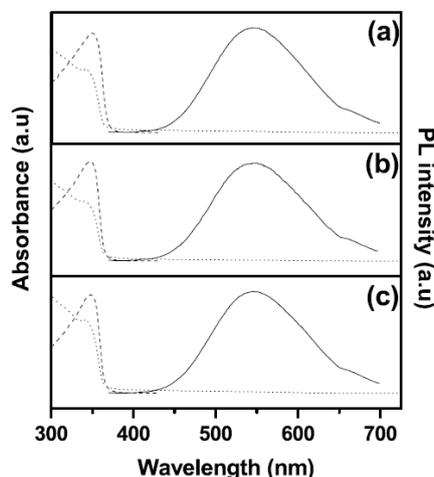


**Figure 1.1.14 Absorption spectra (dotted line), PL excitation (dashed line), and PL emission (solid line) of the three different ZnO@aminosiloxane NPs (a to c) dispersed in water [89].**

These NPs could be used as fluorescent probes in bio-imaging because of their low cytotoxicity [90] where the siloxane shell prevent the ZnO core from complete dissolution and offer large number of functional amine end groups.

ZnO QDs, previously prepared by modified sol-gel route of ultrasonic chemistry at 0 °C, were further modified with a bilayer of two silane compounds; hexadecyltrimethoxysilane (HDS) and aminopropyltriethoxysilane (APS). The complete synthesis procedure is described [91]. In brief, zinc precursor was dissolved in hot ethanol and then the solution was cooled down to 0 °C. Then the LiOH base was then added under ultrasound conditions. The NPs were precipitated in acetone, centrifuged and redispersed in ethanol. Then, the ZnO@HDS@APS nanocomposites were synthesized separately by coating the ZnO QDs first with the hydrophobic HDS layer and then the hydrophilic APS layer by the silane hydrolysis procedure in ethanol resulting in uniform and mono-dispersed 8 nm amine functionalized nanocomposites with tunable fluorescence from blue to green yellow (**Figure 1.1.15**). Systematic investigations verify that the resulting ZnO nanocomposites could present the high aqueous stability and unexpectedly, dramatically enhanced fluorescence intensities comparing to bare ZnO QDs [91].
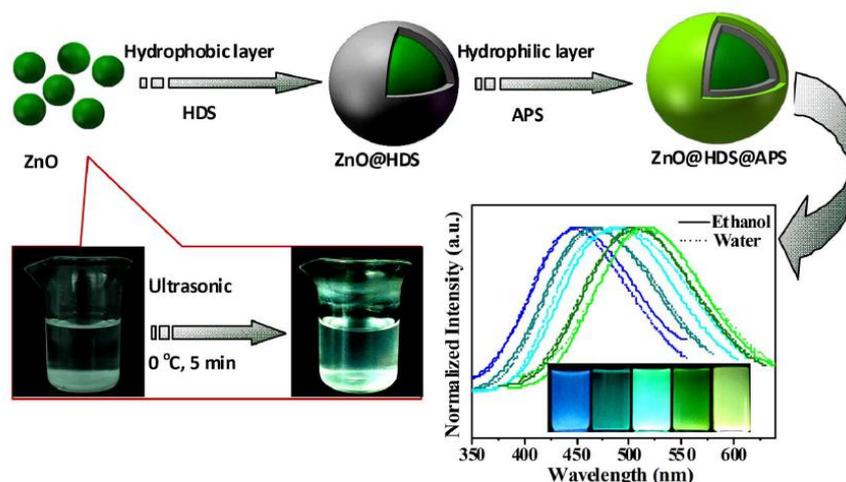
**Figure 1.1.15 The synthesis route to the bi-silanization modification of multicolor ZnO QDs with tunable fluorescence using hydrophobic HDS and further hydrophilic APS [91].**

These amine-functionalized ZnO NPs can promise the potential applications in the biological fields such as molecular labeling, cell or tissue imaging, drug delivery in and designing useful optical devices such as light-emitting diodes.

Coating ZnO QDs with a polymer shell is an efficient method for protecting and stabilizing the photophysical properties of the cores. A limited number of studies have been reported [51, 82, 92-94]. Xiong *et al.* were the first to report the synthesis of ZnO@polymer NPs [93, 95-99].

Xiong *et al.* have prepared stable aqueous ZnO@polymer core-shell NPs using poly (ethylene glycol) methyl ether methacrylate (PEGMEMA, Mn= 475 g/mol) resulting in highly efficient green and yellow emitting ZnO@polymer core-shell NPs that are stable in aqueous solutions. These QDs are not cytotoxic for living cells when their concentrations are below 0.2 mg/mL and are able to penetrate into the living cells labeling the cytoplasm [93].

ZnO NPs were modified with poly (ethylene glycol) (PEG) [82]. PEG-siloxane was covalently grafted on ZnO NPs as illustrated in **Figure 1.1.16**.
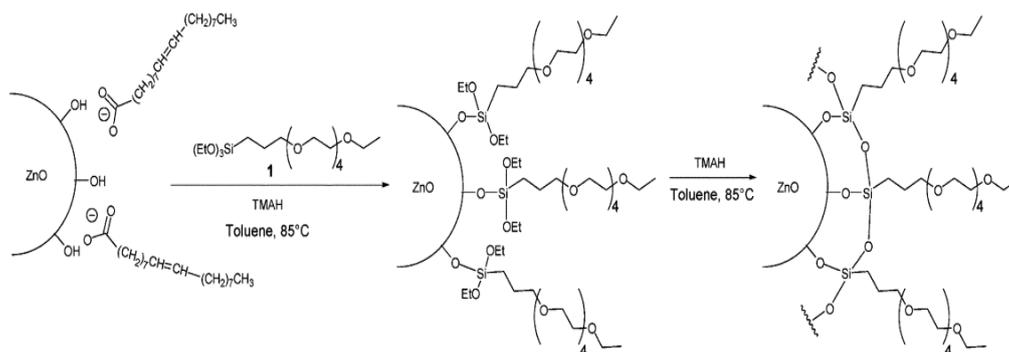
**Figure 1.1.16 Surface modification of ZnO NPs with PEG-siloxane.**

The end function of PEG allowed excellent water solubility for the dots after the siloxane unit bonded to the OH groups on the surface of the ZnO QDs. The QDs diameters didn't significantly change during the ligand exchange (5.9 nm). They almost had the same PL and UV-Vis absorption spectra as the oleate-capped ZnO QDs (no significant shift was observed for the absorption ($\approx$ 350 nm) and emission peak ($\approx$ 540 nm) (**Figure 1.1.17**).
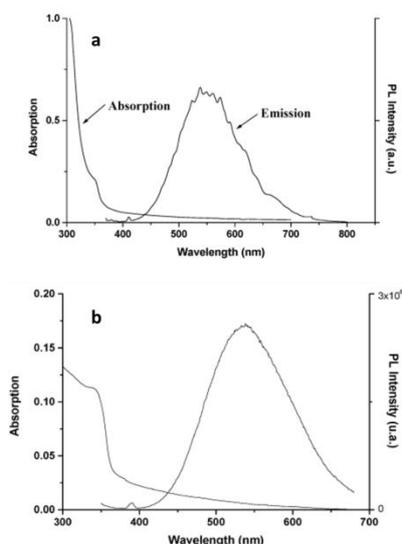


**Figure 1.1.17 Absorption and emission spectra of oleate-capped ZnO NPs in toluene (a) and PEG-siloxane capped ZnO NPs in water (b).**

And although moderate QY were obtained after functionalization ($\approx$ 8 % in water relative to 18 % for oleate-capped QDs), the siloxane coating did not quench the PL of the ZnO QDs. Using this procedure, ZnO NPs could be used as potential fluorescent labels for biological systems.

Biodegradable ZnO@polymer NPs were developed and used as drug delivery system for the treatment of brain cancer [94]. Polyacrylamide was used to graft the surface of the NPs. These

pH responsive, low toxic NPs are very stable in aqueous solution at pH 7.0, but rapidly decompose at pH 6.0, thus ensuring the safety of healthy tissues. After loading the anti-cancer drug DOX in the NPs, the NPs crossed the cell membrane through a cellular uptake pathway, decomposed at the endosomes or lysosomes to release DOX molecules, which finally penetrated into the nuclei to kill the cancer cells.

### 1.1.2. Iron oxide NPs

Magnetic nanoparticles (MNPs), a highly important class of inorganic NPs with sizes less than 100 nm, have special properties like high surface-volume ratios, large surface energy and excellent reactivity [100]. MNPs commonly consist of magnetic elements such as iron (Fe), nickel (Ni) and cobalt (Co). Ni and Co are highly magnetic materials but their drawbacks are their toxicity and sensitivity to oxygen making them easily oxidized. On the other hand, IONPs present a higher performance in terms of biocompatibility and chemical stability especially when used in bio-applications [101].

In this part, we will present the crystalline structure of magnetite ($Fe_3O_4$) and maghemite ($\gamma$-$Fe_2O_3$), the two most stable forms of iron oxide. Then, focusing on $Fe_3O_4$, we will describe its magnetic properties and behavior in aqueous media. After, we will present the different synthesis routes to prepare IONPs with good characteristics and the surface modification methods to enhance its properties. Finally, we will expand the talk about the functionalization of these NPs with polymer coatings and therefore its different applications.

### 1.1.2.1. Crystalline structure

Iron oxide generally exists as two main forms: magnetite ($Fe_3O_4$) and its oxidized form maghemite ($\gamma$-$Fe_2O_3$) [102]. Both $Fe_3O_4$ and $\gamma$-$Fe_2O_3$ have spinal crystal structure with oxygen atoms forming a face centered cubic lattices (fcc) and Fe ions occupying tetrahedral ($T_d$) (Site A) and octahedral ($O_h$) (Site B) sites (**Figure 1.1.18**) [103]. $Fe_3O_4$ possess a cubic inverse spinal structure with equally distributed $Fe^{3+}$ cations between $O_h$ and $T_d$ sites, and $Fe^{2+}$ cations only occupying $O_h$ sites and therefore the resulting magnetization arises only from these uncompensated $Fe^{2+}$ cations in the $O_h$ sites. $\gamma$-$Fe_2O_3$ has the same structure as $Fe_3O_4$ with a difference that it has only $Fe^{3+}$ cations and vacancies in their sub-lattices, and therefore the magnetization arises from uncompensated $Fe^{3+}$ cations distributed randomly over the $T_d$ and $O_h$ sites [104].
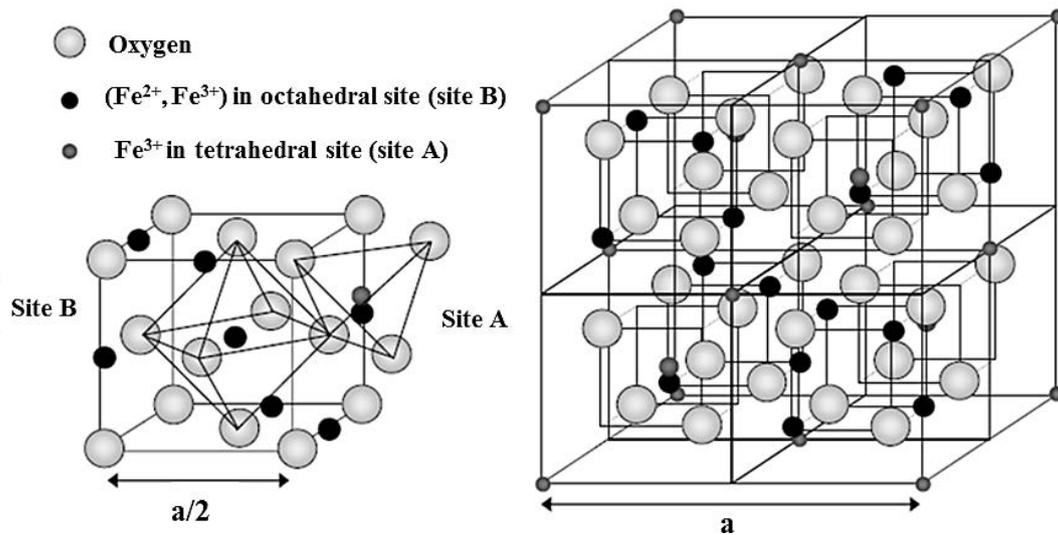
Figure 1.1.18 Representation of the inverse spinal structure of $Fe_3O_4$ (translated from Pauly [103]).

### 1.1.2.2. Magnetic properties

The electron configuration of the $Fe^{3+}$ and $Fe^{2+}$ ions are $1s^2 \, 2s^2 \, 2p^6 \, 3s^2 \, 3p^6 \, 3d^5$ and $1s^2 \, 2s^2 \, 2p^6 \, 3s^2 \, 3p^6 \, 3d^6$ respectively. In the ground state, $Fe^{3+}$ has five unpaired electrons and $Fe^{2+}$ has four unpaired electrons and these electrons in both cations determine the magnetic properties of the iron oxides forms [105]. The Fe atom, due to the 4 unpaired electrons in its 3d orbital, has a strong magnetic moment. Different magnetic states arise when crystals of Fe atoms are formed. Magnetism is a physical phenomenon of the response of a material in a magnetic domain. The principal of magnetism is found in the orbital and spin motions of electrons and how the electrons interact with one another. The description of the material"s magnetic properties is given by their response when exposed to the magnetic fields. The magnetic property of magnetic particles is described by the induced magnetization on the applied magnetic field (**Equation 3**).

$$B = H + 4\pi M \tag{3}$$

Where B is the flux density (T) or (G), H is the applied magnetic field (Oe) or (A/m) and M is the magnetization in electromagnetic units (emu) either per grams, $cm^2$, mole or atom.

The relation between M and H is necessary to understand the magnetism presented by IONPs. With different Fe atom organization, we can have four types of magnetisms with different orientations of magnetic moments (**Figure 1.1.19**) [106]:

– Paramagnetism: the magnetic moments are randomly aligned and the crystal has a zero magnetic moment.

– Ferromagnetism: the magnetic moments are oriented in parallel within the structure resulting in a spontaneous magnetization.

– Antiferromagnetism: the magnetic moments are oriented antiparallel and the crystal has no resultant spontaneous magnetization.

– Ferrimagnetism: the magnetic moments are oriented antiparallel and the net magnetic moment is non-zero due to the different magnitude of the magnetic moments.
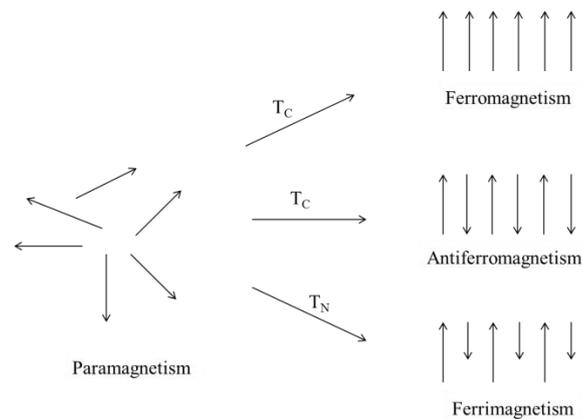


**Figure 1.1.19 Magnetic ordering in different types of materials (Redrawn from Teja *et al.* [106]).**

The magnetism of iron oxide was found to be highly size dependent. Bulk iron $Fe_3O_4$ NPs contain multiple domains and express strong ferromagnetic behavior but as the size is small enough (6 nm [105]), $Fe_3O_4$ is considered in the range of single domain and exhibits a superparamagnetic property at room temperature where it loses its magnetic characteristics in the absence of a magnetic field (**Figure 1.1.20**) [107] and this is considered to be very important because it eliminates the risk of particle aggregation [45]. At room temperature, the saturation magnetization ($M_s$) of bulk magnetite is of $\approx 92$ emu/g [108].
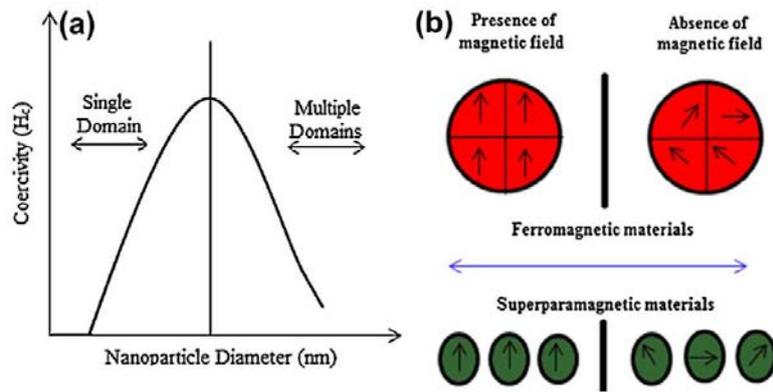
**Figure 1.1.20 Relationship between magnetization behavior of NPs size and the magnetic domain structures.**

In the case of superparamagnetism, when an external magnetic field of strength H is applied, the magnetic moments align with H and the magnetization curve is obtained showing that M increases with H until a saturation value $M_s$ is reached (**Figure 1.1.21**). This curve is not reversible and shows no hysteresis loop when H is removed as in single domains spins return to their original orientations [106]. Meanwhile, ferromagnetic particles could retain their magnetization direction when decreasing H after $M_s$ is reached, and thus have a remanent magnetization ($M_r$) at zero H (**Figure 1.1.21b**) displaying a hysteresis loop on the magnetization curve. $M_r$ can only be removed by applying a coercive field in the opposite direction to the initially applied field where $H_c$ is a measurement of the strength of the magnetic field required to remove the $M_r$ and get zero magnetization [106]. In accordance with superparamagnetic behavior, magnetite NPs exhibit zero coercivity which slowly builds as magnetite particle diameter increases [109].

**a**

Magnetization, M (emu/g)

Applied magnetic field, H (Oe)

**b**

Saturation
magnetization, $M_s$

M (emu/g)

**c**

M (emu/g)

Remanent
magnetization, $M_r$

Coercivity, $H_c$

H (Oe)

H (Oe)
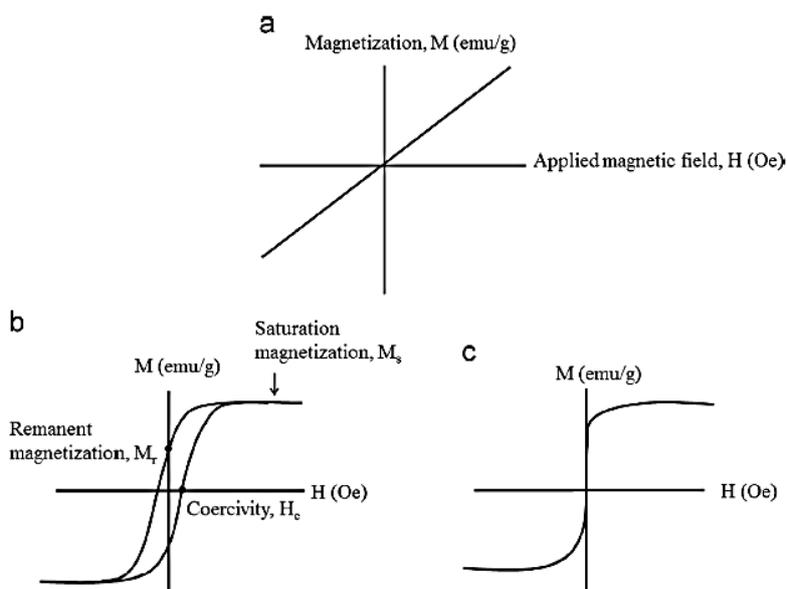
**Figure 1.1.21 Magnetization curves for paramagnetic (a), ferromagnetic (b) and superparamagnetic (c) materials [110].**

The ordered arrangement of magnetic moments decreases with increasing temperature due to thermal fluctuations of the individual moments. Beyond the Curie temperature ($T_c$), the material becomes disordered and loses its magnetization. At room temperature, magnetite has a $T_c$ of 850 K [111].

### 1.1.2.3. Synthesis

The size, shape, crystallinity and surface coatings play an important role in determining the magnetic properties of IONPs and these characteristics are manipulated using different synthesis procedures including co-precipitation [112], thermal decomposition [113], solvothermal and hydrothermal processes [114, 115], microemulsion process [116], microwave-assisted synthesis [117] and sonochemical method [118]. Other methods are also reported in the literature for the preparation of iron oxide nanostructures like physical [119] and chemical vapor deposition [120] and electro-deposition [121].

The advantage and disadvantage of some synthesis methods of IONPs is found in the review paper of Pang *et al.* on iron oxide-based magnetic materials [108]. Thermal decomposition of organometallic compound in the presence of surfactants (like oleylamine and oleic acid) at high temperatures produce highly crystalline and monodisperse IONPs with good control of size and shape [122]. Hydrothermal method has various advantages such as high reactivity of the reactants, facile control of product morphology, and good crystallization of products

[123]. Indeed, every method has its positive and negative points as well, however, co-precipitation is the most commonly used to synthesize IONPs in terms of simplicity, ease and cheapness to obtain large quantities of IONPs [124]. In addition, no special stabilizing agent is needed during the synthesis and the products are water-soluble which is promising for environmental applications [108].

IONPs synthesized by co-precipitation usually exhibit a size below 50 nm. Nano- $Fe_3O_4$ and $\gamma$-$Fe_2O_3$ are obtained through precipitation of ferric ($Fe^{3+}$) and ferrous ($Fe^{2+}$) aqueous salt solutions by the addition of a base like ammonium hydroxide ($NH_4OH$), potassium hydroxide (KOH) or sodium hydroxide (NaOH) [125]. In general, the synthesis process of magnetite involves the precipitation of iron precursors in an oxygen free environment at room or elevated temperatures up to 90 °C at a molar ratio of 2 $Fe^{3+}$:1 $Fe^{2+}$ as expressed in the overall reaction in **Equation 4** [126]:

$$Fe^{2+} + 2\,Fe^{3+} + 8\,OH^- \rightarrow Fe_3O_4 + 4\,H_2O \tag{4}$$
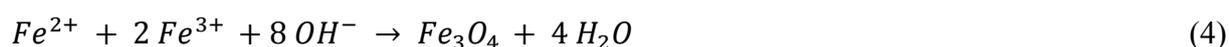
After, the brownish/black iron oxide precipitate is collected by magnetic separation or centrifugation and further treatment with a suitable surfactant or a capping agent like oleic acid or concentrated base or acid solutions is needed to stabilize the magnetic suspension [127]. However, the elimination of oxygen from the reaction medium is very important because $Fe_3O_4$ is sensitive to oxygen and can readily oxidize to $Fe(OH)_3$ or $\alpha$-$Fe_2O_3$, therefore it is necessary to maintain a continuous flow of an inert gas throughout all the synthesis [128]. On the other hand, removing oxygen, for example, also affect the size of the particles where a size reduction in $Fe_3O_4$ NPs was observed in comparison to methods without removing the oxygen [129].

The morphology, composition, magnetic behavior and surface properties of the obtained IONPs are strongly dependent on the experimental conditions which include the stoichiometric ratio of ferric to ferrous salts, the type of the salts used (chlorides, sulfates, or nitrates), the reaction temperature, the nature and concentration of the base, the nature of the stabilizing agent, the pH value and other reaction parameters [130]. As a result, IONPs with suitable diameter and magnetic responsiveness can be obtained by controlling the synthesis conditions. Vikram *et al.* could tune the magnetic properties of the IONPs by simply changing the molar ratio of ferrous to ferric ions and the concentration of ammonium solution where

they obtained superparamagnetic NPs with different particle sizes ranging from 7 to 25 nm and magnetic properties with $M_s$ between 2 to 75 emu/g [131].

$Fe_3O_4$ NPs have been also synthesized by co-precipitation method performed under various precipitation conditions, *i.e.* at pH range between 10 and 13 in the presence of three different bases (NaOH, KOH and tetraethyl ammonium hydroxide [$(C_2H_5)_4NOH$]) at room temperature either by a slow or fast addition of the alkaline solution into the reaction solution [132]. The size reduction of magnetite NPs was affected by both the pH and the slow or fast addition of the basic solution to the solution of mixed $Fe^{2+}$ and $Fe^{3+}$ ions. The resulting NPs showed characteristics of superparamagnetism at room temperature and $M_s$ which was dependent on the crystal size. **Figure 1.1.22** shows the magnetization curves of four samples obtained with different sizes and we can see that the $M_s$ decreased as the magnetite NP size decreased e.g. the sample S1 with a size which is equal to 11.5 nm had a $M_s$ of 75.3 emu/g while this value decreased to 54.1 emu/g for the smaller sized sample $F5_{Na}$ of 8.2 nm. As a result, the $M_s$ values are usually smaller with decreasing the size of the NPs and this effect could be attributed to the presence of defects at the particle surface which affects the magnetic properties as the surface curvature of the NP was larger for smaller particle size, which encouraged disordered crystal orientation on the surface and thus resulted in lower $M_s$ values in smaller NPs [133].
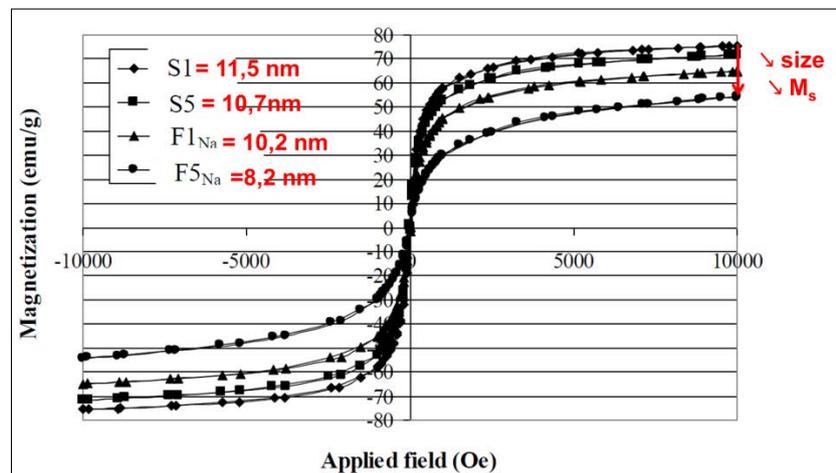


**Figure 1.1.22 Magnetization curves for Fe₃O₄ NPs synthesized by co-precipitation [132].**

### 1.1.2.4. Surface modification

Naked IONPs are not often prepared, probably because of their pH-dependent surface properties and strong aggregation in neutral aqueous media, therefore their surface has to be

modified either during or after their synthesis [134]. The surface modification of the IONPs with different materials like silanes and polymers can effectively render them water soluble and improve their stability under physiological conditions. In terms of the organic/inorganic core/shell NPs; the silane agent is often used to modify the surface of IONPs for the advantage of high density of surface functionality allowing further connection with other metal, polymers and biomolecules [135, 136]. Silane agents render the IONPs more stable with respect to aggregation and keep them well-dispersed in aqueous media in addition to protecting them against mild acid and alkaline environments [137]. The hydroxyl groups on the iron oxide NPs surface reacted with the methoxy groups of the silane molecules leading to the formation of Si–O bonds and leaving the terminal functional groups available for immobilization the other substance like polymers. When combining the IONPs with polymers, these materials have many potential technological applications, such as water treatment, catalysis, cell labeling, cell separation and drug targeting [138, 139].

The covalent anchoring of polymers to IONPs can enhance colloidal stability as compared with a polymer adsorption on the surface [140]. As a result, the coating of IONPs surface with polymers using silane agents as anchoring agents is an interesting approach to obtain IONPs with good colloidal stability in aqueous and biological fluids. Butterworth *et al.* studied the colloidal stability of IONPs coated with PEG modified trimethoxysilanes (PEG-silane) of different molecular weights (340 to 1000 g/mol) in water [141]. These PEG-coated IONPs showed greatly enhanced colloid stability properties with respect to the uncoated particles where the latter was unstable between pH 4 and 9 in the presence of many ionic species including metal ions, $NH_4^+$ and $SO_4^{2-}$. On the other hand, IONPs with low molecular weight PEG showed reversible flocculation upon addition of a saturated salt solution and poor stability in suspension.

Barrera *et al.* also reported the covalent attachment of poly(ethylene glycol) (PEG) to $Fe_3O_4$ NPs [142]. These NPs were coated with PEG-silane by using a ligand exchange reaction to replace the oleic acid molecules on the IONPs during synthesis. As a result, the shell of the NPs consisted of a mixture of PEG and 3-aminopropyl triethoxysilane (APS) (**Figure 1.1.23**). The aim of their work was to study the effect of PEG graft molecular weight (750, 1000, 2000 and 5000 g/mol) on the size, surface, magnetic properties, and colloidal stability in aqueous media and biological buffers of IONPs coated with PEG-silane.
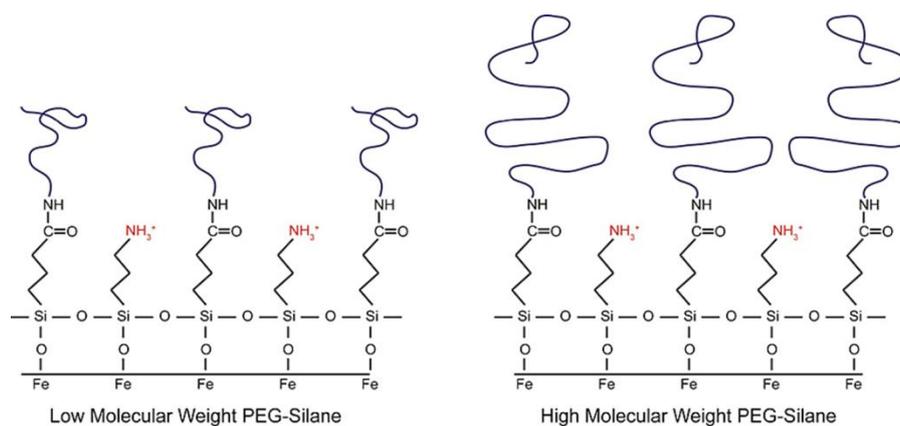
**Figure 1.1.23 The surface of IONPs coated with low and high molecular weight PEG-silane [142].**

For low molecular weight PEG, the amine groups were exposed on the surface of the NPs rendering them positively charged. While for high molecular weight PEG, the amine groups were shielded by the longer polymer chains and the NPs were almost neutrally charged. Particles exhibited a narrow size distribution with no significant agglomeration and the hydrodynamic size was between 10.6 and 11.4 nm. On the other hand, the PEG shell with the different molecular weight didn"t significantly influence the magnetic properties of the IONPs. At 298 K, all the samples were superparamagnetic, with $M_s$ of 15–18 emu/g. Results also showed that colloidal stability was mediated by electrostatic repulsion for low molecular weight PEG (< 1000 g/mol) and by steric repulsion for high molecular weight PEG. As the electrostatic interactions were screened by free ions in solution, the NPs with 750 g/mol PEG and in some cases for 1000 g/mol PEG NPs aggregated in media with high ionic strength and in biological media (PBS). This indicated that a molecular weight of PEG greater than 1000 g/mol is needed to render the NPs colloidally stable in biological media.

## 1.2. Thermo-responsive polymers

### 1.2.1. Properties

Responsive polymers are defined as macromolecules that can undergo changes in their volume in response to external stimulus, *i.e.* chemical one (pH, ionic strength, addition of a chemical agent, …) or physical one (temperature, electric or magnetic fields, mechanical stress, …) [143]. The macroscopic changes that occur are reversible; therefore the system is capable of returning to its initial state when the trigger is removed [144]. According to their physical forms, these polymers are classified into three classes as shown in **Figure 1.1.24**: (a) linear free chains in solution, (b) covalently cross-linked gels and reversible or physical gels,

which can be either microscopic or macroscopic networks and (c) chain adsorbed or surface-grafted, where the polymer reversibly swells or collapses on a surface, converting the interface from hydrophilic to hydrophobic and vice versa, once a specific external parameter is modified [145].
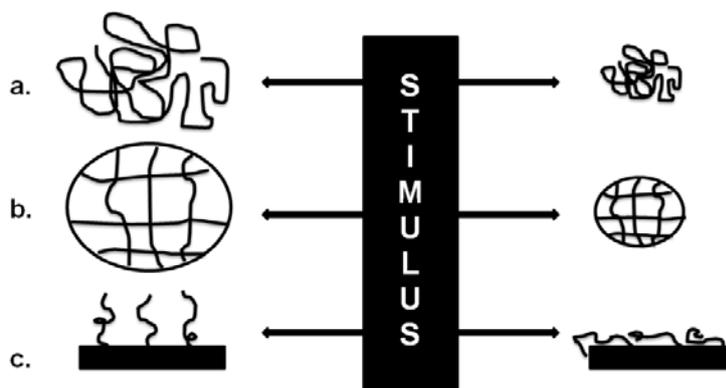


**Figure 1.1.24 Classification of stimuli-responsive polymers by their physical forms: (a) Linear free chains in solution, (b) covalently cross-linked reversible gels and (c) chain adsorbed or surface-grafted forms (redrawn from Kumar *et al.* [145]).**

In the case of core/shell NPs, the polymer chains are grafted on the surface of the inorganic NPs. When applying an external stimulus on these NPs, the polymer swells or collapses on the surface leading to the aggregation of the NPs forming a separate phase (**Figure 1.1.25**). Responsive polymers do not aggregate but the conformational transition from a hydrophilic to a hydrophobic state renders the surface hydrophobic as the surface is hydrophilic when the polymer is in its expanded soluble state and hydrophobic when in its collapsed insoluble state [144].
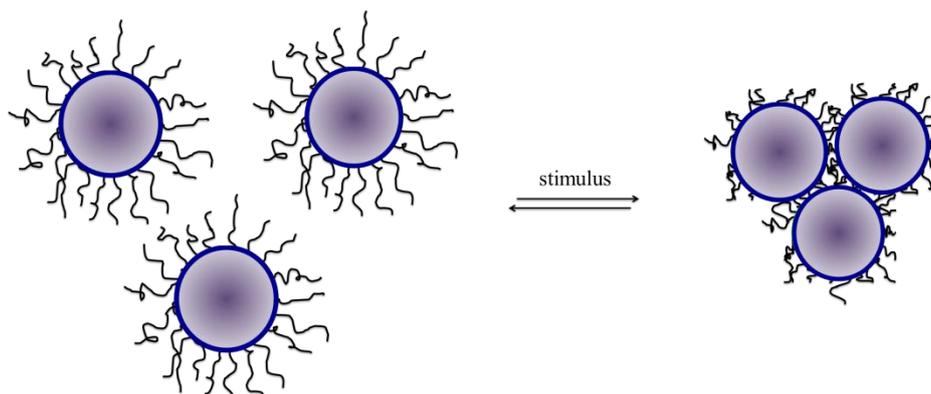


**Figure 1.1.25 Schematic illustration of the phase transition from dispersed to collapse state of the polymer on the surface of the NPs leading to aggregates.**

In the case of thermo-responsive polymers (TRPs), *i.e.* polymers which respond to change in temperature, this change in surface hydrophobicity occurs when the polymer changes its aqueous solubility at a critical solution temperature (CST). TRPs exhibit two types of CST behaviors: a lower critical solution temperature (LCST) and an upper critical solution temperature (UCST).

LCST is the critical temperature point below which the polymer is soluble in aqueous media resulting in one phase e.g. they are completely miscible. While the contrary in the case of UCST; where the polymer is separated from the aqueous media. LCST and UCST are the minimum and the maximum of the phase diagram respectively (**Figure 1.1.26**).
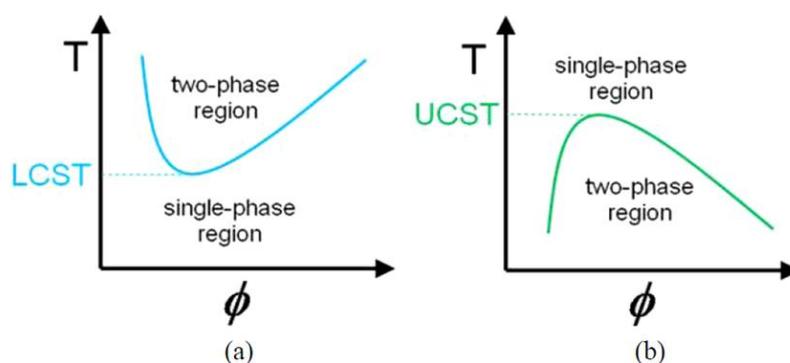


**Figure 1.1.26 Schematic illustration of phase diagrams for polymer solution (a) LCST and (b) UCST behavior.**

At the LCST the hydrophobic polymer chains collapse leading to aggregates, subsequently causing turbidity in solution and the formation of visible particles depending on polymer concentration. **Figure 1.1.27** shows a solution transition from clear to turbid when the temperature is increased above the LCST.



**Figure 1.1.27 Solution transition from clear to turbid when increasing temperature above LCST (left to right).**

The hydrophobicity above the LCST can be explained by the Gibbs equation: which is $\Delta G = \Delta H - T\Delta S$, where G is the Gibbs free energy, H is the enthalpy and S is the entropy of the

system [146]. For a thermodynamically favorable dissolution process of a polymer, the entropy change upon mixing should be positive while the change of Gibbs energy ($\Delta G$) should be negative. The entropy is responsible for the phase separation due to the breaking of hydrogen bonds between water and polymer chains when increasing the temperature. Specifically, the main driving force is the entropy of the water, that when the polymer is not in solution, the water is less ordered and has higher entropy. This is called the "hydrophobic effect". It is noteworthy that LCST is an entropically driven effect while UCST is an enthalpically driven effect [146].
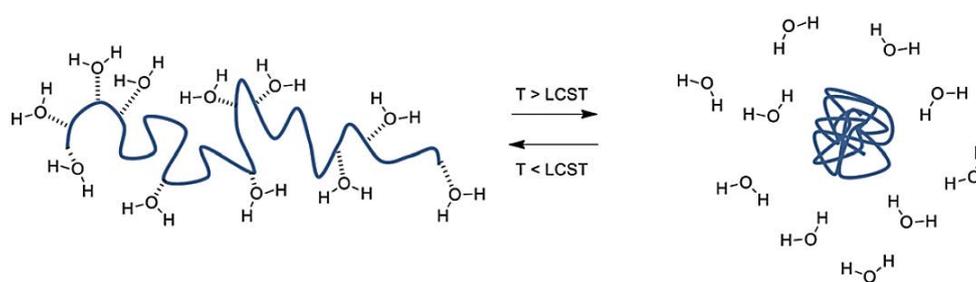


**Figure 1.1.28 Schematic demonstrating the change in polymer conformation (coil – globule) observed when a polymer solution is heated above its LCST [147].**

Below LCST, the polymer is in its soluble state due to the extensive hydrogen bonding interaction with the water molecules. By increasing the temperature, the bonding between the polymer chain and the water molecules is disrupted allowing intra- and intermolecular hydrogen bonding between polymer molecules. As a result, the polymer chains collapse and aggregate in a globule conformation (**Figure 1.1.28**) [147]. As a transition of phases takes place when crossing the CST, the latter could be also referred to as "the transition temperature". This temperature can be modulated by either modifying the structure of the monomer unit, for example copolymers based oligoethylene glycol (meth) acrylate, or by modification of the dispersion medium such as the salt concentration, addition of surfactants or co-solvents [148].

The polymer structure is a very important point and significantly changes the phase transition temperature. A modification of the carbon main chain can cause a significant variation. For example, the presence of methyl group in a monomer unit increased the transition temperature as the methyl group provides additional flexibility to the polymer [149]. The modification may also be made by addition of a hydrophilic or hydrophobic co-monomer; the phase

transition temperature will be higher or lower, respectively. Adding a co-solvent also has an effect on the polymer phase transition. A water/alcohol mixture, for example, leads to a variation of the phase transition temperature. This variation will depend on the molar or volume fraction of alcohol with an inflection point at lower temperatures [150].

Various TRPs with different transition temperatures were reported by Roy *et al*. They almost covered recent examples and results of newly developed TRP systems of LCST and UCST behaviors. Among them are poly N-substituted (meth) acrylamides, poly N-vinylalkylamides, poly dimethylaminoethyl methacrylate, poly alkyloxide copolymers, poly phosphazenes, poly vinyl ethers and polyethers, polypeptide and related artificial poly amino acid and polyphosphoester-based TRPs, TRPs based on dendrimers and hyperbranched polymers, etc … Some of these TRPs, their structure and LCST in water are listed in **Table 1.1.1** [151].

**Table 1.1.1 Structures and transition temperatures of some thermos-responsive polymers [151].**

| Name | Structure | LCST (°C) in water |
|---|---|---|
| Poly(N,N-diethylacrylamide) (PDEAM) |  | 33 |
| Poly(N-vinylisobutyramide) (PNVIBA) |  | 39 |
| Poly(dimethylaminoethyl methacrylate) (PDMAEMA) |  | 14-50 |
| Poly(propylene oxide) (PPO) |  | 0-50 |

| | | |
|---|---|---|
| Poly[bis((ethoxyethoxy)ethoxy) phosphazene] (PBEEP) |  | 38 |
| Poly(2-methoxyethyl vinyl ether) (PMOVE) |  | 70 |
| P(Val-Pro-Gly-Val-Gly); (Val = valine, Pro = proline, Gly = glycine) |  | 27 |
| Poly(methacrylamide) (PMAAm) |  | UCST= 57 |
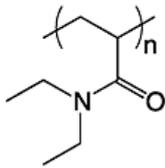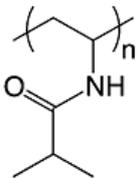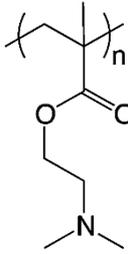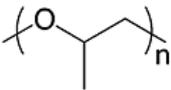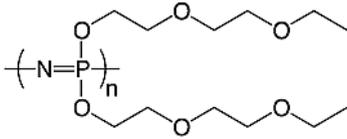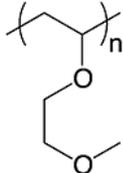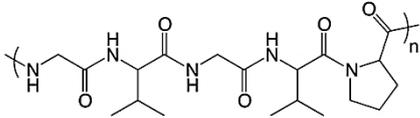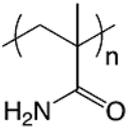
TRPs which have a LCST have gained an increasing interest in the recent years. On the other hand, polymers that have thermo-responsive property in water are especially important since aqueous media are biologically relevant. Such polymers are promising building blocks of smart responsive materials such as biosensors, tissue engineering, and drug carriers [152]. Among different TRPs, poly (N-isopropylacrylamide) (PNIPAM) is the most extensively studied TRP (**Figure 1.1.29**). PNIPAM has a LCST of 32 °C in water [153]. Below the LCST, PNIPAM chains extend due to hydrogen bond formation between the hydrophilic segments in the side chains of the polymer and water. In addition, the hydrogen bonds form a stable hydration shell around the hydrophobic groups leading to fundamental water uptake at low temperatures. Above the LCST, hydrogen bonding weakens, and the intrinsic affinity of PNIPAM chains dominates, causing an abrupt collapse in the polymer free volume due to the release of entrapped water (**Figure 1.1.30**) [154].
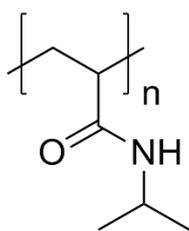
**Figure 1.1.29 The chemical structure of PNIPAM.**

Research groups frequently use PNIPAM because its LCST is approximately close to body temperature and this temperature can easily be adjusted to an appropriate temperature (≈ 40 °C) by the introduction of a hydrophilic co-monomer such as poly (*N, N*-dimethylacrylamide) (PDMAAm) [144]. However, one drawback of using PNIPAM in biological applications is the presence of the amide group in its structure which was recently described as a slightly cytotoxic [41]. The presence of multiple secondary amide functions in its molecular structure may lead to the formation of cooperative H-bonding interactions with other amide or carboxyl groups from the polymers, in particular with proteins [155-157]. In its collapsed state, the amide groups of PNIPAM lead to the formation of intramolecular and intermolecular NH…O=C hydrogen bonding interactions. Hence, during the cooling process, the rehydration of PNIPAM is hindered by these additional interactions, leading to a marked hysteresis [158].
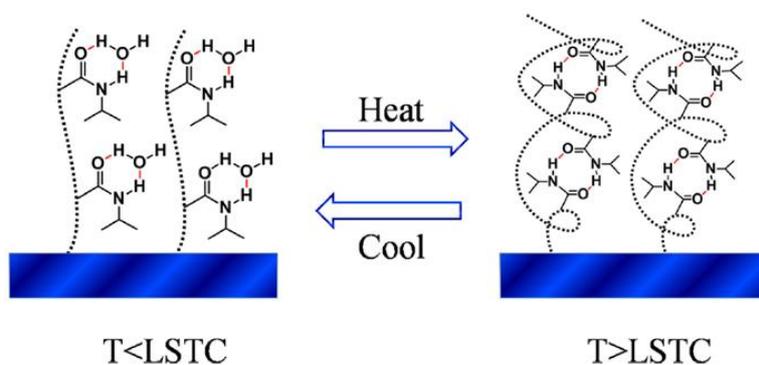


**Figure 1.1.30 Responsive behavior of PNIPAM [154].**

As a good alternative of PNIPAM, poly (oligo (ethylene glycol) methacrylate) co-polymers have attracted great attention in the previous years due to their biocompatibility. These polymers combine the advantages of poly (ethylene glycol) (PEG) and thermo-responsivity in a single macromolecular structure. PEG is well known to be used in biological application because it is biocompatible and improves the circulation time of NPs in the blood [24].

### 1.2.2. Oligo (ethylene glycol) methacrylates

Poly (ethylene glycol)/ poly (ethylene oxide) (PEG/ PEO) is a neutral, non-toxic, uncharged, highly mobile, synthetic polymer that consists of repeating ethylene oxide units. Graft copolymers containing PEO as side chains attached to the backbone have attracted significant interest because of their unique properties. Poly (oligo (Ethylene Glycol) Methyl Ether Methacrylate "Poly (OEGMA)" is a comb-type PEO which includes a short oligo(ethylene glycol) chains that are grafted to the methacrylate backbone (**Figure 1.1.31**) [159].
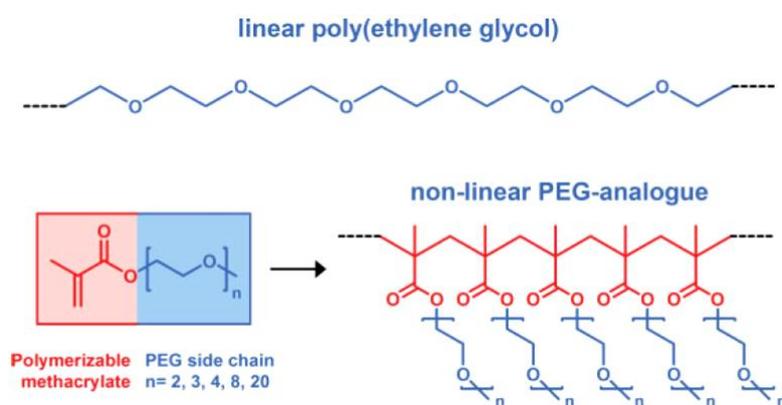


**Figure 1.1.31 Molecular structure of standard linear PEG and nonlinear PEG-analogues constructed with oligo(ethylene glycol) (macro)monomers [159].**

Random copolymers prepared from 2-(2-methoxyethoxy) ethyl methacrylate (MEO$_2$MA) and OEGMA are of great interest to be used as thermo-responsive material for biological applications due to their biocompatibility replacing the PNIPAM which is cytotoxic. On the other hand, their phase transition is generally reversible (*i.e.*, heating and cooling cycles are roughly comparable) as there is no strong hydrogen bond donor in the molecular structure of these polymers and therefore no possibility of forming stabilizing hydrogen bonds in the collapsed state.

The LCST of MEO$_2$MA, OEGMA$_{300}$ and OEGMA$_{475}$ is 26, 64 and 90 °C, respectively [159] and the structures of the individual monomers are presented in **Figure 1.1.32**.
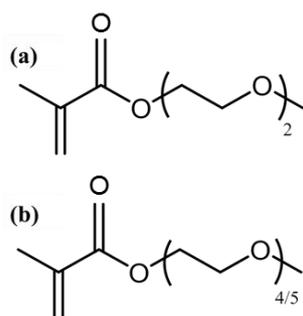
**Figure 1.1.32 Chemical structure of (a) 2-(2-methoxyethoxy) ethyl methacrylate (MEO₂MA) and (b) oligo (ethylene glycol) methacrylate (OEGMA₃₀₀).**

A transition temperature between 26 and 90 °C (26 and 64 °C in case of $MEO_2MA$-$OEGMA_{300}$) can be precisely adjusted by simply varying the co-monomers ratio [160]. And as the LCST values depend on polymer concentration and molecular weight, methacrylates with less ethylene glycol units have smaller LCST as in this case more $MEO_2MA$ molecules are presented in the structure shifting the temperature more towards the LCST of $MEO_2MA$ [159].

**Figure 1.1.33** shows the variation of the LCST as a function of the theoretical average number of $OEGMA_{475}$ units in a copolymer of $MEO_2MA$-$OEGMA_{475}$ [161]. The copolymer becomes more hydrophilic as the average number of OEGMA units in the chains is increased. For example, to obtain a LCST at 37 °C, ≈ 8.5 % by composition of OEGMA should be present in the copolymer.
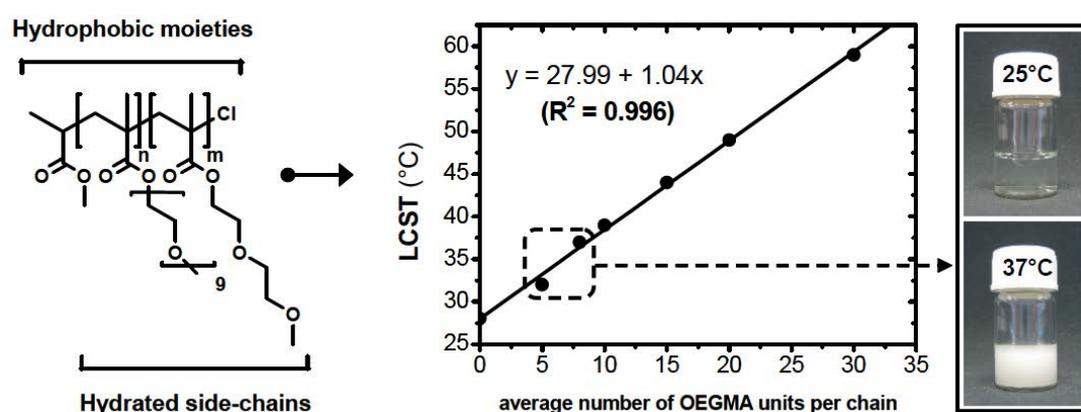


**Figure 1.1.33 Variation of LCST as a function of the theoretical average number of OEGMA₄₇₅ units in a copolymer of MEO₂MA-OEGMA.**

Lutz *et al.* synthesized copolymers of $MEO_2MA$ and $OEGMA_{300}$ [162]. The authors showed that tuning the LCST between the two LCST of each polymer range with a precision of 0.5 °C

was possible by changing co-monomer ratios in the polymerization feed. They reported the transition temperature of the MEO$_2$MA-OEGMA$_{300}$ copolymer to be 26 and 65 °C, respectively. This is expected since the hydrophilicity of OEGMA$_{300}$ is higher than that of MEO$_2$MA.

### 1.2.3. Effect of salt on polymer behavior

For biomedical application, it is very important to consider the effect of salts as the biological media is rich in salts in addition to amino acids, glucose, vitamins and other nutrients [163]. Salts are well known to change the solubility of polymers in water by disrupting the hydration structure surrounding the polymer chains as a result their presence in the solution affects the performance and changing the LCST of TRPs [164]. Increased ionic strength reduces the LCST as the salt deconstructs the weak interactions between the water molecules and the polymer. At a critical salt concentration, the medium is not a good solvent for the polymer [165]. The effect of the salt depends on its nature [166] and it is well known that the influence of ions follow the Hofmeister series, which originates from the abilities of ions to precipitate proteins [167]. The effect of anions increases in the order:

$$CO_3^{2-}> SO_4^{2-}> HPO_4^{2-}> F^-> Cl^-> Br^-> I^-> ClO_4^-> SCN^-$$
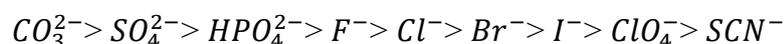
In the work of Lü *et al.* [156], results showed that LCST values decreased as the salt concentration increased (**Figure 1.1.34**).
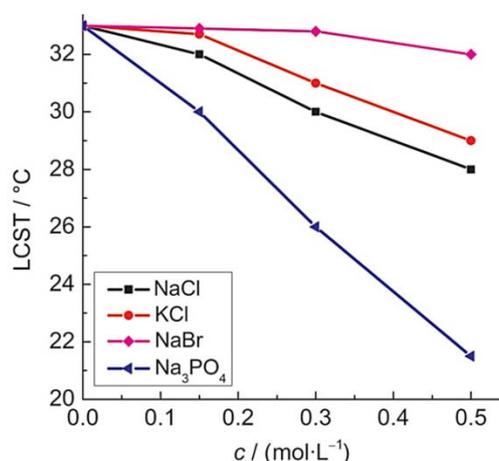


**Figure 1.1.34 Plots of the LCST of MEO$_2$MA-OEGMA as a function of salts concentration (mol/L) [156].**

It can be seen that the four different salts studied have also different effect on the LCST of the copolymer. Trisodium phosphate (Na$_3$PO$_4$) has the biggest effect (decrease of 12 °C with c =

0.5 mol/L). This effect decreased according to the hofmeister series where Br⁻ had the lowest one (decrease of only 1 °C with c = 0.5 mol/L). It was explained that the higher the valence of the anion, the greater the effect on the LCST is.

## 1.3. Polymerization process of polymer on NPs surface

The process of grafting polymer chains on the surface of NPs can impart new properties to materials in carefully controlled ways and it is an essential technique for many applications.

### 1.3.1. Grafting methods "grafting from"

The grafting of polymers (such as TRPs) on the surface of inorganic NPs can not be obtained by simply mixing all the ingredients in one container. Different steps and parameters should be taken into account to establish well defined TRP- inorganic NPs hybrids.

The grafting of polymers to the surface of inorganic NPs could be performed directly or indirectly. The direct route involves physical adsorption as in the case of creating thin films on QDs as a result of hydrophobic interactions, while the indirect route is performed by covalent grafting techniques which require a ligand exchange step to attach the polymer chains by single or multiple bonds [168].

Two methods have been reported in the literature to covalently graft polymer chains on the surface of inorganic particles. The first method is the "grafting to" method in which the end-functionalized polymers react with an appropriate surface. The second method is the "grafting from" method in which polymer chains are grown from an initiator-terminated self-assembled monolayer. The schematic representations of the "grafting to" and "grafting from" methods are shown in **Figure 1.1.35** [87].
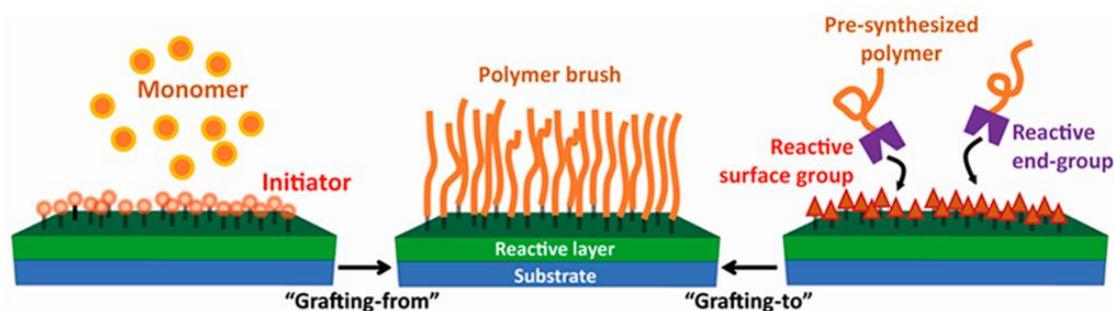


**Figure 1.1.35 Schematic description of the "grafting from" and "grafting to" approaches [169].**

The "grafting-to" approach involves a pre-synthesized polymer chain reacting with a surface to anchor the polymer while in the case of "grafting from" the polymerization starts from the surface by simply anchoring an initiator to the appropriate substrate [169].

The "grafting-to" allows a good control over the length of the polymeric chains and better characterization of the polymer before grafting but it requires the polymer chain-end to have a terminal functionality, moreover it may be less effective for higher loadings or higher molecular weights of polymers [170]. On the contrary, the "grafting-from" method usually yields better coverage densities [171]. It has been the most used in the synthesis of hybrid materials for functional coatings, because it is easy to polymerize a wide variety of monomers and allows the control of functionality, density and thickness of polymer brushes.

Thermo-responsive surfaces were prepared by grafting P(MEO$_2$MA-co-OEGMA) copolymer brushes on silicon wafers via the surface-initiated ATRP method using the "grafting from" approach (**Figure 1.1.36**) [164]. The polymerization process started after the modification of the silicon wafer with a bromo-silane serving as the ATRP initiator. The obtained surfaces of two different ratios of MEO$_2$MA and OEGMA copolymer brushes had a thickness of 1228 and 1161 Å for 95/5 (sample S1) and 85/15 (sample S2) ratios, respectively.
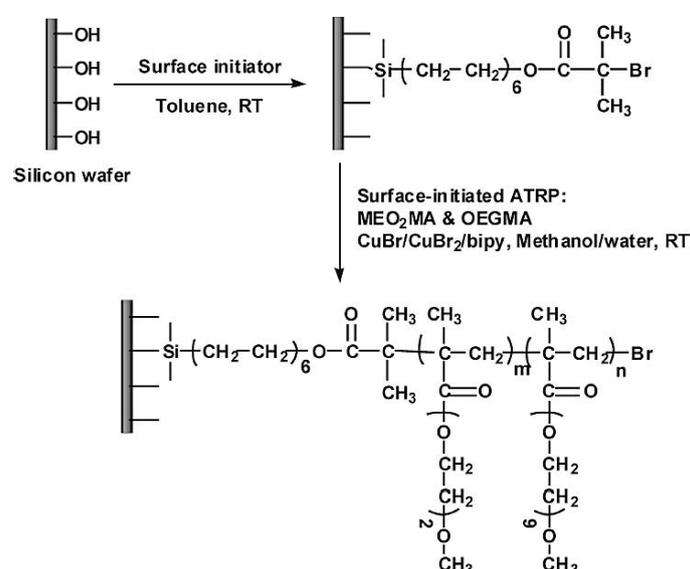


**Figure 1.1.36 Preparation of P(MEO$_2$MA-co-OEGMA) membranes using the "grafting from" approach by modifying a silicon wafer with an initiator function [164].**

On the other hand, the thermo-responsive behavior of the samples in water was studied. For S1 of LCST = 32 °C, at ≈ 15 °C, the copolymer brushes were well extended into water. Increasing the temperature to 25 °C, the copolymer brushes were still hydrophilic, however

when the temperature was increased to 37 °C, the copolymer brushes collapsed. The copolymer brushes conformation in deionized water is presented in **Figure 1.1.37**.



| Dry polymer layer in air | Polymer brushes in water | | |
|---|---|---|---|
| **Dry state** | **Collapsed state** | **Compressed state** | **Extended state** |
| Temperature: R.T. | Temperature: Above LCST | Temperature: Close to LCST | Temperature: Below LCST |
| Swelling ratio: 1 | Swelling ratio: ~1.2 | Swelling ratio: ~1.4 | Swelling ratio: ~1.8 |
| Water fraction: 0% | Water fraction: 20%-30% | Water fraction: >50% | Water fraction: >50% |
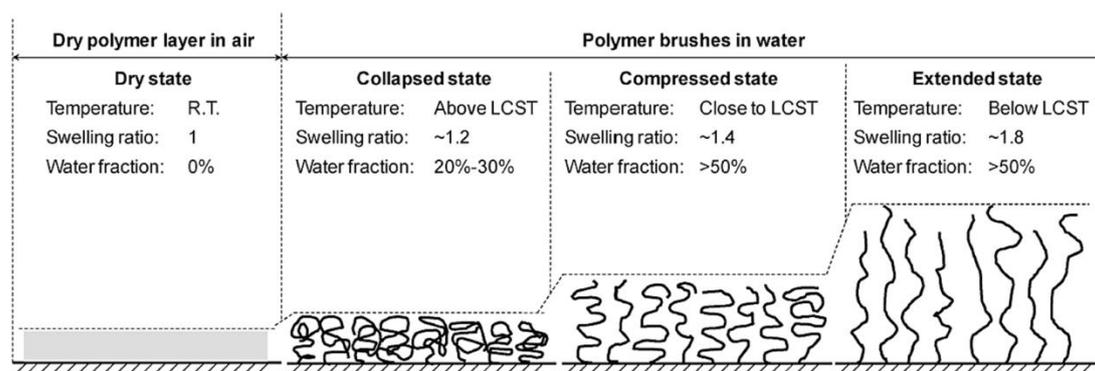
Figure 1.1.37 Behavior of copolymer brushes in water at different temperatures [164].

The swelling ratio in the presented figure corresponds to the thickness of the polymer layer in water divided by its thickness in dry state. At the temperature below the LCST, the swelling ratio in water was about 1.8. As the copolymer brushes can form hydrogen bond with water, a hydration layer was built up surrounding them. As a result, the copolymer brushes extended completely into water. The fraction of water inside the polymer layer was determined to be greater than 50 %, implying that water is a good solvent for P(MEO$_2$MA-co-OEGMA) copolymer brushes at low temperatures. As we see, as the copolymer brushes are more collapsed, the swelling ratio and the water fraction decrease as the polymer brushes exclude more water when they become hydrophobic. As mentioned earlier that salts have an effect on the behavior of thermo-responsive polymers, Gao *et al.* had also studied this effect on the P(MEO$_2$MA-OEGMA) copolymer they prepared. Results showed that the copolymer chains were more compressed in TBS buffer, which contains sodium chloride salt, than in pure water at the same temperature because of the significant disruption of the hydration layer by the salt.

### 1.3.2. Polymerization methods

As polymers play an important role in changing and enhancing the surface properties of inorganic/organic core/shell NPs, it is very important to control the size of the polymer chains on their surface because a homogenous and mild thickness polymer layer helps in preserving the optical and magnetic properties of ZnO and Fe$_3$O$_4$ NPs respectively. On the other hand, in the case of TRPs, the control of the molecular weight is very important as it has a good influence on the final transition temperature [148]. Due to challenges in control over the

molecular weight and molecular weight distribution, and also difficulties in preparation of end group functional polymers and varying polymer architectures via some conventional polymerization methods like ionic or radical polymerization, controlled/living radical polymerization (CRP) techniques became popular. This method can be applied in a wide range of experimental conditions (*i.e.* apolar medium, pure water, physiological medium). The CRP techniques which emerged include nitroxide-mediated polymerization (NMP), reversible addition-fragmentation chain transfer (RAFT) polymerization and atom-transfer radical polymerization (ATRP). Among these techniques, ATRP is the widely adopted because of the ease of initiator formation and relatively mild reaction conditions [154].

### 1.3.2.1. Atom Transfer Radical Polymerization (ATRP)

ATRP is a versatile synthetic tool that enables the preparation of new co-polymers with precisely controlled molecular weight, relatively low dispersity, composition (homo, block, grafted, star-shaped, gradient and hyper branched copolymers), and diverse functionalities [172].

ATRP is based on a reversible equilibrium between dormant species and active species. The radicals (R$^\bullet$) are generated through the abstraction of a halogen atom from an organic halide (R-X) by a transition metal complex ($M_t^n$-Y/ Ligand) to form the oxidized functional group ($X - M_t^{n+1}$-Y/ Ligand) (**Figure 1.1.38**). This process occurs with rate constants of activation $k_{act}$, and deactivation $k_{deact}$ [173].
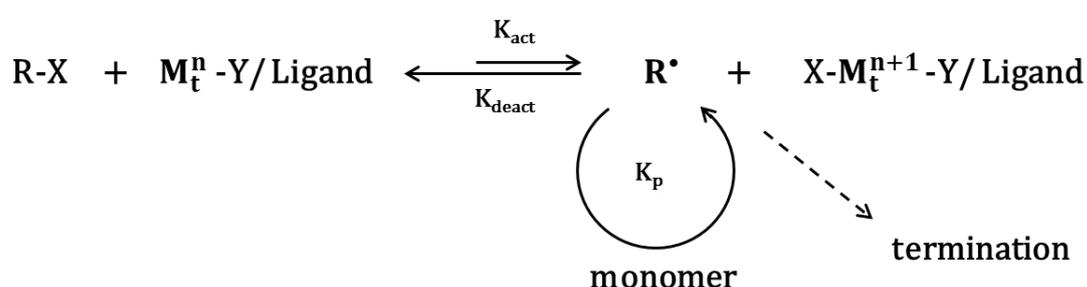


Figure 1.1.38 General mechanism of the ATRP technique.

The mechanism is as follows: the catalyst is oxidized by the transfer of a halogen atom originating from the dormant species (R-X) to generate an active species (R$^\bullet$) and an oxidized complex ($X - M_t^{n+1}$-Y/ Ligand). The kinetics of the polymerization by atom transfer is governed by the persistent radical effect. The excess formation of oxidized complex ensures

the reduction in the stationary concentration of propagating radicals thus reducing the contribution of irreversible termination reactions. That"s why an excess deactivating agent may be introduced at the beginning of the polymerization to improve the control. The addition of monomers to the radical propagating allows growing the polymer chains with a $k_p$ propagation rate constant.

A small percentage of polymer chains undergo a termination reaction due to the low concentration of the R-X resulting in a low quantity of the R$^\bullet$ which will be already taken to initiate the reaction. When termination reaction happens, it is mainly due to a radical coupling.

The ATRP system involves several components: the catalyst, the initiator and the monomer. A good knowledge of the role of each component ensures efficient catalysis and gets good control of the polymerization. Parameters such as solvent, temperature and reaction time can affect the good progress of the ATRP. An ATRP can be carried out in bulk or in solution, in homogeneous or heterogeneous medium like suspension or (mini) emulsion. The solvents used are either nonpolar solvents such as toluene or p-xylene, or polar solvents such as DMSO or DMF. Reaction temperatures are between room and high temperature (150 °C).

**The catalytic system**

One of the most important parameters in ATRP is the choice of the catalyst. The effectiveness of the ATRP catalyst is due to the ability of the transition metal to capture a halogen atom and thus increase its degree of oxidation. ATRP have been successfully carried out in the presence-based complexes, *i.e.* copper [174], nickel [175], iron [176], ruthenium [177]. Metal complexes based on copper (Cu) are yet the most used.

Regarding the ligand, it must be capable of complexing the metal and stabilizing its various oxidation states. On the one hand, it increases the solubility of the catalyst in the polymerization medium and allows to adjust the redox potential of the metal center to allow a suitable reactivity in the polymerization [178]. The ligands commonly used in ATRP are nitrogen or phosphorus compounds. Phosphorus-based ligands are the most used in a controlled ATRP with an iron-based [179] or ruthenium [180] complex but are less effective for ATRP with a copper based complex. In contrast, the nitrogen-containing ligands [181] are widely used in the copper complex to control an ATRP.

Some examples of nitrogen-containing ligands used in ATRP are derivatives of cyclic amines like tris[(2-pyridyl)methyl]amine (TPMA) [182], 2,2'-bipyridine (bpy) [183] and tridents like *N,N,N',N'',N''*-pentamethyldiethylenetriamine (PMDETA) [184] (**Figure 1.1.39**).
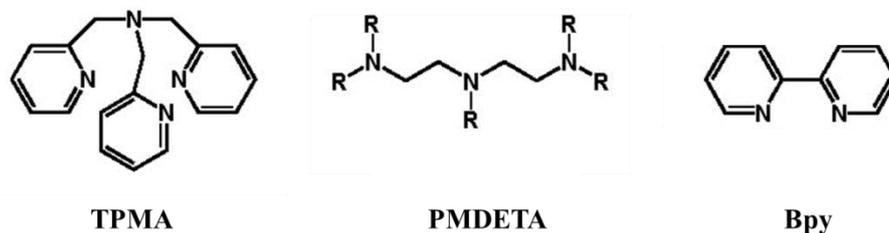


**Figure 1.1.39 The chemical structure of some nitrogen ligands which are used in ATRP process [182-184].**

**The initiator**

Initiator efficiency is of big importance for successful ATRP because it determines the number of initiated chains. Generally, a good ATRP initiator should have a reactivity which is at least comparable to that of the growing chains to obtain polymers with high polydispersity. However, very reactive initiators which produce many radicals in a short time increase the termination rate in early stages of polymerization and reduce the efficiency of initiation. It is known that all initiators are not suitable for polymerization of all monomers. Usually, initiators with structural similarity to the monomer to be polymerized have the good chance to be suitable for polymerization. For example, for polymerization of styrene, the most commonly used initiator is 1-phenylethyl halide [185]. Once the initiator is rapid and quantitative and that the transfer reactions and termination are negligible, then the number of growing chains is constant and equal to the number of initiator molecules initially introduced in the polymerization medium.

Normally, alkyl halides having inductive or resonance stabilizing groups are effective initiators to start ATRP. Alkyl halides having an activated substituent on the α-carbon halogen such as phenyl or carbonyl are most commonly used in ATRP (**Figure 1.1.40**). The halogen X must quickly migrate between the growing chain and the transition metal complex. Generally, the used halogen atom is the same in the initiator and the complex. Chlorine atoms and bromine are the most commonly used (the force of the R-Br bond is weaker than that of the R-Cl bond). Surface initiated polymerization usually requires an initiator with reactive groups which are able to attach to the surface of the NPs. As mentioned earlier, silanes are commonly used in this context, particularly for ZnO and $Fe_3O_4$ NPs.

methyl 2-chloropropanoate     methyl 2-bromo-2-methylpropanoate

(1-bromomethyl) benzene     methyl α-bromophenylacetate
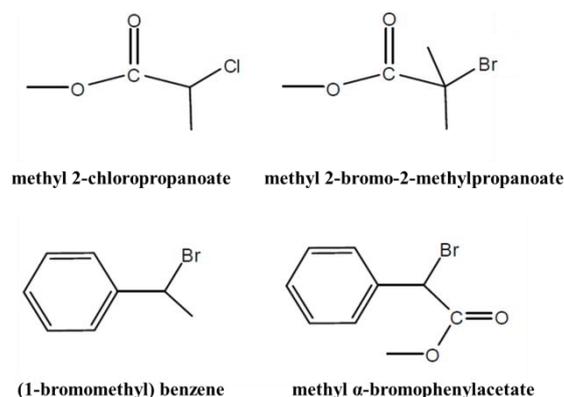
**Figure 1.1.40 Structures of some initiator used in ATRP.**

**The monomer**

A wide variety of monomers can be polymerized by ATRP. Styrene, methacrylamide and acrylonitrile are some typical examples in addition to methacrylates (**Figure 1.1.41**) [186, 187]. In the case of methacrylate-based monomers the ATRP equilibrium constant is high and activation of the dormant species is easy.
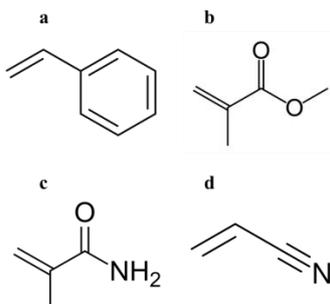


**Figure 1.1.41 Chemical structure of a) Styrene, b) methacrylate, c) methacrylamide and d) acrylonitrile.**

Understanding and controlling the equilibrium and hence the dynamics of the atom transfer process, are basic requirements for running a successful ATRP. As a result, researches working in the polymer science domain, like the Matyjaszewski group, have focused their work on the correlation of the structure with reactivity for each of the involved reagents, both oxidation states of the transition metal complexes, radicals and dormant species, in addition to reaction temperature and solvents effects in order to provide the fundamental understanding needed for the selection of optimum conditions to conduct the desired reaction.

### 1.3.2.2. Activators regenerated by electron transfer (ARGET) ATRP

ARGET ATRP approach was a result of the ATRP development to an environmentally process with a significant reduction of the amount of copper based catalyst complex due to a constant regeneration of the Cu(I) activator species by the addition of an environmentally acceptable reducing agents to Cu(II) [188]. Therefore, when the concentration of the ATRP catalyst is significantly reduced (down to single digit ppm vs. monomer) in the polymerization process, we call it activators regenerated by electron transfer (ARGET ATRP). Using lower concentrations of the catalyst not only results in greener polymerization processes but also allows for the polymers synthesis with high molecular weight and high chain-end functionality [189].

ARGET ATRP eliminates any requirement for the de-oxygenation of reaction mixtures and greatly simplifies the ATRP process obtaining pure block copolymers without contamination by homo-polymers. The polymerization directly starts after the addition of a reducing agent as illustrated in **Figure 1.1.42**.
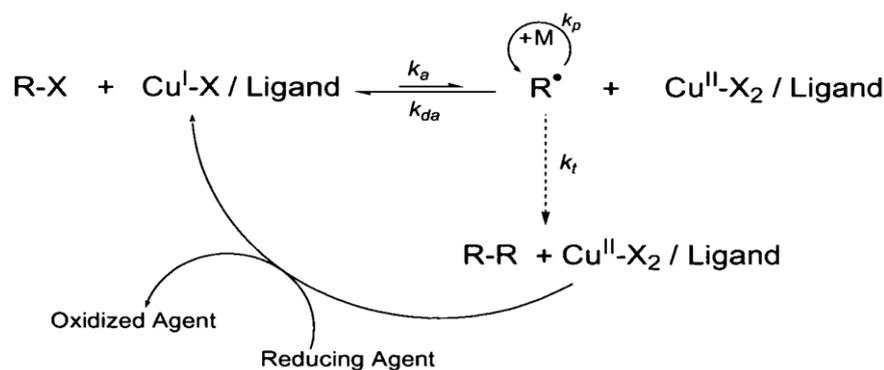


**Figure 1.1.42 General mechanism of ARGET ATRP [190].**

This new technique provides a continuous controlled polymerization with a significant reduction of the amount of Cu based catalyst complex (< 50 ppm) due to a constant regeneration of the Cu(I) activator species by the reducing agent, which compensate for any loss of Cu(I) by termination. A variety of reducing agents, such as tin(II) 2-ethylhexanoate, ascorbic acid, glucose, thio-phenol, phenols, Cu(0) or hydrazine have been successfully used to synthesize a wide variety of polymers with varying architecture and reactivity [191].

ARGET ATRP was successfully applied to relatively non polar monomers (e.g., butyl acrylate, styrene and methyl methacrylate) [192], for the preparation of different types of

polymeric materials with different structures and architectures including homo-polymers, well-defined block copolymers, and development of a scalable process to prepare molecular brushes on flat surfaces.

### 1.3.3. ATRP and ARGET-ATRP for designing functional NPs

In terms of designing functional NPs, various conventional polymerization techniques have been extensively adopted for the grafting of polymers onto inorganic NPs. Among these techniques, ATRP is frequently used. Surface initiated ATRP is one of the most powerful approaches for grafting polymer layer from the surface of inorganic NPs including ZnO, iron oxide, SiO$_2$ NPs by simply grafting the initiator on the NPs surface.

Thermo-responsive ZnO@PNIPAM NPs were prepared via the surface initiated ATRP method (**Figure 1.1.43**) [193]. Firstly, ZnO NPs were treated with 3-aminopropyltriethoxysilane, and then reacted with 2-bromoisobutyryl bromide. The ATRP reaction was conducted on the surface of 2-bromoisobutyrate functionalized ZnO NPs as the initiator. The process was run under N$_2$ atmosphere at 30 °C.
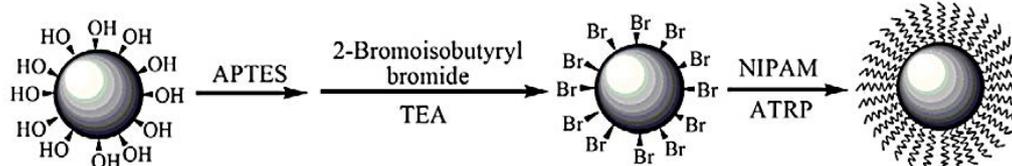


**Figure 1.1.43 Synthesis of PNIPAM modified ZnO NPs via ATRP after the introduction of the halide initiator.**

The obtained NPs were characterized with different techniques to evaluate the grafting process. The amount of the PNIPAM polymer on the surface of ZnO was measured by thermal gravimetric analysis (TGA) and the weight loss was found to be 51.2 %. Furthermore, using transmission electron microscopy, it was seen that the thickness of PNIPAM was ≈ 5–6 nm. In addition, following the photoluminescent properties of the NPs, when PNIPAM modified ZnO NPs were heated above the LCST (*i.e.* 40 °C), the intensity of its PL spectra decreases a lot, which is mainly induced by the shrinking of the polymer chains on the ZnO surface, and thus demonstrating that the PNIPAM modified ZnO NPs possess thermal responsive properties.

Sun *et al.* have reported the synthesis of Fe$_3$O$_4$/PS core/shell NPs via surface initiated ATRP [186]. At first, a method was employed to covalently bond initiators onto the surface of the IONPs, which was the combination of ligands exchange reaction and condensation of triethoxysilane having an ATRP initiating site, 2-bromo-2- methyl-N-(3-(triethoxysilyl)propyl) propanamide. Then the PS shell was grafted from the initiating sites on the surface of iron oxide NPs through ATRP (**Figure 1.1.44**).
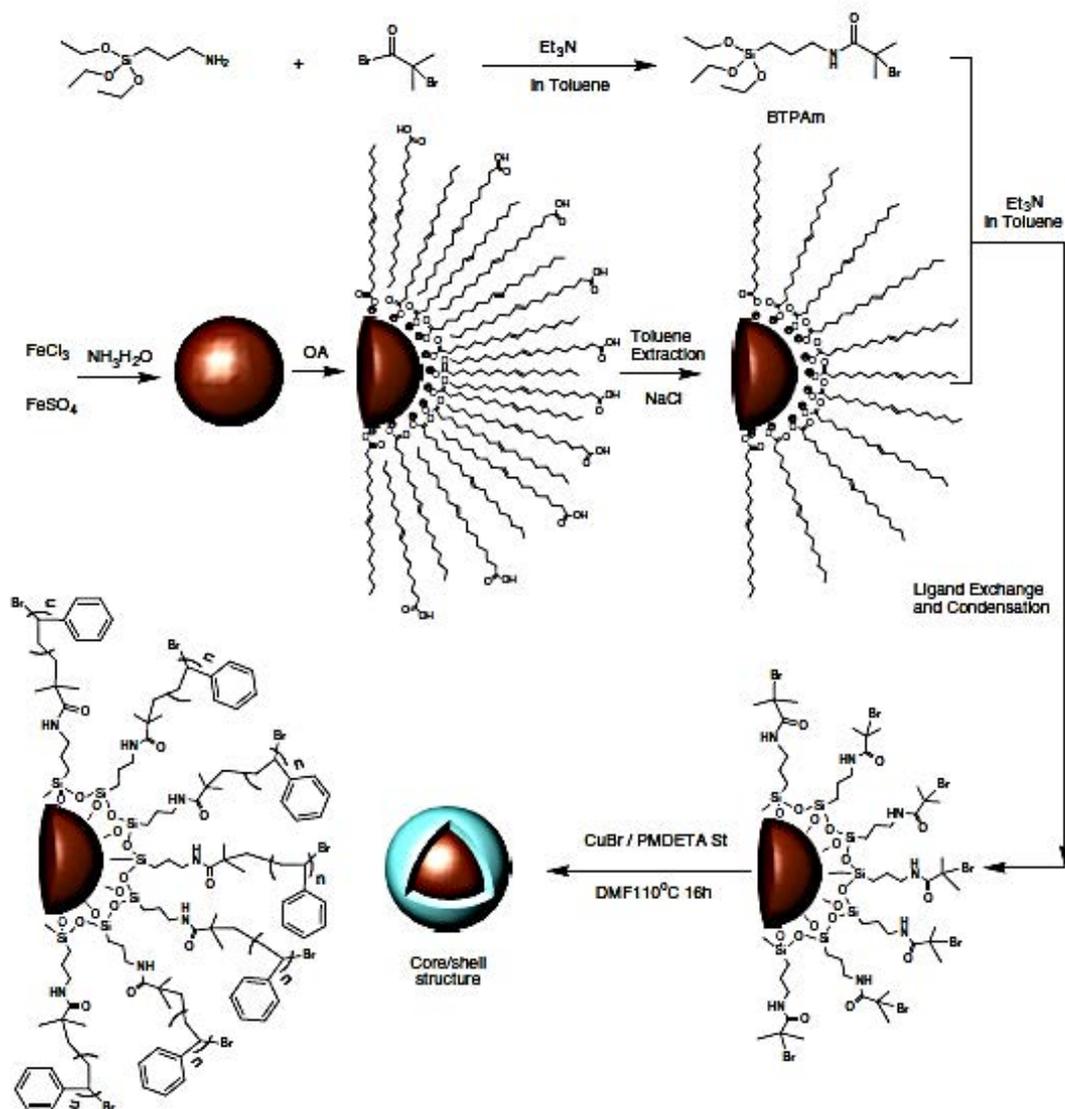


**Figure 1.1.44 Illustration of the synthesis route of polystyrene coated MNPs with core/shell structure.**

The ATRP process was conducted with N$_2$ flow at 110 °C in the presence of CuBr/ PMDETA. A full characterization of the obtained NPs was made demonstrating that this novel approach to immobilize ATRP initiators and „grafting from‟ method of ATRP should

be able to be used in the synthesis of other polymer coated IONPs with increasing complexity and functionality in the polymeric shell.

Random copolymers of OEGMA analogues prepared via ATRP have attracted increasing attention. It was found that the LCST of OEGMA based copolymers can be tuned to the physiological temperature by varying the ratio of monomers. Also their LCSTs are mildly sensitive to salt concentration, ionic strength and in-vitro cell tests of several OEGMA analogues showed excellent biocompatibility. This kind of copolymer has potential applications for drug delivery and other biological applications [194].

Gelbrich *et al.* reported the preparation and characterization of IO core/shell NPs that showed a fully reversible and tailorable thermo-flocculation in water (**Figure 1.1.45**).
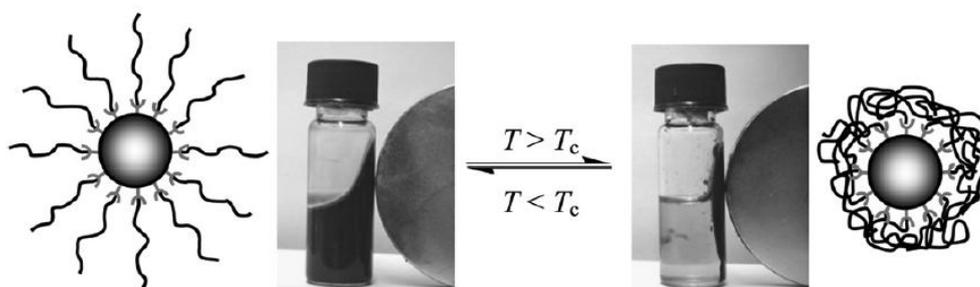


**Figure 1.1.45 Reversible thermo-flocculation of IO@P(OEGMA-co-MEMA) NPs in water.**

OEGMA and methoxyethyl methacrylate (MEMA) copolymers were grafted from the surface of IONPs via ATRP. The synthesis of these NPs is illustrated in **Figure 1.1.46**. 2- bromo-2-methyl propionic acid (BMPA) was used as an initiator to start the polymerization process. Thermo-responsive polymer brushes were formed by the surface-initiated polymerization of MEMA and OEGMA in DMSO from the surface of $Fe_3O_4$@BMPA NPs with varying the co-monomer ratio to achieve copolymer brushes with MEMA content between 0 and 50 molar percentages.
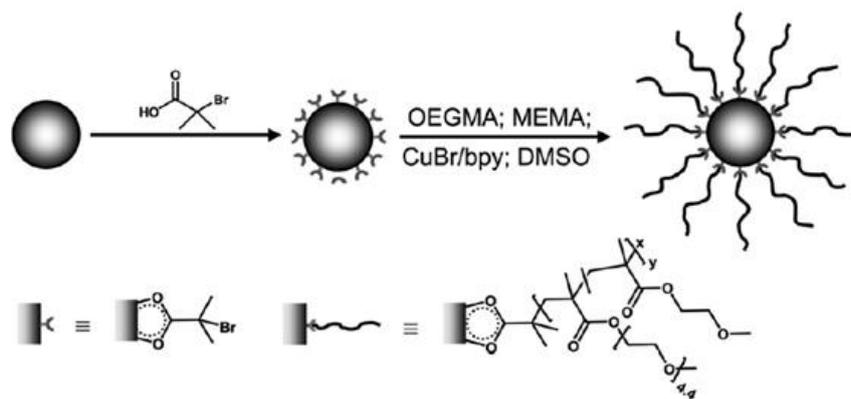
**Figure 1.1.46 Surface initiated ATRP of P(OEGMA-co-MEMA) from the surface of magnetic NPs.**

The resulting core/shell NPs are superparamagnetic, showing a high grafting density, and exhibit a thermos-responsive behavior in water due to the LCST of the polymer chains. The phase transition occurs when heating the NPs above the LCST depending on the amount of MEMA polymer. The LCST was between 36.6 and 61.2 °C for the percentage of MEMA. PEG polymerized onto MNPs, is widely used in this field because of its biocompatibility and anti-biofouling properties, which prevent adsorption of plasma proteins or cells onto NP surfaces, thereby increasing the particles blood circulation time and allowing the NPs to reach their target tissues [195].

In terms of ARGET ATRP, a limited number of studies involving this process for the surface functionalization of inorganic NPs have been reported. Du *et al.* could obtain well-defined poly (methyl methacrylate) (PMMA) shell on the surface of silica NPs via this method. The halogen-functional ATRP initiator was first anchored on the silica NPs and then the polymerization of methyl methacrylate was conducted from the silica surface using iron (III) chloride as a catalyst and ascorbic acid as the reducing agent in the presence of a limited amount of air [196].

The synthesis of poly (methacrylic acid) (PMAA) and poly (butylmethaylate) (PBMA) polymer brushes on Si NPs using ARGET ATRP was reported by Iacono *et al.* [197]. The polymerization process was performed from the surface initiator decorated Si-NPs using $CuCl_2$ and tris-((2-pyridyl)-methyl)-amine (TPMA) as the catalytic system, and tin(II)-2-ethylhexanoate as the reducing agent The functionalization of PBMA yielded hydrophilic PAA decorated Si NPs with high colloidal stability (**Figure 1.1.47**).
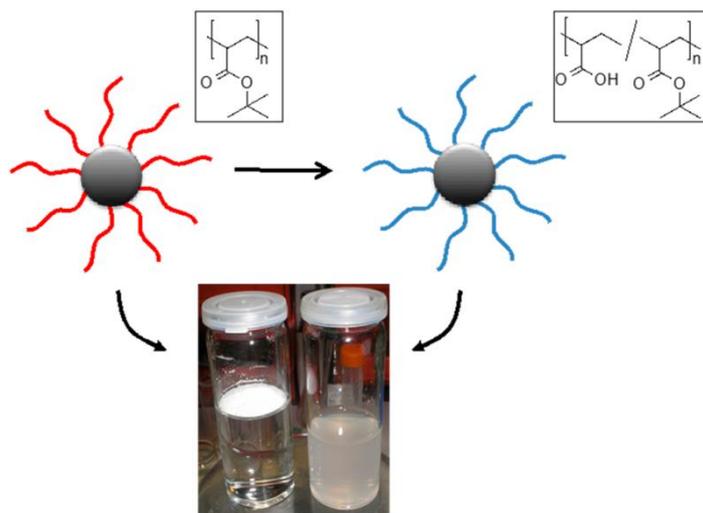
**Figure 1.1.47 Hydrophobic PBMA decorated Si-NPs floating on water (left) and hydrophilic PMAA Si-NP suspended in water [197].**

Another group demonstrated the synthesis of magnetic/fluorescent NPs with well-defined core/shell structure by ARGET-ATRP mediated by the iron (III) catalyst using a magnetic $Fe_3O_4$ core and a fluorescent monomer 9-(4-vinylbenzyl)-9H-carbazole (VBK). The obtained NPs exhibited good fluorescence and magnetic properties [198].

Recently, Alem *et al.* developed a simple process to synthesize responsive core/shell NPs by growing PNIPAM from the surface of ZnO NPs via ARGET ATRP using different initiators structure [199] (**Figure 1.1.48**).
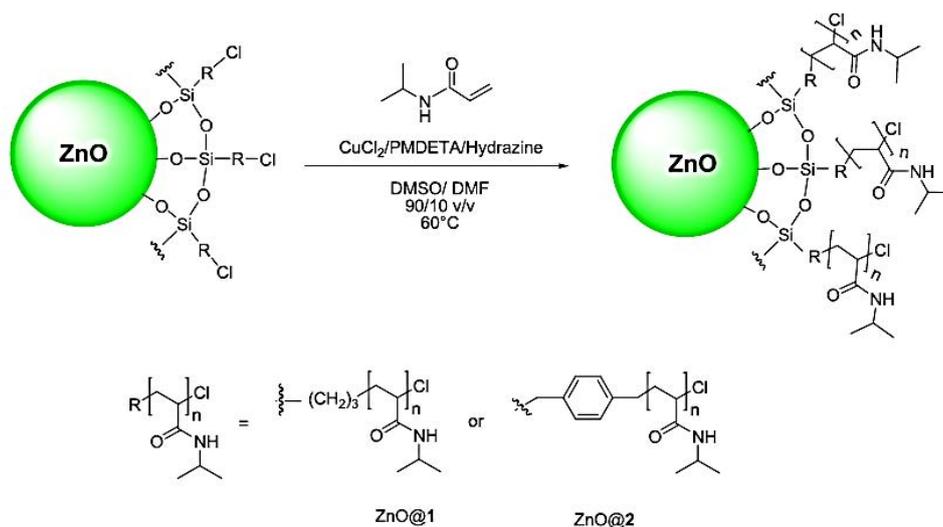


**Figure 1.1.48 Schematic representation of the surface-initiated ARGET-ATRP polymerization of NIPAM from ZnO@1 and ZnO@2 NPs.**

The final NPs displayed temperature-dependent optical and size properties and when the polymer layer is thick enough, it could stabilize the ZnO fluorescence [199]. This process, as an easy and biocompatible route, will be used to modify different inorganic NPs with different polymer brushes during this PhD work.

## 2. Biological applications of inorganic/organic core/shell NPs

### 2.1. NPs engineering

Inorganic/organic core/shell NPs based on ZnO and IONPs are very popular in the biomedical field because of their unique features which present different bio-applications that can be categorized into two typical groups such as "in vitro" and "in vivo" applications [200-203]. In vitro applications include the activities that are performed inside laboratories and outside of living organisms (e.g. immunoassay, bio-separation, purification, and immobilization of biomolecules). On the other hand, the considerable part of bio-applications is related to in vivo (refer to living samples) ones like drug delivery systems (DDS) [204]. In particular, compared to the conventional methods of drug delivery, these NPs are promising drug carriers due to the better specificity to the targeted site and the reduced side effects; with IONPs, only by applying external magnetic field, drug could be accumulated at the desired site to receive much high therapeutic efficiency (**Figure 1.2.1**). As a result, the development and engineering of this kind of NPs is very important to enhance their performance for vivo applications [205].
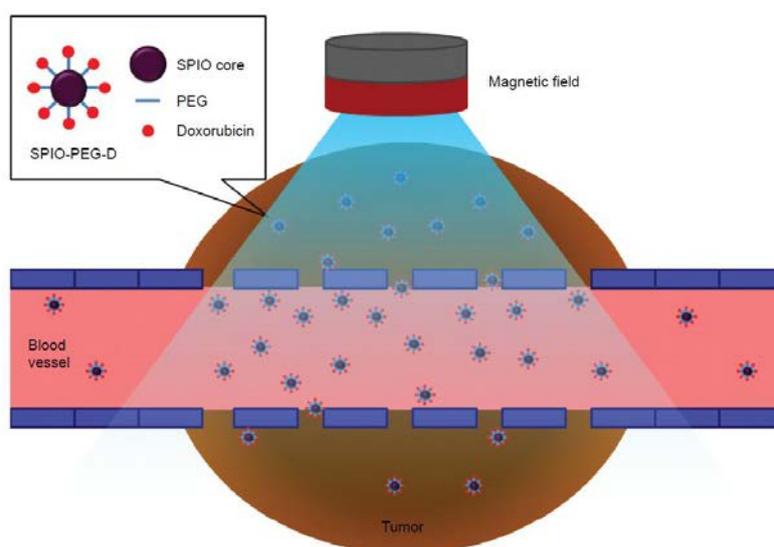


**Figure 1.2.1 Drug transport to tumor cell by applying a magnetic field to SPIO-PEG NPs conjugated with DOX molecules.**

As primary requirements to build an effective DDS with core/shell NPs, the latter should possess the following properties:

1. Very small to freely move in vessels and stable for prolonged circulation in blood stream in vivo

2. They can be monitored to be easily followed in vivo

3. Biocompatible where they cause no harm to healthy cells

4. Able to transport and load sufficient amount of the drug molecules with controllable release at the spots which contain the tumor

5. Available end functions for the attachment of targeting ligands

Thus, in the case of inorganic/organic core/shell NPs, as previously mentioned, a proper polymer coating can effectively render them water soluble, enhance or at least preserve their physical properties, provide more rigidity and improve their colloidal stability under physiological conditions, ensure high degree of non-toxicity and biocompatibility and leave them with different end groups for further functionalization to which drug agents like the cancer cell targeting ligand, folic acid (FA) can be conjugated (**Figure 1.2.2**) [206]. The attachement of FA improves the drug delivery into cancer cells because it has the ability to target cancer cells; its receptor (folate specific receptor) is frequently overexpressed on the surface of cancer cells [202]. FA is widely used for chemical conjugation with therapeutic drugs because it is stable, not toxic, nonimmunogenic and not very expensive [202].
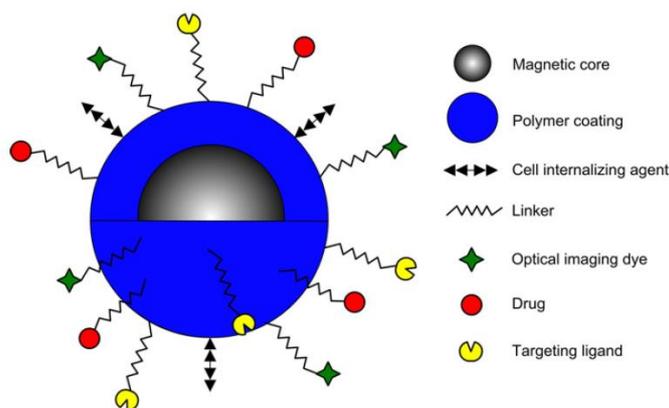


**Figure 1.2.2 The core/shell structure of functionalized IONPs [100].**

On the other hand, to control the drug release and achieve high intracellular concentrations, a responsive polymer shell encapsulating the drug molecules makes the job easier when the core/shell NPs are concentrated at the tumor site; they can release the drug by only a change in the pH or temperature, as at the tumor spots the pH and temperature are different in comparison to normal healthy cells [207]. Hervault *et al.* have loaded DOX in dual pH- and thermo-responsive magnetic nano-carriers. The drug release experiments confirmed that only a small amount of DOX was released at room temperature and physiological pH, while the

highest drug release of 85.2 % was obtained after 48 h at acidic tumor pH under hyperthermia conditions (50 °C) [208].

Some examples of designed DDS based on ZnO and IONPs are introduced here. ZnO NPs encapsulated in a natural and biodegradable polymer named chitosan were used as nano-carriers for the delivery of DOX [209]. The obtained NPs were water dispersible and biocompatible. The schematic representation of the encapsulation of ZnO QDs with folate-conjugated chitosan and the drug-loading step is presented in **Figure 1.2.3**. Chitosan enhances the stability of the QDs because of its hydrophilicity and cationic charge characteristics.
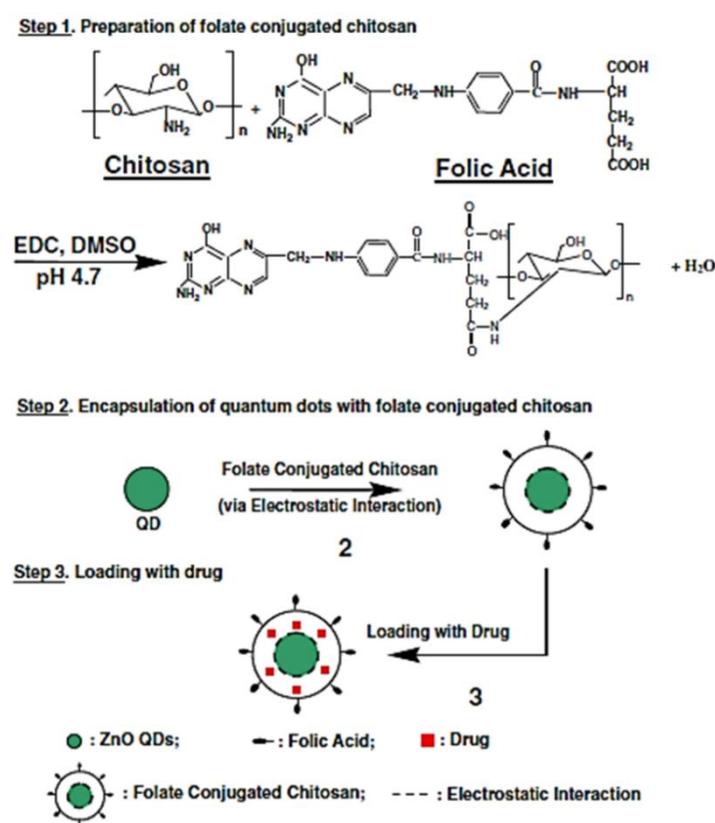


**Figure 1.2.3 The synthetic route to obtain ZnO@chitosan@folate carriers through chemical and physical interactions [209].**

An example of $Fe_3O_4$/polymer core/shell NPs is illustrated in **Figure 1.2.4**. Poly(acrylic acid) poly(AA) was grafted from the surface of magnetite NPs via ATRP of t-butyl acrylate, followed by the hydrolysis of the t-butyl groups [210]. The poy(AA) not only stabilized and promoted NPs dispersibility in water but also served as a platform for conjugating FA. According to their preliminary results, it was found that the dispersions were not toxic against cells up to 50 mg/mL concentration of the sample. These magnetically guidable NPs could be suitable for use as an efficient DDS, particularly for cancer treatment.
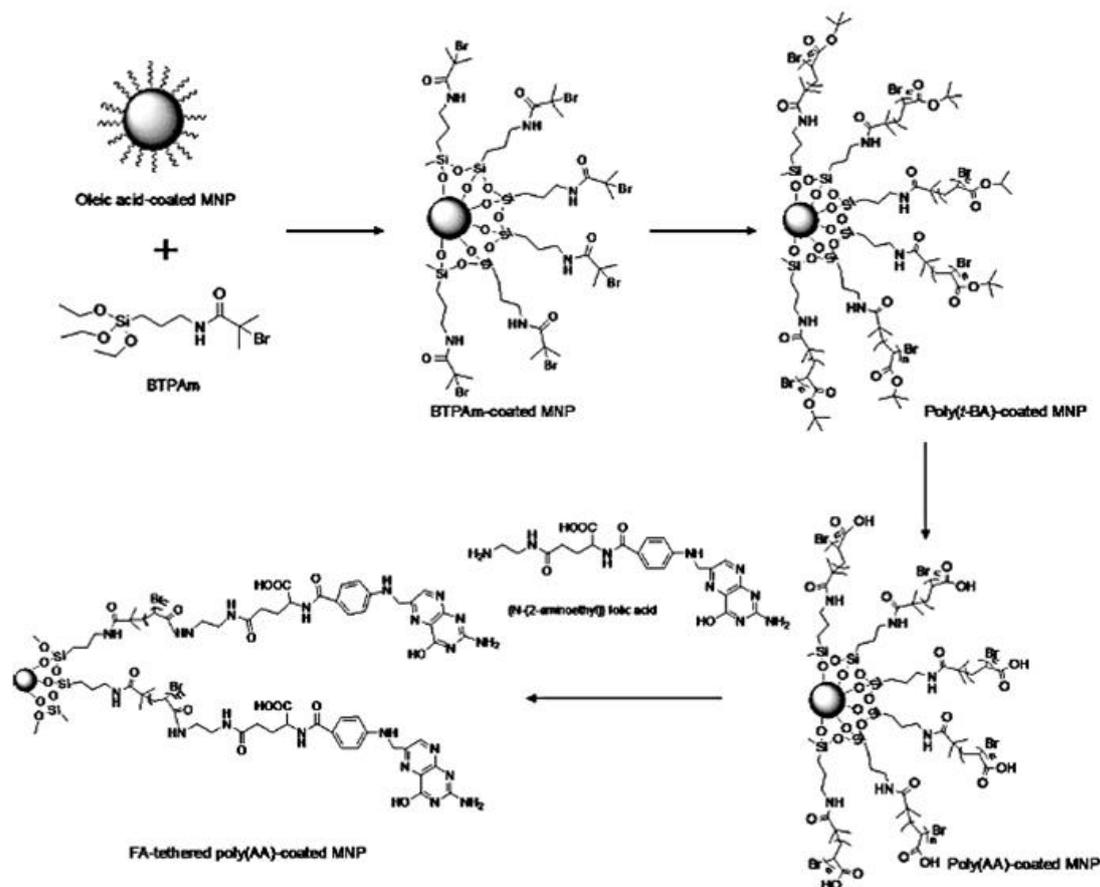
**Figure 1.2.4 Surface modification of Fe₃O₄ with poly(AA) [210].**

Huang *et al.* have reported the synthesis of IONPs which have controllable amounts of conjugated FA to target cancer cells [211]. These NPs were coated with poly (glycidyl methacrylate-co-poly (ethylene glycol) methyl ether methacrylate) (P(GMA-co-PEGMA)) (**Figure 1.2.5**).
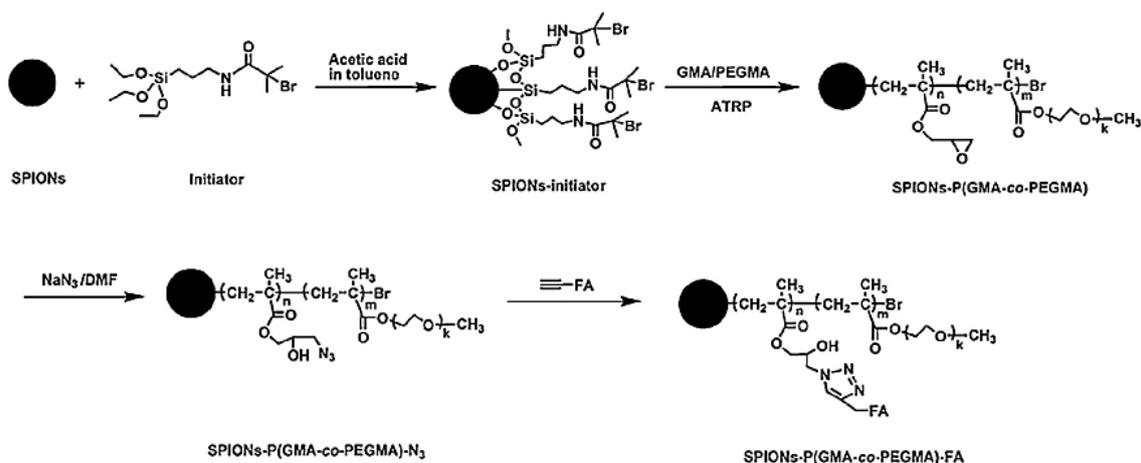


**Figure 1.2.5 Schematic representation of the synthetic route to IONPs-P(GMA-co-PEGMA)-FA) [211].**

The OEGMA part of the copolymer served as a protective layer to increase the stability and blood compatibility of the NPs and to increase their resistance to protein fouling. The GMA polymer then served as reactive sites for conjugation of alkyne-functionalized FA. The resulting IONPs-P(GMA-co-PEGMA)-FA had high dispersibility and stability in aqueous medium.

## 2.2. In vitro and in vivo applications

Synthesizing inorganic/organic core/shell NPs with remarkable properties is only half the job. Positive therapeutic result of these NPs in vitro and in vivo is important and very interesting. Cytotoxicity tests are essential to ensure the biocompatibility of these NPs for clinical use. As a consequence, numerous DDS based on ZnO and $Fe_3O_4$ have been investigated in vitro and in vivo for the delivery a wide range of therapeutic agents.

Recently, a new kind of biocompatible multifunctional pH sensitive nano-platform was built by synthesizing ZnO QDs with polymer shells coordinated with gadolinium ($Gd^{3+}$) ions and adsorbed DOX together to form ZnO-Gd-DOX NPs [212]. The main use of these nano-platforms is to label and treat tumors without detectable toxic side effects. **Figure 1.2.6** shows the in vivo fluorescent and T1-weighted MRI images of BxPC-3 tumor-bearing nude mice under laser irradiation after intra-tumor injection of ZnO-Gd-DOX NPs.
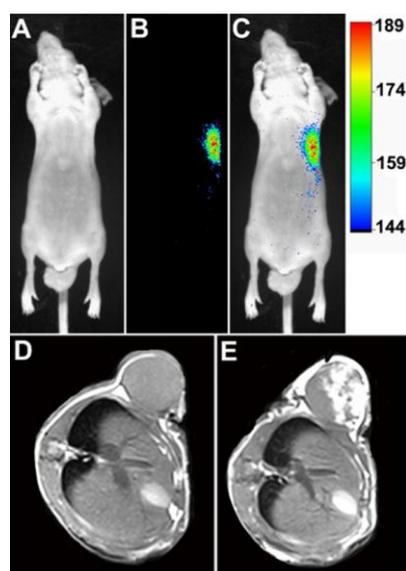


**Figure 1.2.6 In vivo fluorescent images of BxPC-3 tumor-bearing nude mice under A) bright field and B) laser irradiation after intratumor injection of ZnO-Gd-DOX (100 μL, 2 mg/mL). C) Overlay of (A) and (B). T1-weighted images of the same mice D) before injection and E) 2 h after intratumor injection of ZnO-Gd-DOX.**

They were shown to release DOX to cancer cells in vitro and to mouse tumors in vivo, and reveal better specificity and lower toxicity than free DOX, and even better therapeutic efficacy than an FDA approved commercial DOX-loading drug DOX-Liposome Injection. The DOX release was the highest at a lower pH value (**Figure 1.2.7**); more than 90 % of the DOX molecules were released within 10 h under this condition, just like in the acid environment of tumors.
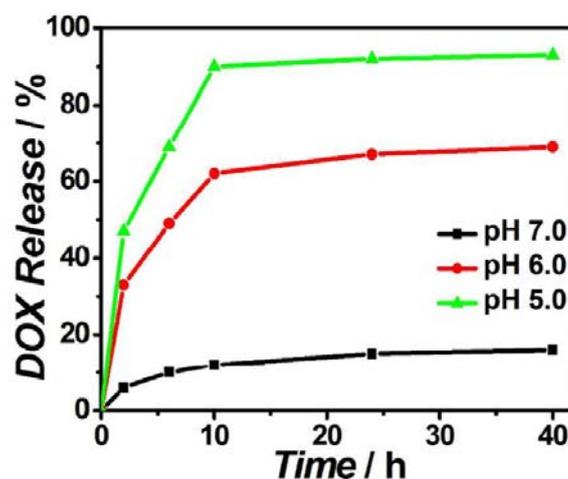


**Figure 1.2.7 DOX release profile of ZnO-Gd-DOX NPs at different pH values.**

Cytotoxicity of DOX, ZnO-Gd, and ZnO-Gd-DOX were evaluated by the conventional MTT assay (MTT=3-(4,5-dimethylthiazol-2-yl)-2,5-diphenyltetrazolium bromide) after incubation with BxPC-3 cells for 24 h. The MTT assay is an important method for evaluating the in vitro cytotoxicity of biomaterials. The results confirmed that ZnO-Gd NPs were nontoxic to BxPC-3 cells even when the $Zn^{2+}$ ions concentration was 8 μg/mL. On the other hand, both ZnO-Gd-DOX NPs and DOX were very toxic to BxPC-3 cells when the corresponding DOX concentrations were only 4 μg/mL (**Figure 1.2.8**).
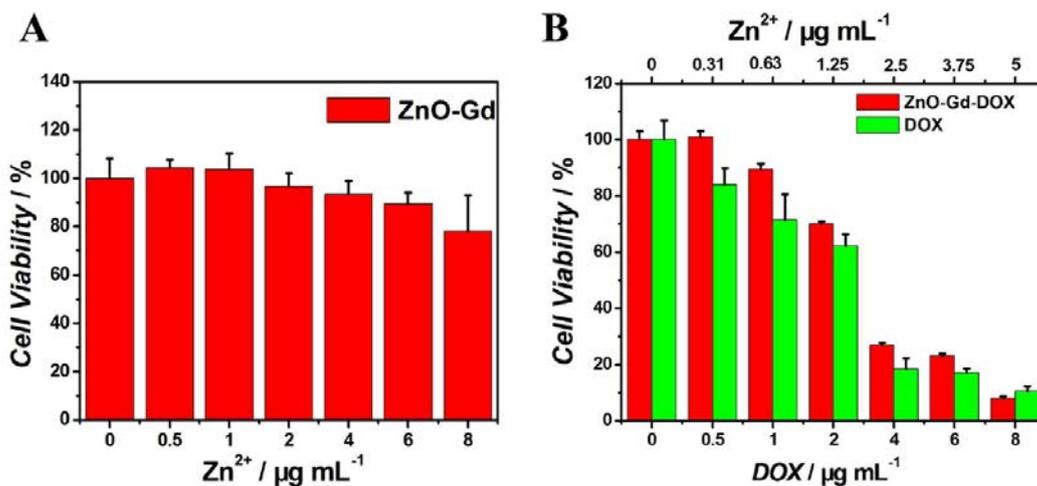
**Figure 1.2.8 Viability of the BxPC-3 cells after 24 h incubation with A) ZnO-Gd NPs, B) ZnO-Gd-DOX NPs and DOX, respectively [212].**

ZnO-Gd NPs were also injected into the tumors of BxPC-3 tumor-bearing nude mice every 2 days and monitored closely for 36 days. The tumor growth wasn¨t affected by ZnO QDs and $Gd^{3+}$ ions as the growth was growing rapidly nearly the same as for the tumors receiving physiological saline. Moreover, the ZnO-Gd treated mice showed a similar body weight evolution as the saline treated ones, indicating that the repeated intratumor injections did no harm to mice. In addition, studying the H&E staining slices of the tumor and the major organs for ZnO-Gd treated mice, only few of the tumor cells were damaged by the NPs and no damage or inflammatory lesion was observed in all major organs.

In a previous work, U251 cells were incubated with polymer modified ZnO NPs loaded with DOX molecules [94]. The NPs were tracked by confocal laser scanning microscopy (CLSM) as shown in **Figure 1.2.9**.
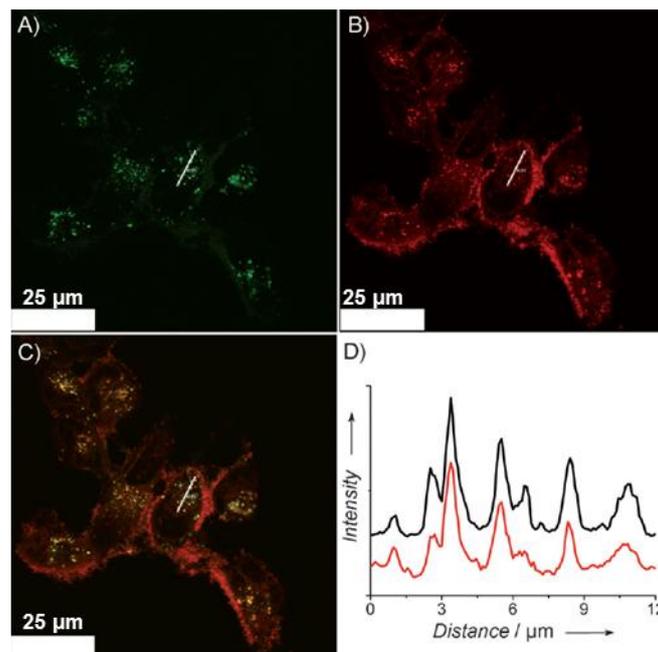
**Figure 1.2.9 CLSM images of U251 cells after incubation with ZnO@polymer–DOX in the presence of LysoTracker for 3 h. A) Lysosomes stained with LysoTracker (green) B) ZnO@polymer–DOX (red). C) Merged picture of A and B D) Fluorescence signals of lysosomes (black) and ZnO@polymer–DOX (red) based on the white lines in images A and B, respectively.**

In vitro experiments showed a good release of DOX molecules from the ZnO@polymer–DOX system at an acidic condition of pH=5. It was explained that at pH=7, a 15 % of the drug molecules were released where they were weakly adsorbed on the surface of the NPs. By contrary, 90 % were released at pH=5 when the polymer layer was degraded at acidic conditions, showing the pH responsivity and good encapsulation property of the drug in the polymer layer. On the other hand, the cytotoxicity of ZnO@polymer, DOX, and ZnO@-polymer–DOX were evaluated. They were incubated with U251 cells for 48 h (**Figure 1.2.10**). The cytotoxicity of ZnO@polymer and ZnO@polymer–DOX were evaluated with regard to their Zn content. The cytotoxicity of DOX and ZnO@polymer–DOX were evaluated with regard to their DOX content.
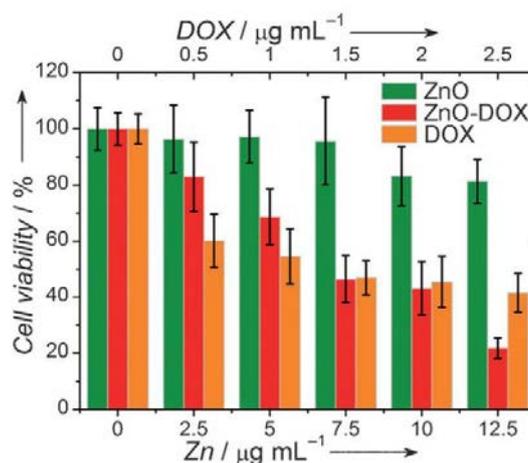
**Figure 1.2.10 Viability of U251 cells after treatment with ZnO@polymer NPs, ZnO@polymer–DOX composites and free DOX for 48 h.**

The polymeric ZnO NPs showed no visible cytotoxic effect on the cells where the cell viability was still high ($\approx$ 80 %) at a concentration of 12.5 µg/mL Zn while this effect increased for ZnO@polymer–DOX when the concentration was above 5 µg/mL Zn due to the presence of DOX molecules. Comparing the NPs loaded with DOX and the free DOX in terms of DOX content, it was seen that the ZnO@polymer–DOX exhibited much stronger cytotoxicity when its DOX concentration is above 2 µg/mL. This showed that DOX molecules are more effective when loaded in the polymeric NPs and which could be explained by the cytotoxicity enhancement effects of the nano-carriers, that resulted in the improved internalization of ZnO@polymer–DOX through endocytosis compared with the passive diffusion of free DOX into cells.

IONPs coated with biocompatible polymer PEG were modified with FA (SPION-DOX-PEG-FA) to target cancer cells [213]. The NPs uptake in vitro was studied in human breast carcinoma cells (MCF-7) by means of LSCM and flow cytometry. The cells were incubated with suspensions of the NPs with and without FA. As shown in **Figure 1.2.11**, the intracellular fluorescence detected corresponds to the presence of NPs where the fluorescent DOX molecules are embedded and protected in the PEG shell.
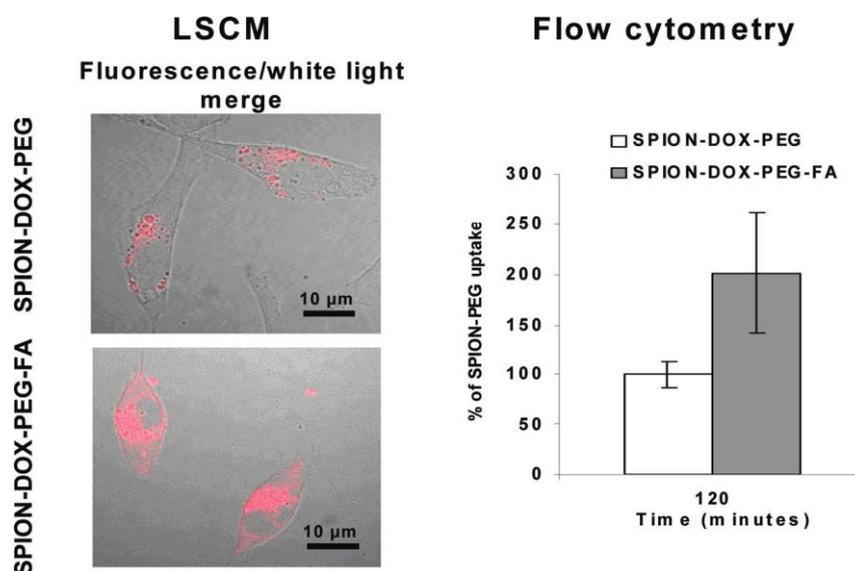
**Figure 1.2.11 The uptake of SPION-DOX-PEG and SPION-DOX-PEG-FA NPs by MCF-7 cancer cells measured by LSCM and flow cytometry [213].**

After 2 hours of cell culture, the cellular uptake of the SPION-DOX-PEG-FA NPs was twice that of SPION-DOX-PEG (**Figure 1.2.11**) which was expected as the FA ligand attached to the NPs is recognized by the folate receptors on the MCF-7 cells, bound together triggering the cellular uptake via endocytosis. It was believed that if the same NPs were tested with HeLa or KB cell lines, the uptake would have be more as these cells overexpress FA receptors particularly strongly.

In another work [214], to reduce or minimize undesired interactions or undesired uptake into normal sites, biodegradable nano-carriers have been developed for DOX, where the amount and site of drug release is controlled by the structure of copolymer coated IONPs and pH. $Fe_3O_4$ NPs were encapsulated in a copolymer composed of two biocompatible polymers; one of them is PEG and the other is PLGA poly (D, L-lactic-co-glycolic acid) [214]. PLGA polymers are not hydrophilic but they exhibit reverse thermal and pH-dependent gelation properties and PEG were introduced to prolong the circulation time of the NPs in the blood stream in vivo. A series of NPs with a hydrodynamic diameter of 25-75 nm were prepared with different molecular weights of PEG to obtain $PEG_{2000}$, $PEG_{3000}$ and $PEG_{4000}$ which were then loaded with DOX. In vitro release and cytotoxicity experiments were performed. The results demonstrated that the DOX loaded $Fe_3O_4$-PLGA-PEG NPs were pH sensitive where they could be applied for targeting extracellular pH, and could be an effective carrier for anticancer drugs. At tumor pH, these NPs can show enhanced cytotoxicity compared with that at normal pH.

In details, the results showed a significant amount of DOX release within 12 h which decreased with the decrease of PEG units; 30.1 % for $Fe_3O_4$-PLGA-$PEG_{4000}$ NPs, 25.6 % for $Fe_3O_4$-PLGA-$PEG_{3000}$, and 20.7 % for $Fe_3O_4$-PLGA-$PEG_{2000}$. The highest release for $Fe_3O_4$-PLGA-$PEG_{4000}$ NPs was due to the increased water uptake capacity with more PEG units, which encapsulated more DOX molecules into its swollen copolymer matrix where the encapsulation efficiency achieved for these NPs was 78 % compared to 73 and 69.5 % for $Fe_3O_4$-PLGA-$PEG_{3000}$ and $Fe_3O_4$-PLGA-$PEG_{2000}$, respectively. The swelling of the copolymer increased in acidic buffered solutions due to protonation of central PEG groups and formation of positively charged chains in the polymer structure resulting in an enhanced DOX release rate at pH 5.8. With time, the hydrolysis of the ester linkage in these polymers caused the swelling to increase more and more release of DOX molecules was achieved where the cumulative amount was 83.4 % from $Fe_3O_4$-PLGA-$PEG_{4000}$, 70 % from $Fe_3O_4$-PLGA-$PEG_{3000}$, and 60.8 % from $Fe_3O_4$-PLGA-$PEG_{2000}$ NPs over 2 days.
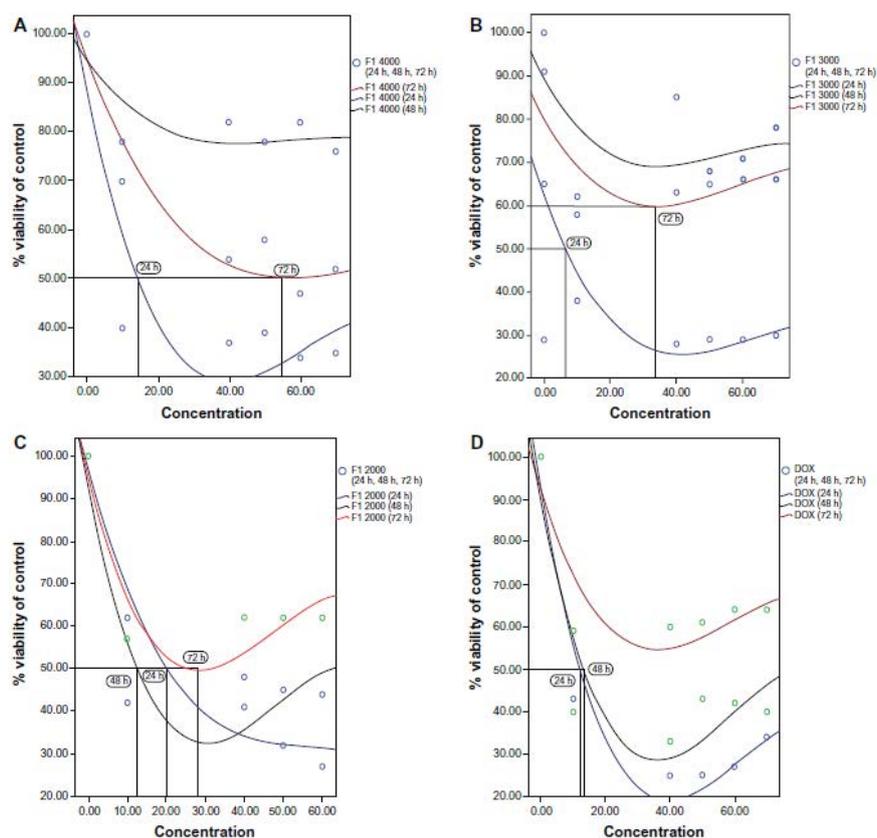


**Figure 1.2.12 IC$_{50}$ of A) $Fe_3O_4$-PLGA-$PEG_{4000}$ -DOX, (B) $Fe_3O_4$-PLGA-$PEG_{3000}$-DOX, C) $Fe_3O_4$-PLGA-$PEG_{2000}$-DOX and D) pure DOX on A549 tumor cell line after 24, 48, and 72 h of treatment. IC$_{50}$ (Inhibitory Concentration 50 %) is the concentration of drug that is require for 50 % inhibition in vitro.**

On the other hand, the cytotoxicity of $Fe_3O_4$-PLGA-PEG NPs was also evaluated by MTT assay. The DOX loaded NPs were incubated with an A549 lung cancer cell line at different concentrations and time. The results showed that $Fe_3O_4$-PLGA-$PEG_{4000}$ were biocompatible; they had no dose-dependent cytotoxicity but does have time dependent cytotoxicity against the cell line ($IC_{50}$ 0.17-0.48 mg/mL) (**Figure 1.2.12**) while the opposite in the case of pure DOX; it has dose-dependent but not time-dependent cytotoxicity against this cell line ($IC_{50}$ 0.15–0.16 mg/mL). However, these results need to be studied more on the A549 lung cancer cell line.

Recently, PEG modified IONPs were examined as DDS for chemotherapeutic agents and contrast agent for MRI [215]. The NPs were studied in two cases: with and without applying a magnetic field (MF) to show that the accumulation of the NPs in cancer tumors is enhanced by applying a MF. Thus, these multifunctional superparamagnetic IONPs consisted of $Fe_3O_4$ core and a shell of aqueous stable PEG conjugated with DOX (SPIO-PEG-D). SPIO-PEG-D/MF indicates the presence of a magnetic field. The cellular uptake in vitro was studied in HT-29 cells. These cells were incubated with SPIO-PEG-D and SPIO-PEG-D/MF NPs at different hours. As shown in **Figure 1.2.13**, SPIO-PEG-D/MF NPs had an enhanced cellular uptake (the rapid and effective magnetic targeting leaded to darkened T2-weighted MR images (**Figure 1.2.13A**), and higher Fe concentration indicated by darker blue color of Prussian blue staining study (**Figure 1.2.13B**)) which was ≈ 60 µg Fe/mL at 24 hours.
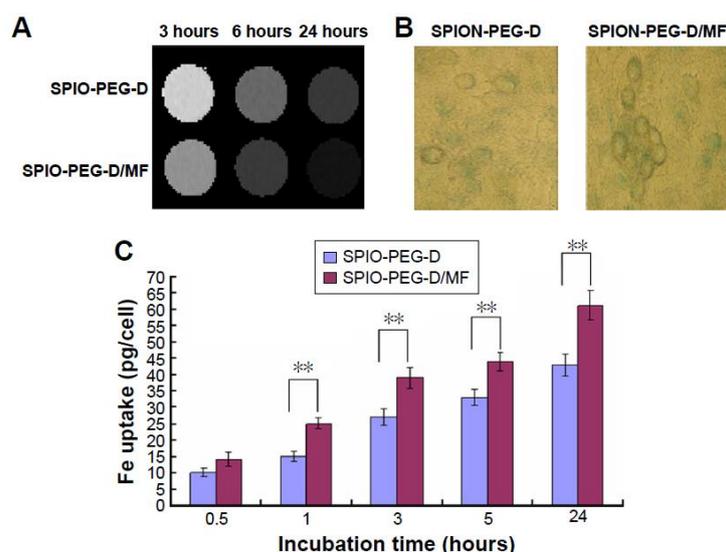


**Figure 1.2.13 A) T2-weighted MR images of HT-29 cells after incubation with SPIO-PEG-D and SPIO-PEG-D/MF for 3, 6 or 24 h (B) Prussian blue staining images of HT-29 cells after 24 h treatment with SPIO-PEG-D and SPIO-PEG-D/MF. (C) Fe uptake in HT-29 cells treated with 100 µg Fe/mL of SPION-PEG-D with and without MF at different incubation time.**

The cytotoxicity of SPIO-PEG-D and SPIO-PEG-D/MF to HT-29 cells was determined using the MTT assay. The results showed that both SPIO-PEG-D and SPIO-PEG-D/MF were toxic to HT-29 cells in a dose-dependent manner (**Figure 1.2.14**). $IC_{50}$ was 3.6 µM for SPIO-PEG-D/MF and 5.7 µM for SPIO-PEG-D NPs and perhaps it is because more SPIO-PEG-D NPs were driven to the cells when the magnetic field was applied to enhance the local drug concentration.
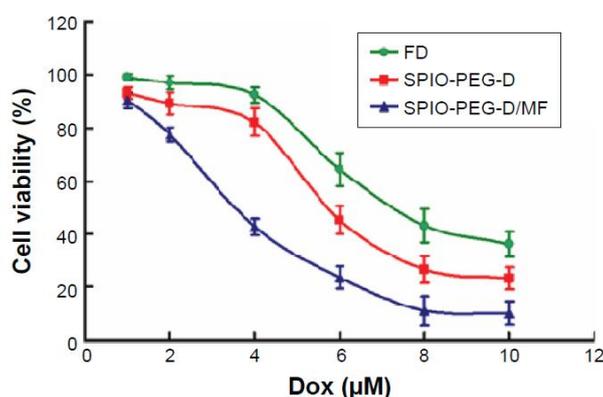


**Figure 1.2.14 Viability of HT-29 cells after incubation with free DOX (FD), SPIO-PEG-D and SPIO-PEG-D/MF.**

The distribution of SPIO-PEG-D NPs in mouse tumor tissues was assessed by T2-weighted MR image before and after an injection of 18 mg Fe/kg after 12 and 24 hours (**Figure 1.2.15A**). Signal intensity in tumor decreased significantly after the injection of SPIO-PEG-D, indicating that the iron deposition in the tumor was locally increased. The in vivo MR image study also showed that the T2-weighted signal of the SPIO-PEG-D/MF was stronger than the SPIO-PEG-D NPs, indicating a better NPs deposition in the tumor when a magnet was applied. The result demonstrated that a local magnetic field could help SPIO-PEG-D target the tumor and have a better retention over time. To validate the existence of SPIO-PEG-D in tumor tissues, microscopic images of Prussian blue-stained tissue slices were performed, and the images revealed the presence of iron as shown in **Figure 1.2.15C**. The Prussian blue staining displayed that the SPIO-PEG-D/MF NPs had a much higher iron density in tumor tissues than the SPIO-PEG-D.
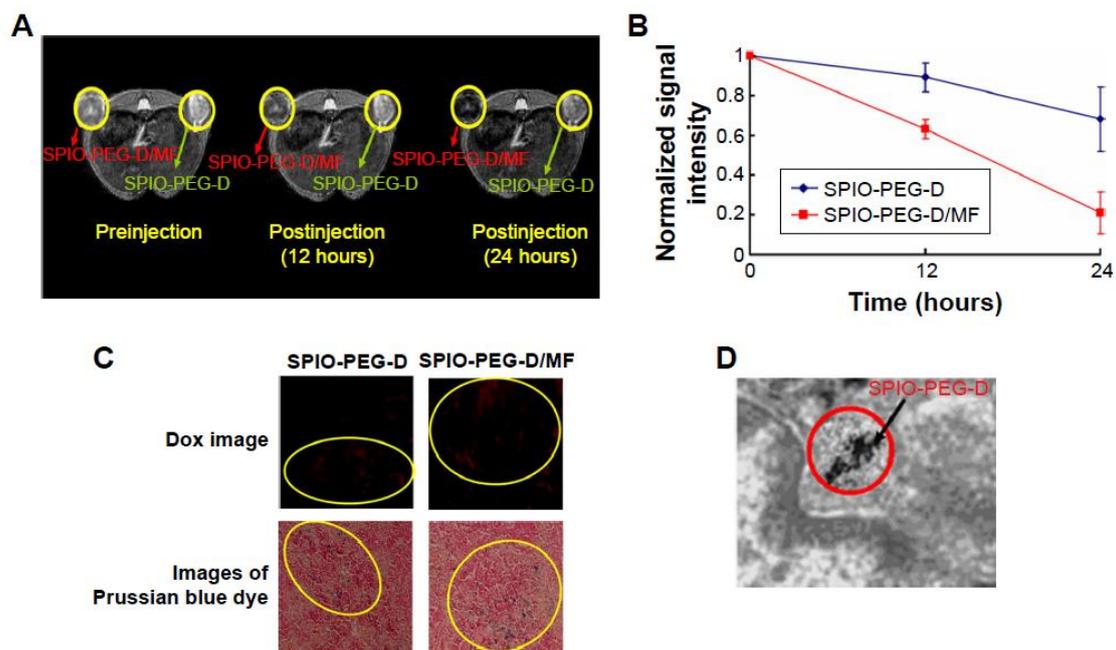
**Figure 1.2.15 In vivo MR imaging and detection of SPIO-PEG-D with and without applying a magnetic field.**

Also, from **Figure 1.2.15C**, the confocal laser scanning microscopic images of DOX in tumor tissues after treatment with SPIO-PEG-D at 24 hours showed that the SPIO-PEG-D/MF NPs had a much higher DOX accumulation in tumor tissues (red fluorescence signals) than for the NPs without applying a MF. **Figure 1.2.15D** shows the TEM image of tumor tissues after treatment with SPIO-PEG-D/MF which indicated the internalized SPIO-PEG-D in tumor cells by endocytosis. Prussian blue staining and TEM images of tumor slices demonstrated that SPIO-PEG-D was guided to and retained in the tumor by applying a magnetic field.

# 3. Characterization techniques

## 3.1. High resolution Transmission electron microscopy (HR-TEM)

HR-TEM permits to obtain the structural characteristics of nanoscale particles or massive compounds, simultaneously in real space and reciprocal space (Fourier space). The structure can thus be visualized at the atomic scale as spatial resolutions are achieved from 0.1 to 0.2 nm. It has the same principle as an ordinary microscope, however it is operated using an electron source instead of a light source.

In HR-TEM the sample is deposited on a carbon grid. The grid is placed on the sample holder and then input into the column of the microscope. A monoenergetic parallel beam is generated by an electron gun (W at 2500 °C, $LaB_6$ at 1500 °C). These electrons are accelerated in the column under vacuum (W: $10^{-3}$-$10^{-4}$ Pa, $LaB_6$: $10^{-5}$-$10^{-6}$ Pa). The acceleration voltage of 200 kV is used. The electrons are focused with the aid of magnetic lenses and the objective lens. The beam width is defined by the choice of the focal plane and influences the illumination of the object. The microscope is provided with a third lens set, projections lenses. They allow transferring the image on the screen and perform magnifications. By changing the focalization of these lenses projections, we can work on either an imaging or a diffraction mode (**Figure 1.3.1**). The resolution of in imaging mode is determined by the wavelength of the irradiation. When using electrons instead of ordinary light the resolution can be greatly enhanced due to the very short wavelength of the electrons observing single atoms and their crystal planes. On the other hand, when using the diffraction mode a diffraction pattern is obtained revealing information concerning the crystalline structure.

HR-TEM images were obtained with a JEOL ARM 200F-Cold FEG (point resolution 0.19 nm) fitted with a GIF Quantum ER. The functionalized NPs were initially dispersed with the aid of ultrasound in ethanol and then one drop of the suspension is deposited onto a microscope carbon copper grid, dried at room temperature and then treated with heat to avoid contamination.
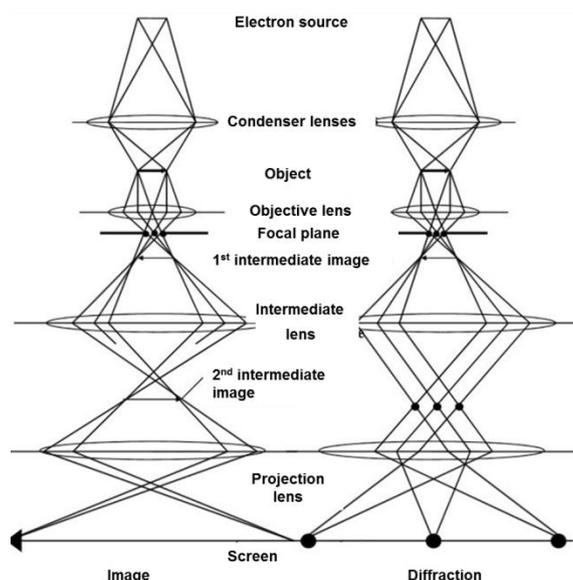
**Figure 1.3.1 General diagram of a TEM (Image mode-diffraction mode).**

ZnO and $Fe_3O_4$ NPs images before and after the grafting of the polymer were obtained at low and high magnification. The calculation of the average diameter of the samples was carried out with the ImageJ software from HR-TEM images containing at least 100 particles.

## 3.2. Dynamic Light Scattering (DLS)

DLS was used to study the behavior of the NPs by following the change in the NPs size with the change in temperature in liquid media by measuring the speed at which the NPs are diffusing due to Brownian motion. Brownian motion is the random movement of particles due to the bombardment by the solvent molecules that surround them, as a result the NPs should be suspended within a liquid when analyzed on DLS and the size is then measured by analyzing the translational diffusion coefficient, which defines the velocity of the Brownian motion, using the Stokes-Einstein (**Equation 5**):

$$d_H = \frac{kT}{3\pi\eta D} \tag{5}$$

$d_H$: hydrodynamic diameter (nm)

T: temperature (K)

D: translational diffusion coefficient ($m^2$/s)

$\eta$: Solvent viscosity (Kg/m.s)

k: Boltzmann contant

Different factors affect the Brownian motion of the NPs including the concentration and ionic strength of the medium, the shape of the NPs and their surface structure. Any surface modification of the NPs affecting the Brownian motion will correspondingly change the apparent size of the particle. Polymer chains projecting out into the medium will reduce the Brownian motion more than if a polymer layer is lying flat on the surface. The nature of the surface and the polymer, as well as the ionic concentration of the medium can affect the polymer conformation, which in turn can change the apparent size by several nanometers [216].

DLS analyses were performed on Malvern "Nanosizer NanoZS" Ltd. At each measurement a delay time is needed to achieve a stable temperature as the viscosity of a liquid is related to the temperature. Diluted samples were prepared by dispersing enough amounts of NPs in milli-Q water with the aid of ultrasound. The suspension is then placed in a cuvette and shot by a laser. The scattered light is collected by a photomultiplier and the resulting image is projected onto a photodetector. This is known as a speckle pattern (**Figure 1.3.2**).
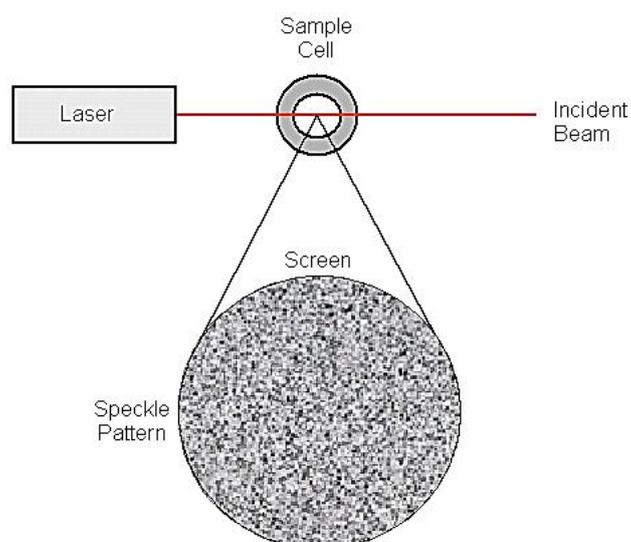


**Figure 1.3.2 Schematic representation of a speckle pattern.**

The scattered light can either interfere constructively resulting in an increased intensity detected (light regions) or destructively resulting in decreased intensity detected (dark regions). This process is repeated at short time intervals and the resulting set of speckle patterns are analyzed by an auto-correlator that compares the intensity of light at each spot over time. The size distribution obtained is a plot of the relative intensity of light scattered by particles.

## 3.3. X-ray diffraction (XRD)

X-ray diffraction (XRD) is a versatile, non-destructive technique used for qualitative and quantitative analysis of a crystalline materials. This technique is used to determine the crystal structure of bulk solids to identify unknown materials, distance between planes in a crystal, orientation of single crystals, orientation of polycrystalline, stress, strain, texture, films thickness etc.

The principle of XRD is described by Bragg"s law (**Equation 6**):

$$n\lambda = 2dsin\theta \tag{6}$$

Where d is the distance between atomic planes, $\theta$ is the angle of incidence, $\lambda$ is the wavelength of the incident light and n is an integer.

Constructive interference occurs when Bragg"s law is satisfied and the difference in length A+B is equal to an integer (n) of oscillations of the light wave (**Figure 1.3.3**).
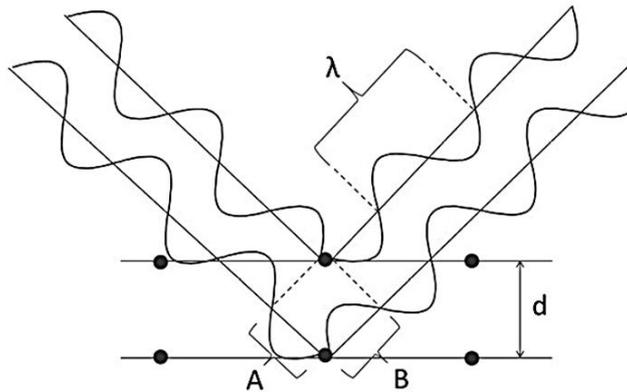


**Figure 1.3.3 Schematic illustration of XRD when Bragg's law is satisfied.**

XRD analysis can provide the crystalline quality and dominant crystallographic planes of the given material. In addition, the diffraction spectrum also provides information regarding the types of phases present in the material and can be used to calculate the mean NPs size (D) using Scherrer"s equation (**Equation 7**) [217]:

$$D = \frac{K\lambda}{Bcos\theta} \tag{7}$$

Where K is the shape factor, λ is the wavelength of CuKα, B is the full width at half maximum and θ is the Bragg angle obtained from 2θ value corresponding to maximum intensity peak in XRD pattern.

In this study, D8 Bruker diffractometer system with a resolution of 0.02° for 2θ and a CuKα x-ray tube (λ=1.54056 Å) was used to investigate the crystallinity of the NPs. X-ray scans were performed between 2θ values of 20° and 80° using a step size of 0.05.

## 3.4. Fourier transmission Infrared Spectroscopy (FT-IR)

FT-IR provides information about the structure of the structures of molecules with the molecules characteristic absorption of IR radiation. It is a technique, which utilizes an interferometer, originally designed by Michelson. The Michelson interferometer consists of two plane mirrors at right to each other and a beam splitter at an angle of 45° to the mirrors (**Figure 1.3.4**). One mirror is fixed in a stationary position and the other can be moved in a direction perpendicular to its front surface at a constant velocity. Between the fixed mirror and the movable mirror is a beam splitter, which divides the incoming light from the source, which is 50 % is transmitted and 50 % is reflected.
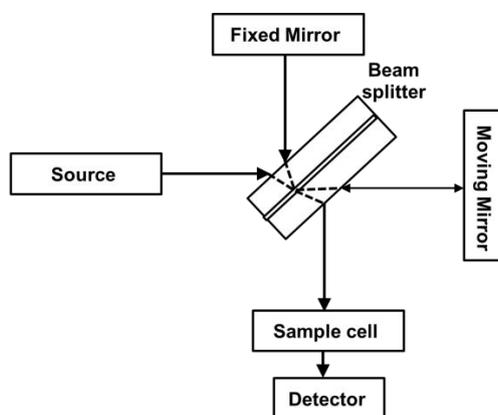


**Figure 1.3.4 The main components of IR spectroscopy.**

The IR spectrum of a sample is established by passing an infrared light beam through the sample. When the wavelength of the emitted beam is close to the energy of vibration of the molecule, the latter absorbs the radiation and recording a decrease in the reflected or transmitted intensity. Thus, the energy of the IR radiation found is decreased after interaction, leading to the appearance of an absorption band at this frequency. This absorption is not systematic; it depends on the geometry of the molecule as well as its symmetry. The position

of these absorption bands depends on the difference in electronegativity of atoms (bond strength) and their mass. Therefore, a given material will present a set of characteristic absorption bands for identification. By analyzing the IR spectrum, we can readily obtain abundant structure information of a molecule.

The bare and functionalized NPs in a dry form were analyzed by a Nicolet 6700 IR spectrometer equipped with a deuterated triglycine sulphate detector in the 400–7000 $cm^{-1}$ wavelength range in a reflexion mode.

## 3.5. Ultraviolet-Visible (UV-Vis) spectroscopy

UV-Vis spectroscopy is the phenomenon which allows observing and quantifying energy form of light in the UV-Vis spectral region (200-700 nm) referring to absorption or reflectance spectroscopy. Molecules containing π-electrons or non-bonding electrons can absorb the energy in the form of UV or visible light to excite these electrons to higher anti-bonding molecular orbitals. In such an electronic transition, the energy absorbed depends on the energy difference between the two states, and thus the wavelength of the transition depends on Bohr relation (**Equation 8**):

$$\Delta E = \frac{hc}{\lambda} = h\nu \tag{8}$$

Where: $\Delta E$ is the energy difference (Joules), h is the Planck''s constant ($6.62*10^{-34}$ J.s), c is the speed of light ($3*10^8$ m/s), λ is the wavelength of light (nm) and ν is the frequency ($s^{-1}$).

UV-Vis spectroscopy can be used to determine the concentration of a solute in a solution following the Beer-Lambert law.

**The Beer-Lambert law:**

When the electromagnetic radiation passes through the solution put in a cuvette (**Figure 1.3.5**), we define the transmittance as the ratio of the intensity of transmitted light (I) to the intensity of the incident light ($I_0$) (**Equation 9**):

$$T = I/I_0 \tag{9}$$
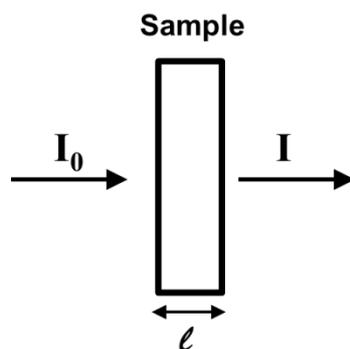
**Figure 1.3.5 The "cuvette" model which forms the basis of the Beer–Lambert law.**

And the absorbance is expressed by **Equation 10**:

$$A = \log(I/I_0) = -\log T \tag{10}$$

The Beer-Lambert law states a linear relation between the absorbance and the concentration of a solute at a precise wavelength (**Equation 11**):

$$A = \log(I/I_0) = \varepsilon l c \tag{11}$$

Where: $\varepsilon$ is the molar absorptivity (L/mole.cm), l is the length of the light pass through the sample (cm) and c is the solute molar concentration (mole/L).

I and $I_0$ intensities are measured simultaneously or sequentially depending on the material used (single or double beam spectrophotometer). The measurement $I_0$ is done using a "blank" which takes into account the fraction of absorbed radiation and/or reflected by the cuvette and the solvent. The solute will absorb a quantity of light at several wavelengths. These values are represented by a graph which is called an absorption spectrum, giving absorbance versus wavelength.

Absorption spectra are recorded on a Thermo Scientific Evolution 220 UV-visible spectrophotometer. The wavelength scan covered the range from 700 to 200 nm. UV-Vis and fluorescence spectroscopies were also used to follow the drug release from the $Fe_3O_4$ NPs by following the change in the absorption and photoluminescence intensity of the DOX model. Absorption spectroscopy is complementary to fluorescence spectroscopy, where fluorescence deals with transitions from the excited state to the ground state, while absorption measures transitions from the ground state to the excited state.

## 3.6. Fluorescence spectroscopy

Fluorescence spectroscopy (also known as spectrofluorometry) is used to analyze fluorescence from a sample. Fluorescence is a phenomenon where light is emitted from a sample when irradiated with light. When a fluorescent sample is irradiated with light, an electron is excited into a higher energy level. The excited electron relaxes via vibrations into a lower energy state and then finally jumps back into its ground state. This final step results in the formation of photons and light is emitted with higher wavelength as the fluorescence energy is lower. **Figure 1.3.6** illustrates the fluorescence process in a Jablonski diagram.
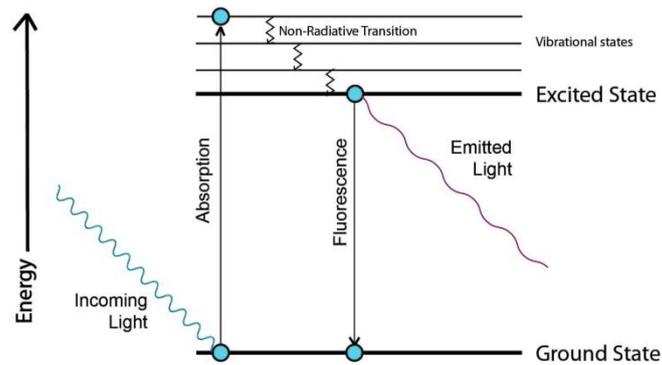


**Figure 1.3.6 The fluorescence process (Jablonski diagram).**

The fluorescence efficiency of a material is described in terms of the PL QY which is the number of photons emitted relative to the number absorbed. The QY of an unknown sample can be measured using a standard sample with a known QY value and the unknown QY value is calculated from **Equation 12**:

$$PL\ QY\ (sample) = \left(\frac{F_{sample}}{F_{ref}}\right)\left(\frac{A_{ref}}{A_{sample}}\right)\left(\frac{n_{sample}^2}{n_{ref}^2}\right) PL\ QY_{(ref)} \tag{12}$$

Where $F$ is the measured fluorescence (area under the emission peak), A is the absorbance at the excitation wavelength and n is the refractive index of the solvent. PL spectra were recorded on a Horiba Fluoromax-4 JobinYvon spectrofluorimeter. Oleate capped and silanalized ZnO NPs were prepared in toluene and copolymer modified ZnO NPs were prepared in milli-Q water. The samples were excited at a wavelength equals to 350 nm.

## 3.7. Thermal Gravimetric Analysis (TGA)

TGA is a method of thermal analysis in which changes in physical and chemical properties of materials are measured as a function of heat (increasing temperature with constant heating rate), or as a function of time (with constant temperature). The influence of the heat causes a thermal decomposition of the material and thus the weight loss allows determining the fractions of organic components present in the material. The instrument for TGA analysis is composed of a thermobalance which measures any changes in the sample mass caused by oxygen adsorption, thermal degradation, oxidation or other heterogeneous reactions when the heat is applied.
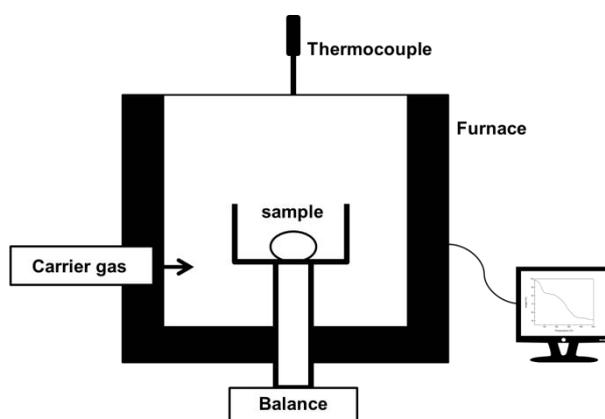


**Figure 1.3.7 A general diagram of TGA system.**

The instrument used in our study is a SETSYS Supersonic thermobalance produced by SETARAM. The furnace can work at high temperatures. It is made up of a graphite element operating from room temperature up to 1600 °C. It is cooled down by water circulation and the regulation is done by a type S thermocouple. The microbalance can be used with a mass variation of ± 200 mg or ± 20 mg with a resolution of $10^{-7}$ g. The max load weight is 20 g. The apparatus is controlled by software appointed Calisto. We used a crucible made of alumina ($Al_2O_3$) with a volume of 30 µL. A general diagram of a TGA system is presented in **Figure 1.3.7**.

Almost dry samples of about 30 mg were put in the crucible. The samples were heated from room temperature to 600 °C at a heating rate of 5 °C/min under argon atmosphere. Percentage weight loss was plotted as a function of temperature enabling to determine the fraction of the copolymer present in the structure of each sample.

# REFERENCES

1.      Feynman, R.P., *There's plenty of room at the bottom.* Engineering and science, 1960. **23**(5): p. 22-36.

2.      Devreese, J.T., *Importance of nanosensors: Feynman's vision and the birth of nanotechnology.* Mrs Bulletin, 2007. **32**(09): p. 718-725.

3.      Borm, P., Klaessig, F.C., Landry, T.D., Moudgil, B., Pauluhn, J., Thomas, K., Trottier, R. and Wood, S., *Research strategies for safety evaluation of nanomaterials, part V: role of dissolution in biological fate and effects of nanoscale particles.* Toxicological Sciences, 2006. **90**(1): p. 23-32.

4.      Nagarajan, R., *Nanoparticles: building blocks for nanotechnology.* Nanoparticles: Synthesis, Stabilization, Passivation, and Functionalization, 2008. **996**: p. 2-14.

5.      Starov, V.M., *Nanoscience: colloidal and interfacial aspects.* CRC Press, 2010. **147**.

6.      Henglein, A., *Small-particle research: physicochemical properties of extremely small colloidal metal and semiconductor particles.* Chemical reviews, 1989. **89**(8): p. 1861-1873.

7.      Ghosh Chaudhuri, R., and Paria, S., *Core/shell nanoparticles: classes, properties, synthesis mechanisms, characterization, and applications.* Chemical reviews, 2011. **112**(4): p. 2373-2433.

8.      Hoener, C.F., Allan, K.A., Bard, A.J., Campion, A., Fox, M.A., Mallouk, T.E., Webber, S.E. and White, J.M., *Demonstration of a shell-core structure in layered cadmium selenide-zinc selenide small particles by x-ray photoelectron and Auger spectroscopies.* The Journal of Physical Chemistry, 1992. **96**(9): p. 3812-3817.

9.      Danek, M., Jensen, K.F., Murray, C.B. and Bawendi, M.G., *Synthesis of luminescent thin-film CdSe/ZnSe quantum dot composites using CdSe quantum dots passivated with an overlayer of ZnSe.* Chemistry of Materials, 1996. **8**(1): p. 173-180.

10.     Huang, J., Yang, Y., Yang, B., Liu, S. and Shen, J., *Preparation and characterization of $Cu_2S/CdS/ZnS$ nanocomposite in polymeric networks.* Polymer Bulletin, 1996. **37**(5): p. 679-682.

11.     Li, M., Chen, X., Guan, J., Wang, X., Wang, J., Williams, C.T. and Liang, C., *A facile and novel approach to magnetic $Fe@SiO_2$ and $FeSi_2@SiO_2$ nanoparticles.* Journal of Materials Chemistry, 2012. **22**(2): p. 609-616.

12.     Mathew, S., Bhardwaj, B.S., Saran, A.D., Radhakrishnan, P., Nampoori, V.P.N., Vallabhan, C.P.G. and Bellare, J.R., *Effect of ZnS shell on optical properties of CdSe–ZnS core–shell quantum dots.* Optical Materials, 2015. **39**: p. 46-51.

13.     Ibnaouf, K.H., Prasad, S., Hamdan, A., Alsalhi, M., Aldwayyan, A.S., Zaman, M.B. and Masilamani, V., *Photoluminescence spectra of CdSe/ZnS quantum dots in solution.* Spectrochimica Acta Part A: Molecular and Biomolecular Spectroscopy, 2014. **121**: p. 339-345.

14.     Bao, F., Yao, J.L. and Gu, R.A., *Synthesis of magnetic $Fe_2O_3/Au$ core/shell nanoparticles for bioseparation and immunoassay based on surface-enhanced Raman spectroscopy.* Langmuir, 2009. **25**(18): p. 10782-10787.

15.     Anbarasu, M., Anandan, M., Chinnasamy, E., Gopinath, V. and Balamurugan, K., *Synthesis and characterization of polyethylene glycol (PEG) coated $Fe_3O_4$ nanoparticles by chemical co-precipitation method for biomedical applications.* Spectrochimica Acta Part A: Molecular and Biomolecular Spectroscopy, 2015. **135**: p. 536-539.

16.     Cui, Y., Zheng, X.S., Ren, B., Wang, R., Zhang, J., Xia, N.S. and Tian, Z.Q., *Au@organosilica multifunctional nanoparticles for the multimodal imaging.* Chemical Science, 2011. **2**(8): p. 1463-1469.

17. Zhao, M., Zhou, G., Zhang, L., Li, X., Li, T. and Liu, F., *Fabrication and photoactivity of a tunable-void SiO$_2$–TiO$_2$ core–shell structure on modified SiO$_2$ nanospheres by grafting an amphiphilic diblock copolymer using ARGET ATRP.* Soft matter, 2014. **10**(8): p. 1110-1120.

18. Shan, W., Hu, L., Lin, X., Chen, M. and Wu, L., *Oil–water interfacial self-assembly of PS/ZnS nanospheres and photoconducting property of corresponding nanofilm.* Journal of Materials Chemistry, 2012. **22**(34): p. 17671-17676.

19. Gong, Z.L., and Tang, D.Y., *The fabrication and self-flocculation effect of hybrid TiO$_2$ nanoparticles grafted with poly (N-isopropylacrylamide) at ambient temperature via surface-initiated atom transfer radical polymerization.* Journal of Materials Chemistry, 2012. **22**(33): p. 16872-16879.

20. Lauhon, L.J., Gudiksen, M.S., Wang, D. and Lieber, C.M., *Epitaxial core–shell and core–multishell nanowire heterostructures.* Nature, 2002. **420**(6911): p. 57-61.

21. Ukaji, E., Furusawa, T., Sato, M. and Suzuki, N., *The effect of surface modification with silane coupling agent on suppressing the photo-catalytic activity of fine TiO$_2$ particles as inorganic UV filter.* Applied Surface Science, 2007. **254**(2): p. 563-569.

22. Tristantini, D., and Mustikasari, R., *Modification of TiO$_2$ nanoparticle with PEG and SiO$_2$ for anti-fogging and self-cleaning application.* International Journal of Engineering & Technology, 2011. **11**(2): p. 73-78.

23. Wang, D., Wang, Y., Li, X., Luo, Q., An, J. and Yue, J., *Sunlight photocatalytic activity of polypyrrole–TiO$_2$ nanocomposites prepared by ‗in situ' method.* Catalysis Communications, 2008. **9**(6): p. 1162-1166.

24. Zhang, Y., Kohler, N. and Zhang, M., *Surface modification of superparamagnetic magnetite nanoparticles and their intracellular uptake.* Biomaterials, 2002. **23**(7): p. 1553-1561.

25. Cheyne, R.W., Smith, T.A., Trembleau, L. and Mclaughlin, A.C., *Synthesis and characterisation of biologically compatible TiO$_2$ nanoparticles.* Nanoscale research letters, 2011. **6**(1): p. 1-6.

26. Chertok, B., David, A.E. and Yang, V.C., *Polyethyleneimine-modified iron oxide nanoparticles for brain tumor drug delivery using magnetic targeting and intra-carotid administration.* Biomaterials, 2010. **31**(24): p. 6317-6324.

27. Schellenberger, E.A., Bogdanov Jr, A., Hogemann, D., Tait, J., Weissleder, R. and Josephson, L., *Annexin V-CLIO: a nanoparticle for detecting apoptosis by MRI.* Mol Imaging, 2002. **1**(2): p. 102-107.

28. Jeon, I.Y., and Baek, J.B., *Nanocomposites derived from polymers and inorganic nanoparticles.* Materials, 2010. **3**(6): p. 3654-3674.

29. Ong, J.L., Appleford, M.R. and Mani, G., *Introduction to biomaterials: basic theory with engineering applications.* Cambridge University Press, 2013.

30. Allemann, E., Gurny, R. and Doelker, E., *Drug-loaded nanoparticles: preparation methods and drug targeting issues.* European journal of pharmaceutics and biopharmaceutics, 1993. **39**(5): p. 173-191.

31. Gao, D., Xu, H., Philbert, M.A. and Kopelman, R., *Bioeliminable nanohydrogels for drug delivery.* Nano letters, 2008. **8**(10): p. 3320-3324.

32. Soppimath, K.S., Aminabhavi, T.M., Dave, A.M., Kumbar, S.G. and Rudzinski, W.E., *Stimulus-responsive ―smart" hydrogels as novel drug delivery systems.* Drug Development and Industrial Pharmacy, 2002. **28**(8): p. 957-974.

33. Achilleos, D.S., and Vamvakaki, M., *End-grafted polymer chains onto inorganic nano-objects.* Materials, 2010. **3**(3): p. 1981-2026.

34.	Mansky, P., Liu, Y., Huang, E., Russell, T.P. and Hawker, C., *Controlling polymer-surface interactions with random copolymer brushes.* Science, 1997. **275**(5305): p. 1458-1460.

35.	Fan, X., Lin, L. and Messersmith, P.B., *Surface-initiated polymerization from TiO₂ nanoparticle surfaces through a biomimetic initiator: a new route toward polymer–matrix nanocomposites.* Composites Science and Technology, 2006. **66**(9): p. 1198-1204.

36.	Braunecker, W.A., and Matyjaszewski, K., *Controlled/living radical polymerization: features, developments, and perspectives.* Progress in Polymer Science, 2007. **32**(1): p. 93-146.

37.	Matyjaszewski, K., *Atom transfer radical polymerization (ATRP): current status and future perspectives.* Macromolecules, 2012. **45**(10): p. 4015-4039.

38.	Hariharan, R., Senthilkumar, S., Suganthi, A. and Rajarajan, M., *Synthesis and characterization of doxorubicin modified ZnO/PEG nanomaterials and its photodynamic action.* Journal of Photochemistry and Photobiology B: Biology, 2012. **116**: p. 56-65.

39.	Liu, G., and Zhang, G., *Conformational Change of Grafted Polymer Chains*, in *QCM-D Studies on Polymer Behavior at Interfaces* 2013, Springer. p. 9-31.

40.	Plunkett, K.N., Zhu, X., Moore, J.S. and Leckband, D.E., *PNIPAM chain collapse depends on the molecular weight and grafting density.* Langmuir, 2006. **22**(9): p. 4259-4266.

41.	Vihola, H., Laukkanen, A., Valtola, L., Tenhu, H. and Hirvonen, J., *Cytotoxicity of thermosensitive polymers poly (N-isopropylacrylamide), poly (N-vinylcaprolactam) and amphiphilically modified poly (N-vinylcaprolactam).* Biomaterials, 2005. **26**(16): p. 3055-3064.

42.	Resch-Genger, U., Grabolle, M., Cavaliere-Jaricot, S., Nitschke, R. and Nann, T., *Quantum dots versus organic dyes as fluorescent labels.* Nature methods, 2008. **5**(9): p. 763-775.

43.	Zrazhevskiy, P., Sena, M. and Gao, X., *Designing multifunctional quantum dots for bioimaging, detection and drug delivery.* Chemical Society Reviews, 2010. **39**(11).

44.	Aswathy, R.G., Yoshida, Y., Maekawa, T. and Kumar, D.S., *Near-infrared quantum dots for deep tissue imaging.* Analytical and Bioanalytical Chemistry, 2010. **397**(4): p. 1417-1435.

45.	Drbohlavova, J., Adam, V., Kizek, R. and Hubalek, J., *Quantum Dots - Characterization, Preparation and Usage in Biological Systems.* International Journal of Molecular Sciences, 2009. **10**(2): p. 656-673.

46.	Zeng, R., Zhang, T., Liu, J., Hu, S., Wan, Q., Liu, X., Peng, Z. and Zou, B., *Aqueous synthesis of type-II CdTe/CdSe core–shell quantum dots for fluorescent probe labeling tumor cells.* Nanotechnology, 2009. **20**(9): p. 095102.

47.	Hu, D., Zhang, P., Gong, P., Lian, S., Lu, Y., Gao, D. and Cai, L., *A fast synthesis of near-infrared emitting CdTe/CdSe quantum dots with small hydrodynamic diameter for in vivo imaging probes.* Nanoscale, 2011. **3**(11): p. 4724-4732.

48.	Aldeek, F., Balan, L., Lambert, J. and Schneider, R., *The influence of capping thioalkyl acid on the growth and photoluminescence efficiency of CdTe and CdSe quantum dots.* Nanotechnology, 2008. **19**(47): p. 475401.

49.	Law, W.C., Yong, K.T., Roy, I., Ding, H., Hu, R., Zhao, W. and Prasad, P.N., *Aqueous-Phase Synthesis of Highly Luminescent CdTe/ZnTe Core/Shell Quantum Dots Optimized for Targeted Bioimaging.* Small, 2009. **5**(11): p. 1302-1310.

50.	Yong, K.T., Wang, Y., Roy, I., Rui, H., Swihart, M.T., Law, W.C., Kwak, S.K., Ye, L., Liu, J., Mahajan, S.D. and Reynolds, J.L., *Preparation of quantum dot/drug*

*nanoparticle formulations for traceable targeted delivery and therapy.* Theranostics, 2012. **2**(7): p. 681-694.

51.     Pan, Z.Y., Liang, J., Zheng, Z.Z., Wang, H.H. and Xiong, H.M., *The application of ZnO luminescent nanoparticles in labeling mice.* Contrast media & molecular imaging, 2011. **6**(4): p. 328-330.

52.     Gulia, S., and Kakkar, R., *ZnO quantum dots for biomedical applications.* Adv. Mater. Lett, 2013. **4**(12): p. 876-887.

53.     Taabouche, A., *Contribution à l'étude structurale et microstructurale de films ZnO obtenus par ablation laser.* Mémoire de magister, Université Constantine, 2010: p. 113.

54.     Vaseem, M., Umar, A. and Hahn, Y.B., *ZnO nanoparticles: growth, properties, and applications.* Metal Oxide Nanostructures and Their Applications, 2010. **5**: p. 1-36.

55.     Kahn, M.L., Cardinal, T., Bousquet, B., Monge, M., Jubera, V. and Chaudret, B., *Optical properties of zinc oxide nanoparticles and nanorods synthesized using an organometallic method.* ChemPhysChem, 2006. **7**(11): p. 2392-2397.

56.     Reshchikov, M.A., Morkoc, H., Nemeth, B., Nause, J., Xie, J., Hertog, B. and Osinsky, A., *Luminescence properties of defects in ZnO.* Physica B: Condensed Matter, 2007. **401**: p. 358-361.

57.     Janotti, A., and Van de Walle, C.G., *Fundamentals of zinc oxide as a semiconductor.* Reports on Progress in Physics, 2009. **72**(12): p. 126501.

58.     Askarinejad, A., Alavi, M.A. and Morsali, A., *Sonochemically assisted synthesis of ZnO nanoparticles: a novel direct method.* Iran. J. Chem. Chem. Eng. Vol, 2011. **30**(3).

59.     Dowling, A., Clift, R., Grobert, N., Hutton, D., Oliver, R., O'neill, O., Pethica, J., Pidgeon, N., Porritt, J., Ryan, J. and Seaton, A., *Nanoscience and nanotechnologies: opportunities and uncertainties.* London: The Royal Society & The Royal Academy of Engineering Report, 2004. **61**: p. e64.

60.     Kołodziejczak-Radzimska, A., and Jesionowski, T., *Zinc oxide - from synthesis to application: a review.* Materials, 2014. **7**(4): p. 2833-2881.

61.     Gnanasangeetha, D., and SaralaThambavani, D., *One pot synthesis of zinc oxide nanoparticles via chemical and green method.* Research Journal of Material Sciences ISSN, 2013. **2320**: p. 6055.

62.     Zelechowska, K., *Methods of ZnO nanoparticles synthesis.* BioTechnologia, 2014. **95**(2): p. 150-159.

63.     Sabir, S., Arshad, M. and Chaudhari, S.K., *Zinc Oxide Nanoparticles for Revolutionizing Agriculture: Synthesis and Applications.* The Scientific World Journal, 2014. **2014**: p. 8.

64.     Nahar, L., and Arachchige, I.U., *Sol-Gel Methods for the Assembly of Metal and Semiconductor Nanoparticles.* JSM Nanotechnol Nanomed, 2013. **1**(1): p. 1004.

65.     Koch, U., Fojtik, A., Weller, H. and Henglein, A., *Photochemistry of semiconductor colloids. Preparation of extremely small ZnO particles, fluorescence phenomena and size quantization effects.* Chemical Physics Letters, 1985. **122**(5): p. 507-510.

66.     Cho, A.R., and Park, S.Y., *Synthesis of titania-and silica-polymer hybrid materials and their application as refractive index-matched layers in touch screens.* Optical Materials Express, 2015. **5**(4): p. 690-703.

67.     Znaidi, L., *Sol–gel-deposited ZnO thin films: a review.* Materials Science and Engineering: B, 2010. **174**(1): p. 18-30.

68.     Singh, N., Mehra, R.M. and Kapoor, A., *Synthesis and characterization of ZnO nanoparticles.* Journal of Nano-and Electronic Physics, 2011. **3**(1): p. 132.

69. Do Kim, K., Choi, D.W., Choa, Y.H. and Kim, H.T., *Optimization of parameters for the synthesis of zinc oxide nanoparticles by Taguchi robust design method.* Colloids and Surfaces A: Physicochemical and Engineering Aspects, 2007. **311**(1): p. 170-173.

70. Rani, S., Suri, P., Shishodia, P.K. and Mehra, R.M., *Synthesis of nanocrystalline ZnO powder via sol–gel route for dye-sensitized solar cells.* Solar Energy Materials and Solar Cells, 2008. **92**(12): p. 1639-1645.

71. Mohanta, S.K., Kim, D.C., Kong, B.H., Cho, H.K., Liu, W. and Tripathy, S., *Optical properties of ZnO nanorods and hybrid structures grown on p-type GaN/sapphire and silicon-on-insulator substrates.* Science of Advanced Materials, 2010. **2**(1): p. 64-68.

72. Bari, A.R., Shinde, M.D., Deo, V. and Patil, L.A., *Effect of solvents on the particle morphology of nanostructured ZnO.* Indian Journal of Pure and Applied Physics, 2009. **47**(1): p. 24-27.

73. Zhang, L., Yin, L., Wang, C., Lun, N., Qi, Y. and Xiang, D., *Origin of visible photoluminescence of ZnO quantum dots: defect-dependent and size-dependent.* The Journal of Physical Chemistry C, 2010. **114**(21): p. 9651-9658.

74. Jurablu, S., Farahmandjou, M. and Firoozabadi, T.P., *Sol-Gel Synthesis of Zinc Oxide (ZnO) Nanoparticles: Study of Structural and Optical Properties.* Journal of Sciences, Islamic Republic of Iran, 2015. **26**(3): p. 281-285.

75. Andrews, D., Scholes, G. and Wiederrecht, G., *Comprehensive Nanoscience and Technology, Five-Volume set: Online Version.* Academic Press, 2010. **Five-Volume set**.

76. Alwan, R.M., Kadhim, Q.A., Sahan, K.M., Ali, R.A., Mahdi, R.J., Kassim, N.A. and Jassim, A.N., *Synthesis of Zinc Oxide Nanoparticles via Sol–Gel Route and Their Characterization.* Nanoscience and Nanotechnology, 2015. **5**(1): p. 1-6.

77. Golic, D.L., Brankovic, G., Nešic, M.P., Vojisavljevic, K., Recnik, A., Daneu, N., Bernik, S., Šcepanovic, M., Poleti, D. and Brankovic, Z., *Structural characterization of self-assembled ZnO nanoparticles obtained by the sol–gel method from $Zn(CH_3COO)_2 \cdot 2H_2O$.* Nanotechnology, 2011. **22**(39): p. 395603.

78. Lundblad, A., and Bergman, B., *Synthesis of $LiCoO_2$ starting from carbonate precursors I. The reaction mechanisms.* Solid State Ionics, 1997. **96**(3): p. 173-181.

79. Schneider, R., Balan, L. and Aldeek, F., *Synthesis, Characterization and Biological Applications of Water-Soluble ZnO Quantum Dots.* InTech nanomaterials, 2011: p. 15.

80. Zhang, P., and Liu, W., *ZnO QD@PMAA-co-PDMAEMA nonviral vector for plasmid DNA delivery and bioimaging.* Biomaterials, 2010. **31**(11): p. 3087-3094.

81. Guo, L., Yang, S., Yang, C., Yu, P., Wang, J., Ge, W. and Wong, G.K., *Synthesis and characterization of poly (vinylpyrrolidone)-modified zinc oxide nanoparticles.* Chemistry of Materials, 2000. **12**(8): p. 2268-2274.

82. Moussodia, R.O., Balan, L. and Schneider, R., *Synthesis and characterization of water-soluble ZnO quantum dots prepared through PEG-siloxane coating.* New Journal of Chemistry, 2008. **32**(8): p. 1388-1393.

83. Jana, N.R., Yu, H.H., Ali, E.M., Zheng, Y. and Ying, J.Y., *Controlled photostability of luminescent nanocrystalline ZnO solution for selective detection of aldehydes.* Chemical Communications, 2007(14): p. 1406-1408.

84. Moussodia, R.O., Balan, L., Merlin, C., Mustin, C. and Schneider, R., *Biocompatible and stable ZnO quantum dots generated by functionalization with siloxane-core PAMAM dendrons.* Journal of Materials Chemistry, 2010. **20**(6): p. 1147-1155.

85. Schejn, A., Balan, L., Piatkowski, D., Mackowski, S., Lulek, J. and Schneider, R., *From visible to white-light emission by siloxane-capped ZnO quantum dots upon interaction with thiols.* Optical Materials, 2012. **34**(8): p. 1357-1361.

86. Schejn, A., Commenge, J.M., Balan, L., Falk, L. and Schneider, R., *Size-controlled synthesis of ZnO quantum dots in microreactors.* Nanotechnology, 2014. **25**(14): p. 145606.

87. Kango, S., Kalia, S., Celli, A., Njuguna, J., Habibi, Y. and Kumar, R., *Surface modification of inorganic nanoparticles for development of organic–inorganic nanocomposites—A review.* Progress in Polymer Science, 2013. **38**(8): p. 1232-1261.

88. Shi, H.Q., Li, W.N., Sun, L.W., Liu, Y., Xiao, H.M. and Fu, S.Y., *Synthesis of silane surface modified ZnO quantum dots with ultrastable, strong and tunable luminescence.* Chemical Communications, 2011. **47**(43): p. 11921-11923.

89. Aboulaich, A., Tilmaciu, C.M., Merlin, C., Mercier, C., Guilloteau, H., Medjahdi, G. and Schneider, R., *Physicochemical properties and cellular toxicity of (poly) aminoalkoxysilanes-functionalized ZnO quantum dots.* Nanotechnology, 2012. **23**(33): p. 335101.

90. Xiong, H.M., *ZnO nanoparticles applied to bioimaging and drug delivery.* Advanced Materials, 2013. **25**(37): p. 5329-5335.

91. Li, S., Sun, Z., Li, R., Dong, M., Zhang, L., Qi, W., Zhang, X. and Wang, H., *ZnO Nanocomposites Modified by Hydrophobic and Hydrophilic Silanes with Dramatically Enhanced Tunable Fluorescence and Aqueous Ultrastability toward Biological Imaging Applications.* Scientific reports, 2015. **5**(8475): p. 8.

92. Shen, W., Xiong, H., Xu, Y., Cai, S., Lu, H. and Yang, P., *ZnO− Poly (methyl methacrylate) Nanobeads for Enriching and Desalting Low-Abundant Proteins Followed by Directly MALDI-TOF MS Analysis.* Analytical chemistry, 2008. **80**(17): p. 6758-6763.

93. Xiong, H.M., Xu, Y., Ren, Q.G. and Xia, Y.Y., *Stable Aqueous ZnO@Polymer Core−Shell Nanoparticles with Tunable Photoluminescence and Their Application in Cell Imaging.* Journal of the American Chemical Society, 2008. **130**(24): p. 7522-7523.

94. Zhang, Z.Y., Xu, Y.D., Ma, Y.Y., Qiu, L.L., Wang, Y., Kong, J.L. and Xiong, H.M., *Biodegradable ZnO@ polymer Core–Shell Nanocarriers: pH-Triggered Release of Doxorubicin In Vitro.* Angewandte Chemie International Edition, 2013. **52**(15): p. 4127-4131.

95. Xiong, H.M., Wang, Z.D., Liu, D.P., Chen, J.S., Wang, Y.G. and Xia, Y.Y., *Bonding polyether onto ZnO nanoparticles: an effective method for preparing polymer nanocomposites with tunable luminescence and stable conductivity.* Advanced functional materials, 2005. **15**(11): p. 1751-1756.

96. Xiong, H.M., Liu, D.P., Xia, Y.Y. and Chen, J.S., *Polyether-grafted ZnO nanoparticles with tunable and stable photoluminescence at room temperature.* Chemistry of Materials, 2005. **17**(12): p. 3062-3064.

97. Xiong, H.M., Wang, Z.D. and Xia, Y.Y., *Polymerization initiated by inherent free radicals on nanoparticle surfaces: a simple method of obtaining ultrastable (ZnO) polymer core–shell nanoparticles with strong blue fluorescence.* Advanced Materials, 2006. **18**(6): p. 748-751.

98. Xiong, H.M., Xie, D.P., Guan, X.Y., Tan, Y.J. and Xia, Y.Y., *Water-stable blue-emitting ZnO@ polymer core–shell microspheres.* Journal of Materials Chemistry, 2007. **17**(24): p. 2490-2496.

99. Xiong, H.M., *Photoluminescent ZnO nanoparticles modified by polymers.* Journal of Materials Chemistry, 2010. **20**(21): p. 4251-4262.

100. Hajba, L., and Guttman, A., *The use of magnetic nanoparticles in cancer theranostics: Toward handheld diagnostic devices.* Biotechnology advances, 2016. **34**(4): p. 354-361.

101. Indira, T.K., and Lakshmi, P.K., *Magnetic nanoparticles—a review.* Int. J. Pharm. Sci. Nanotechnol, 2010. **3**(3): p. 1035-1042.

102. Hasany, S.F., Ahmed, I., Rajan, J. and Rehman, A., *Systematic review of the preparation techniques of iron oxide magnetic nanoparticles.* Nanoscience and Nanotechnology, 2012. **2**(6): p. 148-158.

103. Pauly, M., *Structuration de nanoparticules magnétiques d'oxyde de fer en films et étude de leurs propriétés magnétiques et de magnétotransport.* Strasbourg, 2010: p. 230.

104. Umut, E., *Surface modification of nanoparticles used in biomedical applications.* Mod. Surf. Eng. Treat, 2013. **5**: p. 185-208.

105. Sheng-Nan, S., Chao, W., Zan-Zan, Z., Yang-Long, H., Venkatraman, S.S. and Zhi-Chuan, X., *Magnetic iron oxide nanoparticles: Synthesis and surface coating techniques for biomedical applications.* Chinese Physics B, 2014. **23**(3): p. 037503.

106. Teja, A.S., and Koh, P.Y. , *Synthesis, properties, and applications of magnetic iron oxide nanoparticles.* Progress in Crystal Growth and Characterization of Materials, 2009. **55**(1): p. 22-45.

107. Santhosh, P.B., and Ulrih, N.P., *Multifunctional superparamagnetic iron oxide nanoparticles: promising tools in cancer theranostics.* Cancer letters, 2013. **336**(1): p. 8-17.

108. Pang, Y.L., Lim, S., Ong, H.C. and Chong, W.T., *Research progress on iron oxide-based magnetic materials: Synthesis techniques and photocatalytic applications.* Ceramics International, 2016. **42**(1): p. 9-34.

109. Blaney, L., *Magnetite (Fe₃O₄): Properties, synthesis, and applications.* Lehigh Preserve, 2007. **15**(5): p. 33-81.

110. Pankhurst, Q.A., Connolly, J., Jones, S.K. and Dobson, J.J., *Applications of magnetic nanoparticles in biomedicine.* Journal of Physics D: Applied Physics, 2003. **36**(13): p. R167.

111. Tombácz, E., Turcu, R., Socoliuc, V. and Vékás, L., *Magnetic iron oxide nanoparticles: Recent trends in design and synthesis of magnetoresponsive nanosystems.* Biochemical and biophysical research communications, 2015. **468**(3): p. 442-453.

112. Petcharoen, K., and Sirivat, A., *Synthesis and characterization of magnetite nanoparticles via the chemical co-precipitation method.* Materials Science and Engineering: B, 2012. **177**(5): p. 421-427.

113. Maity, D., Choo, S.G., Yi, J., Ding, J. and Xue, J.M., *Synthesis of magnetite nanoparticles via a solvent-free thermal decomposition route.* Journal of Magnetism and Magnetic Materials, 2009. **321**(9): p. 1256-1259.

114. Zhu, M., and Diao, G., *Synthesis of porous Fe₃O₄ nanospheres and its application for the catalytic degradation of xylenol orange.* The Journal of Physical Chemistry C, 2011. **115**(39): p. 18923-18934.

115. Ramesh, R., Rajalakshmi, M., Muthamizhchelvan, C. and Ponnusamy, S., *Synthesis of Fe₃O₄ nanoflowers by one pot surfactant assisted hydrothermal method and its properties.* Materials Letters, 2012. **70**: p. 73-75.

116. Lu, T., Wang, J., Yin, J., Wang, A., Wang, X. and Zhang, T., *Surfactant effects on the microstructures of Fe₃O₄ nanoparticles synthesized by microemulsion method.* Colloids and Surfaces A: Physicochemical and Engineering Aspects, 2013. **436**: p. 675-683.

117. Carenza, E., Barceló, V., Morancho, A., Montaner, J., Rosell, A. and Roig, A., *Rapid synthesis of water-dispersible superparamagnetic iron oxide nanoparticles by a*

*microwave-assisted route for safe labeling of endothelial progenitor cells.* Acta biomaterialia, 2014. **10**(8): p. 3775-3785.

118. Dolores, R., Raquel, S. and Adianez, G.L., *Sonochemical synthesis of iron oxide nanoparticles loaded with folate and cisplatin: effect of ultrasonic frequency.* Ultrasonics sonochemistry, 2015. **23**: p. 391-398.

119. Yanagihara, H., Myoka, M., Isaka, D., Niizeki, T., Mibu, K. and Kita, E., *Selective growth of $Fe_3O_4$ and $\gamma$-$Fe_2O_3$ films with reactive magnetron sputtering.* Journal of Physics D: Applied Physics, 2013. **46**(17): p. 175004.

120. Tristao, J.C., Oliveira, A.A., Ardisson, J.D., Dias, A. and Lago, R.M., *Facile preparation of carbon coated magnetic $Fe_3O_4$ particles by a combined reduction/CVD process.* Materials Research Bulletin, 2011. **46**(5): p. 748-754.

121. Peulon, S., Antony, H., Legrand, L. and Chausse, A., *Thin layers of iron corrosion products electrochemically deposited on inert substrates: synthesis and behaviour.* Electrochimica acta, 2004. **49**(17): p. 2891-2899.

122. Xu, Z., Shen, C., Hou, Y., Gao, H. and Sun, S., *Oleylamine as both reducing agent and stabilizer in a facile synthesis of magnetite nanoparticles.* Chemistry of Materials, 2009. **21**(9): p. 1778-1780.

123. Byrappa, K., and Adschiri, T., *Hydrothermal technology for nanotechnology.* Progress in Crystal Growth and Characterization of Materials, 2007. **53**(2): p. 117-166.

124. Wu, W., He, Q. and Jiang, C., *Magnetic iron oxide nanoparticles: synthesis and surface functionalization strategies.* Nanoscale Research Letters, 2008. **3**(11): p. 397.

125. Kandasamy, G., and Maity, D., *Recent advances in superparamagnetic iron oxide nanoparticles (SPIONs) for in vitro and in vivo cancer nanotheranostics.* International journal of pharmaceutics, 2015. **496**(2): p. 191-218.

126. Massart, R., *Preparation of aqueous magnetic liquids in alkaline and acidic media.* IEEE Transactions on Magnetics, 1981. **17**(2): p. 1247-1248.

127. Shylesh, S., Schünemann, V. and Thiel, W.R., *Magnetically separable nanocatalysts: bridges between homogeneous and heterogeneous catalysis.* Angewandte Chemie International Edition, 2010. **49**(20): p. 3428-3459.

128. Otake, T., Wesolowski, D.J., Anovitz, L.M., Allard, L.F. and Ohmoto, H., *Experimental evidence for non-redox transformations between magnetite and hematite under $H_2$-rich hydrothermal conditions.* Earth and Planetary Science Letters, 2007. **257**(1): p. 60-70.

129. Gupta, A.K., and Wells, S., *Surface-modified superparamagnetic nanoparticles for drug delivery: preparation, characterization, and cytotoxicity studies.* IEEE Transactions on nanobioscience, 2004. **3**(1): p. 66-73.

130. Reddy, L.H., Arias, J.L., Nicolas, J. and Couvreur, P., *Magnetic nanoparticles: design and characterization, toxicity and biocompatibility, pharmaceutical and biomedical applications.* Chemical reviews, 2012. **112**(11): p. 5818-5878.

131. Vikram, S., Dhakshnamoorthy, M., Vasanthakumari, R., Rajamani, A.R., Rangarajan, M. and Tsuzuki, T., *Tuning the Magnetic Properties of Iron Oxide Nanoparticles by a Room-Temperature Air-Atmosphere (RTAA) Co-Precipitation Method.* Journal of nanoscience and nanotechnology, 2015. **15**(5): p. 3870-3878.

132. Mascolo, M.C., Pei, Y. and Ring, T.A., *Room temperature co-precipitation synthesis of magnetite nanoparticles in a large pH window with different bases.* Materials, 2013. **6**(12): p. 5549-5567.

133. Gupta, A.K., and Gupta, M., *Synthesis and surface engineering of iron oxide nanoparticles for biomedical applications.* Biomaterials, 2005. **26**(18): p. 3995-4021.

134. Forge, D., Laurent, S., Gossuin, Y., Roch, A., Vander Elst, L. and Muller, R.N., *An original route to stabilize and functionalize magnetite nanoparticles for theranosis applications*. Journal of magnetism and magnetic materials, 2011. **323**(5): p. 410-415.

135. Shen, X.C., Fang, X.Z., Zhou, Y.H. and Liang, H., *Synthesis and characterization of 3-aminopropyltriethoxysilane-modified superparamagnetic magnetite nanoparticles*. Chemistry Letters, 2004. **33**(11): p. 1468-1469.

136. Ma, M., Zhang, Y., Yu, W., Shen, H.Y., Zhang, H.Q. and Gu, N., *Preparation and characterization of magnetite nanoparticles coated by amino silane*. Colloids and Surfaces A: Physicochemical and Engineering Aspects, 2003. **212**(2): p. 219-226.

137. De Palma, R., Peeters, S., Van Bael, M.J., Van den Rul, H., Bonroy, K., Laureyn, W., Mullens, J., Borghs, G. and Maes, G., *Silane ligand exchange to make hydrophobic superparamagnetic nanoparticles water-dispersible*. Chemistry of Materials, 2007. **19**(7): p. 1821-1831.

138. Conceição, B.M.D., Costa, M.A., Santa Maria, L.C.D., Silva, M.R. and Wang, S.H., *A study of the initiator concentrations effect on styrene-divinylbenzene polymerization with iron particles*. Polímeros, 2011. **21**(5): p. 409-415.

139. Green, L.A.W., and Thanh, N.T.K., *High pressure synthesis of FePt nanoparticles with controlled morphology and Fe content*. RSC Advances, 2014. **4**(3): p. 1168-1173.

140. Creixell, M., Herrera, A.P., Latorre-Esteves, M., Ayala, V., Torres-Lugo, M. and Rinaldi, C., *The effect of grafting method on the colloidal stability and in vitro cytotoxicity of carboxymethyl dextran coated magnetic nanoparticles*. Journal of Materials Chemistry, 2010. **20**(39): p. 8539-8547.

141. Butterworth, M.D., Illum, L. and Davis, S.S., *Preparation of ultrafine silica-and PEG-coated magnetite particles*. Colloids and Surfaces A: Physicochemical and Engineering Aspects, 2001. **179**(1): p. 93-102.

142. Barrera, C., Herrera, A.P., Bezares, N. and Fachini, E., *Effect of poly (ethylene oxide)-silane graft molecular weight on the colloidal properties of iron oxide nanoparticles for biomedical applications*. Journal of colloid and interface science, 2012. **377**(1): p. 40-50.

143. Zhang, L., Zhang, S., He, B., Wu, Z. and Zhang, Z., *TiO₂ nanoparticles functionalized by a temperature-sensitive poly (N-isopropylacrylamide)(PNIPAM): synthesis and characterization*. Zeitschrift für Naturforschung B, 2008. **63**(8): p. 973-976.

144. Bawa, P., Pillay, V., Choonara, Y.E. and Du Toit, L.C., *Stimuli-responsive polymers and their applications in drug delivery*. Biomedical materials, 2009. **4**(2): p. 022001.

145. Kumar, A., Srivastava, A., Galaev, I.Y. and Mattiasson, B., *Smart polymers: physical forms and bioengineering applications*. Progress in Polymer Science, 2007. **32**(10): p. 1205-1237.

146. Ward, M.A., and Georgiou, T.K., *Thermoresponsive polymers for biomedical applications*. Polymers, 2011. **3**(3): p. 1215-1242.

147. Phillips, D.J., and Gibson, M.I., *Towards being genuinely smart: isothermally-responsive 'polymers as versatile, programmable scaffolds for biologically-adaptable materials*. Polymer chemistry, 2015. **6**(7): p. 1033-1043.

148. Gandhi, A., Paul, A., Sen, S.O. and Sen, K.K., *Studies on thermoresponsive polymers: Phase behaviour, drug delivery and biomedical applications*. asian journal of pharmaceutical sciences, 2015. **10**(2): p. 99-107.

149. Fujishige, S., Kubota, K. and Ando, I., *Phase transition of aqueous solutions of poly (N-isopropylacrylamide) and poly (N-isopropylmethacrylamide)*. The Journal of Physical Chemistry, 1989. **93**(8): p. 3311-3313.

150. Winnik, F.M., Ringsdorf, H. and Venzmer, J., *Methanol-water as a co-nonsolvent system for poly (N-isopropylacrylamide)*. Macromolecules, 1990. **23**(8): p. 2415-2416.

151.   Roy, D., Brooks, W.L. and Sumerlin, B.S., *New directions in thermoresponsive polymers.* Chemical Society Reviews, 2013. **42**(17): p. 7214-7243.

152.   Sun, S., and Wu, P., *On the thermally reversible dynamic hydration behavior of oligo (ethylene glycol) methacrylate-based polymers in water.* Macromolecules, 2012. **46**(1): p. 236-246.

153.   Stuart, M.A.C., Huck, W.T., Genzer, J., Müller, M., Ober, C., Stamm, M., Sukhorukov, G.B., Szleifer, I., Tsukruk, V.V., Urban, M. and Winnik, F., *Emerging applications of stimuli-responsive polymer materials.* Nature materials, 2010. **9**(2): p. 101-113.

154.   Ran, J., Wu, L., Zhang, Z. and Xu, T., *Atom transfer radical polymerization (ATRP): a versatile and forceful tool for functional membranes.* Progress in Polymer Science, 2014. **39**(1): p. 124-144.

155.   Wang, Z.K., Wang, D., Wang, H., Yan, J.J., You, Y.Z. and Wang, Z.G., *Preparation of biocompatible nanocapsules with temperature-responsive and bioreducible properties.* Journal of Materials Chemistry, 2011. **21**(40): p. 15950-15956.

156.   Lü, H.Y., Liu, S.X., Xu, C., Tian, R. and Wang, L., *Synthesis and Characterization of Temperature-Sensitivity P (MEO$_2$MA-co-OEGMA) Copolymers.* Acta Phys Chim Sin, 2012. **28**(11): p. 2683-2689.

157.   Fruneaux, T., Hill, A., Kaminski, A. and Anderson, L.S. *Controlling cell adhesion on thermoresponsive P(MEO$_2$MA-co-OEGMA) substrates.* in *Bioengineering Conference (NEBEC), 2014 40th Annual Northeast.* 2014.

158.   Lutz, J.F., Akdemir, Ö. and Hoth, A., *Point by point comparison of two thermosensitive polymers exhibiting a similar LCST: is the age of poly (NIPAM) over?.* Journal of the American Chemical Society, 2006. **128**(40): p. 13046-13047.

159.   Lutz, J.F., *Polymerization of oligo (ethylene glycol)(meth) acrylates: toward new generations of smart biocompatible materials.* Journal of Polymer Science Part A: Polymer Chemistry, 2008. **46**(11): p. 3459-3470.

160.   Hu, Y., Darcos, V., Monge, S. and Li, S., *Thermo-responsive drug release from self-assembled micelles of brush-like PLA/PEG analogues block copolymers.* International journal of pharmaceutics, 2015. **491**(1): p. 152-161.

161.   Lutz, J.F., *Synthesis of Smart Materials by ATRP of Oligo (Ethylene Glycol) Methacrylates. New Smart Materials via Metal Mediated Macromolecular Engineering.* Springer Netherlands, 2009: p. 37-47.

162.   Lutz, J.F., Hoth, A. and Schade, K., *Design of oligo (ethylene glycol)-based thermoresponsive polymers: an optimization study.* Designed Monomers and Polymers, 2009. **12**(4): p. 343-353.

163.   Arora, M., *Cell culture media: A review.* Mater. Meth., 2013. **3**.

164.   Gao, X., Kucerka, N., Nieh, M.P., Katsaras, J., Zhu, S., Brash, J.L. and Sheardown, H., *Chain conformation of a new class of PEG-based thermoresponsive polymer brushes grafted on silicon as determined by neutron reflectometry.* Langmuir, 2009. **25**(17): p. 10271-10278.

165.   Zhang, Y., Furyk, S., Sagle, L.B., Cho, Y., Bergbreiter, D.E. and Cremer, P.S., *Effects of Hofmeister anions on the LCST of PNIPAM as a function of molecular weight.* The Journal of Physical Chemistry C, 2007. **111**(25): p. 8916-8924.

166.   Hofmeister, F., *On the understanding of the effects of salts.* Arch. Exp. Pathol. Pharmakol.(Leipzig), 1888. **24**: p. 247-260.

167.   Joshi, S.C., *Sol-Gel behavior of hydroxypropyl methylcellulose (hpmc) in ionic media including drug release.* Materials, 2011. **4**(10): p. 1861-1905.

168.   Tomczak, N., Jańczewski, D., Han, M. and Vancso, G.J., *Designer polymer–quantum dot architectures.* Progress in Polymer Science, 2009. **34**(5): p. 393-430.

169. Kim, M., Schmitt, S.K., Choi, J.W., Krutty, J.D. and Gopalan, P., *From Self-Assembled Monolayers to Coatings: Advances in the Synthesis and Nanobio Applications of Polymer Brushes.* Polymers, 2015. **7**(7): p. 1346-1378.

170. Cao, L., Man, T., Zhuang, J. and Kruk, M., *Poly (N-isopropylacrylamide) and poly (2-(dimethylamino) ethyl methacrylate) grafted on an ordered mesoporous silica surface using atom transfer radical polymerization with activators regenerated by electron transfer.* Journal of Materials Chemistry, 2012. **22**(14): p. 6939-6946.

171. Ribeiro, T., Baleizão, C. and Farinha, J.P.S., *Functional films from silica/polymer nanoparticles.* Materials, 2014. **7**(5): p. 3881-3900.

172. Ying, L.I., Ya-Feng, W.U., Liang, Y.U.A.N. and Song-Qin, L.I.U., *Application of Atom Transfer Radical Polymerization in Biosensing.* Chinese Journal of Analytical Chemistry, 2012. **40**(12): p. 1797-1802.

173. Siegwart, D.J., Oh, J.K. and Matyjaszewski, K., *ATRP in the design of functional materials for biomedical applications.* Progress in Polymer Science, 2012. **37**(1): p. 18-37.

174. Wang, J.S., and Matyjaszewski, K., *Controlled/" living" radical polymerization. Atom transfer radical polymerization in the presence of transition-metal complexes.* Journal of the American Chemical Society, 1995. **117**(20): p. 5614-5615.

175. Granel, C., Dubois, P., Jérôme, R. and Teyssié, P., *Controlled radical polymerization of methacrylic monomers in the presence of a bis (ortho-chelated) arylnickel (II) complex and different activated alkyl halides.* Macromolecules, 1996. **29**(27): p. 8576-8582.

176. Matyjaszewski, K., Wei, M., Xia, J. and McDermott, N.E., *Controlled/―Living" Radical Polymerization of Styrene and Methyl Methacrylate Catalyzed by Iron Complexes 1.* Macromolecules, 1997. **30**(26): p. 8161-8164.

177. Kato, M., Kamigaito, M., Sawamoto, M. and Higashimura, T., *Polymerization of methyl methacrylate with the carbon tetrachloride/dichlorotris-(triphenylphosphine) ruthenium (II)/methylaluminum bis (2, 6-di-tert-butylphenoxide) initiating system: possibility of living radical polymerization.* Macromolecules, 1995. **28**(5): p. 1721-1723.

178. Qiu, J., Matyjaszewski, K., Thouin, L. and Amatore, C., *Cyclic voltammetric studies of copper complexes catalyzing atom transfer radical polymerization.* Macromolecular Chemistry and Physics, 2000. **201**(14): p. 1625-1631.

179. O'Reilly, R.K., Gibson, V.C., White, A.J. and Williams, D.J., *Five-coordinate iron (II) complexes bearing tridentate nitrogen donor ligands as catalysts for atom transfer radical polymerisation.* Polyhedron, 2004. **23**(17): p. 2921-2928.

180. Simal, F., Demonceau, A. and Noels, A.F., *Highly Efficient Ruthenium-Based Catalytic Systems for the Controlled Free-Radical Polymerization of Vinyl Monomers.* Angewandte Chemie International Edition, 1999. **38**(4): p. 538-540.

181. Huang, J., and Matyjaszewski, K., *Atom transfer radical polymerization of dimethyl (1-ethoxycarbonyl) vinyl phosphate and corresponding block copolymers.* Macromolecules, 2005. **38**(9): p. 3577-3583.

182. Tang, H., Shen, Y., Li, B.G. and Radosz, M., *Tertiary amine—enhanced activity of ATRP catalysts CuBr/TPMA and CuBr/Me$_6$TREN.* Macromolecular Rapid Communications, 2008. **29**(22): p. 1834-1838.

183. Haddleton, D.M., Crossman, M.C., Dana, B.H., Duncalf, D.J., Heming, A.M., Kukulj, D. and Shooter, A.J., *Atom transfer polymerization of methyl methacrylate mediated by alkylpyridylmethanimine type ligands, copper (I) bromide, and alkyl halides in hydrocarbon solution.* Macromolecules, 1999. **32**(7): p. 2110-2119.

184. Nanda, A.K., and Matyjaszewski, K., *Effect of [PMDETA]/[Cu (I)] ratio, monomer, solvent, counterion, ligand, and alkyl bromide on the activation rate constants in atom transfer radical polymerization.* Macromolecules, 2003. **36**(5): p. 1487-1493.

185. Coessens, V., Pintauer, T. and Matyjaszewski, K., *Functional polymers by atom transfer radical polymerization.* Progress in Polymer Science, 2001. **26**(3): p. 337-377.

186. Sun, Y., Ding, X., Zheng, Z., Cheng, X., Hu, X. and Peng, Y., *Surface initiated ATRP in the synthesis of iron oxide/polystyrene core/shell nanoparticles.* European polymer journal, 2007. **43**(3): p. 762-772.

187. Matyjaszewski, K., and Xia, J., *Atom transfer radical polymerization.* Chemical reviews, 2001. **101**(9): p. 2921-2990.

188. Jakubowski, W., and Matyjaszewski, K., *Activators Regenerated by Electron Transfer for Atom-Transfer Radical Polymerization of (Meth) acrylates and Related Block Copolymers.* Angewandte Chemie, 2006. **118**(27): p. 4594-4598.

189. Jakubowski, W., Kirci-Denizli, B., Gil, R.R. and Matyjaszewski, K., *Polystyrene with Improved Chain-End Functionality and Higher Molecular Weight by ARGET ATRP.* Macromolecular Chemistry and Physics, 2008. **209**(1): p. 32-39.

190. Jakubowski, W., Min, K. and Matyjaszewski, K., *Activators regenerated by electron transfer for atom transfer radical polymerization of styrene.* Macromolecules, 2006. **39**(1): p. 39-45.

191. Król, P., and Chmielarz, P., *Recent advances in ATRP methods in relation to the synthesis of copolymer coating materials.* Progress in Organic Coatings, 2014. **77**(5): p. 913-948.

192. Dong, H., and Matyjaszewski, K., *ARGET ATRP of 2-(dimethylamino) ethyl methacrylate as an intrinsic reducing agent.* Macromolecules, 2008. **41**(19): p. 6868-6870.

193. Tan, L., Liu, J., Zhou, W., Wei, J. and Peng, Z., *A novel thermal and pH responsive drug delivery system based on ZnO@PNIPAM hybrid nanoparticles.* Materials Science and Engineering: C, 2014. **45**: p. 524-529.

194. Yao, Z.L., and Tam, K.C., *Temperature induced micellization and aggregation of biocompatible poly (oligo (ethylene glycol) methyl ether methacrylate) block copolymer analogs in aqueous solutions.* Polymer, 2012. **53**(16): p. 3446-3453.

195. Lu, C., Bhatt, L.R., Jun, H.Y., Park, S.H. and Chai, K.Y., *Carboxyl–polyethylene glycol–phosphoric acid: a ligand for highly stabilized iron oxide nanoparticles.* Journal of Materials Chemistry, 2012. **22**(37): p. 19806-19811.

196. Du, S., Zhou, G., Wang, X., Li, T., Xu, Y. and Zhang, L., *Surface modification of silica nanoparticles by grafting poly (methyl methacrylate) using atom transfer radical polymerisation with activators regenerated by electron transfer.* IET Micro & Nano Letters, 2011. **6**(3): p. 154-156.

197. Iacono, M., and Heise, A., *Stable Poly (methacrylic acid) Brush Decorated Silica Nano-Particles by ARGET ATRP for Bioconjugation.* Polymers, 2015. **7**(8): p. 1427-1443.

198. Liu, J., He, W., Zhang, L., Zhang, Z., Zhu, J., Yuan, L., Chen, H., Cheng, Z. and Zhu, X., *Bifunctional nanoparticles with fluorescence and magnetism via surface-initiated AGET ATRP mediated by an iron catalyst.* Langmuir, 2011. **27**(20): p. 12684-12692.

199. Alem, H., Schejn, A., Roques-Carmes, T., Ghanbaja, J. and Schneider, R., *Thermo-responsive and aqueous dispersible ZnO/PNIPAM core/shell nanoparticles.* Nanotechnology, 2015. **26**(33): p. 335605.

200. Oka, C., Ushimaru, K., Horiishi, N., Tsuge, T. and Kitamoto, Y., *Core–shell composite particles composed of biodegradable polymer particles and magnetic iron*

*oxide nanoparticles for targeted drug delivery.* Journal of magnetism and magnetic materials, 2015. **381**: p. 278-284.

201. Hałupka-Bryl, M., Bednarowicz, M., Dobosz, B., Krzyminiewski, R., Zalewski, T., Wereszczyńska, B., Nowaczyk, G., Jarek, M. and Nagasaki, Y., *Doxorubicin loaded PEG-b-poly (4-vinylbenzylphosphonate) coated magnetic iron oxide nanoparticles for targeted drug delivery.* Journal of magnetism and magnetic materials, 2015. **384**: p. 320-327.

202. Kaaki, K., Herv -Aubert, K., Chiper, M., Shkilnyy, A., Souc , M., Benoit, R., Paillard, A., Dubois, P., Saboungi, M.L. and Chourpa, I., *Magnetic nanocarriers of doxorubicin coated with poly (ethylene glycol) and folic acid: relation between coating structure, surface properties, colloidal stability, and cancer cell targeting.* Langmuir, 2011. **28**(2): p. 1496-1505.

203. Zhang, Z.Y., and Xiong, H. M., *Photoluminescent ZnO nanoparticles and their biological applications.* Materials, 2015. **8**(6): p. 3101-3127.

204. Mahmoudi, M., Stroeve, P., Milani, A.S. and Arbab, A.S., *Superparamagnetic iron oxide nanoparticles: Synthesis, Surface Engineering, Cytotoxicity and Biomedical Applications*2011: Nova Science Publishers, Inc. 225.

205. Amstad, E., Textor, M. and Reimhult, E., *Stabilization and functionalization of iron oxide nanoparticles for biomedical applications.* Nanoscale, 2011. **3**(7): p. 2819-2843.

206. Xu, J.K., Zhang, F.F., Sun, J.J., Sheng, J., Wang, F. and Sun, M., *Bio and Nanomaterials Based on Fe₃O₄.* Molecules, 2014. **19**(12): p. 21506-21528.

207. Zhang, J., and Misra, R.D.K., *Magnetic drug-targeting carrier encapsulated with thermosensitive smart polymer: core–shell nanoparticle carrier and drug release response.* Acta biomaterialia, 2007. **3**(6): p. 838-850.

208. Hervault, A., Dunn, A.E., Lim, M., Boyer, C., Mott, D., Maenosono, S. and Thanh, N.T., *Doxorubicin loaded dual pH-and thermo-responsive magnetic nanocarrier for combined magnetic hyperthermia and targeted controlled drug delivery applications.* Nanoscale, 2016. **8**: p. 12152-12161.

209. Yuan, Q., Hein, S. and Misra, R.D.K., *New generation of chitosan-encapsulated ZnO quantum dots loaded with drug: synthesis, characterization and in vitro drug delivery response.* Acta biomaterialia, 2010. **6**(7): p. 2732-2739.

210. Rutnakornpituk, M., Puangsin, N., Theamdee, P., Rutnakornpituk, B. and Wichai, U., *Poly (acrylic acid)-grafted magnetic nanoparticle for conjugation with folic acid.* Polymer, 2011. **52**(4): p. 987-995.

211. Huang, C., Neoh, K.G. and Kang, E.T., *Combined ATRP and _dick'chemistry for designing stable tumor-targeting superparamagnetic iron oxide nanoparticles.* Langmuir, 2011. **28**(1): p. 563-571.

212. Ye, D.X., Ma, Y.Y., Zhao, W., Cao, H.M., Kong, J.L., Xiong, H.M. and M hwa ld, H., *ZnO-Based Nanoplatforms for Labeling and Treatment of Mouse Tumors without Detectable Toxic Side Effects.* ACS nano, 2016. **10**(4): p. 4294-4300.

213. Sun, C., Sze, R. and Zhang, M., *Folic acid-PEG conjugated superparamagnetic nanoparticles for targeted cellular uptake and detection by MRI.* Journal of Biomedical Materials Research Part A, 2006. **78**(3): p. 550-557.

214. Akbarzadeh, A., Mikaeili, H., Zarghami, N., Mohammad, R., Barkhordari, A. and Davaran, S., *Preparation and in vitro evaluation of doxorubicin-loaded Fe₃O₄ magnetic nanoparticles modified with biocompatible copolymers.* International journal of nanomedicine, 2012. **7**: p. 511-526.

215. Liang, P.C., Chen, Y.C., Chiang, C.F., Mo, L.R., Wei, S.Y., Hsieh, W.Y. and Lin, W.L., *Doxorubicin-modified magnetic nanoparticles as a drug delivery system for*

*magnetic resonance imaging-monitoring magnet-enhancing tumor chemotherapy.* International journal of nanomedicine, 2016. **11**: p. 2021.

216. Instruments, M., *Dynamic light scattering: an introduction in 30 minutes.* Technical Note Malvern, 2012. **MRK656-01**: p. 1-8.

217. Zak, A.K., Majid, W.A., Abrishami, M.E. and Yousefi, R., *X-ray analysis of ZnO nanoparticles by Williamson–Hall and size–strain plot methods.* Solid State Sciences, 2011. **13**(1): p. 251-256.

# *Chapter 2: Efficient synthetic access to thermo-responsive core/shell nanoparticles*

# ABSTRACT

Core/shell nanomaterials based on silica ($SiO_2$), fluorescent ZnO quantum dots (QDs) and superparamagnetic $Fe_3O_4$ nanoparticles (NPs) were prepared and fully characterized by the combination of different techniques and the physical properties of the nanomaterials were studied. We demonstrate the efficiency of the Atom Transfer Radical Polymerization with Activators ReGenerated by Electron Transfer (ARGET-ATRP) process to graft copolymers of different structures and polarity at the surface of metal oxide NPs. The influence of the polymer chain configuration on the optical properties of the ZnO/copolymer core/shell nanomaterials was enlightened. Concerning the magnetic properties of the $Fe_3O_4$/copolymer nanomaterials, only the amount of the grafted polymer plays a role on the saturation magnetization ($M_s$) of the NPs and no influence of the aggregation was evidenced. The simple and fast process described in this work is efficient for the grafting of copolymers from surfaces and the derived NPs display the combination of the physical properties of the core and the macromolecular behavior of the shell.

Keywords: Core/shell nanoparticles, ARGET ATRP, surface-initiated polymerization, responsive copolymers.

# 1. INTRODUCTION

The design of core/shell heterostructures, in which the core is an inorganic material and the shell a polymer, has gained wide interest due to the potential applications of such NPs in environmental and pharmaceutical sciences, in nanomedicine, … [1]. Among the different nanohybrids developed, core/shell nanomaterials based on QDs or magnetic NPs (MNPs) are of high interest, especially for biomedical applications [2-4]. Although ZnO QDs and $Fe_3O_4$ NPs display good biocompatibility [5, 6], these NPs suffer from low stability in biological media. It has been found that biodegradation and/or aggregation of the NPs may occur leading to the loss of their physical properties. It is thus not surprising that many efforts have been devoted to stabilize and protect those functional nanomaterials for their further use as fluorescent probes or as contrast agents in magnetic resonance imaging (MRI) [1, 7]. Indeed, in the last decades, the synthesis of biocompatible NPs (especially those derived from ZnO and $Fe_3O_4$) with diameters less than 20 nm, has received great attention in biomedical applications such as MRI contrast enhancement [2, 8], drug delivery and cancer therapy [1, 9] and detoxification of biological fluids [1, 10, 11]. For all biomedical applications, a high stability and the ability to disperse the NPs are key parameters in order to control their state of aggregation in aqueous media at physiological temperature. These properties can be modulated by coating NPs with a biocompatible polymer [12, 13]. The grafting of polymer chains at the surface of these NPs appears then as an ideal route for their stabilization in physiological media [8]. Even though, the "grafting to" process was largely used and showed good efficiency in the anchorage of pre-synthesized polymers leading to responsive magnetic NPs [9-11] as recently demonstrated by Hervault *et al.* [9]. The "grafting from" method is nevertheless preferred since it leads to polymer brushes with higher grafting density than by grafting end-functionalized polymer chains onto a surface, the so-called "grafting to" method [12]. The "grafting from" process involves the anchorage of the polymerization initiator at the NPs surface to allow the growth of the macromolecules from the surface [12]. Many polymerization processes can be used, but thanks to the development of the controlled radical polymerization (CRP) processes, NPs with a perfect control in size, dispersion and grafting density could be developed [12-16]. In a recent report [17], we have demonstrated that the functionalization of ZnO QDs by poly(*N*-isopropyl acrylamide) (PNIPAM) lead to aqueous stable fluorescent NPs and that PNIPAM prevents the degradation of the dots in aqueous solution, and thus the preservation of their optical properties. Among the surface-initiated controlled radical polymerizations (SI-CRPs), surface initiated Atom Transfer Radical

Polymerization with Activators ReGenerated by electron Transfer (ARGET-ATRP) has become an emerging method to engineer well-defined and controlled polymer chains using only ppm amounts of catalyst, which is commercially and environmentally beneficial [8, 18]. So far, a limited number of studies involving ARGET-ATRP for the surface functionalization of inorganic NPs have been reported [15, 16, 19-22]. This study aims to demonstrate that this process, initially developed for the grafting of PNIPAM at the surface of ZnO QDs [15] can be easily extended to the preparation of various particle/polymer systems. In this paper, we first describe the use of the ARGET-ATRP method for the preparation of silica NPs coated with poly(styrene) (PS). Next, responsive biocompatible and bio-repellent polymers such as $P(MOE_2MA_X-OEGMA_{100-X})$ (poly co-2-(2-methoxyethoxy) ethyl methacrylate)$_X$-hydroxyl-terminated oligo(ethylene glycol) methacrylate)$_{100-X}$) were grown from ZnO and $Fe_3O_4$ surfaces. All the nanomaterials were fully characterized by combining complementary methods.

## 2. MATERIALS AND METHODS

### 2.1. Materials

Styrene was purified following the procedure described elsewhere [23]. All the chemical reagents were purchased from Sigma-Aldrich, except ((chloromethyl)phenylethyl)-trimethoxysilane (Gelest, > 95%) (CMPETMS). All the reagents were used as received.

### 2.2. Synthesis of ZnO QDs coated with the silane derivatives

#### 2.2.1. Synthesis of hydrophobic ZnO@oleate QDs

Oleate-capped ZnO QDs were synthesized by using standard airless technique. In brief, anhydrous zinc acetate (220 mg, 1.2 mmol) was dissolved in 20 mL of ethanol at 50 °C. When the solution became clear, 70 µL (0.22 mmol) of oleic acid were added, the mixture stirred for 5 min and the temperature was increased to reflux. In a separate flask, 360 mg (1.99 mmol) of tetramethyl ammonium hydroxide pentahydrate (TMAH) were dissolved in 5 mL of hot ethanol and injected quickly to the reaction flask. After 2 min, the temperature was decreased to 0 °C by using an ice bath and addition of 50 mL of ethanol (or 25 mL EtOH + 25 mL MeOH). Then the QDs were separated with centrifugation and washed two times with ethanol. This synthesis yields ZnO NPs of a mass = 50 mg.

#### 2.2.2. Silanization of ZnO QDs

a) First step: ZnO@oleate QDs were redispersed in 10 mL of toluene and CMPETMS (0.2 mmol, V = 49.1 µL) was injected to the reaction mixture and stirred for 2 min. Next, 2 mL of TMAH solution (108.75 mg in 6 mL of ethanol) were added and the mixture stirred for 15 min in reflux. The mixture was cooled with a water bath and QDs were separated by centrifugation and washed two times with EtOH.

b) Second step: QDs were redispersed in 10 mL of toluene and 4 mL TMAH solution were injected. The reaction was conducted for 30 min in reflux. After cooling, QDs were separated with centrifugation and washed two times with EtOH.

#### 2.2.3. Synthesis of ZnO QDs coated with the P(MEO$_2$MA$_X$-OEGMA$_{100-X}$)

The growths of the P(MEO$_2$MA$_X$-OEGMA$_{100-X}$) (X/100-X = 100/0, 80/20 or 60/40) were initiated in 10 mL of a mixture of DMF/DMSO (10/90, v/v) using CuCl$_2$/TPMA (tris(2-

pyridylmethyl) amine) in the presence of hydrazine (**Scheme 2.2.1b**). In a 30 mL Schlenk reactor, 50 mg of silanized QDs were dispersed under stirring in a DMF/DMSO mixture (10/90, v/v). Next, 17.7 mmol of a mixture of $MEO_2MA$/OEGMA at different ratio (three different ratios $MEO_2MA_X$-OEGMA$_{100-X}$ (%) were used: 100/0, 80/20 and 60/40 which led to ZnO@P($MEO_2MA_X$-OEGMA$_{100-X}$) QDs and 200 µL of stock solution (in DMSO) of $CuCl_2$/TPMA (0.884 µmol $CuCl_2$, 4.3 µmol) were added. The reaction mixture was degassed by three freeze-pump-thaw cycles. The reaction was conducted at room temperature. When the media was completely homogeneous, 250 µL of a solution of hydrazine in DMSO (7.1 mg/mL) was added. The reaction was conducted during 2 h for each sample. The polymerization mixtures were poured into hot Milli-Q water to precipitate the insoluble components. The solution was then centrifuged three times using hot Milli-Q water.

### 2.2.4. Preparation of $Fe_3O_4$ NPs

$FeCl_3.6H_2O$ (6 mmol, 1.622 g) and $FeSO_4.7H_2O$ (5 mmol, 1.39 g) were dissolved in 40 mL of water. Next, 5 mL of a 28 % ammonia solution were added and the mixture heated at 90 °C. Then, 4.4 g (14.9 mmol) of sodium citrate were added to the flask and the mixture vigorously stirred for 30 min. $Fe_3O_4$ NPs were recovered by magnetic separation, washed several times with EtOH and re-dispersed in water (100 mL).

### 2.2.5. Silanization of $Fe_3O_4$ NPs

a) First step: 50 mg of $Fe_3O_4$ magnetic NPs were dispersed in 10 mL of toluene and CMPETMS was injected to the reaction mixture (0.2 mmol, V = 49.1 µL) and stirred for 2 min. Next, 2 mL of a TMAH solution (108.75 mg in 6 mL EtOH) were added and the mixture stirred for 15 min in reflux. The mixture was cooled with a water bath and the NPs were recovered by magnetic separation and washed several times with EtOH.

b) Second step: In the second step of silanization, QDs were redispersed in 10 mL of toluene and 4 mL TMAH solution were then injected. The reaction was conducted for 30 min in reflux. NPs were recovered by magnetic separation, washed several times with EtOH.

### 2.2.6. Synthesis of $Fe_3O_4$ coated with the P($MEO_2MA_X$-OEGMA$_{100-X}$)

The growth of the P($MEO_2MA_X$-OEGMA$_{100-X}$) (X/100-X = 100/0, 80/20 or 60/40) (**Scheme 2.2.1b**) was conducted following the same procedure described for the ZnO@copolymer derivatives.
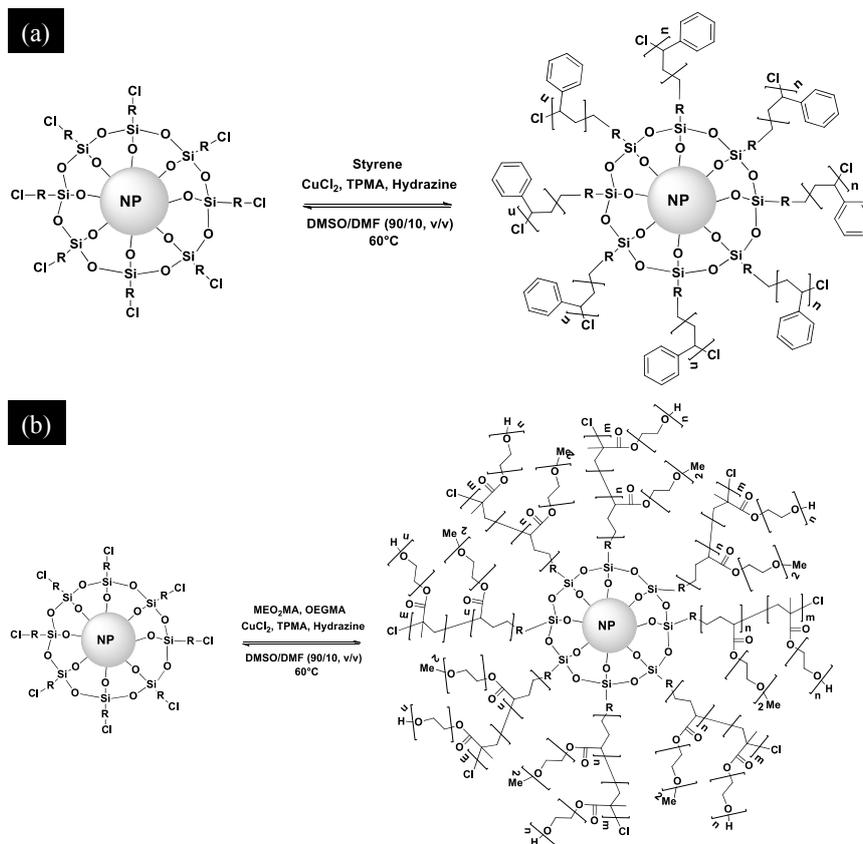
**Scheme 2.2.1 Schematic representation of the surface-initiated ARGET-ATRP polymerization of a) styrene from SiO$_2$@Ph-Cl NPs and b) X MEO$_2$MA with 100-X OEGMA from ZnO@Ph-Cl or Fe$_3$O$_4$@Ph-Cl NPs, where X and 100-X are the molar ratio of MEO$_2$MA and OEGMA, respectively.**

## 2.2.7. SiO$_2$ NPs

Commercial silica NPs were modified by using the same synthetic procedure than for ZnO NPs. The resulting NPs will be called SiO$_2$@Ph-Cl. Afterwards, growth of PS was conducted in a mixture of DMSO/DMF (90/10, v/v) in the presence of 17.7 mmol of styrene and hydrazine and a catalytic amount of CuCl$_2$/TPMA as described in a previous work [15]. The resulting NPs will be called SiO$_2$@PS.

## 2.3. Characterization Methods

Dynamic light scattering (DLS) was performed at room temperature using a Malvern zetasizer HsA instrument with a He-Ne laser ($4\ 10^{-3}$ W) at a wavelength of 633 nm. The NPs aqueous solutions were filtered through Millipore membranes (0.2 μm pore size). The data was analyzed by the CONTIN method to obtain the hydrodynamic diameters ($H_D$) and size distributions in each aqueous dispersion of NPs.

Transmission Electron Microscopy (TEM) Characterization: For each sample, one drop of a dispersed solution (for each step of the synthesis) was deposited on holey carbon grids and imaged by TEM. The Microscope used is an ARM 200F.

For the TGA measurements, a SETSYS Supersonic thermo-balance (SETARAM) was used. The furnace is made up of a graphite element operating from room temperature up to 1600 °C. The apparatus is controlled by software appointed Calisto. Dry samples of 30 mg were put in an alumina crucible with a volume of 30 μL. The samples were heated from room temperature to 600 °C at a heating rate of 5 °C/min under argon atmosphere.

The crystallographic structure of VN thin films was identified by X-Ray Diffraction (XRD) using Philips PW3710 diffractometer with CuKα radiation.

# 3. RESULTS AND DISCUSSION

## 3.1. Growth of PS from SiO$_2$@Ph-Cl

Different polymerization times were evaluated (2, 5 and 8 h) for the growth of PS at the surface of SiO$_2$ NPs and the evolution of H$_D$ is presented in **Figure 2.3.1**.
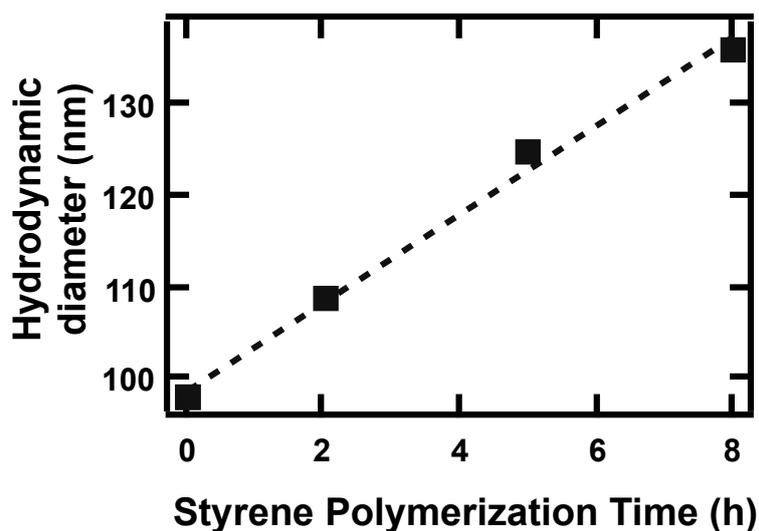


**Figure 2.3.1 Evolution of the H$_D$ of SiO$_2$@PS NPs with the time of polymerization. The H$_D$ was measured in DMSO at room temperature by DLS.**

Commercial SiO$_2$ NPs exhibit a diameter of ca. $100 \pm 8$ nm (**Figure 2.3.2a**) as determined by TEM. As can be seen in **Figure 2.3.1**, the polymer shell layer thickness increased with the polymerization time and a linear kinetic profile is observed. This indicates the living character of the ARGET-ATRP process when it is conducted on nanomaterials exhibiting large diameters (ca. 100 nm).
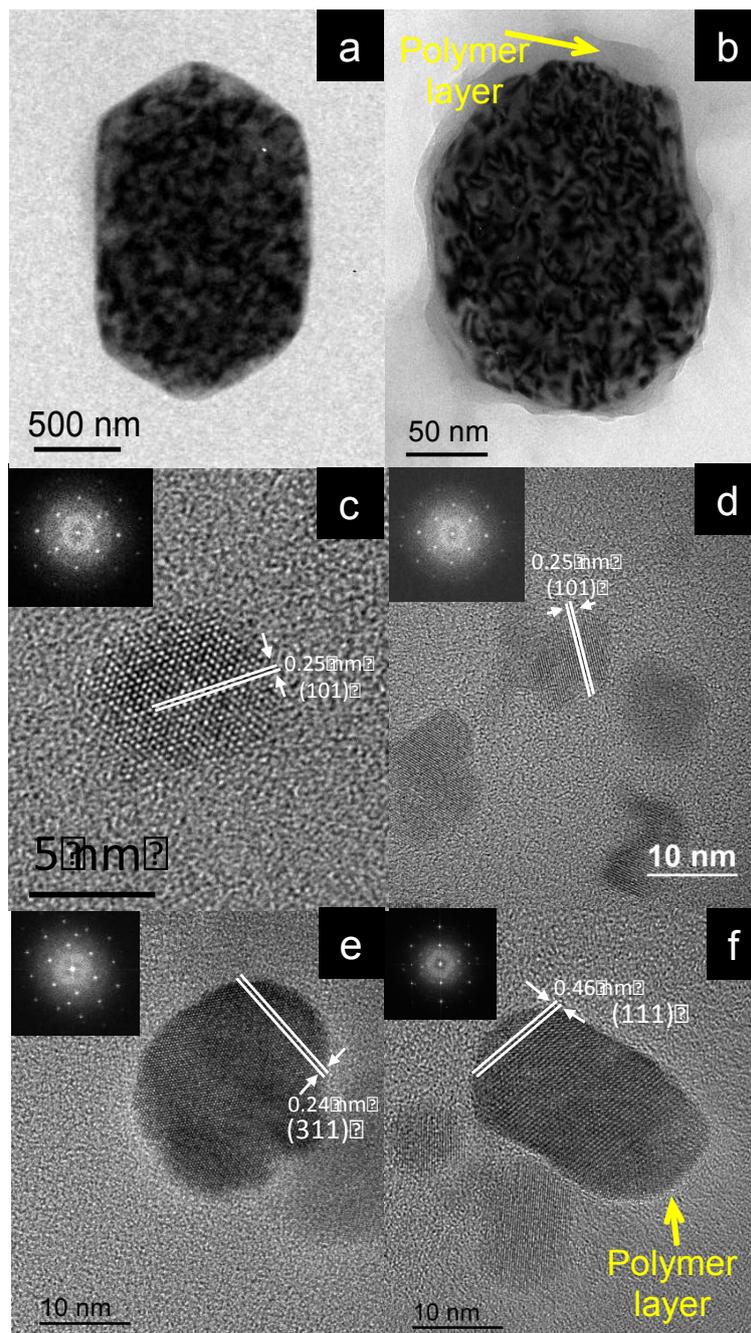
**Figure 2.3.2 HR-TEM micrographs of a) SiO$_2$@Ph-Cl NPs, b) SiO$_2$@PS after 8 h of polymerization, c) ZnO@Ph-Cl NPs, d) ZnO@P(MEO$_2$MA$_{80}$-OEGMA$_{40}$) NPs, e) Fe$_3$O$_4$@Ph-Cl NPs, and f) Fe$_3$O$_4$@P(MEO$_2$MA$_{80}$-OEGMA$_{40}$) NPs (the insets of figures 2c-f correspond to the FFT).**

At the same time, the linear growth of the polymer thickness points out that the polymer chains are in brush regime, *i.e.* they are in a stretched configuration perpendicularly to the surface. Consequently, the chain end is easily available to react with new monomers. The thin amorphous and homogeneous polymer layer is well evidenced in the TEM image (**Figure 2.3.2b**). The polymer shell surrounds the SiO$_2$ NPs and its lower density allows its differentiation from the silica NP which is darker as it absorbs a higher amount of electrons.

These results demonstrate that the ARGET-ATRP process can easily lead to a homogeneous covalent grafting of PS at the surface of the $SiO_2$ NPs [24].

## 3.2. Growth of P(MEO$_2$MA$_X$-OEGMA$_{100-X}$) from ZnO and Fe$_3$O$_4$@Ph-Cl NPs

For a biological concern, the ARGET-ATRP process has been extended to modify fluorescent ZnO QDs and magnetic $Fe_3O_4$ NPs. Both of those NPs are of low cytotoxicity [5, 23], and are referred as very promising tools for diagnostic in medical field. $MOE_2MA$ and OEGMA random responsive copolymers were grown from each NP surfaces following the method previously described. By varying the amount of OEGMA, the collapse temperature of the copolymer (LCST) can be tuned from 23 to 45 °C [25-27]. Moreover, the oligo ethylene groups ensure the complete biocompatibility of the derived core/shell nanomaterial [27]. So, combining the physical properties of the core (ZnO or $Fe_3O_4$) with the responsive properties of the polymers allows the development of new functional core/shell nano-materials with high potential for bio-imaging and/or as drug release platform. Three $MEO_2MA_X$-OEGMA$_{100-X}$ molar ratios were studied (100/0, 80/20 and 60/40) to prepare ZnO@P(MEO$_2$MA$_X$-OEGMA$_{100-X}$) and Fe$_3$O$_4$@P(MEO$_2$MA$_X$-OEGMA$_{100-X}$) NPs, where X and 100-X represent the molar fraction of $MEO_2MA$ and OEGMA, respectively. **Table 2.3.1** describes the evolution of $H_D$ of the core/shell NPs, measured by DLS at 20 °C, *i.e.* below the collapse temperature.

**Table 2.3.1 $H_D$ of the core/shell NPs measured in water at 20 °C.**

| NPs | H$_D$ at 20 °C (nm) | TEM Diameter (nm) |
|---|---|---|
| ZnO@P(MEO$_2$MA$_{100}$-OEGMA$_0$) | 15.4 (± 0.6) | 6 (± 0.5) |
| ZnO@P(MEO$_2$MA$_{80}$-OEGMA$_{20}$) | 10 (± 0.6) | 6 (± 0.5) |
| ZnO@P(MEO$_2$MA$_{60}$-OEGMA$_{40}$) | 14 (± 0.7) | 6 (± 0.5) |
| Fe$_3$O$_4$@P(MEO$_2$MA$_{100}$-OEGMA$_0$) | 20 (± 0.7) | 12 (± 0.5) |
| Fe$_3$O$_4$@P(MEO$_2$MA$_{80}$-OEGMA$_{20}$) | 16 (± 0.7) | 13 (± 0.5) |
| Fe$_3$O$_4$@P(MEO$_2$MA$_{60}$-OEGMA$_{40}$) | 22 (± 0.7 ) | 12 (± 0.5) |

The $H_D$ in water were found to depend on the amount of OEGMA. A swelled $P(MEO_2MA)$ and $P(MEO_2MA_{60}-OEGMA_{40})$ shell of about 5 nm is measured, but for a small amount of OEGMA (20 %), the swelled copolymer layer is only of about 2.5 nm. Once the copolymer is grafted, the polymer shell thickness increased with the later as it holds highly hydrated ethylene oxide groups.

## 3.3. Physical characterization of the core/shell NPs

**Figures 2.3.2-5** show the HR-TEM micrographs and the XRD patterns of the synthesized NPs.
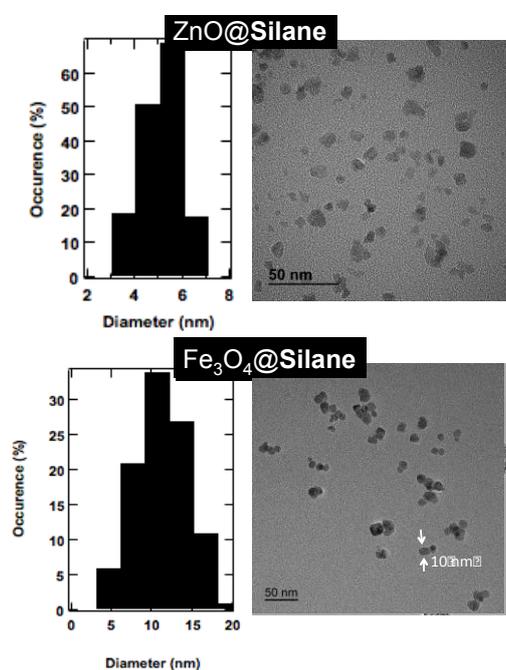


**Figure 2.3.3 Size distributions (left) and TEM micrographs (right) of the silanized ZnO and Fe₃O₄ NPs.**

At each step of the functionalization process, ZnO and $Fe_3O_4$ NPs were of spherical shape with an average diameter of 6 ± 1 nm and 10 ± 1.5 nm, respectively (**Figures 2.3.2-3**). For ZnO, the (100), (002), (101), (102), (110), (103), (200), (112) and (201) diffraction peaks could be indexed to the standard hexagonal wurtzite structure of ZnO (JCPDS No 36-1451) (**Figure 2.3.4**). The ZnO crystalline structure was not altered by the silane capping and the polymerization process (**Figure 2.3.4**).
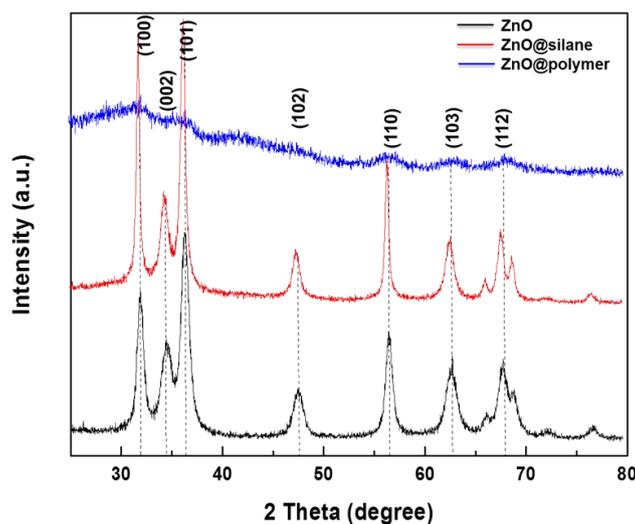
**Figure 2.3.4 XRD patterns of a) ZnO QDs, b) ZnO@Ph-Cl and c) ZnO@copolymer NPs.**
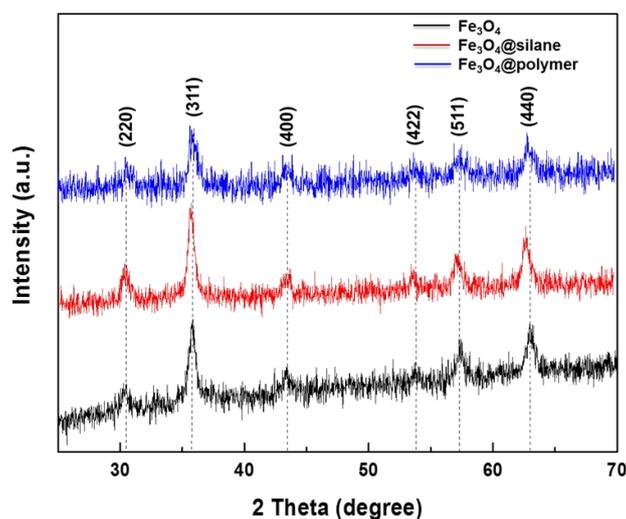


**Figure 2.3.5 XRD patterns of a) Fe₃O₄, b) Fe₃O₄@Ph-Cl and c) Fe₃O₄@copolymer NPs.**

Similar results were obtained with $Fe_3O_4$ NPs. The characteristic diffraction peaks can be attributed to the (200), (311), (400), (422), (511) and (440) planes of magnetite (JCPDS No 00-019-0629) and the crystalline structure of the NPs were not altered by the silanization and polymerization processes (**Figure 2.3.5**). HR-TEM analyses were also conducted to get more information on the NPs. The HR-TEM image of ZnO QDs shows clear lattice fringes with d-spacing of 0.25 nm, value consistent with the distance between two (101) crystal planes of hexagonal ZnO (**Figures 2.3.2c-d**). The polymer layer could not be evidenced by HR-TEM, essentially due to the low NPs diameter (about 6 nm) which prevented a high contrast difference between the polymer layer (which is essentially composed of carbon) and the carbon film of the TEM grid. For $Fe_3O_4$ NPs, the HR-TEM images and the interplanar spacing measured (0.24 nm and 0.46 nm were extracted from the FFT analyses and correspond to the

(311) and (111) planes of the magnetite structure, respectively) confirm the crystalline structure of the NPs (**Figures 2.3.2e-f**). A thin amorphous polymer layer could be seen on the HR-TEM image (**Figure 2.3.2f**), which indicates that a polymer layer surrounds $Fe_3O_4$ NPs.

## 3.4.  Amount of copolymer grafted at the surface of the NPs

TGA was used to determine the amount of the copolymer on the core/shell structures (**Figure 2.3.6**). A two-stage weight loss was observed for each NP. The first one, from 0 to 160 °C, can be assigned to the evaporation of the adsorbed water molecules. The second one, from 225 °C to 350 °C, is attributed to the decomposition of the copolymer shell.
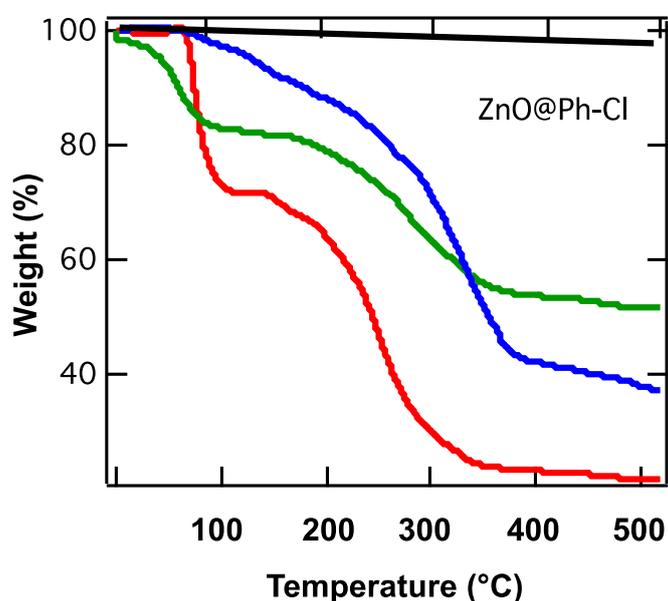


**Figure 2.3.6 Weight loss curves versus temperature for ZnO@Ph-Cl (black), ZnO@P(MEO₂MA) (red),**
**ZnO@P(MEO₂MA₈₀-OEGMA₂₀) (blue) and ZnO@P(MEO₂MA₆₀-OEGMA₄₀) NPs (green).**

Based on TGA results, the amount of adsorbed water molecules and of the copolymer can be estimated for each composition. The mass concentration of the copolymer is very similar for both ZnO and $Fe_3O_4$ cores and only the results obtained with ZnO will be discussed here. The mass concentration of the copolymer varies from 76 % for the $ZnO@PMEO_2MA$ to 36 % for the $ZnO@P(MEO_2MA_{60}\text{-}OEGMA_{40})$. This confirms that the sterically hindered OEGMA monomer does not incorporate as easily as $MEO_2MA$ during the co-polymer chain growth. On the other hand, the higher content of ethylene oxide groups implies a higher amount of adsorbed water molecules. This is confirmed by the increased amount of water molecules from 8 % for $ZnO@PMEO_2MA$ NPs to 18 % for the $ZnO@P(MEO_2MA_{60}\text{-}OEGMA_{40})$ NPs.

We can thus assume that those nanomaterials can be employed as drug nano-carriers thanks to the copolymer ability to be covered by water molecules.

### 3.5. Temperature responsive properties of the core/shell NPs

The temperature dependence of the NPs dispersions was monitored by DLS from 20 to 50 °C (**Figure 2.3.7**). No temperature influence on the $H_D$ of the silanized NPs (ZnO@Ph-Cl and Fe$_3$O$_4$@Ph-Cl) was observed.
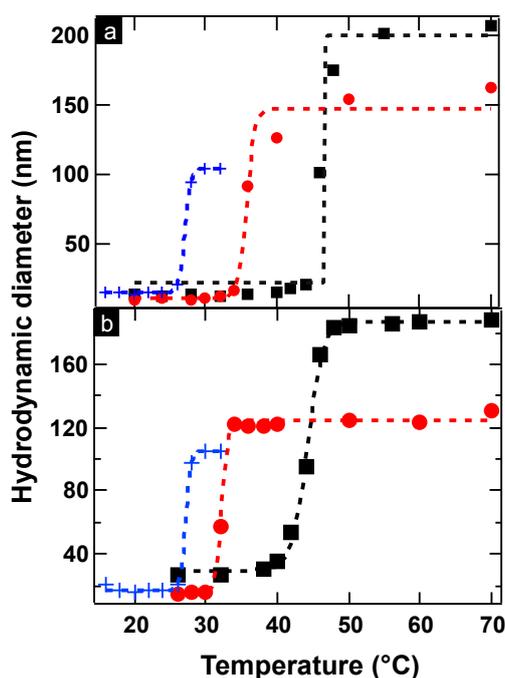


**Figure 2.3.7 Evolution of the H$_D$ of a) ZnO@PMEO$_2$MA (blue), ZnO@P(MEO$_2$MA$_{80}$-OEGMA$_{20}$) (red), ZnO@P(MEO$_2$MA$_{60}$-OEGMA$_{40}$) (black) and b) Fe$_3$O$_4$@P(MEO$_2$MA) (blue), ZnO@P(MEO$_2$MA$_{80}$-OEGMA$_{20}$) (red), ZnO@P(MEO$_2$MA$_{60}$-OEGMA$_{40}$) (black). The lines are drawn to guide the eyes.**

By heating the NPs dispersions (at a temperature rate of 1 °C/min), the evolution of the NPs diameter and their coalescence above the LCST was monitored. Indeed, the increase of the diameter is directly related to the NPs aggregation above the LCST and is induced by the gradual collapse of the polymer chains at the surface of the NPs. The shift of the LCST towards higher temperatures with the increase of incorporated OEGMA amount (26 °C for the ZnO@PMEO$_2$MA to 44 °C for ZnO@P(MEO$_2$MA$_{60}$-OEGMA$_{40}$) confirms that the thermal properties of the core/shell NPs are completely driven by the macromolecular properties of the copolymers chains properties. Finally, in order to ensure that the processes are completely reversible, five successive cycles of heating (T > LCST) and cooling (T <

LCST) were performed. All the measurements for each sample are presented in **Figure 2.3.8**. A complete reversible behavior in water upon heating and cooling was demonstrated for all the samples.
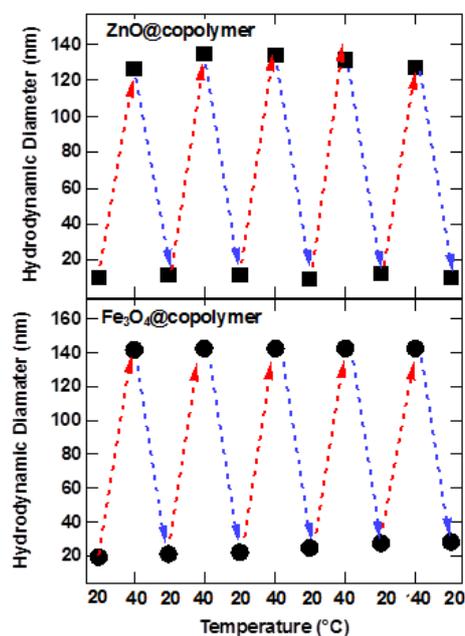


**Figure 2.3.8 Reversibility of ZnO@(MEO$_2$MA$_{80}$-OEGMA$_{20}$) (top) and Fe$_3$O$_4$@P(MEO$_2$MA$_{80}$-OEGMA$_{20}$) (bottom) core/shell NPs H$_D$ with temperature.**

This behavior is in perfect agreement with the high hydration capacity of the ethylene glycol groups below the collapse temperature and the chains configuration changes above the latter.

## 3.6. Fluorescence properties of the ZnO@copolymer samples

Upon excitation at 335 nm, the photoluminescence (PL) spectrum of ZnO@Ph-Cl shows a broad blue-green-to yellow emission (**Figure 2.3.9**) [28].
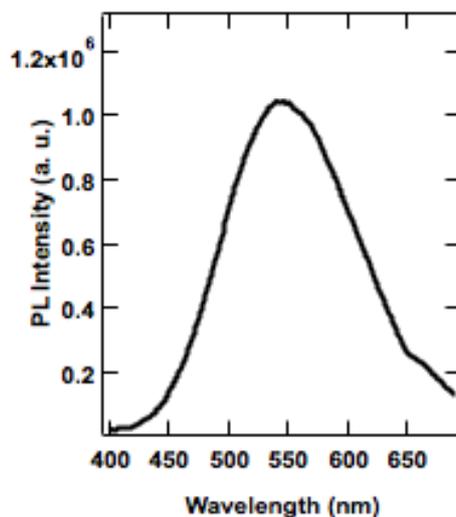
This visible emission is generally considered as originating from intrinsic defects of ZnO QDs such as oxygen vacancies, zinc interstitials, zinc vacancies, antisite oxygen, donor-acceptors pairs, and surface defects. Recent findings also demonstrated that hydroxyl groups present at the periphery of ZnO QDs act as surface traps for photo-generated charge carriers, thus enhancing visible emission [29].

A decrease of the PL quantum yield from 21 to 11% was observed upon introduction of P(MEO$_2$MA$_{80}$-OEGMA$_{20}$) at the surface of ZnO@Ph-Cl QDs and transfer of the dots in water. Concerning the responsive NPs, we have recently shown that the optical properties of the core/shell NPs can be tuned by the temperature, *i.e.* the aggregation of the NPs leads to a drastic decrease of the ZnO PL intensity [15]. The same behavior was observed for ZnO@P(MEO$_2$MA$_{80}$-OEGMA$_{20}$) QDs (**Figure 2.3.10**). Above the LCST, the P(MEO$_2$MA$_{80}$-OEGMA$_{20}$) chains collapse, the surface of the NPs becomes hydrophobic, the NPs aggregate and a marked decrease of the PL intensity is observed. The PL quantum yield decreased from 11 % to 4.5 % in water when the temperature was increased from 30 to 40 °C. In the course of this temperature increase, the PL peak maximum (ca. 530 nm) and the full-width at half-maximum of the PL peak (ca. 150 nm) remained unchanged, indicating that the surface and the defects involved in the visible emission of ZnO dots were not affected by NPs aggregation.
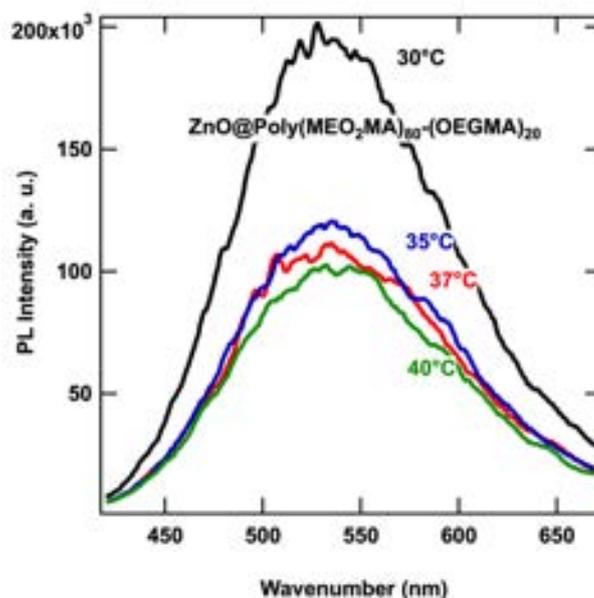
**Figure 2.3.10 PL intensity of the ZnO@P(MEO$_2$MA$_{80}$-OEGMA$_{20}$) NPs versus temperature.**

## 3.7. Magnetic properties of the Fe$_3$O$_4$@copolymers

The magnetic properties of the core/shell Fe$_3$O$_4$@copolymers NPs before and after the collapse temperature were studied using a Vibrating Sample Magnetometer (VSM). The VSM allows the determination of the magnetic moments (field versus magnetization H-M) with a resolution of 10$^{-6}$ emu under a rotating magnetic field (0 to 2.5 Tesla) and for temperatures varying from 300 K to 600 K. H-M measurements were used to ascertain the induced magnetization from the NPs under an applied field at different temperatures. The temperature was varied from 30 to 42 °C. The magnetization curves of all Fe$_3$O$_4$ core NPs showed no hysteresis and were fully reversible for all temperatures (**Figure 2.3.11**).
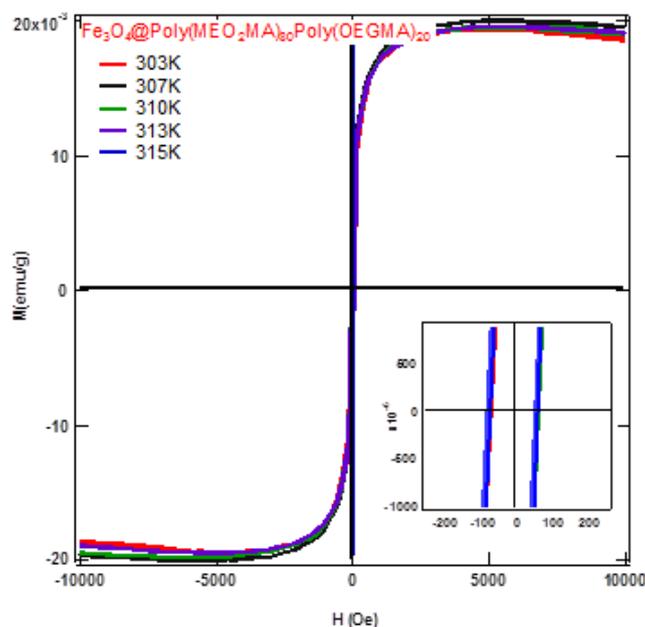
**Figure 2.3.11 Magnetization curves of the Fe$_3$O$_4$@P(MEO$_2$MA$_{80}$-OEGMA$_{20}$) MNPs at different temperatures.**

Moreover, above the LCST, the hysteresis loop of the modified NPs still passes through zero. This indicates that the aggregation of NPs does not influence their magnetic properties contrary to the changes in PL intensity observed for ZnO QDs and that the superparamagnetic properties of the Fe$_3$O$_4$ NPs are maintained below and above the LCST. Concerning the shell composition, its influence is clearly demonstrated in **Figure 2.3.12**.
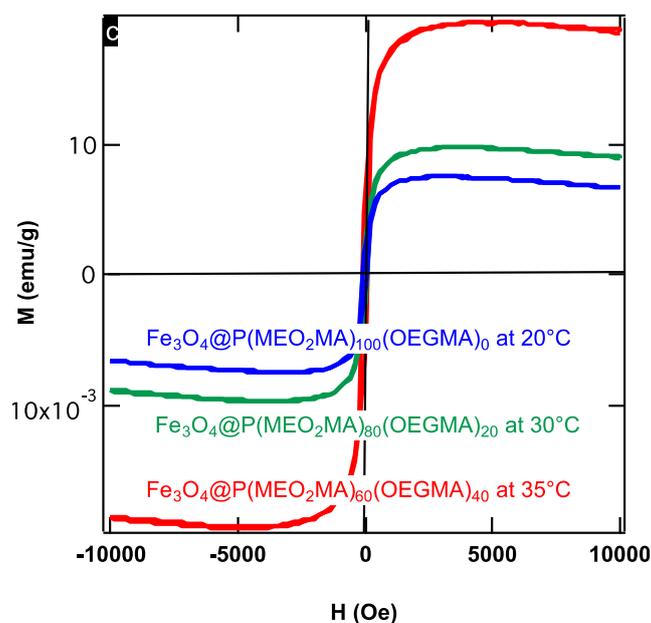


**Figure 2.3.12 Evolution of the magnetization curves of core/shell MNPs with the amount of OEGMA grafted at their periphery (0 blue, 20 green, and 40 red).**

115

The $M_s$ is of ca. 0.006 emu/g for the $Fe_3O_4$@P($MEO_2MA$) NPs while it became equal to 0.009 and 0.019 emu/g for the $Fe_3O_4$@P($MEO_2MA_{80}$-$OEGMA_{20}$) and $Fe_3O_4$@P($MEO_2MA_{60}$-$OEGMA_{40}$) NPs, respectively. According to previous reports, the $M_s$ can only depend on the particle size [30, 31]. However, as shown by TEM experiments, the NPs display a 10 nm diameter with a very small dispersion (**Figures 2.3.2(e-f)-3**). Our results are in accordance with previous reports and confirm that the introduction of non-magnetic mass can reduce the $M_s$ [2, 31]. TGA results show that $Fe_3O_4$@$PMEO_2MA$ NPs contain the maximum amount of polymer whereas the $Fe_3O_4$@P($MEO_2MA_{60}$-$OEGMA_{40}$) contains the minimum amount, and that the lowest polymer content (36 %) leads to the highest $M_s$ value. These results confirm that the superparamagnetic properties of the core/shell NPs are only driven by the core structure and were absolutely not altered by the shell structure (chain conformation changes with temperature), and the distance between the NPs (aggregation that takes place after the LCST). The influence of the amount of non-magnetic organic shell is clearly seen.

# 4. CONCLUSION

Core/shell NPs could be easily synthesized by the simple growth of a polymer or a copolymer from different metal oxides NPs. The ARGET-ATRP process used in this work has been found to allow the growth of macromolecules, either responsive or not, from silanized $SiO_2$ NPs, ZnO QDs and $Fe_3O_4$ NPs. We have demonstrated that ZnO QDs display temperature-dependent optical properties whereas no influence of the shell structure was detected on the magnetic properties of the $Fe_3O_4$ NPs. This first work paves the way for the elaboration by an efficient process of completely biocompatible nanomaterials that exhibit potential as drug release platform.

# REFERENCES

1.  Ghosh Chaudhuri, R., and Paria, S., *Core/shell nanoparticles: classes, properties, synthesis mechanisms, characterization, and applications.* Chemical reviews, 2011. **112**(4): p. 2373-2433.

2.  Oh, J.K., and Park, J. M., *Iron oxide-based superparamagnetic polymeric nanomaterials: design, preparation, and biomedical application.* Progress in Polymer Science, 2011. **36**(1): p. 168-189.

3.  Michalet, X., Pinaud, F.F., Bentolila, L.A., Tsay, J.M., Doose, S.J.J.L., Li, J.J., Sundaresan, G., Wu, A.M., Gambhir, S.S. and Weiss, S., *Quantum dots for live cells, in vivo imaging, and diagnostics.* Science, 2005. **307**(5709): p. 538-544.

4.  Le Droumaguet, B., Nicolas, J., Brambilla, D., Mura, S., Maksimenko, A., De Kimpe, L., Salvati, E., Zona, C., Airoldi, C., Canovi, M. and Gobbi, M., *Versatile and efficient targeting using a single nanoparticulate platform: application to cancer and Alzheimer's disease.* ACS nano, 2012. **6**(7): p. 5866-5879.

5.  Zheng, Y., Li, R., & Wang, Y., *In vitro and in vivo biocompatibility studies of ZnO nanoparticles.* International Journal of Modern Physics B, 2009. **23**(06n07): p. 1566-1571.

6.  Ankamwar, B., Lai, T.C., Huang, J.H., Liu, R.S., Hsiao, M., Chen, C.H. and Hwu, Y.K., *Biocompatibility of $Fe_3O_4$ nanoparticles evaluated by in vitro cytotoxicity assays using normal, glia and breast cancer cells.* Nanotechnology, 2010. **21**(7): p. 075102.

7.  Cayre, O.J., Chagneux, N. and Biggs, S., *Stimulus responsive core-shell nanoparticles: synthesis and applications of polymer based aqueous systems.* Soft matter, 2011. **7**(6): p. 2211-2234.

8.  Xie, J., Huang, J., Li, X., Sun, S. and Chen, X., *Iron oxide nanoparticle platform for biomedical applications.* Current medicinal chemistry, 2009. **16**(10): p. 1278-1294.

9.  Hervault, A., Dunn, A.E., Lim, M., Boyer, C., Mott, D., Maenosono, S. and Thanh, N.T., *Doxorubicin loaded dual pH-and thermo-responsive magnetic nanocarrier for combined magnetic hyperthermia and targeted controlled drug delivery applications.* Nanoscale, 2016. **8**: p. 12152-12161.

10. Parak, W.J., Pellegrino, T. and Plank, C., *Labelling of cells with quantum dots.* Nanotechnology, 2005. **16**(2): p. R9.

11. Frey, N.A., Peng, S., Cheng, K. and Sun, S., *Magnetic nanoparticles: synthesis, functionalization, and applications in bioimaging and magnetic energy storage.* Chemical Society Reviews, 2009. **38**(9): p. 2532-2542.

12. Teja, A.S., and Koh, P.Y. , *Synthesis, properties, and applications of magnetic iron oxide nanoparticles.* Progress in Crystal Growth and Characterization of Materials, 2009. **55**(1): p. 22-45.

13. Hui, C.M., Pietrasik, J., Schmitt, M., Mahoney, C., Choi, J., Bockstaller, M.R. and Matyjaszewski, K., *Surface-initiated polymerization as an enabling tool for multifunctional (nano-) engineered hybrid materials.* Chemistry of Materials, 2013. **26**(1): p. 745-762.

14. Azzaroni, O., *Polymer brushes here, there, and everywhere: Recent advances in their practical applications and emerging opportunities in multiple research fields.* Journal of Polymer Science Part A: Polymer Chemistry, 2012. **50**(16): p. 3225-3258.

15. Boyer, C., Whittaker, M.R., Bulmus, V., Liu, J. and Davis, T.P., *The design and utility of polymer-stabilized iron-oxide nanoparticles for nanomedicine applications.* NPG Asia Materials, 2010. **2**(1): p. 23-30.

16.    Kango, S., Kalia, S., Celli, A., Njuguna, J., Habibi, Y. and Kumar, R., *Surface modification of inorganic nanoparticles for development of organic–inorganic nanocomposites—A review*. Progress in Polymer Science, 2013. **38**(8): p. 1232-1261.

17.    Matyjaszewski, K., *Atom transfer radical polymerization (ATRP): current status and future perspectives*. Macromolecules, 2012. **45**(10): p. 4015-4039.

18.    Barbey, R., Lavanant, L., Paripovic, D., Sch wer, N., Sugnaux, C., Tugulu, S. and Klok, H.A., *Polymer brushes via surface-initiated controlled radical polymerization: synthesis, characterization, properties, and applications*. Chemical reviews, 2009. **109**(11): p. 5437-5527.

19.    Alem, H., Schejn, A., Roques-Carmes, T., Ghanbaja, J. and Schneider, R., *Thermo-responsive and aqueous dispersible ZnO/PNIPAM core/shell nanoparticles*. Nanotechnology, 2015. **26**(33): p. 335605.

20.    Cheesman, B.T., Willott, J.D., Webber, G.B., Edmondson, S. and Wanless, E.J., *pH-responsive brush-modified silica hybrids synthesized by surface-initiated ARGET ATRP*. ACS Macro Letters, 2012. **1**(10): p. 1161-1165.

21.    Olivier, A., Meyer, F., Raquez, J.M., Damman, P. and Dubois, P., *Surface-initiated controlled polymerization as a convenient method for designing functional polymer brushes: From self-assembled monolayers to patterned surfaces*. Progress in Polymer Science, 2012. **37**(1): p. 157-181.

22.    Saha, N., Dubey, A.K. and Basu, B., *Cellular proliferation, cellular viability, and biocompatibility of HA-ZnO composites*. Journal of Biomedical Materials Research Part B: Applied Biomaterials, 2012. **100**(1): p. 256-264.

23.    Du, S., Zhou, G., Wang, X., Li, T., Xu, Y. and Zhang, L., *Surface modification of silica nanoparticles by grafting poly (methyl methacrylate) using atom transfer radical polymerisation with activators regenerated by electron transfer*. IET Micro & Nano Letters, 2011. **6**(3): p. 154-156.

24.    Iacono, M., and Heise, A., *Stable Poly (methacrylic acid) Brush Decorated Silica Nano-Particles by ARGET ATRP for Bioconjugation*. Polymers, 2015. **7**(8): p. 1427-1443.

25.    Liu, J., He, W., Zhang, L., Zhang, Z., Zhu, J., Yuan, L., Chen, H., Cheng, Z. and Zhu, X., *Bifunctional nanoparticles with fluorescence and magnetism via surface-initiated AGET ATRP mediated by an iron catalyst*. Langmuir, 2011. **27**(20): p. 12684-12692.

26.    Alem, H., Duwez, A.S., Lussis, P., Lipnik, P., Jonas, A.M. and Demoustier-Champagne, S., *Microstructure and thermo-responsive behavior of poly (N-isopropylacrylamide) brushes grafted in nanopores of track-etched membranes*. Journal of Membrane Science, 2008. **308**(1): p. 75-86.

27.    Granitzer, P., Rumpf, K., Tian, Y., Coffer, J., Akkaraju, G., Poelt, P. and Reissner, M., *Assessment of Cytocompatibility and Magnetic Properties of Nanostructured Silicon Loaded with Superparamagnetic Iron Oxide Nanoparticles*. ECS Transactions, 2015. **64**(47): p. 1-7.

28.    Lutz, J.F., Weichenhan, K., Akdemir, Ö. and Hoth, A., *About the phase transitions in aqueous solutions of thermoresponsive copolymers and hydrogels based on 2-(2-methoxyethoxy) ethyl methacrylate and oligo (ethylene glycol) methacrylate*. Macromolecules, 2007. **40**(7): p. 2503-2508.

29.    Lutz, J.F., Hoth, A. and Schade, K., *Design of oligo (ethylene glycol)-based thermoresponsive polymers: an optimization study*. Designed Monomers and Polymers, 2009. **12**(4): p. 343-353.

30.    Chanana, M., Jahn, S., Georgieva, R., Lutz, J.F., B umler, H. and Wang, D., *Fabrication of colloidal stable, thermosensitive, and biocompatible magnetite*

*nanoparticles and study of their reversible agglomeration in aqueous milieu.* Chemistry of Materials, 2009. **21**(9): p. 1906-1914.

31. Lutz, J.F., *Polymerization of oligo (ethylene glycol)(meth) acrylates: toward new generations of smart biocompatible materials.* Journal of Polymer Science Part A: Polymer Chemistry, 2008. **46**(11): p. 3459-3470.

# Chapter 3: Synthesis, characterization and cytotoxicity of ZnO@P(MEO$_2$MA$_X$-OEGMA$_{100-X}$) NPs

# ABSTRACT

The grafting of responsive polymers at the surface of inorganic nanoparticles (NPs) resulting in core/shell NPs has been widely considered with a view towards new opportunities for constructing effective drug delivery systems. In this context, ZnO quantum dots (QDs) have gained lot of attention due to their low cost and relative nontoxicity. In addition, their high luminescence enables them to be easily tracked in the blood stream after injection. Their combination with responsive polymers is very promising as the polymer layer could enhance their stability in physiological media which is necessary for their prolonged circulation once released in the body. For all these reasons, a biocompatible thermo-responsive copolymer of 2-(2-methoxyethoxy) ethyl methacrylate ($MEO_2MA$) and oligo (ethylene glycol) methacrylate (OEGMA) was grown from the surface of ZnO QDs by SI-ARGET ATRP to design a stable core/shell system that can be used as drug delivery platform in the frame of cancer therapy application. The lower critical solution temperature (LCST) of the copolymer shell could be tuned by playing with the monomer ratio. Different LCST values were obtained in water and in physiological medium. The covalent grafting of the initiator and the copolymer were confirmed by FT-IR. The morphology and the structure of the core/shell NPs were observed by HR-TEM. The amount of the copolymer shell was measured by TGA. Absorbance and fluorescence measurements revealed that the different steps of the functionalization process did not affect the ZnO optical properties. DLS measurements were performed to monitor the behavior of the ZnO/copolymer core/shell NPs in water and physiological media. Finally, the cytotoxicity of the core/shell NPs was tested for HT29 cells. The results have been shown that the core/shell NPs toxicity was concentration dependent and that the cytotoxicity of DOX loaded in the NPs was higher compared to free DOX.

# 1. INTRODUCTION

Inorganic/organic core/shell NPs based on ZnO QDs are very popular in the biomedical field because of their unique feature which allow different bio-applications [1-5] essentially based on their optical properties. Indeed, their fascinating fluorescence properties and biocompatibility (depending on their concentration) make them an ideal candidate to be used as fluorescent probe [6]. Indeed ZnO QDs were found to be a good alternative to the use of cadmium-based semiconductor QDs in terms of toxicity and cost, therefore they are believed to perform better as biological labels [7]. Nanosized ZnO QDs have been found to exhibit unusual chemical and optical properties due to quantum confinement effects [8]. However these QDs suffer from low stability in aqueous media because water molecules are able to exchange the organic protecting groups on the ZnO surface causing their aggregation and therefore quenching their luminescence immediately [9]. This behavior is considered as a weakness point of ZnO QDs because water stability appears necessary in biomedical applications [2]. To overcome this issue, a proper surface coating of the ZnO QDs is introduced. Different strategies have been employed for this purpose, among them are the grafting of polymer layer [10]. A proper polymer coating can enhance the stability of ZnO QDs, by preventing their aggregation and by rendering them water dispersible. Also, it helped to prevent the dissociation into $Zn^{2+}$ ions which could be highly toxic to the cells [11]. Xiong *et al.* [12] prepared ZnO QDs with a copolymer shell of an internal hydrophobic polymethacrylate layer and an external hydrophilic poly(ethylene glycol) methyl ether groups with the aim to isolate the ZnO core from water on one hand and to obtain NPs which are miscible in water on the other hand. The final core/shell NPs exhibited a very stable photoluminescence in water and were almost nontoxic when their concentrations were below 0.2 mg/mL. Another group [1] used pH responsive polyacrylamide as a protecting shell for the ZnO QDs. These NPs displayed stable luminescence properties in aqueous solutions and the results showed no visible cytotoxic effect on the cells when tested up to a concentration of 12.5 µg/mL. This kind of polymer is called stimuli-responsive polymers (SRPs). SRPs, known as smart materials, have great potential in the biomedical field due to their remarkable responsive behaviors in response to external stimuli, e.g. temperature, pH, light and magnetic field [13-16], particularly, in drug delivery applications. The SRPs are capable of encapsulating drugs and release them at the desired spots which could improve their therapeutic efficacy and minimize the undesired side effects of drugs [15]. The combination of SRPs with fluorescent ZnO QDs resulting in core/shell responsive NPs appeared to be very

an interesting route to build an efficient drug delivery platform as the final nanomaterial could combine the physical properties of the core and the responsive particularity of the shell. Regarding this, temperature and pH are predominantly studied systems in drug delivery as tumor cells display higher temperature and lower pH due to fast cell metabolism [17]. Polymers which respond to changes in temperature are called thermo-responsive polymers [16]. The biggest family of these polymers are characterized by a lower critical solution temperature (LCST) [18]. The observed phase transition is due to a coil-to-globule transition governed by cooperative dehydration of hydrophilic chains. Applying in drug delivery, below the LCST, the polymer chains are expanded in the solvent medium and the drug molecules are embedded in the chains. Once heated above the LCST, the polymer chains show a conformational transition from expanded to collapse state inducing the drug release in the medium. As well-known biocompatible materials, copolymers of 2-(2-methoxyethoxy) ethyl methacrylate ($MEO_2MA$) and oligo (ethylene glycol) methacrylate (OEGMA) are very attractive in drug delivery due to their LCST which can be tuned by changing the monomer ratio in the copolymer chains thus achieving a LCST close to tumor temperature [19]. It is also well established that the thermo-responsive behavior and the LCST in aqueous solution can be also affected by the presence of salts which are known to disrupt the hydration structure surrounding the polymer chains [20]. This effect is ion dependent, which can be represented by the Hofmeister series which originates from the ability of ions to precipitate proteins, for both anions and cations [21]. It is thus necessary to study the core/shell NPs behavior either in aqueous media but also in physiological media.
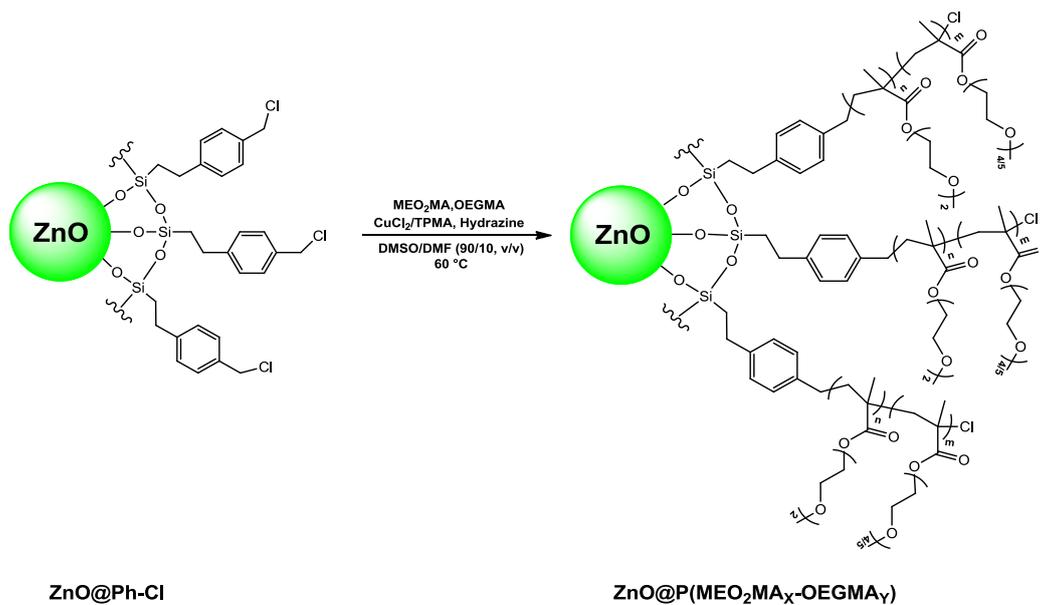
**Scheme 3.1.1 Schematic illustration of the preparation procedure of ZnO@P(MEO$_2$MA$_X$-OEGMA$_{100-X}$) NPs by SI-ARGET ATRP.**

A careful and controlled grafting of the polymers from the surface of ZnO QDs could preserve their fluorescence and could also hinder the diffusion of the dissociated Zn$^{2+}$ ions outside the NPs. In addition, it has been found to provide a sufficient matrix for the encapsulation of drug molecules. In this work, thermo-responsive fluorescent core/shell NPs were designed by grafting a copolymer shell of MEO$_2$MA$_X$ and OEGMA$_{100-X}$ (where X and 100-X represent the molar ratio of MEO$_2$MA and OEGMA, respectively) from the surface of ZnO QDs (**Scheme 3.1.1**) via surface initiated Atom Transfer Radical Polymerization with Activators Regenerated by electron Transfer (SI-ARGET-ATRP) as eco-friendly and effective polymerization technique. LCST values around the physiological temperature could be obtained by playing with the molar ratio of the monomers and by considering the presence of salts in the solvent. Various characterizations revealed the successful grafting of the copolymer and the cytotoxicity tests toward cancer cells suggested the potential of using these core/shell NPs in drug delivery. ZnO based NPs have demonstrated a high efficiency on T98G cells, moderate one on KB cells and least toxic on normal HEK cells [22]. The high drug resistance property of HT29 cells makes them important cells to kill. To the best of our knowledge, only one report describes the effect of ZnO QDs on the HT29 cancer cells [23]. In this work, Fakhroueian *et al.* have shown that ZnO NPs exhibit a low toxicity in normal cells (MDBK) but high toxicity against HT29 cancer cells. Consequently, developing a responsive platform based on a ZnO core and a responsive copolymer shell appeared to be promising since it can take advantage of all the cytotoxicity of the ZnO core and also the cancer drug

delivered by the responsive shell. Indeed, combining both effects was thought to increase both efficiencies, *i.e.* ZnO core and Doxorubicin (DOX). This effect was clearly demonstrated at the end of this chapter, where the high efficiency against HT29 cancer cells are the systems based on the core/shell nanostructures developed in this chapter, where the drug efficiency was at least 50 % higher compared to the free DOX.

# 2. MATERIALS AND METHODS

## 2.1. Materials

RPMI 1640 culture medium, purchased from Gibco® in liquid form, was used to study the behavior of NPs in physiological medium. Milli-Q water was purified using a Millipore water system in our lab.

## 2.2. Synthesis of ZnO@P(MEO$_2$MA$_X$-OEGMA$_{100-X}$) NPs

ZnO NPs with different copolymer ratios were synthesized using the same synthesis procedure detailed previously. The samples which are presented in this chapter are ZnO@P(MEO$_2$MA$_{80}$-OEGMA$_{20}$), ZnO@P(MEO$_2$MA$_{75}$-OEGMA$_{25}$), ZnO@P(MEO$_2$MA$_{65}$-OEGMA$_{35}$) and ZnO@P(MEO$_2$MA$_{60}$-OEGMA$_{40}$) NPs.

ZnO@P(MEO$_2$MA$_X$-OEGMA$_{100-X}$) samples of different molar ratios (X/100-X) were characterized with different characterization methods.

## 2.3. Cytotoxicity tests

MTT cytotoxicity test was used to analyze the cytotoxic effect of ZnO@P(MEO$_2$MA$_X$-OEGMA$_{100-X}$) NPs on human cancer cells (HT29 cells). The procedure was as follows:

### 2.3.1. Cell culture

Three days before adding the NPs, HT29 cells (human colon adenocarcinoma) were trypsinized and recovered in complete RPMI containing 9 % fetal calf serum and 5 % glutamine 200 mM. After counting, they were seeded in 96-well plate at a rate of $10^5$ cells/mL (200 µL, $2.5*10^4$ cells per well) or $2*10^4$ cells/mL (200 µL, $0.4*10^4$ cells per well) for the 24 h or 72 h incubation times, respectively with the NPs. For the control cells without the NPs and for 7 concentrations of NPs, 8 columns of 6 wells were seeded. The plates were placed in the incubator at 37 °C with 95 % humidified air containing 5 % $CO_2$.

### 2.3.2. Adding the NPs

The NPs suspensions were removed from the freezer and diluted twice with RPMI before use. In each column were added respectively: 0 - 1.6 - 3.2 - 6.3 - 12.5 - 25 - 50 and 100 µL of NPs

suspensions and the volume was completed to 200 µL with complete RPMI thus having concentrations of 0 – 0.0016 – 0.003 – 0.006 – 0.0125 – 0.025 – 0.05 – 0.1 mg/mL. The plates returned then to the incubator for 24 or 72 h.

### 2.3.3. Performing the MTT cell viability test

After incubation, the wells of the plate were washed 2 times with RPMI and 150 µL complete medium were added before 50 µL of MTT solution (2.5 mg/mL phosphate-buffered solution (PBS)). The plates were then incubated for 2 h. After removing the contents of the wells, 100 µL of pure dimethyl sulfoxide (DMSO) was added to the wells and the absorbance of each well was read at 540 nm on the MSC multi scan plate reader.

# 3. RESULTS AND DISCUSSION

## 3.1. Characterization of ZnO and ZnO@P(MEO$_2$MA$_X$-OEGMA$_{100-X}$) NPs

### 3.1.1. Chemical Characterization

Thermo-responsive copolymers of MEO$_2$MA$_X$-OEGMA$_{100-X}$ were grafted from the surface of ZnO QDs by SI-ARGET ATRP as illustrated in **Scheme 3.1.1**. The introduction of the ATRP initiator at the ZnO surface was achieved by a simple grafting of silane ligands via a ligand exchange process with the oleate capped ZnO QDs as shown in **Scheme 3.3.1**. The successful grafting of the initiator and the copolymer was confirmed by FTIR spectra in **Figure 3.3.1** with the main characteristic absorption bands summarized in **Table 3.3.1**.

The vibration bands observed at about 470 cm$^{-1}$ in all spectra are attributed to the stretching mode of Zn–O bonds. For the oleate capped ZnO QDs (**Figure 3.3.1a**), two absorption bands at around 2851 and 2923 cm$^{-1}$, arisen from symmetric and asymmetric C–H stretching, respectively, in the oleyl chains [24]. Moreover, the asymmetric and symmetric vibrations of the carboxylate ion located at 1570 and 1409 cm$^{-1}$ revealed the formation of zinc carboxylate bonds [25], while the presence of a broad peak at 3450 cm$^{-1}$confirmed the hydroxyl –OH groups on the surface of the ZnO QDs (**Figure 3.3.1b**).
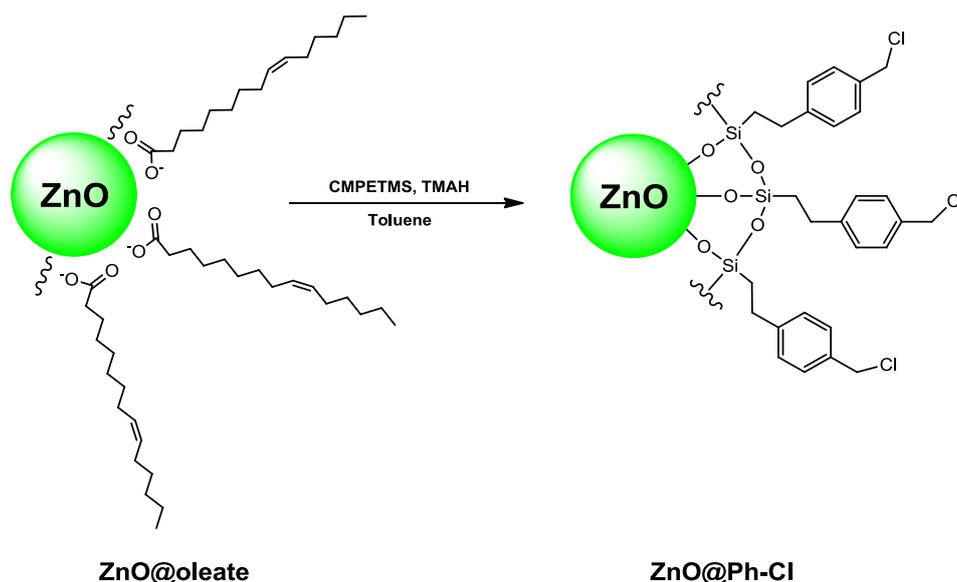


**Scheme 3.3.1 Schematic illustration of the preparation procedure of the silanized ZnO NPs.**

The bands at 950 and 1107 cm$^{-1}$ are assigned to the Zn–O–Si and Si–O–Si symmetrical stretching vibrations, respectively. The vibration bands at 699 and 761 cm$^{-1}$ are attributed to the C-Cl stretching vibrations while the bands at 1378-1550 cm$^{-1}$ are attributed to the C-C stretching in the aromatic ring of the silane.
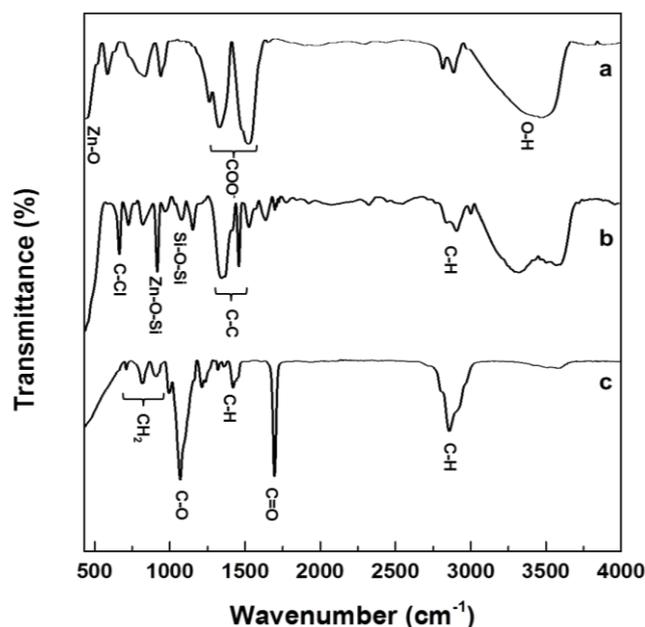


**Figure 3.3.1 FT-IR spectra of a) ZnO QDs, b) ZnO@Ph-Cl and (c) ZnO@copolymer NPs.**

In addition, the bands located at 2922 and 2857 cm$^{-1}$ are due to symmetric and asymmetric C–H stretching vibrations of its CH$_2$ groups. These peaks confirmed that the silane ligands are covalently grafted to the ZnO surface. The grafting of the P(MEO$_2$MA$_X$-OEGMA$_{100-X}$) was confirmed by the screening of the characteristic bands of the silane ligand (**Figure 3.3.1c)** by the appearance of new peaks. Indeed the sharp bands located at 1724 and 1104 cm$^{-1}$ are assigned to the C=O (ketone) and C-O (ether) stretching vibrations. The bands located at 748 and 945 cm$^{-1}$ are assigned to the CH$_2$ group of the methacrylate backbone, while the bands located at 2857 and 1451 cm$^{-1}$ correspond to the C-H stretch and bending in the PEG chain, respectively.

**Table 3.3.1 FTIR characteristic absorption bands of ZnO derivatives.**

| Functional groups | Wavenumber (cm$^{-1}$) |
|:---:|:---:|
| Zn-O | 470 |
| Zn-O-Si | 950 |

| | |
|---|---|
| Si-O-Si | 1107 |
| C=C | 1550 |
| C-H | 2857-2922 |
| C-Cl | 699-761 |
| COO⁻ | 1409-1570 |
| C-O | 1104 |
| C=O | 1724 |
| O-H | 3450 |

### 3.1.2. Microstructural Characterization of the core/shell NPs

HR-TEM and XRD experiments have been performed to investigate the morphology and the crystalline structure of the ZnO QDs and modified ZnO NPs. In **Figure 3.3.2,** an enhanced dispersion of the ZnO QDs after the introduction of the silane ligands is revealed. This confirms the importance of the surface modification to prevent the agglomeration of the ZnO QDs. The insets correspond to the ring electron diffraction patterns showing the good crystallinity of the ZnO NPs which was confirmed by further XRD analysis. The ZnO surface modification did not produce any peak shift with respect to oleate capped ZnO QDs (**Figure 3.3.3**).
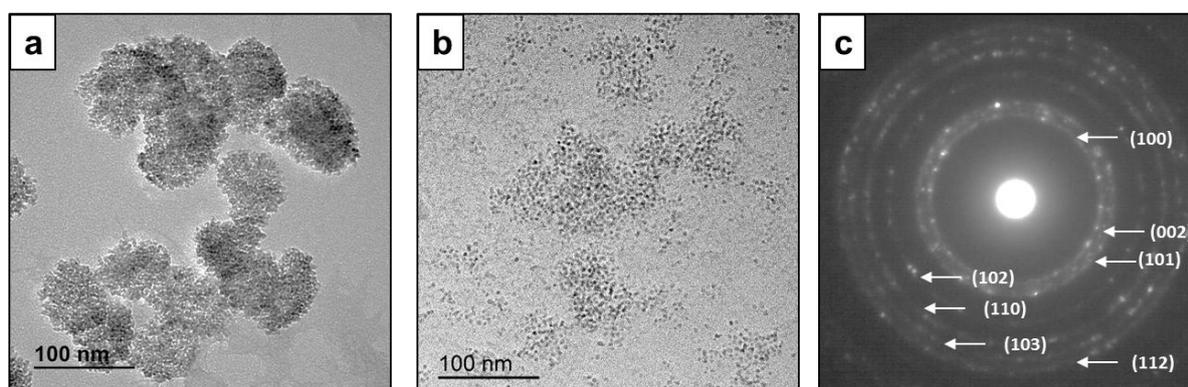


**Figure 3.3.2 Bright field HR-TEM micrographs of a) oleate capped ZnO, b) ZnO@Ph-Cl and c) the corresponding selected area electron diffraction pattern for ZnO@Ph-Cl NPs.**

In the XRD spectra of ZnO NPs (CuKα (λ=1.54056 Å)), the main diffraction peaks at 2θ = 31.77°, 34.30°, 36.29°, 47.45°, 56.53°, 62.86° and 67.84° correspond well to the typical diffractions of (100), (002), (101), (102), (110), (103) and (112) planes of ZnO NPs which is in good agreement with the wurtzite crystal structure of ZnO. The crystalline size was calculated and the estimated average size calculated using the Scherrer equation from the peaks at 2θ = 36.29° of spectra (a) and (b) was found to be 4.3 and 4.8 nm for the bare and the modified NPs, respectively.
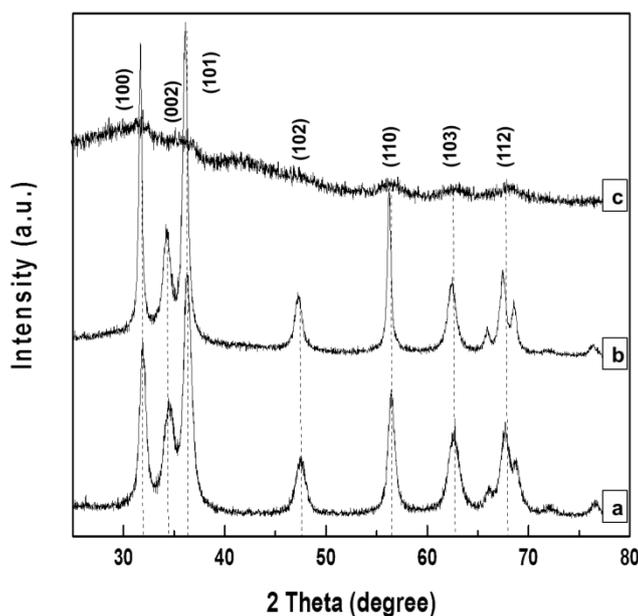


**Figure 3.3.3 XRD patterns of a) ZnO QDs, b) ZnO@Ph-Cl and (c) ZnO@copolymer NPs.**

In **Figure 3.3.4**, bright and dark field TEM images have been selected to show the homogenous dispersion of the ZnO@P(MEO$_2$MA$_{60}$-OEGMA$_{40}$) NPs. At high magnification, the NPs showed a spherical crystalline shape and an amorphous phase around the crystalline core could be observed (**Figure 3.3.4c**). This amorphous phase demonstrated the presence of a polymer layer. One of these NPs was highlighted and the interplanar spacing was found to be 0.25 nm which is in good agreement with the (101) plane of ZnO wurtzite structure.

136
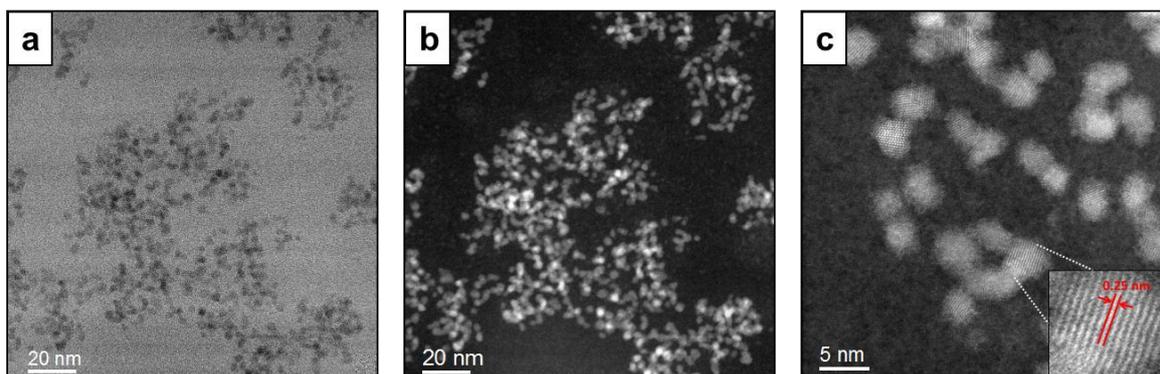
**Figure 3.3.4 a) Bright and b) dark field HR-TEM micrographs of ZnO@P(MEO$_2$MA$_{60}$-OEGMA$_{40}$) NPs with a high magnification image showing the interplanar spacing.**

For all the investigated ZnO@P(MEO$_2$MA$_X$-OEGMA$_{100-X}$) NPs, the results showed high crystallinity and size uniformity; the average particle size was measured to be 5-6 nm. The corresponding TEM images of the different compositions with their size distribution are shown in **Figure 3.3.5**. It was seen that the NPs are well dispersed with a narrow size distribution.
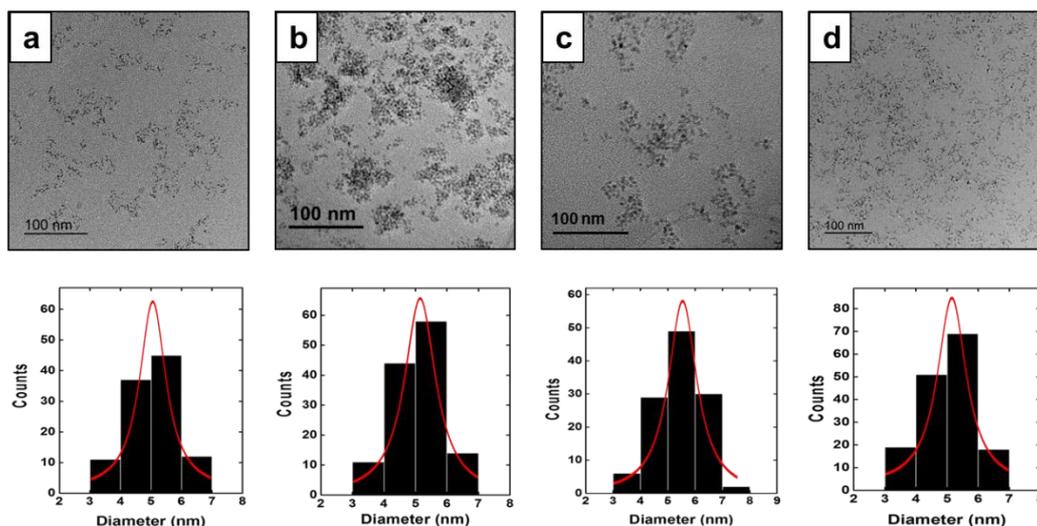


**Figure 3.3.5 Bright field HR-TEM micrographs of a) ZnO@P(MEO$_2$MA$_{80}$-OEGMA$_{20}$), b) ZnO@P(MEO$_2$MA$_{75}$-OEGMA$_{25}$), c) ZnO@P(MEO$_2$MA$_{65}$-OEGMA$_{35}$) and d) ZnO@P(MEO$_2$MA$_{60}$-OEGMA$_{40}$) NPs and their corresponding size distribution with the gaussian.**

### 3.1.3.  Amount of the grafted copolymer

TGA analysis was used to estimate the grafting amount of the copolymer on the surface of ZnO QDs. The weight loss (TG, %) was recorded as a function of the temperature at a rate of 5 °C/min, starting from room temperature up to 450 °C. As shown in **Figure 3.3.6**, the oleate

capped ZnO QDs curve shows a weight loss of about 2 % in the whole temperature range. This slight weight loss could be attributed to the removal of the absorbed water molecules or the decomposition of the hydroxide group onto the surface.
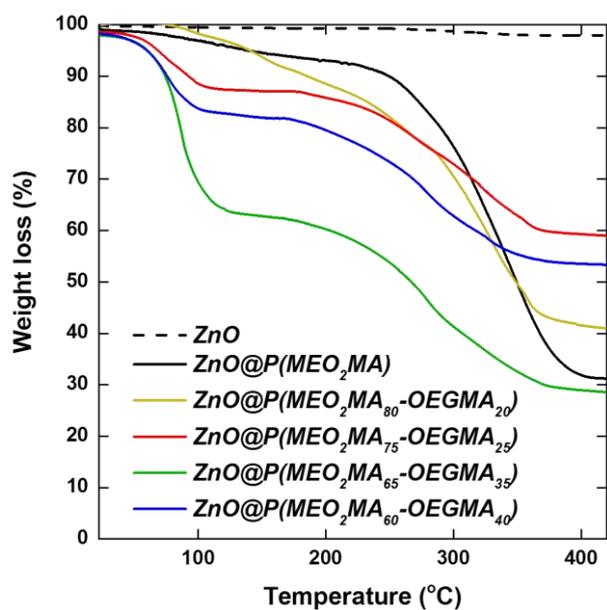


**Figure 3.3.6 TGA thermograms of ZnO NPs.**

For the modified ZnO NPs, two stages of weight loss occurred. The first stage occurred between the room temperature and 160 °C. At this stage, the weight loss could be related to the escape of solvent from the surface of the NPs. In the second stage, which takes place between 160 °C and 400 °C, the weight loss is related to the decomposition of the organic groups grafted at the surface of the ZnO QDs. For the $ZnO@P(MEO_2MA_X-OEGMA_{100-X})$ NPs, the grafting amounts obtained are summarized in **Table 3.3.1**.
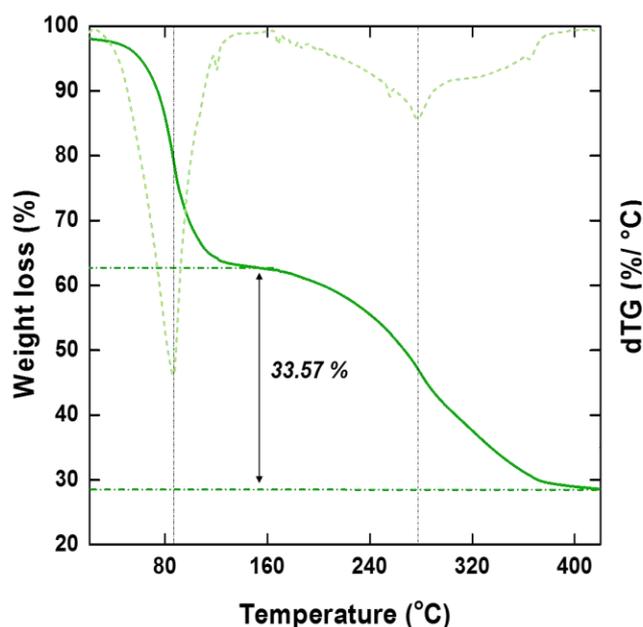
**Figure 3.3.7 Weight loss (TG, %) and weight loss derivative (dTG, %/ °C) curves of ZnO@P(MEO$_2$MA$_{65}$-OEGMA$_{35}$) NPs as a function of temperature.**

The evaporation of the water molecules explains the first loss before 160 °C while the weight loss occurred up to 400 °C is related to the decomposition of the organic groups including the silane ligands and the copolymer groups and the temperature at which the copolymers were degraded could be obtained by plotting the derivation curve of the weight loss (**Figure 3.3.7**).

**Table 3.3.2 TGA data obtained following the composition of the OEMGA groups in ZnO NPs.**

| Composition of OEGMA | Weight loss below 160 °C (%) | Weight loss of organic phase (%) |
|---|---|---|
| 0 | 6.32 | 62.43 |
| 20 | 7.74 | 51.34 |
| 25 | 12.85 | 28.03 |
| 35 | 37.70 | 33.57 |
| 40 | 18.20 | 28.56 |

139

### 3.1.4. Optical properties of the core/shell NPs
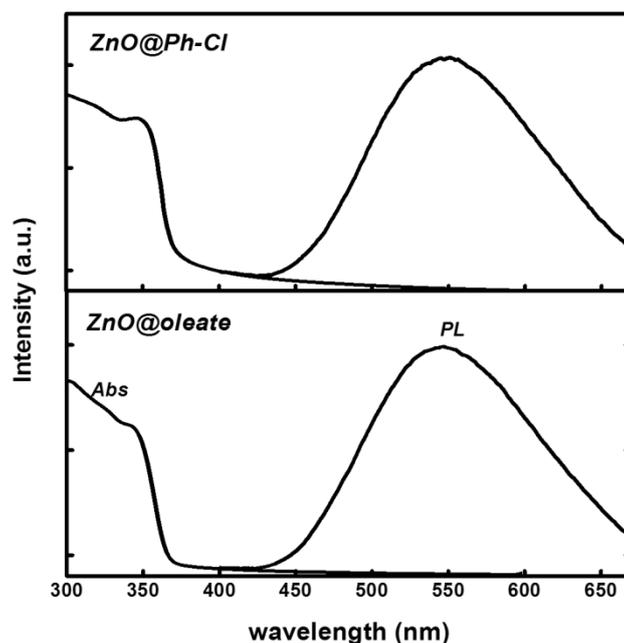


**Figure 3.3.8 Absorption and PL emission spectra of ZnO@oleate QDs and ZnO@Ph-Cl NPs.**

The copolymer grafting at the surface of the ZnO QDs did not alter their optical properties. This aspect was confirmed by recording the absorption and the photoluminescence (PL) spectra of all the modified samples of concentration 0.1 mg/ mL. All the samples displayed similar spectra. They exhibit an absorption peak below 350 nm and PL emission spectra in the visible region compared to ZnO@oleate QDs and ZnO@Ph-Cl NPs (**Figure 3.3.8**). In **Figure 3.3.9**, aqueous dispersions of the ZnO@P(MEO$_2$MA$_X$-OEGMA$_{100-X}$) NPs exhibited a bright yellow luminescence under UV light which originates from intrinsic defects of ZnO QDs [26].
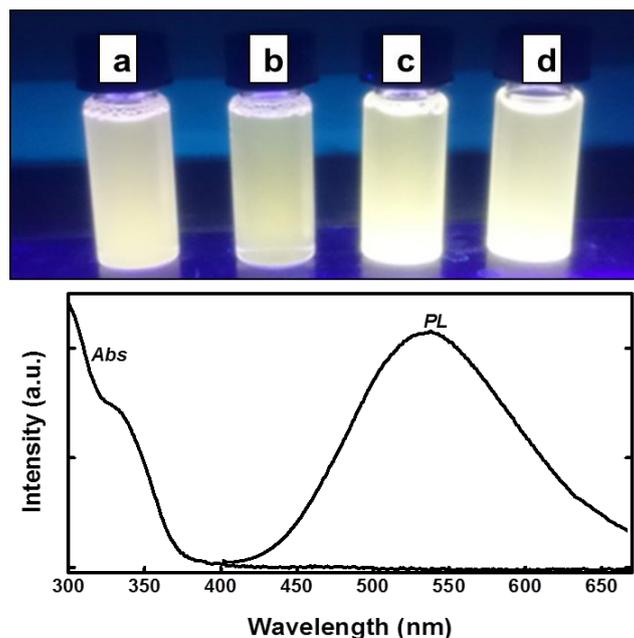
**Figure 3.3.9 Optical photographs of a) ZnO@P(MEO$_2$MA$_{80}$-OEGMA$_{20}$), b) ZnO@P(MEO$_2$MA$_{75}$-OEGMA$_{25}$), c) ZnO@P(MEO$_2$MA$_{65}$-OEGMA$_{35}$) and d) ZnO@P(MEO$_2$MA$_{60}$-OEGMA$_{40}$) dispersions in water under UV light and the corresponding absorption and PL spectra of ZnO@P(MEO$_2$MA$_{60}$-OEGMA$_{40}$) NPs.**

## 3.2. Thermo-responsive behavior of ZnO@P(MEO$_2$MA$_X$-OEGMA$_{100-X}$) NPs

### 3.2.1. In water

DLS analysis was carried out to study the thermal behavior of the ZnO@P(MEO$_2$MA$_X$-OEGMA$_{100-X}$) NPs in aqueous dispersion by following the changes of the hydrodynamic diameter at various temperatures. The analysis was firstly performed in water. The samples were dispersed in milli-Q water at adequate concentration (0.1 mg/mL). The suspensions were then subjected to continuous stirring and ultrasonication in order to facilitate the dispersion of the NPs. For each sample, the temperature was increased from 20 to 70 °C. In **Figure 3.3.10,** the evolution of the hydrodynamic diameter of ZnO@P(MEO$_2$MA$_{75}$-OEGMA$_{25}$) NPs as a function of the temperature is reported. The solvated NPs diameter was constant upon heating until 36 °C and then it started to increase gradually from 38 °C to reach a steady state from 45 to 70 °C. At the LCST, a phase transition occurs and the organization of the NPs in aqueous media changes from dispersions (left drawing) to agglomerations (right drawing). When the temperature is increased, the NPs started to collapse and aggregate, as indicated by the increase of the hydrodynamic diameter which indicates that the NPs that are merged together. Above the LCST, the copolymer chains collapse and render the surface of the NPs

hydrophobic, which force the NPs to aggregate (**Figure 3.3.10**). The equivalence point of this window could be simply obtained by drawing the first derivative of the plot as shown in **Figure 3.3.11**. Therefore, the LCST of ZnO@P(MEO$_2$MA$_{75}$-OEGMA$_{25}$) NPs in water is 40 °C.
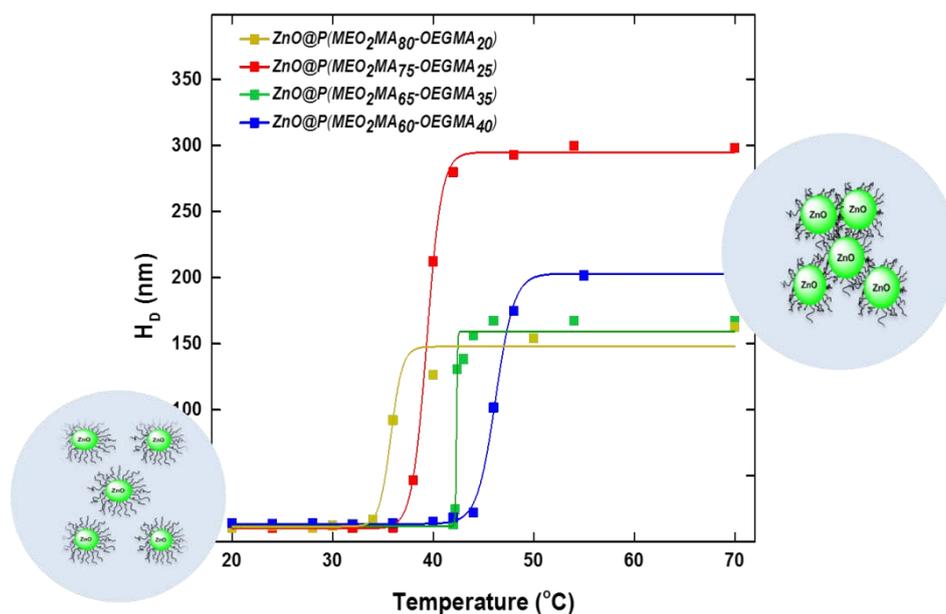


Figure 3.3.10 Evolution of ZnO@P(MEO$_2$MA$_{75}$-OEGMA$_{25}$) diameter with temperature; the drawing on the left illustrates the NPs in their dispersed state and the one on the right illustrates the aggregation of the NPs.

All the compositions were studied, and the related LCST could be extracted following the same procedure. The LCST values for the various copolymer compositions are depicted in **Table 3.3.2**. The LCST could be tuned by changing the content of MOE$_2$MA and OEGMA units in the copolymers. The higher the LCST, the higher the number of OEGMA units. This finding was consistent with literature data. Lutz *et al.* reported a linear increase of the LCST of P(MEO$_2$MA-co-OEGMA) copolymers with increasing the content of OEGMA [27].
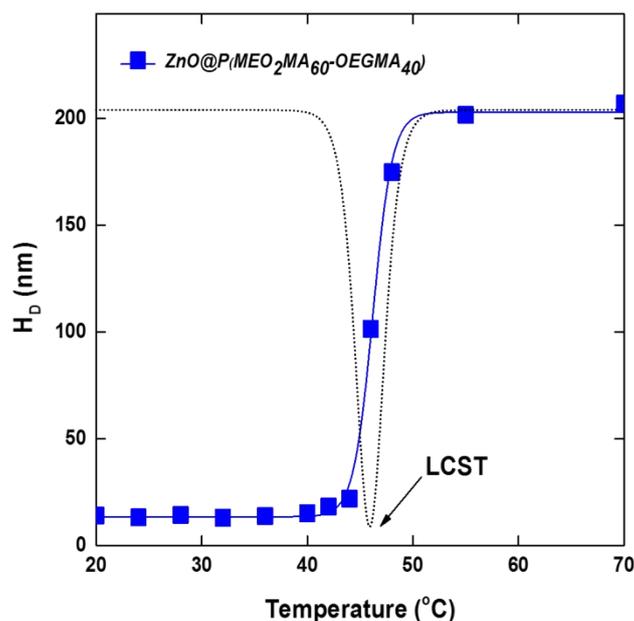
**Figure 3.3.11 Obtaining the LCST of ZnO@P(MEO$_2$MA$_{60}$-OEGMA$_{40}$) by derivation.**

The LCST values equal to 32, 37, or 39-40 °C were observed in pure water for copolymers possessing in average respectively 5, 8 or 10 % of OEGMA units per chain. This shift of the LCST towards higher temperature with the larger amount of incorporated OEGMA units confirms that the thermal properties of the ZnO@P(MEO$_2$MA$_X$-OEGMA$_{100-X}$) NPs are dependent of the molecular copolymers chains properties. For example, NPs with 20 % OEGMA units exhibited a LCST of 36 °C whereas this temperature increased up to 42 °C for NPs with 35 % of the incorporated OEGMA units (**Figure 3.3.12**).
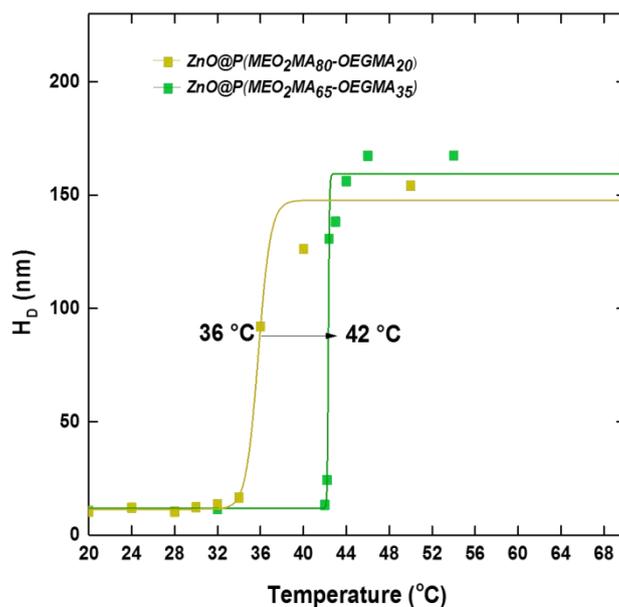
**Figure 3.3.12 Evolution of ZnO@P(MEO$_2$MA$_{80}$-OEGMA$_{20}$) and ZnO@P(MEO$_2$MA$_{65}$-OEGMA$_{35}$) diameter with temperature showing the shift of the LCST.**

The grafting of these thermo-responsive copolymers at the surface of ZnO NPs enhanced their stability and allowed good dispersion in aqueous media at lower temperature. This could be well seen when the NPs are dispersed in water below the LCST; the solution is clear as shown in **Figure 3.3.13a**. Below the LCST, the copolymer chains are in their expanded state as a result of the extensive hydrogen bonding interaction with the water molecules.
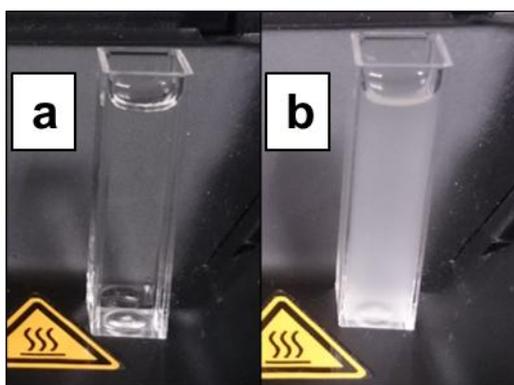


**Figure 3.3.13 Optical photograph of ZnO@P(MEO$_2$MA$_{75}$-OEGMA$_{25}$) at a) 20 °C and b) 70 °C during DLS measurements.**

Increasing the temperature above the LCST, intra- and intermolecular hydrogen bonding between polymer molecules dominates resulting in their collapse state and therefore aggregates form and the solution looks more turbid (**Figure 3.3.13b**).

Heating and cooling cycles were also performed to ensure that the conformational change of these NPs, *i.e.* the behavior of the copolymer chains at the surface of the NPs, was completely reversible. **Figure 3.3.14** displays the temperature dependence of ZnO@P(MEO$_2$MA$_{60}$-OEGMA$_{40}$) NPs in four heating and cooling cycles. It was observed that the NPs showed a complete reversible behavior. At low temperatures, water was a good solvent for the MEO$_2$MA-OEGMA copolymer, though the chains strongly interact with water molecules. As the temperature increased above the LCST, the dehydration occurred and the chains collapsed at the surface forming aggregates. These aggregates were monitored by the DLS. In the opposite sense, the collapsed MEO$_2$MA-OEGMA brushes became swollen and rehydrated again during the cooling process which allowed the re-dispersion of the NPs.
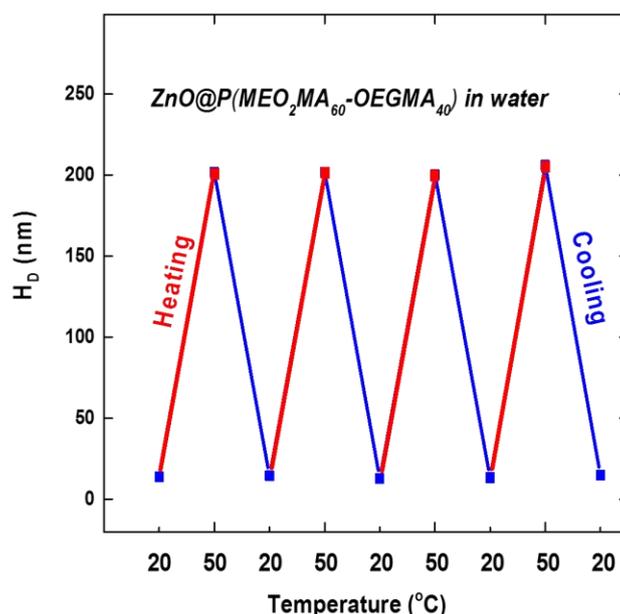


**Figure 3.3.14 Reversible diameter change of ZnO@P(MEO$_2$MA$_{60}$-OEGMA$_{40}$) NPs in water with successive heating and cooling cycles.**

### 3.2.2. In physiological media

The same experiments were conducted in culture media (CM). The CM formulation contains amino acids, vitamins and a lot of inorganic salts. Among these salts are Magnesium Sulfate (MgSO$_4$.7H$_2$O), Potassium Chloride (KCl), Sodium Bicarbonate (NaHCO$_3$), Sodium Chloride (NaCl) and Sodium Phosphate dibasic (Na$_2$HPO$_4$) anhydrous. Thus, all the samples were expected to have a shift in their LCST because the salt ions which are kosmotropes, will (or are expected to) affect the interaction of the copolymer brushes with the water molecules following the Hofmeister series for anions ($CO_3^{2-} > SO_4^{2-} > H_2PO_4^{2-} > Cl^-$).

A decrease of 4-6 °C in the LCST was observed in all the samples and the obtained values are listed in **Table 3.3.2**.

Table 3.3.3 LSCT of the investigated ZnO@P(MEO$_2$MA$_X$-OEGMA$_{100-X}$).

| Core/shell NPs | LCST in water (°C) | LCST in CM (°C) |
|---|---|---|
| ZnO@P(MEO$_2$MA$_{80}$-OEGMA$_{20}$) | 36 | 32 |
| ZnO@P(MEO$_2$MA$_{75}$-OEGMA$_{25}$) | 40 | 34 |
| ZnO@P(MEO$_2$MA$_{65}$-OEGMA$_{35}$) | 42 | 38 |
| ZnO@P(MEO$_2$MA$_{60}$-OEGMA$_{40}$) | 46 | 40 |

In **Figure 3.3.15**, the LCST of ZnO@P(MEO$_2$MA$_{65}$-OEGMA$_{35}$) NPs has been found to shift from 42 to 38 °C following path 1. It was shown that kosmotropic anions decreased the LCST of the polymer by polarizing interfacial water molecules [28]. This polarization effect weakened the hydrogen bonding of water molecules to the lone pairs on the oxygen of the ether groups in MEO$_2$MA-OEGMA copolymers [29]. Therefore, the copolymer chains showed a hydrophobic behavior and induced the aggregation of the NPs. This aggregation was more significant than in pure water and this could be seen in **Figure 3.3.15** (path 2). The hydrogen bonding of the copolymer chains with water molecules was completely disrupted inducing and early aggregation of the NPs.
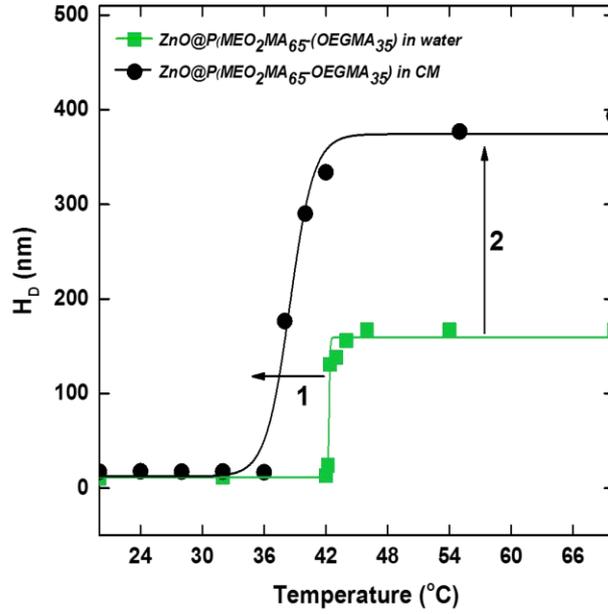
**Figure 3.3.15 Evolution of ZnO@P(MEO$_2$MA$_{65}$-OEGMA$_{35}$) NPs diameter showing a shift in the LCST in CM (1) and increase in the aggregates size (2).**

In CM, the copolymer chains could still maintain their reversible behavior for some samples when performing heating and cooling cycles. In **Figure 3.3.16**, ZnO@P(MEO$_2$MA$_{60}$-OEGMA$_{40}$) NPs had almost consistent size during the cycles. This sample could be of major importance for the biological application as it showed a phase transition around 40 °C in CM.
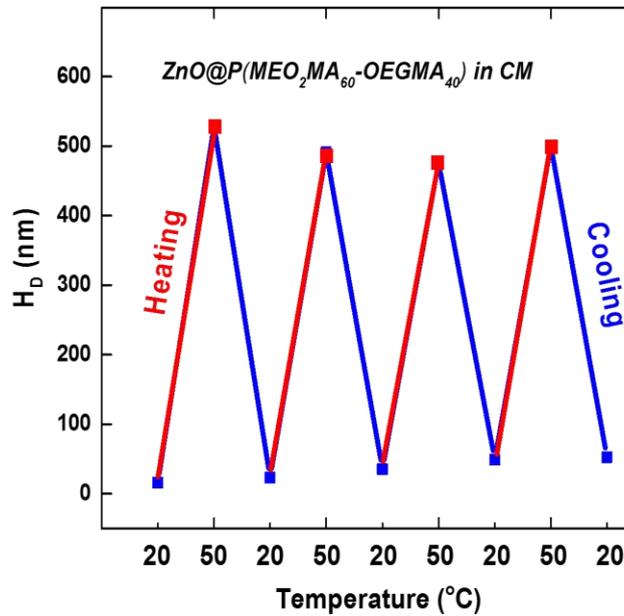


**Figure 3.3.16 Reversible diameter change of ZnO@P(MEO$_2$MA$_{60}$-OEGMA$_{40}$) NPs in CM with successive heating and cooling cycles.**

147

## 3.3. Cytotoxicity Tests

### 3.3.1. Cytotoxicity of ZnO@P(MEO$_2$MA$_X$-OEGMA$_{100-X}$) NPs

Over 60 cell lines derived from colorectal cancers are available from the general cell collection (ECACC). These colorectal cell lines are derived from tumours at various levels of differentiation and stages of development. The human colon adenocarcinoma cell line HT29 is one of the colorectal cell lines which was isolated from a primary tumor of a 44 years old Caucasian female in 1964 by Fogh and Trempe. Since then, many cell lines have been derived from human colon cancers [30] but HT29 remains probably one of the most resistant to anticancer drugs like DOX [31].

The concentration-dependent cytotoxicity of ZnO@P(MEO$_2$MA$_X$-OEGMA$_{100-X}$) NPs was evaluated by the conventional MTT assays after incubation with HT29 cells for 24 and 72 h. **Figure 3.3.17** shows the cell viability after 24 or 72 h of exposure to the NPs.
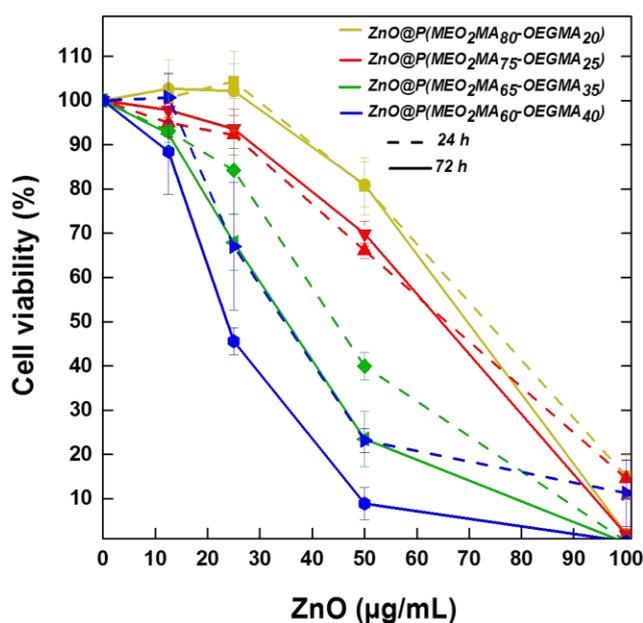


**Figure 3.3.17 Viability of HT29 cells after 24 and 72 h of exposure to ZnO@P(MEO$_2$MA$_X$-OEGMA$_{100-X}$) NPs.**

The results for the ZnO@P(MEO$_2$MA-OEGMA) NPs with the different compositions confirmed the biocompatibility of the NPs up to 12.5 µg/mL Zn concentration with a cell viability above 90 %. Samples with 20 and 25 % of OEGMA groups showed the greatest biocompatibility at higher concentrations; ≈ 90-100 % at 25 µg/mL and 70-80 % at 50 µg/mL, which means that copolymer shells with lower quantities of the OEGMA units display an

unexpected influence on the cytocompatibility of the core/shell NPs. In addition, the viability showed almost no change for these samples when increasing the exposure time from 24 to 72 h, while it decreased to some extent for the samples with 35 and 40 % of OEGMA groups. At 50 µg/mL, the viability of HT29 cells was equal to $\approx$ 80 % for ZnO@P(MEO$_2$MA$_{80}$-OEGMA$_{20}$) NPs at both 24 and 72 h, while for ZnO@P(MEO$_2$MA$_{60}$-OEGMA$_{40}$) NPs the viability decreased from 23 % at 24 h up to 8 % at 72 h (**Figure 3.3.18**).
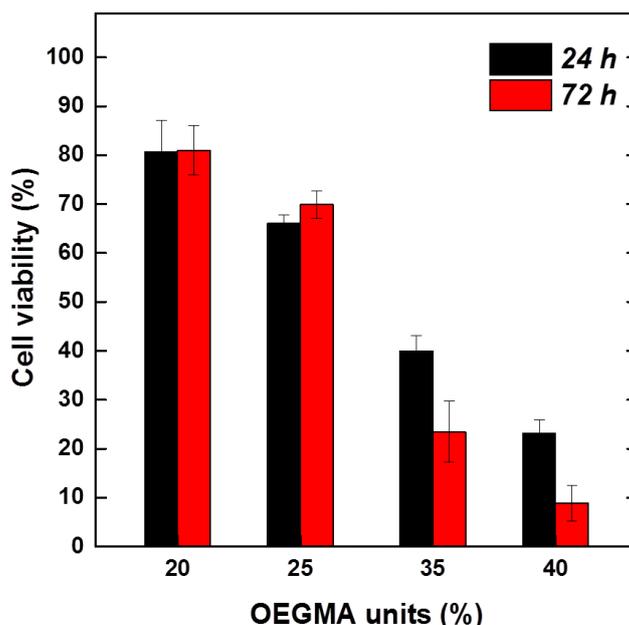


**Figure 3.3.18 Viability of HT29 cells after 24 and 72 h of exposure to ZnO@P(MEO$_2$MA$_X$-OEGMA$_{100-X}$) NPs at 50 µg/mL Zn$^{2+}$.**

The cytotoxicity of ZnO NPs mainly results from the dissociation of the Zn ions which are well known to be toxic for cells [32]. Cytotoxicity results from ZnO dissolution in culture medium and endosomes and is mediated in cells by the generation of oxygen species [33]. Cai *et al.* [5] showed that ZnO QDs incubated with human carcinoma A549 cells for 48 h exhibited at 10 µg/mL Zn$^{2+}$ concentration about 70 % cell viability. As a result, a careful coverage of the ZnO surface should decrease the release of the Zn$^{2+}$ ions especially in aqueous media. OEGMA segments are longer than MEO$_2$MA segments. When the polymerization takes place from the surface of the ZnO NPs in the case of high amount of OEGMA monomers, a competition exists between the two monomers and the presence of more OEGMA segments in the copolymer chain reduces the access of the initiator to the monomer units, hence decreasing the coverage of the ZnO surface. In this case, only a copolymer shell with low amount of OEGMA units is able to fully cover the ZnO core and thus to trap a great part of Zn ions.

### 3.3.2. ZnO@P(MEO$_2$MA$_X$-OEGMA$_{100-X}$) NPs loaded with DOX

The cytotoxicity of DOX loaded in ZnO@P(MEO$_2$MA$_{65}$-OEGMA$_{35}$) and ZnO@P(MEO$_2$MA$_{60}$-OEGMA$_{40}$) NPs was evaluated 24 h after the NPs addition in HT29 cells for 5 h at 37 °C or 41 °C. Forty µg/mL DOX were loaded in 0.1 mg/mL of the ZnO@P(MEO$_2$MA$_X$-OEGMA$_{100-X}$) NPs. The corresponding concentrations for the NPs and NPs loaded with DOX are presented with x-axis as Zn concentration and corresponding DOX concentration, respectively. The NPs loaded with DOX are referenced as ZnO@P(MEO$_2$MA$_X$-OEGMA$_{100-X}$)-DOX.

The results showed that ZnO@P(MEO$_2$MA$_X$-OEGMA$_{100-X}$)-DOX NPs exhibited an increased toxicity of HT29 cells even for a non-toxic concentration of NPs without DOX (**Figure 3.3.19**). At Zn concentration of 25 µg/mL, the viability of HT29 cells could be assumed to be higher than 60 %, with ZnO@P(MEO$_2$MA$_{65}$-OEGMA$_{35}$) NPs while it dropped below 20 % after 5 h of incubation with ZnO@P(MEO$_2$MA$_{65}$-OEGMA$_{35}$)-DOX NPs. And as clearly seen, the toxicity of both ZnO@P(MEO$_2$MA$_{65}$-OEGMA$_{35}$)-DOX and ZnO@P(MEO$_2$MA$_{60}$-OEGMA$_{40}$)-DOX NPs increased with the DOX concentration.
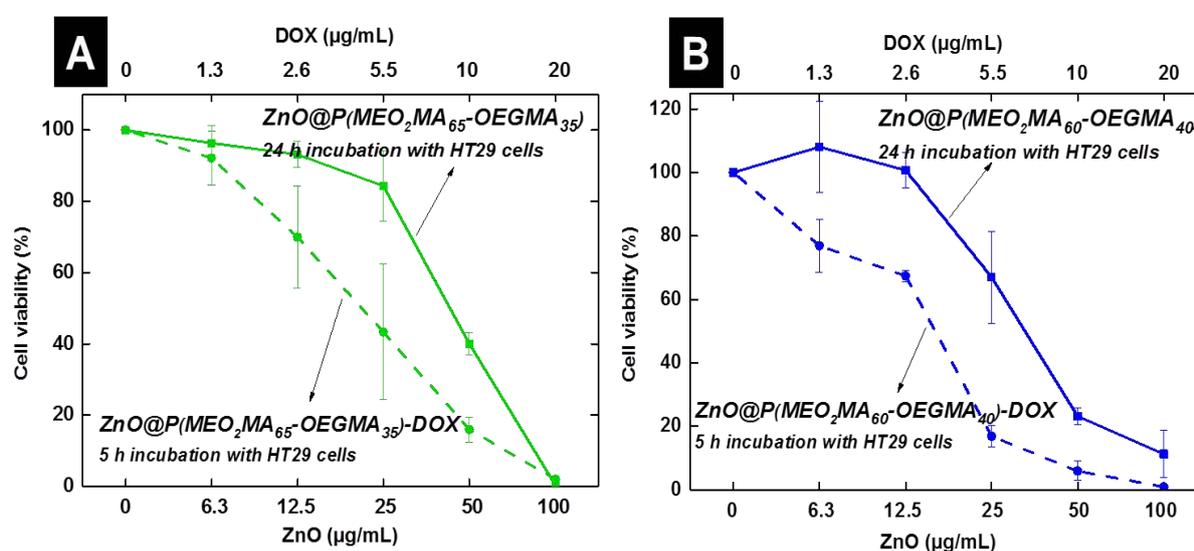


**Figure 3.3.19 Viability of HT29 cells after 24 or 5 h of exposure to A) ZnO@P(MEO$_2$MA$_{65}$-OEGMA$_{35}$) and ZnO@P(MEO$_2$MA$_{65}$-OEGMA$_{35}$)-DOX NPs, and B) ZnO@P(MEO$_2$MA$_{60}$-OEGMA$_{40}$) and ZnO@P(MEO$_2$MA$_{60}$-OEGMA$_{40}$)-DOX NPs, respectively.**

Similar results were obtained Cai *et al.* [5] with ZnO-PEG-DOX NPs. They have reported the surface modification of ZnO with biodegradable polyethylene glycol (PEG) loaded with DOX for drug delivery. The prepared NPs were tested for the viability of lung cancer A549 cells at

different times and concentrations. The results of the incubation of A549 cells with ZnO-PEG-DOX NPs showed a concentration-dependent cytotoxicity but to a lesser extent than free DOX.
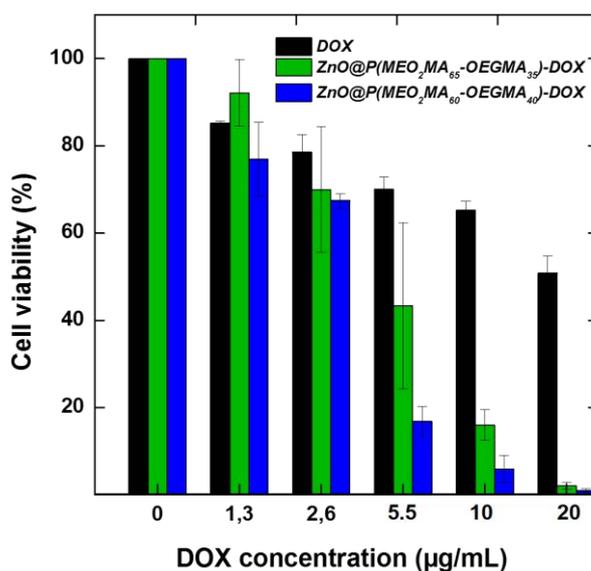


**Figure 3.3.20 Viability of HT29 cells after 5 h of exposure to free DOX, ZnO@P(MEO$_2$MA$_{65}$-OEGMA$_{35}$)-DOX and ZnO@P(MEO$_2$MA$_{60}$-OEGMA$_{40}$)-DOX NPs.**

Considering the cytotoxicity of ZnO@P(MEO$_2$MA$_X$-OEGMA$_{100-X}$)-DOX NPs compared to free DOX, we observed that both NPs were more cytotoxic from 5.5 µg/mL DOX. And that the ZnO@P(MEO$_2$MA$_{60}$-OEGMA$_{40}$)-DOX NPs exhibited the most significant effect on cells. This result was unexpected because the NPs, particularly ZnO@P(MEO$_2$MA$_{60}$-OEGMA$_{40}$)-DOX NPs should retain DOX at 37 °C. In fact, it could be assumed that cell internalization for ZnO@P(MEO$_2$MA$_{60}$-OEGMA$_{40}$) NPs was more efficient than for their counterparts and free DOX and thus higher quantity of DOX could be delivered over the incubation time. In addition, we cannot rule out the cytotoxic effect of NPs alone (without DOX) at this concentration range (5.5-20 µg/ml DOX corresponded to 25-100 Zn$^{2+}$). One explanation for that results could be in part given by Xiong *et al.* [34] with ZnO@polymer-DOX NPs. These NPs were incubated with human brain cancer cells U251 and the results showed an enhanced toxicity of DOX loaded in ZnO@polymer NPs with respect to free DOX. They have explained that the reason behind this cytotoxicity enhancement effect could be drug internalization improvement by using polymeric ZnO NPs. The polymeric ZnO NPs are engulfed by the endosomes and lysosomes when taken by the cells, so more ZnO@polymer-DOX NPs would be taken up continuously and finally the NPs decompose in the lysosomes to

release high concentrations of DOX molecules, thus achieving higher cytotoxicity [34]. Thus, ZnO@P(MEO$_2$MA$_X$-OEGMA$_{100-X}$)-DOX NPs exhibit higher cytotoxicity compared to free DOX (**Figure 3.3.20**).

ZnO@P(MEO$_2$MA$_{65}$-OEGMA$_{35}$) and ZnO@P(MEO$_2$MA$_{60}$-OEGMA$_{40}$) NPs were tested for the viability of HT29 cells because both compounds exhibit a LCST at 38 and 40 °C, respectively, above the temperature required for living cells in normal conditions. By subjecting the cells over a short period of time (5 h in our conditions) at 41 °C, it was expected that NPs release DOX to obtain greater cytotoxic effect. **Figure 3.3.21** represents the cell viability at 37 °C and 41 °C for 5 h with ZnO@P(MEO$_2$MA$_{65}$-OEGMA$_{35}$)-DOX, ZnO@P(MEO$_2$MA$_{60}$-OEGMA$_{40}$)-DOX NPs and free DOX at 2.6 µg/mL DOX concentration.
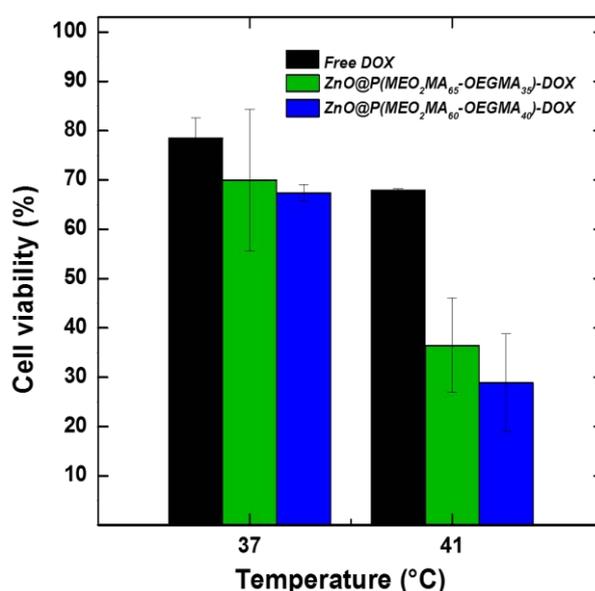


**Figure 3.3.21 HT29 cell viability in presence of 2.6 µg/mL free DOX, ZnO@P(MEO$_2$MA$_{65}$-OEGMA$_{35}$)-DOX and ZnO@P(MEO$_2$MA$_{60}$-OEGMA$_{40}$)-DOX NPs at 37 or 41 °C for 5 h.**

A decrease in the HT29 cell viability when increasing the incubation temperature from 37 to 41 °C with the two samples, ZnO@P(MEO$_2$MA$_{65}$-OEGMA$_{35}$)-DOX and ZnO@P(MEO$_2$MA$_{60}$-OEGMA$_{40}$)-DOX NPs is highlighted. The greatest effect was obtained with ZnO@P(MEO$_2$MA$_{60}$-OEGMA$_{40}$)-DOX NPs but the difference with ZnO@P(MEO$_2$MA$_{65}$-OEGMA$_{35}$)-DOX NPs was not significant. When compared to free DOX, NPs cytotoxic effect was significantly more pronounced. Below 2.6 µg/mL, the temperature had no effect on the cell viability for the free DOX and less pronounced in presence of both NPs. ZnO@P(MEO$_2$MA$_{65}$-OEGMA$_{35}$)-DOX NPs showed a non-significant

decrease from 85 to 78 % cell viability at 1.3 µg/mL DOX (**Figure 3.3.22**). The decrease in cell viability from 37 to 41 °C could be attributed to the release of more DOX molecules due to the phase transition of the copolymer grafted on the surface of ZnO NPs. Above 2.5 µg/mL DOX, the cytotoxicity increased dramatically with both NPs and at both temperatures whereas free DOX remained by far the lowest toxic with cell viability above 40 %. From 5 µg/mL DOX ZnO@P(MEO$_2$MA$_{60}$-OEGMA$_{40}$)-DOX NPs at 41 °C for 5 h produced the almost complete death of HT29 cells.
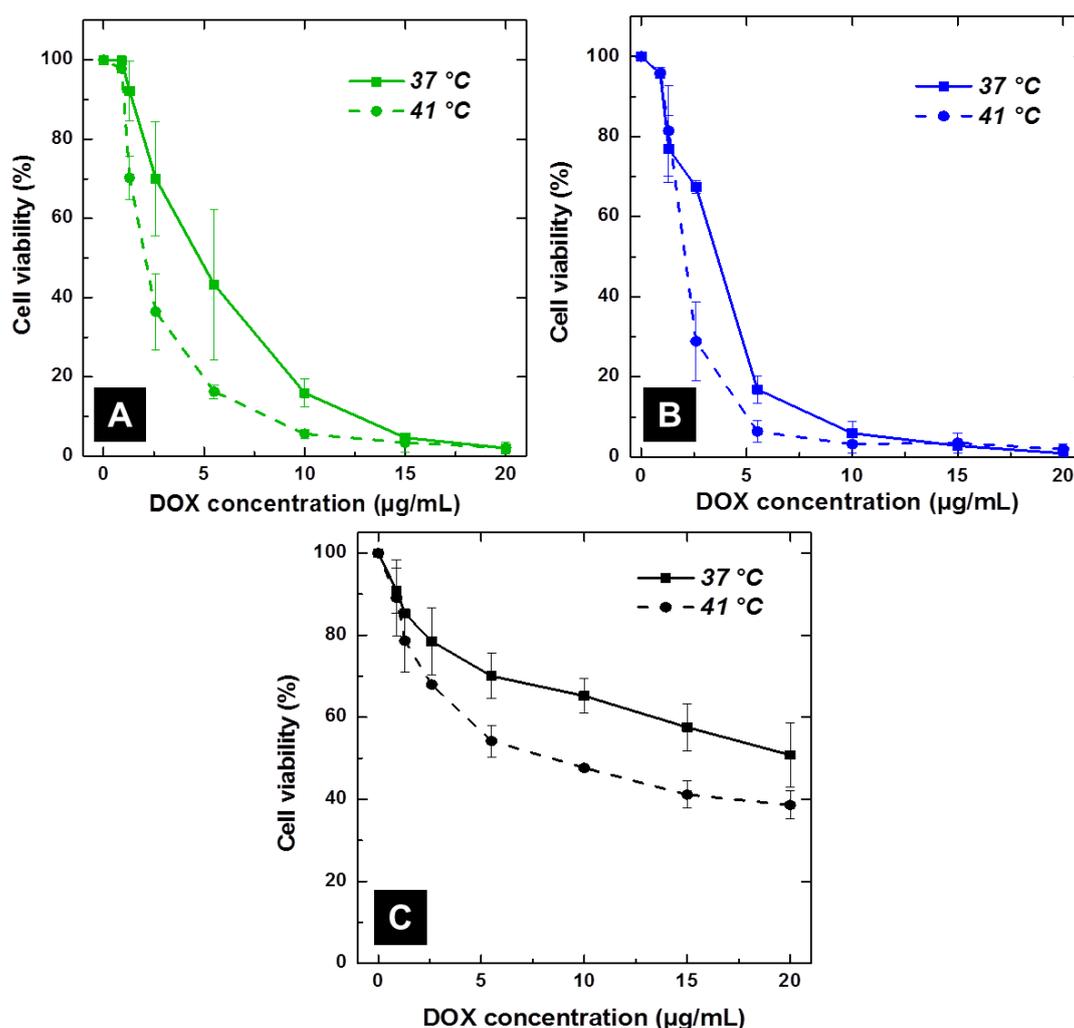


**Figure 3.3.22 HT29 cell viability after incubation with A) ZnO@P(MEO$_2$MA$_{65}$-OEGMA$_{35}$)-DOX, B) ZnO@P(MEO$_2$MA$_{60}$-OEGMA$_{40}$)-DOX NPs and C) free DOX at 37 and 41 °C for 5 h.**

# 4. CONCLUSION

Core/shell ZnO@P(MEO$_2$MA$_X$-OEGMA$_{100-X}$) NPs have been synthesized via SI-ARGET ATRP to graft MEO$_2$MA$_X$-OEGMA$_{100-X}$ copolymers from the surface of ZnO QDs. These core/shell NPs showed a thermo-responsive behavior that could be controlled by tuning the molar ratio of MEO$_2$MA and OEGMA monomers. The thermo-responsive behavior denoted by a LCST showed lower values in CM. The presence of salts following the Hofmeister series caused the LCST of the NPs to decrease by 4-6 °C in CM. The cytotoxic tests suggested that these NPs have potential to be used as nano-carriers for drug delivery with more development of the method.

# REFERENCES

1. Zhang, Z.Y., Xu, Y.D., Ma, Y.Y., Qiu, L.L., Wang, Y., Kong, J.L. and Xiong, H.M., *Biodegradable ZnO@ polymer Core–Shell Nanocarriers: pH-Triggered Release of Doxorubicin In Vitro.* Angewandte Chemie International Edition, 2013. **52**(15): p. 4127-4131.
2. Zhang, Z.Y., and Xiong, H. M., *Photoluminescent ZnO nanoparticles and their biological applications.* Materials, 2015. **8**(6): p. 3101-3127.
3. Zhang, P., and Liu, W., *ZnO QD@PMAA-co-PDMAEMA nonviral vector for plasmid DNA delivery and bioimaging.* Biomaterials, 2010. **31**(11): p. 3087-3094.
4. Li, S., Sun, Z., Li, R., Dong, M., Zhang, L., Qi, W., Zhang, X. and Wang, H., *ZnO Nanocomposites Modified by Hydrophobic and Hydrophilic Silanes with Dramatically Enhanced Tunable Fluorescence and Aqueous Ultrastability toward Biological Imaging Applications.* Scientific reports, 2015. **5**(8475): p. 8.
5. Cai, X., Luo, Y., Zhang, W., Du, D. and Lin, Y., *pH-Sensitive ZnO Quantum Dots–Doxorubicin Nanoparticles for Lung Cancer Targeted Drug Delivery.* ACS Applied Materials & Interfaces, 2016. **8**(34): p. 22442-22450.
6. Resch-Genger, U., Grabolle, M., Cavaliere-Jaricot, S., Nitschke, R. and Nann, T., *Quantum dots versus organic dyes as fluorescent labels.* Nature methods, 2008. **5**(9): p. 763-775.
7. Pan, Z.Y., Liang, J., Zheng, Z.Z., Wang, H.H. and Xiong, H.M., *The application of ZnO luminescent nanoparticles in labeling mice.* Contrast media & molecular imaging, 2011. **6**(4): p. 328-330.
8. Gulia, S., and Kakkar, R., *ZnO quantum dots for biomedical applications.* Adv. Mater. Lett, 2013. **4**(12): p. 876-887.
9. Xiong, H.M., Wang, Z.D. and Xia, Y.Y., *Polymerization initiated by inherent free radicals on nanoparticle surfaces: a simple method of obtaining ultrastable (ZnO) polymer core–shell nanoparticles with strong blue fluorescence.* Advanced Materials, 2006. **18**(6): p. 748-751.
10. Kango, S., Kalia, S., Celli, A., Njuguna, J., Habibi, Y. and Kumar, R., *Surface modification of inorganic nanoparticles for development of organic–inorganic nanocomposites—A review.* Progress in Polymer Science, 2013. **38**(8): p. 1232-1261.
11. Xiong, H.M., Xie, D.P., Guan, X.Y., Tan, Y.J. and Xia, Y.Y., *Water-stable blue-emitting ZnO@ polymer core–shell microspheres.* Journal of Materials Chemistry, 2007. **17**(24): p. 2490-2496.
12. Xiong, H.M., Xu, Y., Ren, Q.G. and Xia, Y.Y., *Stable Aqueous ZnO@Polymer Core−Shell Nanoparticles with Tunable Photoluminescence and Their Application in Cell Imaging.* Journal of the American Chemical Society, 2008. **130**(24): p. 7522-7523.
13. Kumar, A., Srivastava, A., Galaev, I.Y. and Mattiasson, B., *Smart polymers: physical forms and bioengineering applications.* Progress in Polymer Science, 2007. **32**(10): p. 1205-1237.
14. Zhang, L., Zhang, S., He, B., Wu, Z. and Zhang, Z., *TiO$_2$ nanoparticles functionalized by a temperature-sensitive poly (N-isopropylacrylamide)(PNIPAM): synthesis and characterization.* Zeitschrift für Naturforschung B, 2008. **63**(8): p. 973-976.
15. Bawa, P., Pillay, V., Choonara, Y.E. and Du Toit, L.C., *Stimuli-responsive polymers and their applications in drug delivery.* Biomedical materials, 2009. **4**(2): p. 022001.

16. Gandhi, A., Paul, A., Sen, S.O. and Sen, K.K., *Studies on thermoresponsive polymers: Phase behaviour, drug delivery and biomedical applications.* asian journal of pharmaceutical sciences, 2015. **10**(2): p. 99-107.

17. Schmaljohann, D., *Thermo-and pH-responsive polymers in drug delivery.* Advanced drug delivery reviews, 2006. **58**(15): p. 1655-1670.

18. Gibson, M.I., and O'Reilly, R. K., *To aggregate, or not to aggregate? considerations in the design and application of polymeric thermally-responsive nanoparticles.* Chemical Society Reviews, 2013. **42**(17): p. 7204-7213.

19. Hu, Y., Darcos, V., Monge, S. and Li, S., *Thermo-responsive drug release from self-assembled micelles of brush-like PLA/PEG analogues block copolymers.* International journal of pharmaceutics, 2015. **491**(1): p. 152-161.

20. Du, H., Wickramasinghe, R., and Qian, X., *Effects of salt on the lower critical solution temperature of poly (N-isopropylacrylamide).* The Journal of Physical Chemistry B, 2010. **114**(49): p. 16594-16604.

21. Van Durme, K., Rahier, H. and Van Mele, B., *Influence of additives on the thermoresponsive behavior of polymers in aqueous solution.* Macromolecules, 2005. **38**(24): p. 10155-10163.

22. Beegam, A., Prasad, P., Jose, J., Oliveira, M., Costa, F.G., Soares, A.M., Gonçalves, P.P., Trindade, T., Kalarikkal, N., Thomas, S. and de Lourdes Pereira, M., *Environmental Fate of Zinc Oxide Nanoparticles: Risks and Benefits.* Toxicology-New Aspects To This Scientific Conundrum, 2016: p. 81.

23. Fakhroueian, Z., Dehshiri, A.M., Katouzian, F. and Esmaeilzadeh, P., *In vitro cytotoxic effects of modified zinc oxide quantum dots on breast cancer cell lines (MCF7), colon cancer cell lines (HT29) and various fungi.* Journal of nanoparticle research, 2014. **16**(7): p. 2483.

24. Lu, C., Bhatt, L.R., Jun, H.Y., Park, S.H. and Chai, K.Y., *Carboxyl–polyethylene glycol–phosphoric acid: a ligand for highly stabilized iron oxide nanoparticles.* Journal of Materials Chemistry, 2012. **22**(37): p. 19806-19811.

25. Green, L.A.W., and Thanh, N.T.K., *High pressure synthesis of FePt nanoparticles with controlled morphology and Fe content.* RSC Advances, 2014. **4**(3): p. 1168-1173.

26. Aboulaich, A., Tilmaciu, C.M., Merlin, C., Mercier, C., Guilloteau, H., Medjahdi, G. and Schneider, R., *Physicochemical properties and cellular toxicity of (poly) aminoalkoxysilanes-functionalized ZnO quantum dots.* Nanotechnology, 2012. **23**(33): p. 335101.

27. Lutz, J.F., *Synthesis of Smart Materials by ATRP of Oligo (Ethylene Glycol) Methacrylates. New Smart Materials via Metal Mediated Macromolecular Engineering.* Springer Netherlands, 2009: p. 37-47.

28. Chiu, J.J., Kim, B.J., Kramer, E.J. and Pine, D.J., *Control of nanoparticle location in block copolymers.* Journal of the American Chemical Society, 2005. **127**(14): p. 5036-5037.

29. Cho, Y., Zhang, Y., Christensen, T., Sagle, L.B., Chilkoti, A. and Cremer, P.S., *Effects of Hofmeister anions on the phase transition temperature of elastin-like polypeptides.* The Journal of Physical Chemistry B, 2008. **112**(44): p. 13765-13771.

30. Martínez-Maqueda, D., Miralles, B. and Recio, I., *HT29 Cell Line,* in *The Impact of Food Bioactives on Health: in vitro and ex vivo models.* Springer International Publishing, 2015. p. 113-124.

31. Ravizza, R., Gariboldi, M.B., Passarelli, L. and Monti, E., *Role of the p53/p21 system in the response of human colon carcinoma cells to Doxorubicin. BMC cancer*, 2004. **4**(1), p.92.

32. Franklin, N.M., Rogers, N.J., Apte, S.C., Batley, G.E., Gadd, G.E. and Casey, P.S., *Comparative toxicity of nanoparticulate ZnO, bulk ZnO, and ZnCl$_2$ to a freshwater microalga (Pseudokirchneriella subcapitata): the importance of particle solubility.* Environmental science & technology, 2007. **41**(24): p. 8484-8490.

33. Xia, T., Kovochich, M., Liong, M., M dler, L., Gilbert, B., Shi, H., Yeh, J.I., Zink, J.I. and Nel, A.E., *Comparison of the mechanism of toxicity of zinc oxide and cerium oxide nanoparticles based on dissolution and oxidative stress properties*. *ACS nano*, 2008. **2**(10), pp.2121-2134.

34. Xiong, H.M., *ZnO nanoparticles applied to bioimaging and drug delivery.* Advanced Materials, 2013. **25**(37): p. 5329-5335.

# *Chapter 4: Thermo-responsive magnetic Fe$_3$O$_4$@P(MEO$_2$MA$_X$-OEGMA$_{100-X}$) NPs and their applications as drug delivery systems*

# ABSTRACT

Superparamagnetic nanoparticles (NPs), due to their unique physical properties, have been widely used in nanomedicine for diagnostic imaging, therapeutic applications and drug delivery. They have found to be useful carriers for delivering anticancer drugs in targeted cancer treatment. In our study, superparamagnetic $Fe_3O_4$ NPs were grafted with a biocompatible thermoresponsive copolymer to obtain the responsive core/shell NPs. The aim of this work was to build a drug delivery system which is able to release anticancer drugs in cancer cells at physiological temperatures. The core/shell NPs were characterized for their physical, magnetic and thermal properties. It was important to tune the lower critical solution temperature (LCST) of the core/shell NPs at a temperature above the one required for living cells in normal conditions as the release of the drug from the copolymer shell of NPs should only occur at the tumor sites which is in this case controlled by the application of a heating source. The core/shell NPs exhibiting the targeted LCST were loaded with Doxurubicin (DOX) and studied for the drug delivery. The results have shown that the significant release occurred around the LCST in water and CM which could be promising for using these core/shell NPs in drug delivery. The cytotoxicity tests have shown that loading DOX molecules in the core/shell NPs didn"t enhance their cytotoxicity compared to the free DOX, which suggested the low cellular uptake of the NPs by the cancer cells.

# 1. INTRODUCTION

The cancer is one of the leading causes of death in the world nowadays. Based on the GLOBOCAN worldwide estimates of cancer incidence and mortality produced by the International Agency for Research on Cancer (IARC) for 2012, about 14.1 million new cancer cases and 8.2 million deaths occurred in 2012 (56.8 % of the cases and 64.9 % of the deaths in less developed countries) and this number is predicted to increase to 13.1 million deaths over the next two decades [1, 2]. Controlling the growing and then the complete elimination of this deadly disease is still challenging due to clinical limitations of traditional therapies such as surgery, radiotherapy, and chemotherapy which have been regarded as standard forms of clinical therapy for most types of cancer [3]. However, these conventional therapies have major drawbacks. Indeed side effects due to the usage of harmful radiations, poor biocompatibility, the poor solubility of hydrophobic anti-cancer drugs and moreover the multidrug resistance of cancer cells are one of the major reason of the low efficiency of the current treatment. Enhancing targeted delivery and release of the drugs could also help in preventing the formation of secondary tumors in distant organ (metastases) [3, 4]. As efficient and biocompatible alternatives, NPs represent an opportunity to overcome some of the major issues related to the traditional treatment of cancer [5]. Various NPs have been proposed as efficient carriers for therapeutic anticancer drugs. It was shown that drugs associated with NPs may avoid recognition by the P-glycoprotein efflux pump which is the best known mechanism of drug resistance, leading to higher intracellular drug concentrations [6].

Hybrid core/shell NPs, which are composed of inorganic core and organic shell, have been widely studied for cancer therapy as drug carriers [7, 8]. Among inorganic NPs, superparamagnetic NPs hold great promise to improve therapeutic strategies against cancer for their good biocompatibility, hyperthermia options, screening with magnetic resonance imaging (MRI). Their ability to be directed to the site of the tumor by an external magnetic field makes them a powerful tool for controlled targeting clinically, therefore increasing the anticancer drug efficacy and reducing potential side effects (as they can be used at very low concentration compared to the conventional methods) [9]. In addition, they can be easily removed from the blood circulation due to the fact that they lose their magnetization after the removal of the magnetic field; in the case of superparamagnetic character of the magnetic NPs, they constitute magnetic mono-domains. When an external magnetic field of strength H is applied, the magnetic moments align with H and the magnetization curve is obtained

showing that M increases with H until a saturation value $M_s$ is reached and when H is removed the related spin moments return to their original orientations, as a result the interaction between the NPs decreases, thus lowering their tendency to aggregate [10]. The surface engineering of the magnetic NPs with a polymeric coating can enhance their specific properties, principally their stability especially in vivo [11, 12]. Furthermore, a polymer shell can allow multifunctional layer for conjugation with bioactive molecules [13]. Moreover, when the drug is loaded in core/shell NPs acting as nanocarriers, the drug release process can be controlled [14].

Thermo-responsive polymers (TRPs) are considered as ideal candidates for coating strategy of magnetic NPs for the engineering of efficient drug delivery systems [15, 16]. They are widely selected for their thermal sensitivity as a controlled mechanism of drug delivery to tumor cells [17]. TRPs are characterized by a lower critical solution temperature (LCST) [18]. Heating above the LCST, a phase transition occurs and the polymer becomes hydrophobic. At this stage, the polymer chains shrinks at the surface of the NPs and the drug molecules incorporated inside the polymer are diffused outside at the tumor cells (see **Figure 4.3.12**). The combination of the TRPs feature with the magnetic hyperthermia is very useful [19]; the heat produced by the magnetic NPs when subjected to a magnetic field is used as a heat source for the thermo-responsive polymers which should exhibit a LCST in the temperature range of 40-45 °C [20]. Poly-(N-isopropyl acrylamide) (PNIPAM), the most studied TRP, has been used to modify magnetic NPs [15, 16, 21]. However, this polymer has a LCST which is lower than the physiological temperature and suffers from low biocompatibility towards human cells. Thus a well-known biocompatible co-polymer composed of 2-(2-methoxyethoxy) ethyl methacrylate ($MEO_2MA$) and oligo (ethylene glycol) methacrylate (OEGMA) could be a better alternative [22, 23]. This kind of co-polymer exhibits LCST in water, which could be finely tuned above the physiological temperature 37 °C by varying the molar ratio $MEO_2MA$/OEGMA [24]. At adequate molar ratio, a LCST of about 40-41°C, which could be easily reached by magnetic hyperthermia [19], could be obtained.

Core/shell magnetic NPs were studied in vitro and in vivo as drug carriers on wide range of cancer cells [25] like KB (epidermal carcinoma) [26], MCF-7 (breast carcinoma) [27, 28], A549 (lung cancer) [29], HeLa (cervical cancer) [30] and HT29 cell lines [31]. For each study, different factors could affect the performance of the core/shell magnetic NPs. The same core/shell NPs have better efficiency on one cell line than the other depending of their physicochemical nature and the characteristics of the cell line. Dorniani *et al.* [32] have

166

coated their magnetic NPs with chitosan and gallic acid. By performing the in vitro MTT assays, it has been shown that HT29 cells were more sensitive to MCF7 cells than NPs containing gallic acid, resulting in higher anticancer activity in HT29 cells. The efficiency of the magnetic core/shell NPs has been demonstrated to be dependent on their behavior in vivo which, in turn, depending on their physicochemical properties. The size, morphology, charge and surface chemistry of the magnetic NPs have been found to determine their fate and their effectivness, in vivo. Reducing their size and functionalizing their surface with hydrophilic polymers are necessary to increase their blood circulation and cellular uptake [29]. In the study of Liang *et al.* [31], polymeric superparamagnetic NPs conjugated with DOX, an anticancer drug, were incubated with HT29 cells at different times. The results of the in vitro experiments have shown that the polymeric NPs conjugated with DOX could cause more serious DNA crosslink than the free DOX, resulting in a lower DNA expression and a higher cell apoptosis for HT29 cancer cells. In addition, a larger cellular uptake of the NPs was established when applying a magnetic field which resulted in higher iron accumulation in the HT29 cells. More precisely, the cell viablity had decreased from about 80 to 40 % at 2.2 µg/mL DOX concentration for the polymeric magnetic NPs with an applied magnetic field.

In our work, we have reported the development and the characterization of superparamagnetic/thermo-responsive core/shell NPs which could be used as a drug delivery system. Our system is composed of $Fe_3O_4$ NPs coated with $MEO_2MA_X$-$OEGMA_{100-X}$ TRPs and loaded with DOX and tested in-vitro. The synthesis of the magnetic NPs and the grafting of the copolymer from their surface were performed following the same synthetic procedure mentioned previously in the second chapter. The TRP was engineered to display a LCST around 40 °C, required for living cells in normal conditions. The core/shell NPs exhibiting the targeted LCST was studied for DOX release using UV-Vis spectroscopy. The cytotoxicity of the same sample loaded with DOX was studied before and after the LCST and compared with free DOX on human colon cancer cell lines HT29. The characterization of the NPs showed good properties of the material. The drug release experiments showed that the DOX release is dependent on temperature and the type of the medium where in culture medium (CM) the release ocured around 41 °C with a cumulative DOX release of about 35 %. The cytotoxicity results showed that the core/shell NPs display a close toxicity effect towards the HT29 cells compared to one of the free DOX which could be due to the low diffusion of the NPs into the cancer cells.

## 2. MATERIALS AND METHODS

### 2.1. Materials

Chemical reagents were purchased from Sigma-Aldrich. Di(ethylene glycol) methyl ether methacrylate (MEO$_2$MA), 95% (447927-100ML ALDRICH), Poly(ethylene glycol) methyl ether methacrylate (HOEGMA), average Mn of 300 g/mol, contains 100 ppm MEHQ as inhibitor, 300 ppm BHT as inhibitor (447935-100ML ALDRICH). Phosphate buffered saline (PBS), P4417-100TAB SIGMA. Doxorubicin (DOX) 2 mg/mL (TEVA 15B25NE).

### 2.2. Synthesis process

The synthesis of the MNPs, the grafting of the silane (Fe$_3$O$_4$@Ph-Cl) and the growth of the copolymer (Fe$_3$O$_4$@P(MEO$_2$MA$_X$-OEGMA$_{100-X}$)) from the surface of the NPs were performed by surface initiated copolymerization following the method described in the second chapter.

### 2.3. Drug release

The DOX was incorporated in Fe$_3$O$_4$@P(MEO$_2$MA$_X$-OEGMA$_{100-X}$) NPs by mixing 2.5 mg/mL of the NPs with 5 ml of 1 mg/mL of DOX solutions. The suspension was left under stirring for 24 h at room temperature. Afterwards the NPs were separated by a magnet and washed several times until obtaining a clear solution. The washed NPs were re-dispersed in 5 mL of milli-Q water and physiological media (PBS) and the temperature was increased by 1 °C before each measurement. The NPs were separated again by a magnet and the supernatant was analyzed by UV-Vis spectroscopy.

### 2.4. Cytotoxicity

MTT (3- (4,5-dimethylthiazol-2-yl) -2,5 diphenyltetrazolium bromide) cytotoxicity test was used to analyze the cytotoxic effect of Fe$_3$O$_4$@P(MEO$_2$MA$_X$-OEGMA$_{100-X}$) NPs on human cancer cells (HT29 cells). The procedure was performed as described in chapter three.

## 2.5. Characterization Methods

Dynamic light scattering (DLS) was performed at room temperature using a Malvern zetasizer HsA instrument with a He-Ne laser (4 mW) emitting at 633 nm. The NPs aqueous solutions were filtered through Millipore membranes (Acrodisc® syringe filters 0.2 μm pore size). The data were analyzed by the ImageJ software program (ImageJ 1.45s/ imagej.nih.gov/ij) to obtain the hydrodynamic diameter and the particle size distribution in each aqueous dispersion of NPs.

Transmission electron microscopy (TEM) investigations were carried out using a JEM- ARM 200F Cold FEG TEM/STEM operating at 200 kV and equipped with a spherical aberration (Cs) probe corrector. For each sample, one drop of a dispersed solution (for each step of the synthesis process) was deposited on holey carbon grids. Electron Microscopy Characterization: For each sample, one drop of a dispersed solution (for each step of the synthesis) was deposited on holey carbon grids and imaged by transmission electron microscopy (TEM). The Microscope used is an ARM 200F.

The magnetic properties of the MNPs were studied using a Vibrating Sample Magnetometer (VSM). The VSM device allows the determination of the magnetic moments (field vs. magnetization H-M) with a resolution of $10^{-6}$ emu under a ramping magnetic field (0 to 2.5 Tesla) and for temperatures varying from 298 K to 600 K.

For the TGA measurements, a SETSYS Supersonic thermobalance (SETARAM) was used. The furnace is made up of a graphite element operating from room temperature up to 1600 °C. The apparatus is controlled by Calisto software. Dry samples of 30 mg were put in an alumina crucible with a volume of 30 μL. The samples were heated from room temperature to 600 °C at a heating rate of 5 °C/min under argon atmosphere.

The crystallographic structure of VN thin films was identified by X-Ray Diffraction (XRD) investigations using a Philips PW3710 diffractometer with Cu Kα radiation.

Absorption spectra are recorded on a Thermo Scientific Evolution 220 UV-visible spectrophotometer. The wavelength scan covered the range from 700 up to 200 nm.

# 3. RESULTS AND DISCUSSION

## 3.1. Chemical characterization

FTIR spectra of bare, silanized and co-polymer modified $Fe_3O_4$ NPs are displayed in **Figure 4.3.1**. The signal corresponding to the Fe-O bonds was observed in the domain 520-570 cm$^{-1}$ for the three samples of NPs. The signals in the spectrum of $Fe_3O_4$ (**Figure 4.3.1**.black line) between 1330 and 1630 cm$^{-1}$ correspond to the symmetric and anti-symmetric stretching of COO$^-$ due to the presence of citrate ions at the surface of $Fe_3O_4$ NPs. For the $Fe_3O_4@Ph$-Cl NPs, the signal at 1051 cm$^{-1}$ is assigned to the Fe–O–Si stretching vibrations. The bands at 1200-1400 cm$^{-1}$ are attributed to the C-C stretching in the silane structure. Bands located at 2987 and 2900 cm$^{-1}$ are respectively due to symmetric and asymmetric C–H stretching vibrations of its $CH_2$ groups.
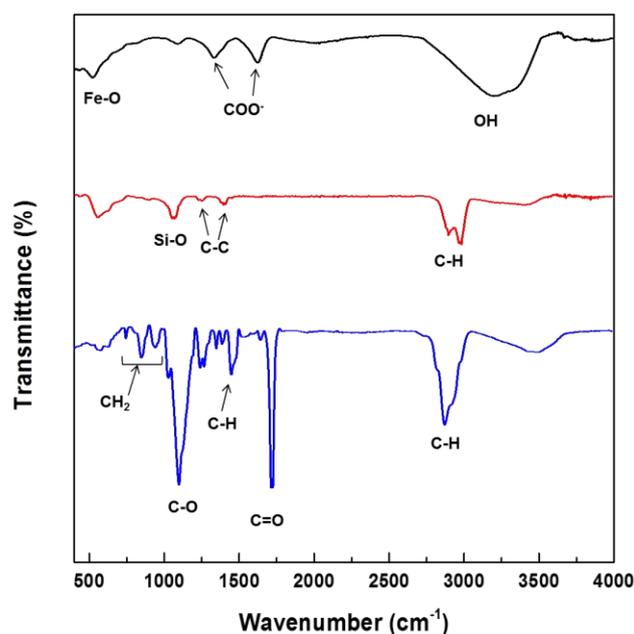


**Figure 4.3.1 FTIR spectra of $Fe_3O_4$ (black), $Fe_3O_4@Ph$-Cl (red) and $Fe_3O_4@$co-polymer (blue) NPs.**

In the spectrum of the polymer coated $Fe_3O_4$ NPs, the main peaks of the different groups in the copolymer structure indicated the successful grafting of the polymer chains from the $Fe_3O_4@Ph$-Cl NPs. Ester signals located at 1102 and 1723 cm$^{-1}$ are assigned to the C-O and C=O stretching vibrations, respectively. The peaks, situated between 748 and 945 cm$^{-1}$, are assigned to the $CH_2$ group of the methacrylate part of the polymer. In addition, the peaks located at 2875 and 1452 cm$^{-1}$ correspond to the C-H stretch and bending in the PEG part, respectively.

## 3.2. Microstructural characterization of the NPs

TEM and XRD analysis were performed to detemine the morphology of the core/shell NPs before and after coating with the polymer. **Figure 4.3.2c** shows the XRD patterns of bare $Fe_3O_4$ and $Fe_3O_4$ NPs modified with Ph-Cl and coated with $MEO_2MA$-OEGMA copolymers. The diffraction pattern of $Fe_3O_4$ NPs well corresponds to the standard pattern of magnetite $Fe_3O_4$ NPs. The characteristic diffraction peaks at $2\theta = 30.10°$, $35.60°$, $43.14°$, $53.49°$, $57.11°$ and $62.88°$ have been found to correspond perfectly to the characteristic diffractions of (220), (311), (400), (422), (511) and (440) planes of $Fe_3O_4$ NPs, respectively, which are well indexed to the inverse cubic spinel structure of $Fe_3O_4$ (JCPDS No 00-019-0629). Characteristic diffraction peaks for $Fe_3O_4$@Ph-Cl and $Fe_3O_4$ NPs coated with $MEO_2MA$-OEGMA copolymers matched these of bare $Fe_3O_4$. This highlighted that the modification of the $Fe_3O_4$ NPs did not affect their crystal phase. The average crystallite size D, obtained from the Sherrer equation $D = K\lambda/(\beta \cos \theta)$, where K is the constant, $\lambda$ is the X-ray wavelength (CuK$\alpha$), and $\beta$ is the full width at half maximum of the peak at $2\theta = 35.60°$, was calculated to be 11.3, 10.6 and 10.9 nm for $Fe_3O_4$, $Fe_3O_4$@Ph-Cl and polymeric $Fe_3O_4$ NPs, respectively.
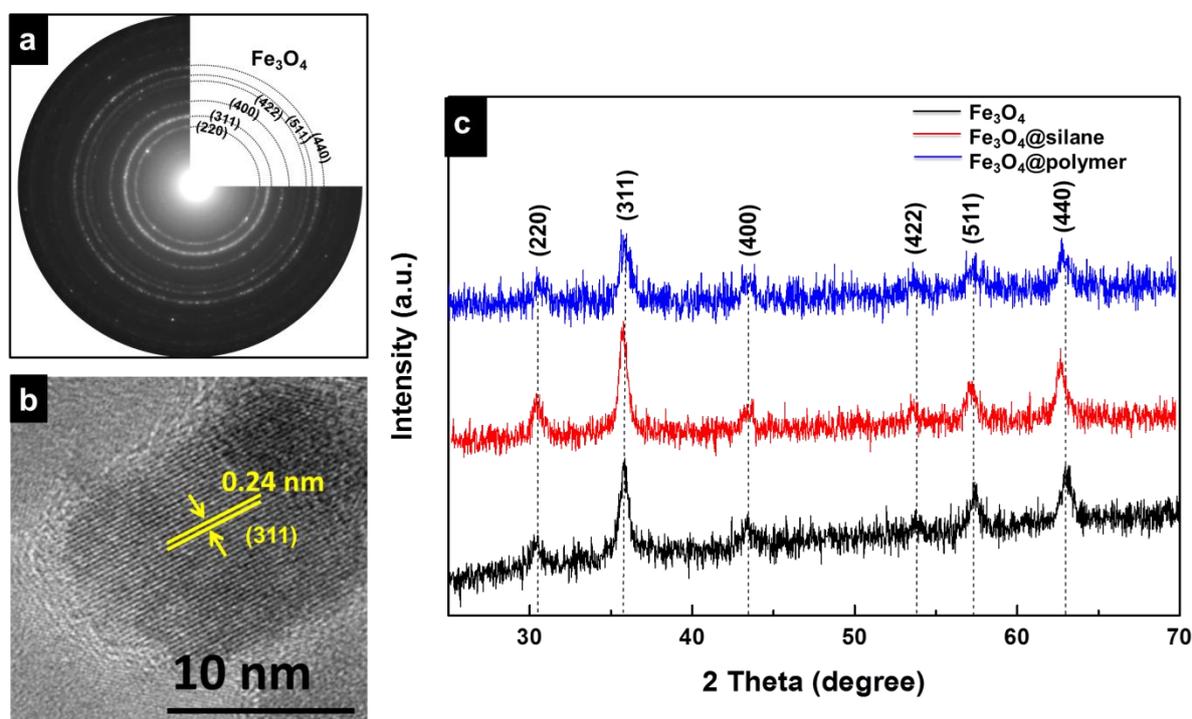


**Figure 4.3.2 a) Selected area electron diffraction pattern of the silanized $Fe_3O_4$, b) HR-TEM micrograph of copolymer coated $Fe_3O_4$ and c) XRD spectra of $Fe_3O_4$ derivatives.**

The TEM images show that the NPs were predominantly spherical with narrow size distribution (**Figure 4.3.3**). The size and size distribution of the NPs were calculated from the obtained images using Imagej software from at least 100 particles. The average size of the $Fe_3O_4$@Ph-Cl and $Fe_3O_4$@co-polymer was 10.6 nm which is in accordance with the result of XRD analysis. The NPs showed good crystallinity. A high magnification image confirmed the high crystallinity of the NPs with the interplanar spacing of 0.24 nm (**Figure 4.3.2b**) while the ring electron diffraction pattern indicating the planes of $Fe_3O_4$ NPs (**Figure 4.3.2a**).
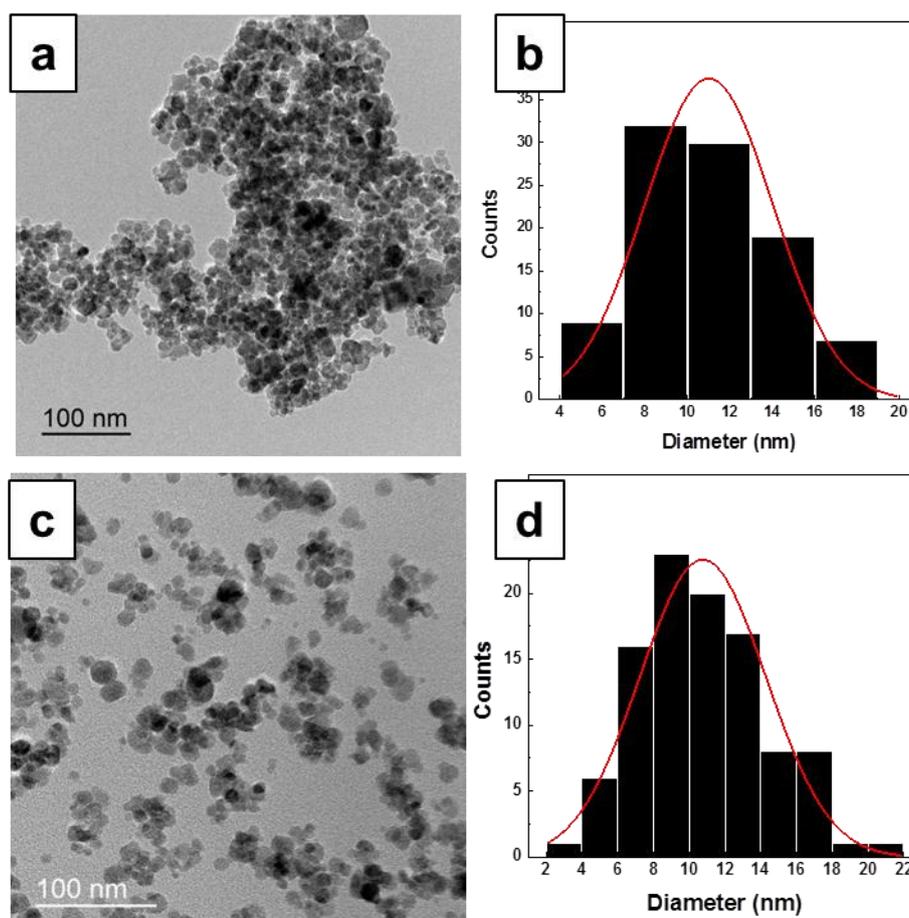


**Figure 4.3.3 Bright fieldTEM micrographs of a) $Fe_3O_4$@Ph-Cl NPs with their corresponding b) size distribution and c) $Fe_3O_4$@P(MEO$_2$MA$_X$-OEGMA$_{100-X}$) NPs with d) their normal size distribution.**

## 3.3. Amount of grafted co-polymer

The TGA analysis was used to estimate the amount of $MEO_2MA$-OEGMA co-polymer on the surface of $Fe_3O_4$ NPs. The weight loss (TG, %) was recorded as a function of the temperature at a rate of 5 °C/min from room temperature up to 500 °C.
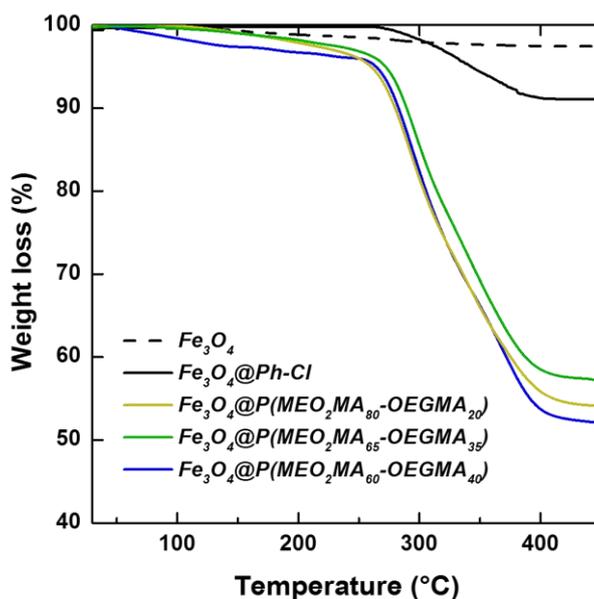
**Figure 4.3.4 TGA thermograms of Fe$_3$O$_4$ derivatives.**

**Figure 4.3.4** shows the weight loss in the Fe$_3$O$_4$ derivatives. Bare Fe$_3$O$_4$ did not show a significant weight loss in the whole temperature range. The weight loss in the Fe$_3$O$_4$@Ph-Cl was found to be about 8.7 % while for the Fe$_3$O$_4$ NPs modified with MEO$_2$MA-OEGMA co-polymers, the weight loss increased to about 45 % for all the samples. This weight loss took place between 250 and 450 °C is attributed to the weight loss of the organic groups at the surface of Fe$_3$O$_4$ NPs. Subtracting the amount of the silane ligand from the total weight loss of the organic shell, the amount of the copolymer in the core/shell NPs could be estimated to be about 36 %.

## 3.4. Magnetic properties

The evolution of the magnetization of the Fe$_3$O$_4$ derivatives as a function of the magnetic field are illustrated in **Figures 4.3.5-6**. The NPs have showed superparamagnetic behavior at room temperature. The saturation magnetization (M$_s$) was found to be ≈ 80 emu/g for Fe$_3$O$_4$ NPs. For the Fe$_3$O$_4$ derivatives, the M$_s$ was found to be ≈ 70 emu/g for the silanized Fe$_3$O$_4$, 0.09 emu/g for the compositions P(MEO$_2$MA$_{80}$-OEGMA$_{20}$) and P(MEO$_2$MA$_{75}$-OEGMA$_{25}$) and 0.03 emu/g for P(MEO$_2$MA$_{65}$-OEGMA$_{35}$) and P(MEO$_2$MA$_{60}$-OEGMA$_{40}$). This value is lower than that of the bulk Fe$_3$O$_4$ NPs.
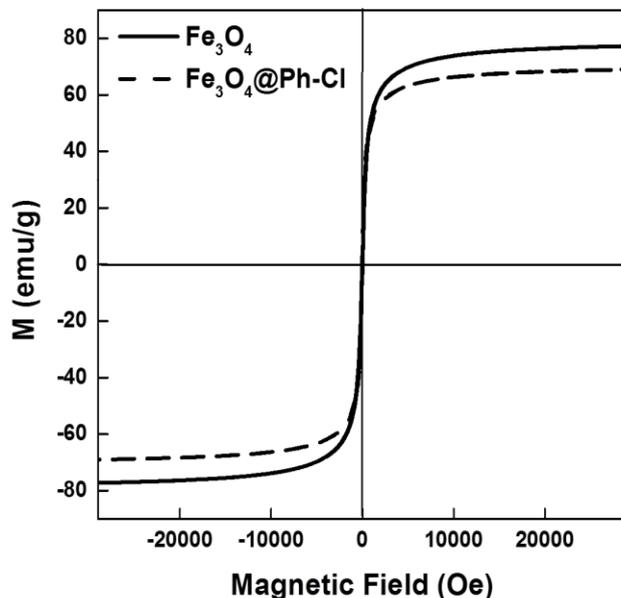
**Figure 4.3.5 Magnetization curves of Fe$_3$O$_4$ and Fe$_3$O$_4$@Ph-Cl NPs showing their superparamagnetic character.**

The presence of the organic material at the surface of the Fe$_3$O$_4$ NPs is suggested to be responsible for the decrease in the M$_s$ [33]. Indeed, the difference in the M$_s$ for the different compositions might be due to the higher density of the polymer shell. This high density is due to the increase in the quantity of the OEGMA units (lower M$_s$ for the compositions P(MEO$_2$MA$_{65}$-OEGMA$_{35}$) and P(MEO$_2$MA$_{60}$-OEGMA$_{40}$)) (**Figure 4.3.6**).
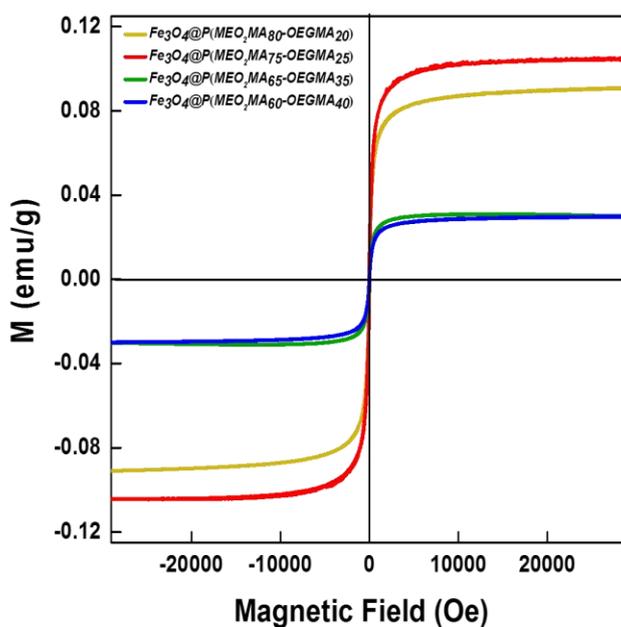


**Figure 4.3.6 Magnetization curves of Fe$_3$O$_4$ derivatives.**

The magnetic behavior of the $Fe_3O_4$ derivatives was also studied with increased temperature. As the NPs show a thermo-responsive property, it was necessary to study the effect of temperature on the magnetization of the MNPs. As shown in **Figure 4.3.7** for $Fe_3O_4@P(MEO_2MA_{60}\text{-}OEGMA_{40})$ NPs, the temperature didn"t affect the magnetic properties of the NPs when increased from 298 to 318 K (25 to 45 °C) considering the LCST range of the samples.
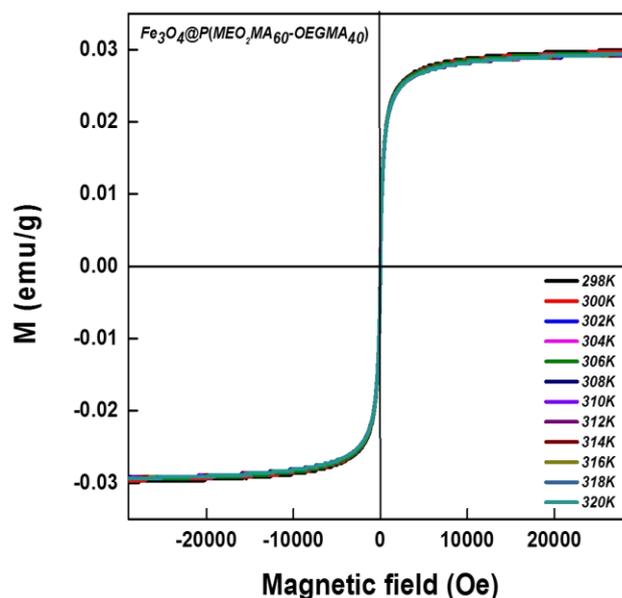


**Figure 4.3.7 The magnetic behavior of $Fe_3O_4@P(MEO_2MA_{60}\text{-}OEGMA_{40})$ NPs with increased temperature.**

## 3.5. Thermo-responsive behavior of the core/shell NPs

The DLS analysis were performed to determine the thermal transition of the $Fe_3O_4@P(MEO_2MA_X\text{-}OEGMA_{100-X})$ NPs in aqueous dispersion. The experiments were conducted in both water and CM considering that the nature of the medium affects the properties of the polymer shell at the surface of the $Fe_3O_4$ NPs.
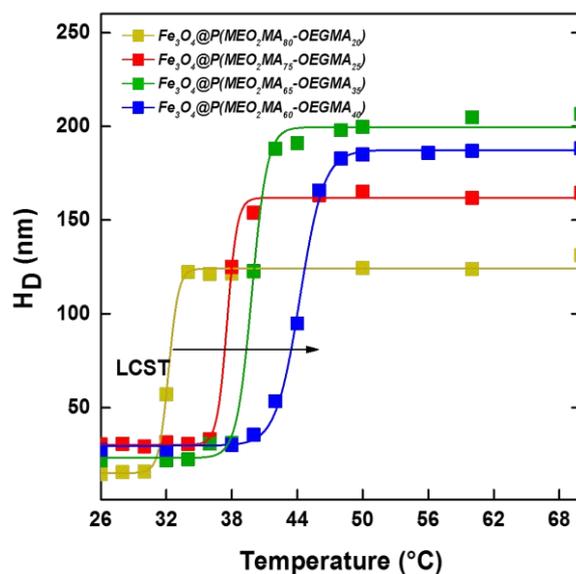
**Figure 4.3.8 Evolution of the diameter of Fe₃O₄ derivatives with temperature.**

The core/shell NPs were well dispersed in water and then the evolution of the hydrodynamic diameter was recorded throughout a temperature range of 20 to 70 °C (**Figure 4.3.8**). At the low temperatures, the solvated NPs show no change in their diameter and at a certain temperature it started an abruptly increase reaching a steady state where no significant change is seen. This confirms that the core/shell NPs undergo a thermal transition as indicated by the increase of the hydrodynamic diameter which indicates that the NPs that are merged together at a temperature which is referred to the LCST.
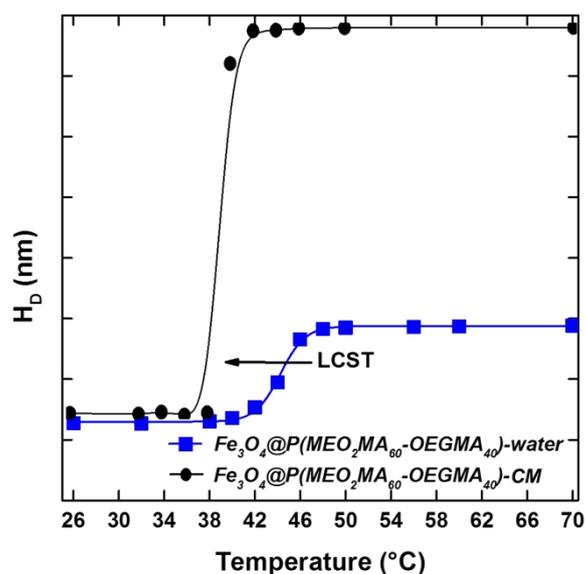


**Figure 4.3.9 Evolution of Fe₃O₄@P(MEO₂MA₆₀-OEGMA₄₀) diameter with temperature showing the decrease in the LCST in CM.**

177

Above the LCST, the organization of the NPs in aqueous media changes from dispersions to agglomerations (**Figure 4.3.10**). This process is expressed by the gradual increase in the hydrodynamic diameter where at this point the surface of the NPs become hydrophobic, which force the NPs to agglomerate. The same behavior for all the core/shell NPs was is seen in **Figure 4.3.8** with a change in the value of the LCST depending on the content of the OEGMA. The estimated LCSTs of the $Fe_3O_4@P(MEO_2MA_X\text{-}OEGMA_{100\text{-}X})$ NPs are listed in **Table 4.3.1**.

**Table 4.3.1 Estimated LCST of the core/shell NPs in water and CM.**

| Core/shell NPs | LCST in water (°C) | LCST in CM (°C) |
|---|---|---|
| $Fe_3O_4@P(MEO_2MA_{80}\text{-}OEGMA_{20})$ | 32 | 30 |
| $Fe_3O_4@P(MEO_2MA_{75}\text{-}OEGMA_{25})$ | 38 | 36 |
| $Fe_3O_4@P(MEO_2MA_{65}\text{-}OEGMA_{35})$ | 40 | 38 |
| $Fe_3O_4@P(MEO_2MA_{60}\text{-}OEGMA_{40})$ | 44 | 40 |

In **Table 4.3.1**, we can see the difference in the LCST between water and CM. The LCSTs in CM are shifted to lower values due to the salt effect (**Table 4.3.1**). **Figure 4.3.9** shows a shift in the LCST of $Fe_3O_4@P(MEO_2MA_{60}\text{-}OEGMA_{40})$ from 44 °C in water to 40 °C in CM with more significant aggregation. This can be seen for the higher increase of the hydrodynamic diameter. The NPs aggregation is clearly seen in **Figure 4.3.10**. Below the LCST, the NPs are well dispersed in water (**Figure 4.3.10a**) whereas when the same solution is heated above the LCST, the NPs started to aggregate and the solution is much more blurry as illustrated in **Figure 4.3.10b**.
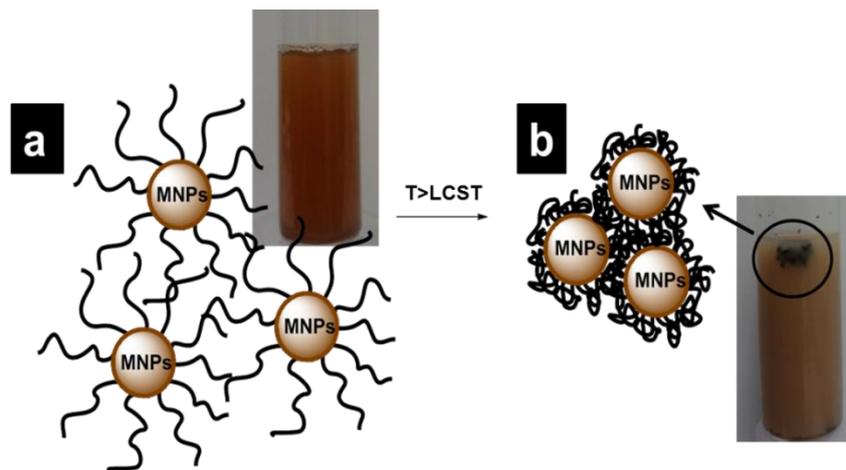
**Figure 4.3.10 The organization of the NPs in aqueous media from dispersions (a) to agglomerations (b).**

**Figure 4.3.11** shows a complete reversible behavior of the core/shell NPs. At room temperature, which is below LCST for $Fe_3O_4$@P($MEO_2MA_{60}$-$OEGMA_{40}$) NPs, the polymer shell is hydrophilic and the NPs are well dispersed in CM. At 50 °C (Above LCST which is 40 °C for these NPs), the shell becomes hydrophobic and therefore aggregates leading to the increase of the hydrodynamic diameter. In the opposite sense, the co-polymer shell is rehydrated during the cooling process which allows the re-dispersion of the NPs.
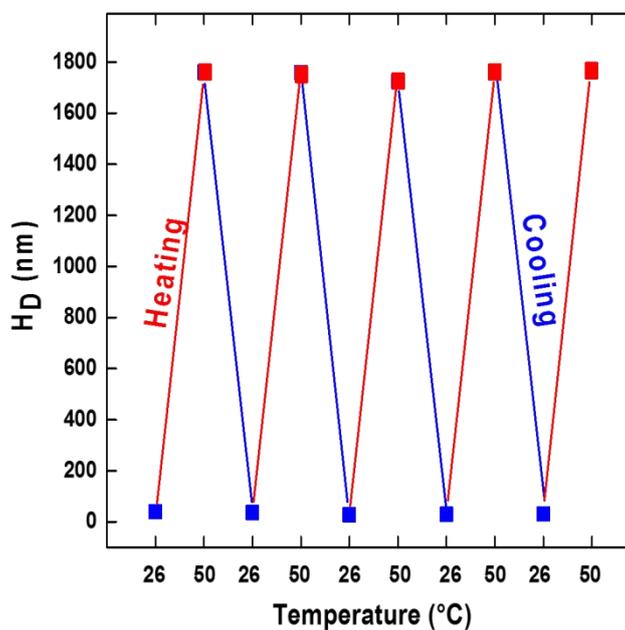


**Figure 4.3.11 Reversibility of $Fe_3O_4$@P($MEO_2MA_{60}$-$OEGMA_{40}$) NPs in CM with successive heating and cooling cycles.**

## 3.6.  Drug release from $Fe_3O_4@P(MEO_2MA_X\text{-}OEGMA_{100\text{-}X})$ NPs

The efficiency of the core/shell NPs for drug encapsulation and release was tested with DOX. DOX was loaded inside the NPs through electrostatic forces with the polymer chains and released by using a heat stimulus. As illustrated in **Figure 4.3.12**, increasing the temperature above the LCST, the polymer chains shrinks and DOX molecules are released into the medium containing the NPs. This release is expected to become more significant when the temperature is increased further.
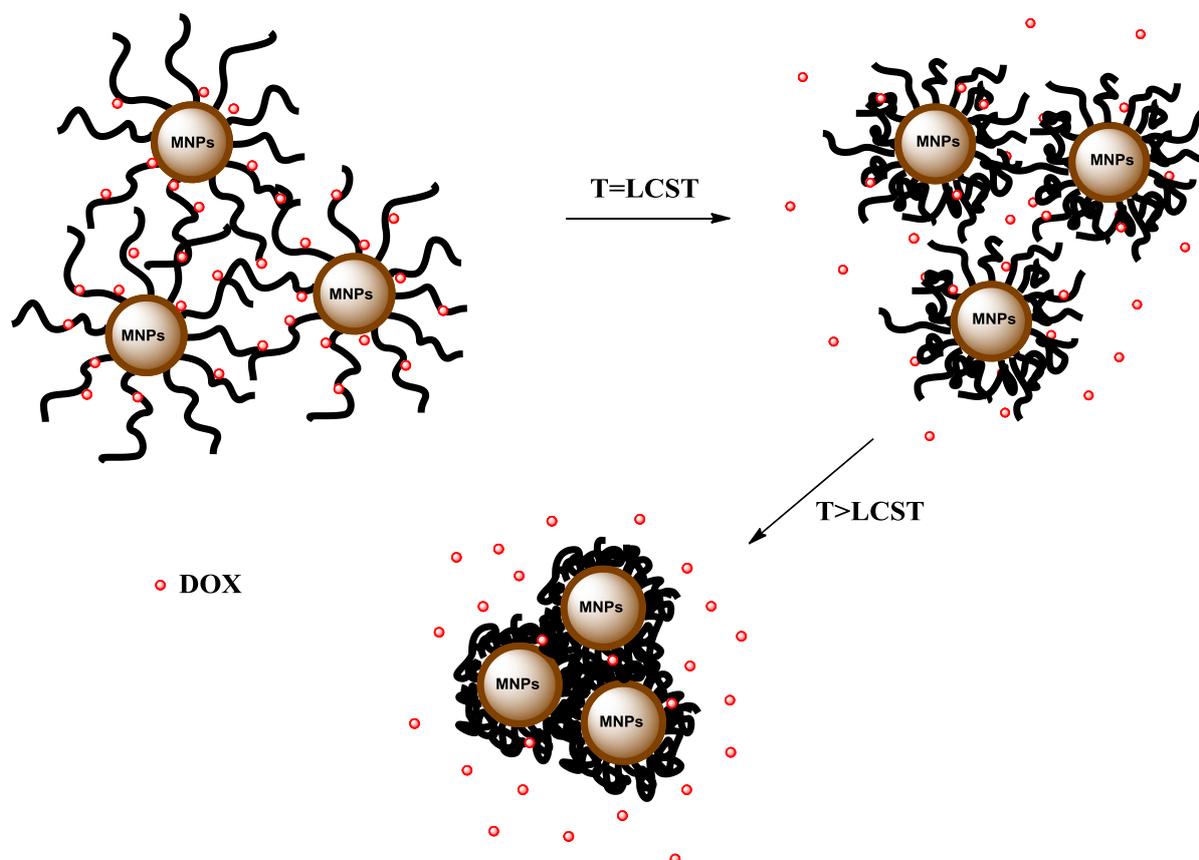


**Figure 4.3.12 Diffusion of the DOX molecules from the core/shell NPs with increasing the temperature above LCST.**

### 3.6.1.  DOX release

DOX was encapsulated in the $Fe_3O_4@P(MEO_2MA_{60}\text{-}OEGMA_{40})$ NPs acting as nanocarriers which controlled drug delivery by the variation of temperature. The NPs were soaked in the DOX solution and thus the DOX was stabilized and bounded to the polymeric shell by non-covalent interactions. In turn, at low temperature (below the LCST) the polymer chains are soluble in water due to the extensive hydrogen bonding interaction with the water molecules. Increasing the temperature principally above the LCST, these interactions are disrupted and

the polymer chains shrink leading to the release of the DOX. This release is expected to become more significant when the temperature is increased further. **Figure 4.3.13** shows the cumulative release of DOX loaded in $Fe_3O_4@P(MEO_2MA_{60}\text{-}OEGMA_{40})$ NPs referenced as $Fe_3O_4@P(MEO_2MA_{60}\text{-}OEGMA_{40})$-DOX in water. The drug release profile of $Fe_3O_4@P(MEO_2MA_{60}\text{-}OEGMA_{40})$-DOX shows an evolution around 42 to 43 °C in water. At these temperatures, the hydrogen bonds between the polymer chains and water begin to weaken favoring intra- and intermolecular hydrogen bonding between polymer molecules. At this point, the electrostatic interactions between the DOX and the polymer chains begin to break and the DOX is dissociated from the binding site. The DOX release increased gradually with the temperature reaching 48 % at 50 °C. As the temperature increases, more DOX is released due to major breaking of the non-covalent hydrophobic-hydrophobic interactions.
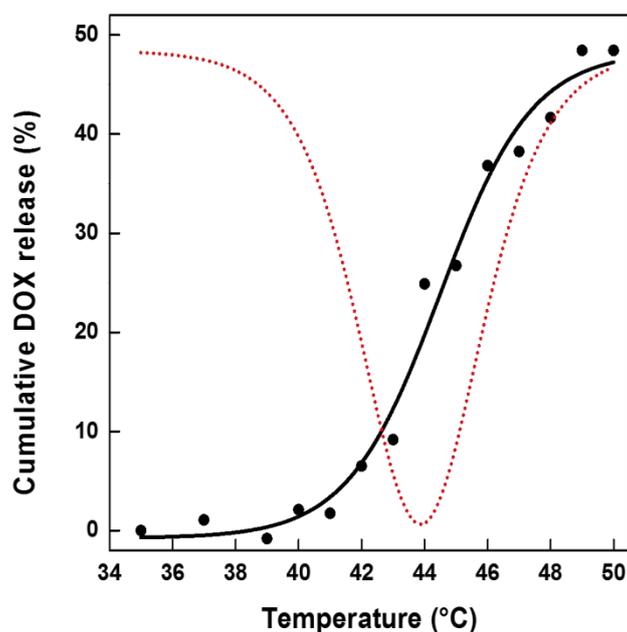


**Figure 4.3.13 Cumulative DOX release profile of $Fe_3O_4@P(MEO_2MA_{60}\text{-}OEGMA_{40})$-DOX dispersed in water.**

The DOX release from $Fe_3O_4@P(MEO_2MA_{60}\text{-}OEGMA_{40})$ NPs was also studied in CM. The release profile is displayed in **Figure 4.3.14**. The evolution in the DOX release started at 40 °C. As previously discussed, the salt effect is responsible for the earlier dissociation of the electrostatic interactions in CM than water. Above 40°C, the DOX release increase gradually with the temperature evidencing the thermoresponsive character of the magnetic nanocarriers. Therefore, we can conclude that these magnetic core/shell NPs have potential for use as drug delivery systems.
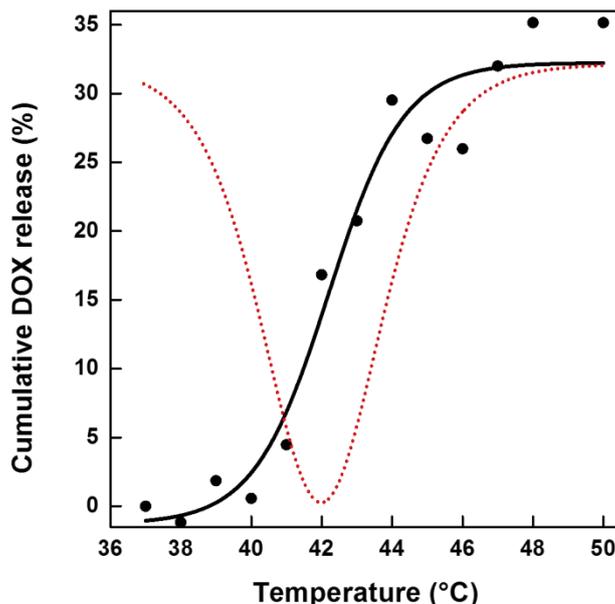
**Figure 4.3.14 Cumulative DOX release profile of Fe₃O₄@P(MEO₂MA₆₀-OEGMA₄₀)-DOX dispersed in CM.**

On the other hand, the cumulative DOX release in both media did not exceed 50 % because the release from the core/shell NPs was studied for a short time range (only 30 min). Actually, in the usual studies of the drug release in aqueous media several hours are necessary. It will be then necessary to perform new experiments to optimize the time and other parameters like the pH. It is well established that the pH at the tumor cells is lower than in normal tissues. It therefore necessitates studying the release as function of both temperature and pH. Recently, a study conducted by Hervault *et al.* [19] have reported a maximal release of DOX from thermo-responsive nanocarriers at pH=5.7 than at pH of 7.4 at the same temperature.

### 3.6.2. In vitro cytotoxicity study

MTT cytotoxicity assay was used to evaluate the cytotoxic effect of Fe₃O₄@P(MEO₂MA$_X$-OEGMA$_{100-X}$) NPs on human cancer cells HT29 by following the same procedure detailed above in chapter three.

The magnetic core/shell NPs have limited cytotoxicity up to 25 µg/mL but the effect of the shell properties on the cell viability was not very clear because the devolution in the cell viability was not dependent on the molecular composition of the polymer shell. Above 6.3 µg/mL, Fe₃O₄@P(MEO₂MA₇₅-OEGMA₂₅) NPs have been shown to cause the major decrease in the cell viability (60 % at 100 µg/mL) after 24 h (**Figure 4.3.15**). For the other samples, the cell viability was higher than 70 % up to 100 µg/mL. After 72 h, the cytotoxicity profiles of

the core/shell NPs show that these NPs are still biocompatible up to 12.5 µg/mL. Above this value, the cell viability has shown a little more decrease to 50 % than after 24 h. The dose-dependent cytotoxicity of the magnetic NPs could be explained by the higher concentration of the metal ions as the leaching of free metal ions from the core/shell NPs could cause toxicity towards the cells [34]. However, these NPs still exhibit a favorable biocompatibility which makes them useful for biomedical applications. Moreover, $Fe_3O_4$ NPs exhibited lower cytotoxic profile compared to ZnO NPs due to the fact that high proliferating cancer cells have a higher requirement for iron than normal cells. The altered iron metabolism in cancer cells is reflected by higher numbers of Transferrin receptors (TfR) on their cell surface These TfR mediate a high rate of iron uptake [35].
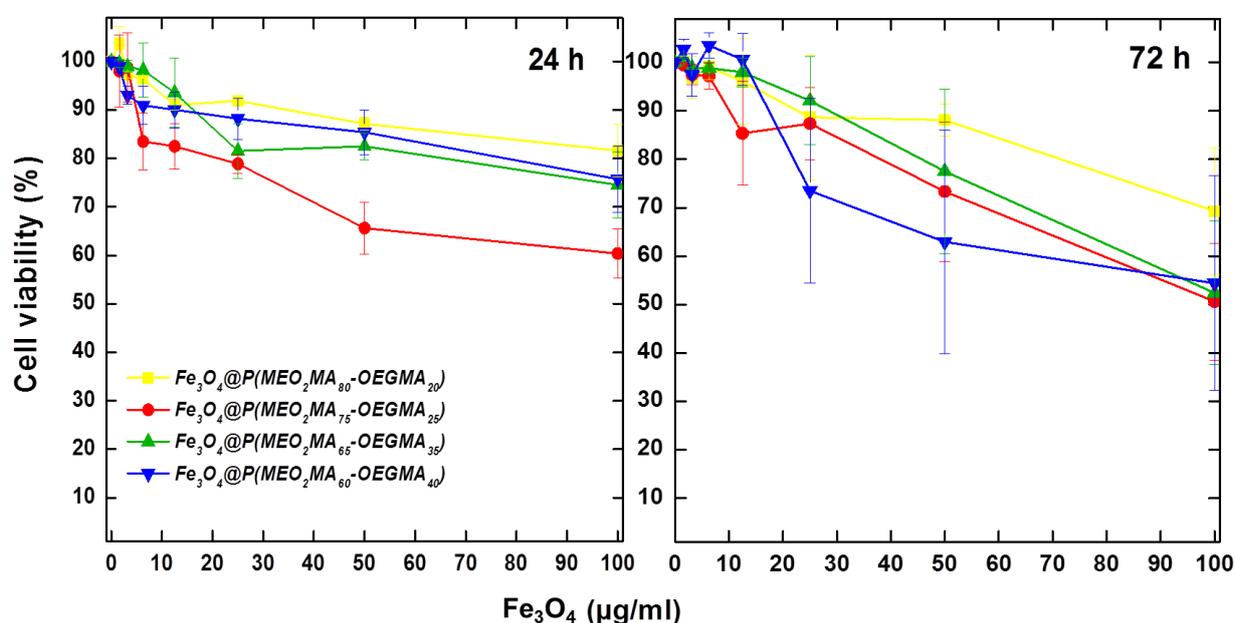


**Figure 4.3.15 Viability of HT29 cells after 24 and 72 h of exposure to $Fe_3O_4$@P(MEO$_2$MA$_X$-OEGMA$_{100-X}$) NPs.**

Similarly to ZnO NPs, the toxicity of $Fe_3O_4$@P(MEO$_2$MA$_{60}$-OEGMA$_{40}$)-DOX in HT29 cells was determined at 37 and 41 °C. At 20 µg/mL DOX concentration, highest cytotoxicity was observed at 41 °C (**Figure 4.3.16**). However, the cytotoxicity obtained with DOX alone showed that the temperature itself is responsible for the reduction in the cell viability along with the effect of DOX (**Figure 4.3.17**).
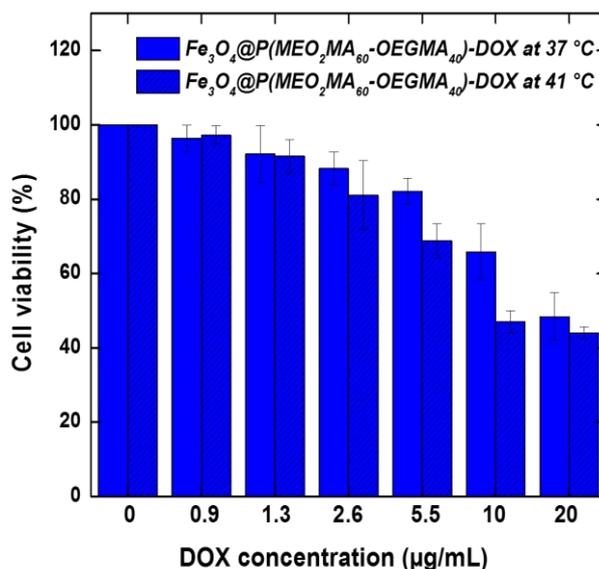
**Figure 4.3.16 Viability of HT29 cells after 5 h of exposure to Fe$_3$O$_4$@P(MEO$_2$MA$_{60}$-OEGMA$_{40}$)-DOX at 37 and 41 °C.**
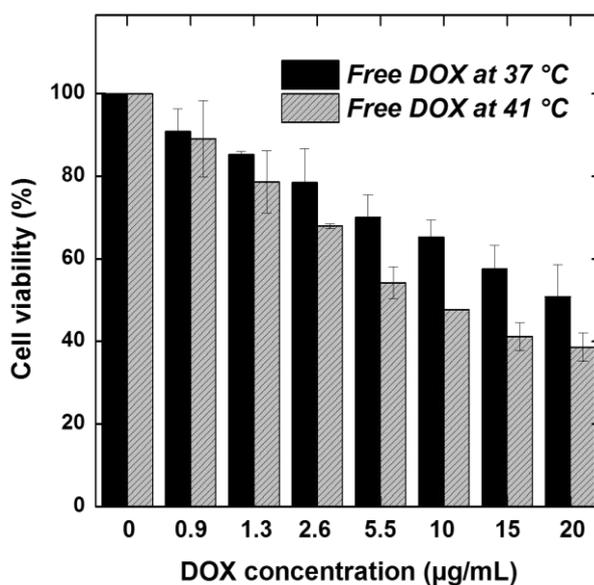


**Figure 4.3.17 Viability of HT29 cells after 5 h of exposure to free DOX at 37 and 41 °C.**

As compared with free DOX, Fe$_3$O$_4$@P(MEO$_2$MA$_{60}$-OEGMA$_{40}$)-DOX presented similar cytotoxic profile although slightly higher for free DOX at lower DOX concentrations (**Figure 4.3.18**) which demonstrates the efficiency of the magnetic core/shell NPs as nanocarriers for the DOX, where the encapsulation of the DOX in the NPs helps to reduce the side effects of this drug on healthy tissues.
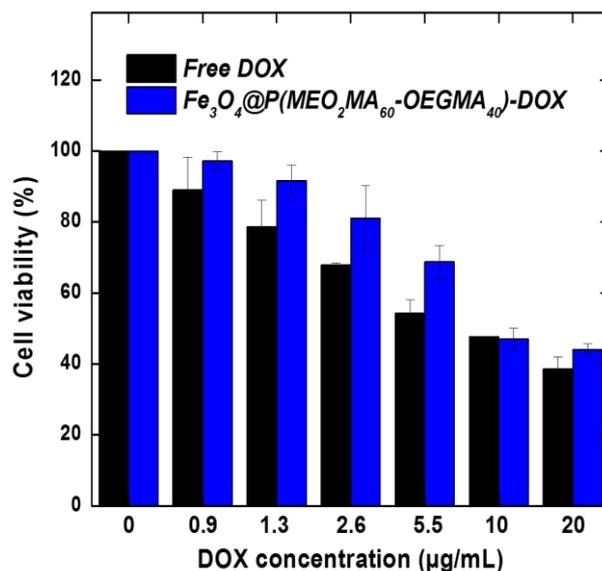
**Figure 4.3.18 Viability of HT29 cells after 5 h of exposure to free DOX and Fe$_3$O$_4$@P(MEO$_2$MA$_{60}$-OEGMA$_{40}$)-DOX at 41 °C.**

Comparing the results of the DOX loaded magnetic NPs with ZnO NPs, ZnO@P(MEO$_2$MA$_{60}$-OEGMA$_{40}$)-DOX NPs provided higher toxicity at 41 °C than free DOX which was almost zero for ZnO@P(MEO$_2$MA$_{60}$-OEGMA$_{40}$)-DOX and about 40 % for free DOX at DOX concentration of 20 µg/mL. Whereas, Fe$_3$O$_4$@P(MEO$_2$MA$_{60}$-OEGMA$_{40}$)-DOX presented similar cytotoxic profile of free DOX at 20 µg/mL, *i.e.* ≈ 40 % which could be explained by the very low toxicity of Fe$^{2+}$ cations released from these NPs compared to the initial toxicity of ZnO NPs.

# 4. CONCLUSION

In summary, superparamagnetic thermo-responsive core/shell NPs were synthesized for drug delivery applications. These NPs combine the features of controlled drug delivery and biocompatibility. The core/shell NPs are able to encapsulate anticancer drugs in their polymer shell and, then, release them by applying an external magnetic field or any source of heat at the LCST where this temperature could be manipulated by changing the molar ratio in their copolymer structure. The drug release experiments showed a release at 44 °C in water and 42 °C in CM, but these are better performed by considering the pH parameter as the pH at the tumor sites is more acidic. Performing the MTT assays, magnetic core/shell NPs showed almost similar cytotoxic profile as free DOX which diminishes the toxicity of $Fe^{2+}$ cations released from these NPs. In this case, the encapsulation of DOX in these magnetic nanocarriers is very interesting for future in vivo experiments, because it can reduce the harmful side-effects of DOX (cardiotoxicity) by orienting the bio-distribution of drug at the tumor site as opposed to healthy tissues as ascribed to enhanced permeation and retention effect (EPR).

# REFERENCES

1.      Torre, L.A., Bray, F., Siegel, R.L., Ferlay, J., Lortet-Tieulent, J. and Jemal, A., *Global cancer statistics, 2012.* CA: A cancer journal for clinicians, 2015. **65**(2): p. 87-108.

2.      Santhosh, P.B., and Ulrih, N.P., *Multifunctional superparamagnetic iron oxide nanoparticles: promising tools in cancer theranostics.* Cancer letters, 2013. **336**(1): p. 8-17.

3.      Alvarez-Berríos, M.P., Sosa-Cintron, N., Rodriguez-Lugo, M., Juneja, R. and Vivero-Escoto, J.L., *Hybrid Nanomaterials Based on Iron Oxide Nanoparticles and Mesoporous Silica Nanoparticles: Overcoming Challenges in Current Cancer Treatments.* Journal of Chemistry, 2016. **2016**: p. 15.

4.      Kandasamy, G., and Maity, D., *Recent advances in superparamagnetic iron oxide nanoparticles (SPIONs) for in vitro and in vivo cancer nanotheranostics.* International journal of pharmaceutics, 2015. **496**(2): p. 191-218.

5.      Sailor, M.J., and Park, J. H., *Hybrid nanoparticles for detection and treatment of cancer.* Advanced Materials, 2012. **24**(28): p. 3779-3802.

6.      Cho, K., Wang, X.U., Nie, S. and Shin, D.M., *Therapeutic nanoparticles for drug delivery in cancer.* Clinical cancer research, 2008. **14**(5): p. 1310-1316.

7.      Vivero-Escoto, J.L., and Huang, Y. T., *Inorganic-organic hybrid nanomaterials for therapeutic and diagnostic imaging applications.* International Journal of Molecular Sciences, 2011. **12**(6): p. 3888-3927.

8.      Sun, H.W., Zhang, L.Y., Zhu, X.J. and Wang, X.F., *Magnetic poly (PEGMA–MAA) nanoparticles: photochemical preparation and potential application in drug delivery.* Journal of Biomaterials Science, Polymer Edition, 2009. **20**(12): p. 1675-1686.

9.      Plank, C., Schillinger, U., Scherer, F., Bergemann, C., Rémy, J.S., Krötz, F., Anton, M., Lausier, J. and Rosenecker, J., *The magnetofection method: using magnetic force to enhance gene delivery.* Biological chemistry, 2003. **384**(5): p. 737-747.

10.     Ghosh Chaudhuri, R., and Paria, S., *Core/shell nanoparticles: classes, properties, synthesis mechanisms, characterization, and applications.* Chemical reviews, 2011. **112**(4): p. 2373-2433.

11.     Huang, J., Shu, Q., Wang, L., Wu, H., Wang, A.Y. and Mao, H., *Layer-by-layer assembled milk protein coated magnetic nanoparticle enabled oral drug delivery with high stability in stomach and enzyme-responsive release in small intestine.* Biomaterials, 2015. **39**: p. 105-113.

12.     Prabha, G., and Raj, V., *Preparation and characterization of polymer nanocomposites coated magnetic nanoparticles for drug delivery applications.* Journal of magnetism and magnetic materials, 2016. **408**: p. 26-34.

13.     Umut, E., *Surface modification of nanoparticles used in biomedical applications.* Modern Surface Engineering Treatments, 2013: p. 185-208.

14.     J Wang, Y.X., Xuan, S., Port, M. and Idee, J.M., *Recent advances in superparamagnetic iron oxide nanoparticles for cellular imaging and targeted therapy research.* Current pharmaceutical design, 2013. **19**(37): p. 6575-6593.

15.     Zhang, J., and Misra, R.D.K., *Magnetic drug-targeting carrier encapsulated with thermosensitive smart polymer: core–shell nanoparticle carrier and drug release response.* Acta biomaterialia, 2007. **3**(6): p. 838-850.

16.     Zhang, J.L., Srivastava, R.S. and Misra, R.D.K., *Core– shell magnetite nanoparticles surface encapsulated with smart stimuli-responsive polymer: Synthesis, characterization, and LCST of viable drug-targeting delivery system.* Langmuir, 2007. **23**(11): p. 6342-6351.

17. Hayashi, K., Nakamura, M., Miki, H., Ozaki, S., Abe, M., Matsumoto, T., Sakamoto, W., Yogo, T. and Ishimura, K., *Magnetically responsive smart nanoparticles for cancer treatment with a combination of magnetic hyperthermia and remote-control drug release.* Theranostics, 2014. **4**(8): p. 834.

18. Stuart, M.A.C., Huck, W.T., Genzer, J., Müller, M., Ober, C., Stamm, M., Sukhorukov, G.B., Szleifer, I., Tsukruk, V.V., Urban, M. and Winnik, F., *Emerging applications of stimuli-responsive polymer materials.* Nature materials, 2010. **9**(2): p. 101-113.

19. Hervault, A., Dunn, A.E., Lim, M., Boyer, C., Mott, D., Maenosono, S. and Thanh, N.T., *Doxorubicin loaded dual pH-and thermo-responsive magnetic nanocarrier for combined magnetic hyperthermia and targeted controlled drug delivery applications.* Nanoscale, 2016. **8**: p. 12152-12161.

20. Chicheł, A., Skowronek, J., Kubaszewska, M. and Kanikowski, M., *Hyperthermia–description of a method and a review of clinical applications.* Reports of Practical Oncology & Radiotherapy, 2007. **12**(5): p. 267-275.

21. Rahimi, M., Wadajkar, A., Subramanian, K., Yousef, M., Cui, W., Hsieh, J.T. and Nguyen, K.T., *In vitro evaluation of novel polymer-coated magnetic nanoparticles for controlled drug delivery.* Nanomedicine: Nanotechnology, Biology and Medicine, 2010. **6**(5): p. 672-680.

22. Gao, X., Kucerka, N., Nieh, M.P., Katsaras, J., Zhu, S., Brash, J.L. and Sheardown, H., *Chain conformation of a new class of PEG-based thermoresponsive polymer brushes grafted on silicon as determined by neutron reflectometry.* Langmuir, 2009. **25**(17): p. 10271-10278.

23. Laloyaux, X., Fautré, E., Blin, T., Purohit, V., Leprince, J., Jouenne, T., Jonas, A.M. and Glinel, K., *Temperature-Responsive Polymer Brushes Switching from Bactericidal to Cell-Repellent.* Advanced Materials, 2010. **22**(44): p. 5024-5028.

24. Hu, Y., Darcos, V., Monge, S. and Li, S., *Thermo-responsive drug release from self-assembled micelles of brush-like PLA/PEG analogues block copolymers.* International journal of pharmaceutics, 2015. **491**(1): p. 152-161.

25. Rosen, J.E., Chan, L., Shieh, D.B. and Gu, F.X., *Iron oxide nanoparticles for targeted cancer imaging and diagnostics.* Nanomedicine: Nanotechnology, Biology and Medicine, 2012. **8**(3): p. 275-290.

26. Chen, T.J., Cheng, T.H., Hung, Y.C., Lin, K.T., Liu, G.C. and Wang, Y.M., *Targeted folic acid-PEG nanoparticles for noninvasive imaging of folate receptor by MRI.* Journal of Biomedical Materials Research Part A, 2008. **87**(1): p. 165-175.

27. Sun, C., Sze, R. and Zhang, M., *Folic acid-PEG conjugated superparamagnetic nanoparticles for targeted cellular uptake and detection by MRI.* Journal of Biomedical Materials Research Part A, 2006. **78**(3): p. 550-557.

28. Kaaki, K., Herv -Aubert, K., Chiper, M., Shkilnyy, A., Souc , M., Benoit, R., Paillard, A., Dubois, P., Saboungi, M.L. and Chourpa, I., *Magnetic nanocarriers of doxorubicin coated with poly (ethylene glycol) and folic acid: relation between coating structure, surface properties, colloidal stability, and cancer cell targeting.* Langmuir, 2011. **28**(2): p. 1496-1505.

29. Akbarzadeh, A., Mikaeili, H., Zarghami, N., Mohammad, R., Barkhordari, A. and Davaran, S., *Preparation and in vitro evaluation of doxorubicin-loaded $Fe_3O_4$ magnetic nanoparticles modified with biocompatible copolymers.* International journal of nanomedicine, 2012. **7**: p. 511-526.

30. Chen, Y., Ai, K., Liu, J., Sun, G., Yin, Q. and Lu, L., *Multifunctional envelope-type mesoporous silica nanoparticles for pH-responsive drug delivery and magnetic resonance imaging.* Biomaterials, 2015. **60**: p. 111-120.

31. Liang, P.C., Chen, Y.C., Chiang, C.F., Mo, L.R., Wei, S.Y., Hsieh, W.Y. and Lin, W.L., *Doxorubicin-modified magnetic nanoparticles as a drug delivery system for magnetic resonance imaging-monitoring magnet-enhancing tumor chemotherapy.* International journal of nanomedicine, 2016. **11**: p. 2021.

32. Dorniani, D., Hussein, M. Z. B., Kura, A. U., Fakurazi, S., Shaari, A. H., and Ahmad, Z., *Preparation of $Fe_3O_4$ magnetic nanoparticles coated with gallic acid for drug delivery.* International journal of nanomedicine, 2012. **7**: p. 5745-5756.

33. Nadeem, M., Ahmad, M., Akhtar, M.S., Shaari, A., Riaz, S., Naseem, S., Masood, M. and Saeed, M.A., *Magnetic Properties of Polyvinyl Alcohol and Doxorubicine Loaded Iron Oxide Nanoparticles for Anticancer Drug Delivery Applications.* PloS one, 2016. **11**(6): p. e0158084.

34. Chen, Y., Ai, K., Liu, J., Sun, G., Yin, Q. and Lu, L., *Multifunctional envelopetype mesoporous silica nanoparticles for pH-responsive drug delivery and magnetic resonance imaging.* Biomaterials, 2015. **60**: p. 111-120.

35. Kwok, J.C. and Richardson, D.R, *The iron metabolism of neoplastic cells: alterations that facilitate proliferation?.* Critical reviews in oncology/hematology, 2002. **42**(1): p. 65-78.

# GENERAL CONCLUSION & PERSPECTIVES

# CONCLUSION

In this thesis, we have synthesized inorganic/organic core/shell NPs by grafting polymer and a biocompatible thermo-responsive copolymer based on 2-(2-Methoxyethoxy) ethyl methacrylate (MEO$_2$MA) and oligo (ethylene glycol) methacrylate (OEGMA) from SiO$_2$, ZnO QDs and magnetic Fe$_3$O$_4$ NPs surfaces. The thermo-responsive polymers are characterized by a lower critical solution temperature (LCST) where below this temperature the polymer chains are hydrophilic, and above they are hydrophobic. The first objective of this work was to develop an efficient process to lead to core/shell nanostructures and then to develop a new responsive drug delivery systems which are able to carry anticancer drugs, deliver them to cancer cells and perform the release at the physiological temperature. To specifically address the objective, the study performed was focused on achieving the following points:

1. Designing aqueous dispersible and responsive ZnO@P(MEO$_2$MA$_X$-OEGMA$_{100-X}$) and Fe$_3$O$_4$@P(MEO$_2$MA$_X$-OEGMA$_{100-X}$) NPs while preserving the physical properties of the ZnO and Fe$_3$O$_4$ core.

2. Tuning the LCST above the temperature required for living cells in normal conditions, to target the cancer cells by tuning the composition of the MEO$_2$MA$_X$-OEGMA$_{100-X}$ monomers.

3. Achieving a drug release profile at the targeted temperature.

4. Evaluating the cytotoxicity of the core/shell NPs on the HT29 cell lines and comparing the efficiency of the core/shell NPs as drug DOX carriers compared to the free DOX.

The first point was achieved by coating SiO$_2$, ZnO and Fe$_3$O$_4$ surfaces with styrene and (MEO$_2$MA$_X$-OEGMA$_{100-X}$) copolymer. Atom Transfer Radical Polymerization with Activator ReGenerated by Electron Transfer (ARGET-ATRP) was used to prepare the coated ZnO and Fe$_3$O$_4$ NPs. As a first step, a silane ligand possessing a halogen end group was introduced to the inorganic surface and then the polymerization was conducted from the silane initiator by ARGET ATRP.

The ARGET ATRP process has been found to allow the growth of the polystyrene and P(MEO$_2$MA$_X$-OEGMA$_{100-X}$) copolymer from silanized SiO$_2$ and ZnO and Fe$_3$O$_4$ NPs. By performing TEM imaging, the core/shell NPs have shown a good dispersion in aqueous media

and were found to have a spherical shape with an average diameter of $100 \pm 8$ nm, $6 \pm 1$ nm and $10 \pm 1.5$ nm for the coated $SiO_2$, ZnO and $Fe_3O_4$ NPs, respectively. The respective hexagonal wurtzite and the inverse cubic crystalline structures of ZnO and $Fe_3O_4$ NPs were not altered by the silanization and the polymerization process as observed by the XRD experiments. The ZnO NPs have been shown to display temperature dependent optical properties. When the temperature was increased above the LCST, the polymer chains became hydrophobic and collapsed at the ZnO surface forcing the NPs to aggregate. This aggregation has led to a drastic decrease of the ZnO PL intensity. As an example, for the $ZnO@P(MEO_2MA_{80}-OEGMA_{20})$, the PL quantum yield was decreased from 11 % at 30 °C to 4.5 % at 40 °C. Meanwhile, the aggregation of the NPs resulting from the collapse of the copolymers chains at the surface of the $Fe_3O_4$ NPs had shown no influence on their magnetic properties. In addition, their superparamagnetic properties were maintained below and above the LCST. However, the influence of the copolymer composition as a function of the (100-X) values was clearly demonstrated. The compositions with higher percentage of the OEGMA units, *i.e* 35 and 40 %, had lower saturation magnetization ($M_s$) values compared to 20 and 25 %.

The targeted LCST (above 37 °C and below 42 °C) was achieved by playing with the composition of the $MEO_2MA_X-OEGMA_{100-X}$ copolymer. Different compositions were prepared and then the temperature dependence of the obtained NPs was monitored by DLS. DLS analysis was performed in water and culture media (CM) considering the change of the thermal behavior of the core/shell NPs with the change of the medium salts content. The studied compositions were the following: $MEO_2MA_{80}-OEGMA_{20}$, $MEO_2MA_{75}-OEGMA_{25}$, $MEO_2MA_{65}-OEGMA_{35}$ and $MEO_2MA_{60}-OEGMA_{40}$. These compositions were considered for both ZnO and $Fe_3O_4$ NPs. The change in the hydrodynamic diameter ($H_D$) of the core/shell NPs as a function of the temperature allowed to obtain the LCST of each composed NPs. Below the LCST, the $H_D$ was small corresponding to their dispersed size. As the temperature was increased, the $H_D$ was showing a gradual increase due to the aggregation of the NPs at the LCST. The LCST obtained for the lowest amount of OEGMA units have shown to shift towards higher temperatures with the increase of the incorporated OEGMA units, as presented in chapters 2-4 for the ZnO and $Fe_3O_4$ NPs in water and CM, which confirmed that the thermal properties of the core/shell NPs are completely driven by the macromolecular properties of the copolymer chains.

Copolymer coated $Fe_3O_4$ NPs were chosen to perform the drug release experiments because

these NPs were easily separated from the aqueous media by simply using a magnet. DOX was loaded inside the core/shell NPs and then released outside by heating the solution. The concentration of the DOX has been shown to increase with increasing the temperature and the significant release was clearly seen around the LCST. The coated $Fe_3O_4$ NPs with the composition $MEO_2MA_{60}$-$OEGMA_{40}$ have shown a cumulative increase around 44 °C in water which is the obtained LCST from DLS experiments. In CM, the significant release occurred at 42 °C which is 2 °C higher for the LCST obtained by DLS. The increase of the DOX release around the LCST has demonstrated that efficiency of these core/shell NPs in releasing DOX at controlled temperature which allowed to achieve the third point.

Finally, the MTT cytotoxicity assays were performed to evaluate the cytotoxicity effect of the ZnO and $Fe_3O_4$ core/shell NPs on the human cancer cells HT29 on one hand and of DOX loaded in the polymeric NPs compared to free DOX, on the other hand. The NPs with the compositions $MEO_2MA_{65}$-$OEGMA_{35}$ and $MEO_2MA_{60}$-$OEGMA_{40}$ were selected in this study as both compounds exhibit a LCST in CM of 38 and 40 °C, respectively. In general, the cytotoxicity tests have shown that ZnO and $Fe_3O_4$ NPs cytotoxicity depends on their concentration in CM (up to 12.5 and 20 μg/mL for ZnO and $Fe_3O_4$ core/shell NPs, respectively), where $Fe_3O_4$ NPs showed lower cytotoxicity compared to ZnO NPs which could be explained by the fact that high proliferating cancer cells have a higher requirement for iron than normal cells. The altered iron metabolism in cancer cells is reflected by higher numbers of Transferrin receptors (TfR) on their cell surface. These TfR mediate a high rate of iron uptake. For the DOX loaded in the NPS, at a concentration equal to 10 μg/mL DOX, these NPs have been shown to exhibit higher cytotoxicity (5 % cell viability with ZnO@P($MEO_2MA_{60}$-$OEGMA_{40}$) NPs) compared to free DOX (65 %) where for the DOX loaded in $Fe_3O_4$ NPs at the same concentration, their effect has been shown to be similar to that of free DOX ($\approx$ 65 %). These results suggest that the release of $Zn^{2+}$ from the ZnO NPs at the physiological pH could contribute to the increase in the toxicity effect of the DOX loaded ZnO NPs compared to the absence toxicity of $Fe^{2+}$ released from the magnetic NPs. So far, the development of these systems is essential to enhance their activity and therefore their release properties at controlled temperatures. For the cytotoxicity tests which were performed to evaluate the toxicity of the coated NPs containing the DOX before and after the LCST, the cell viability for HT29 cells has shown a decrease when increasing the temperature from 37 to 41 °C. When compared to free DOX, NPs cytotoxic effect was significantly more pronounced. As a result, more careful and detailed experiments have to be performed to well

understand the mechanism of the cellular uptake of the copolymer coated ZnO and $Fe_3O_4$ NPs.

## PERSPECTIVES

In the perspective to our study, we would propose:

1. A complete developed study of the behavior of ZnO and $Fe_3O_4$ NPs as drug nanocarriers where, for example, it would be very interesting to perform the cytotoxicity assay with the magnetic sample at x=60 (of LCST above 37°C) after applying an alternating magnetic field: in that case one can expect synergy between DOX release and local (nanoscale) heating, even in absence of a macroscopic raise of temperature.

2. The attachment of specific biomolecules to the synthesized core/shell NPs surface to enhance their cellular uptake and thus their antitumor action. These biomolecules are usually recognized by receptors expressed on the external membrane of the cancer cells. The binding of the biomolecules with the corresponding receptors increase the internalization of the core/shell NPs within the cancer. Various biomolecules could be used to functionalize the copolymer coated ZnO and $Fe_3O_4$ NPs including antibodies, proteins, peptides or small molecules like folic acid (FA).

3. The adoption of the same grafting process to synthesize different core/shell inorganic/organic NPs depending on the targeting application.

# TABLE OF FIGURES

# TABLE OF SCHEMES

# TABLE OF TABLES

# Synthesis and characterization of smart nanoparticles

## ABSTRACT

One of the major challenges in nanomedicine is to develop nanoparticulate systems able to serve as efficient diagnostic and/or therapeutic tools against sever diseases, such as infectious or neurodegenerative disorders. To enhance the detection and interpretation contrast agents were developed to increase the signal/noise ratio. Among them, Superparamagnetic Iron Oxide (SPIO) and Quantum Dots (QDs) nanoparticles (NPs) have received a great attention since their development as a liver contrasting agent 20 years ago for the SPIO [1, 2]. Furthermore, their properties, originating from the nanosized dimension and shape, allow different bio-distribution and opportunities beyond the conventional chemical imaging agents [3]. The opportunity to coat those biocompatible NPs by a polymer shell that can ensure a better stability of the materials in the body, enhance their bio-distribution and give them new functionalities. It has appeared then that they are very challenging for medicinal applications. In this work, we have developed new responsive SPIO and QDs based NPs that are able to carry the anticancer drug doxorubicin (DOX) and release it in physiological media and at the physiological temperature. Two families of NPs were synthesized, the first one consist in superparamagnetic $Fe_3O_4$ NPs that were functionalized by a biocompatible responsive copolymer based on 2-(2-methoxy) ethyl methacrylate ($MEO_2MA$), oligo (ethylene glycol) methacrylate (OEGMA) [4]. The second family consists in the ZnO NPs coated by the same copolymer [4, 5]. For the first time, $P(MEO_2MA_X\text{-}OEGMA_{100\text{-}X})$ was grown by *activator regenerated by electron transfer–atom radical polymerization* (ARGET-ATRP) from the NPs surfaces by surface-initiated polymerization [4]. The core/shell NPs were fully characterized by the combination of transmission electron microscopy (TEM), thermogravimetric analysis (TGA), and by the physical properties of the nanostructures studied. We demonstrate the efficiency of the ARGET-ATRP process to graft polymers and copolymers at the surface of $Fe_3O_4$ and ZnO NPs. The influence of the polymer chain configuration (which leads to the aggregation of the NPs above the collapse temperature of the copolymer (LCST)) was studied. We have demonstrated that the magnetic properties of the core/shell $Fe_3O_4$-based nanostructures were only influenced by the amount of the grafted polymer and no influence of the aggregation was evidenced [4]. This simple and fast developed process is efficient for the grafting of various co-polymers from any surfaces and the derived nanostructured materials display the combination of the physical properties of the core and the macromolecular

behavior of the shell. The drug release experiments confirmed that DOX was largely released above the co-polymer LCST. Moreover, the cytocompatibility test showed that those developed NPs do not display any cytotoxicity depending on their concentration in physiological media. From the results obtained, it can be concluded that the new nanomaterials developed can be considered for further use as multi-modal cancer therapy tools.

# Synthèse et caractérisation des nanoparticules intelligentes

## RESUME

L'un des enjeux majeurs en nanom de cine est de d velopper des systèmes capables à la fois de permettre un diagnostic efficace et également de servir plateforme thérapeutique pour combattre les infections et les neuro-dégénérescences. Dans cette optique, et afin d'am liore r la d tection de tumeurs, des agents de contraste ont  t  d velopp s dans le but d'augmenter le rapport signal sur bruit. Parmi ces agents, les nanoparticules (NPs) d'oxyde de fer superparamagnétiques (SPIOs) et les quantum dots (QDs) sont des candidats idéaux et ont reçu une grande attention depuis une vingtaine d'ann es [1, 2]. De surcroit, leurs propriétés spécifiques dues à leurs dimensions nanométriques et leurs formes permettent de moduler leur bio-distribution dans l'organisme [3]. L'opportunit de revêtir ces NPs biocompatibles par des couches de polymères devraient permettre d'am l iorer la stabilit de ces nanomat riaux dans l'organisme. Et par conséquent, favoriser leur biodistribution et également leur conférer de nouvelles applications en l'occurrence des applications biom dic ales. Dans ce travail de thèse, nous avons développé de nouveaux systèmes thermo-r pondant bas s sur un cœur SPIOs ou QDs qui sont capables, à la fois, de transporter un principe actif anticancéreux, *i.e.* la doxorubicine (DOX) et de le relarguer dans le milieu physiologique à une température contrôlée. Deux familles de NPs ont été synthétisées. La première concerne des NPs de $Fe_3O_4$ SPIO qui ont été modifiées en surface par un copolymère thermorépondant biocompatible à base de 2-(2-methoxy) m tha crylate d' thyle ($MEO_2MA$), oligo (éthylène glycol) méthacrylate (OEGMA) [4]. La seconde famille, consiste en des NPs de ZnO recouverte du même copolymère [4, 5]. Pour la première fois, le copolymère de type $P(MEO_2MA_X\text{-}OEGMA_{100\text{-}X})$ a été polymérisé par *activateur-régénéré par transfert d'électron-polymérisation radicalaire par transfert d'atome* (ARGET-ATRP). La polymérisation et copolymérisation ont été initiées à partir de la surface [4]. Les NPs cœur/coquilles ont  t caractérisées par microscopie électronique à transmission (TEM), analyse thermogravimétrique (TGA), *etc*. Nous avons montr que l'efficacit du proc d ARGET-ATRP pour modifier les surfaces des NPs de $SiO_2$, $Fe_3O_4$ et de ZnO. L'influence de la configuration de la chaîne de copolymère et des propriétés interfaciales avec le solvant ou le milieu biologique en fonction de la température a été étudiée. Nous avons montré que les propriétés magnétiques des systèmes coeur/coquilles à base de $Fe_3O_4$ ne sont influencées que par la quantité de polymère greffée contrairement au QDs qui vient leur propriété optique

réduire au-delà de la température de transition [4]. Ce procédé simple et rapide que nous avons développé est efficace pour le greffage de nombreux copolymères à partir de surfaces de chimie diff rentes. Les exp riences de largage et relarguage d"un mol c ule modèle telle que la DOX ont montré que ces nanosystèmes sont capables de relarguer la DOX à une temp rature bien contrôl e, à la fois dans l"œau que dans des milieux complexes tels que les milieux biologique. De plus, les tests de cytocompatibilité ont montré que les NPs coeur/coquilles ne sont pas cytotoxiques en fonction de leur concentration dans le milieu biologique. A partir de nos résultats, il apparaît que ces nouveaux nanomatériaux pourront être envisagés comme une plateforme prometteuse pour le traitement du cancer.

**MOTS-CLES**:

Nanoparticules cœur/coquilles, ARGET-ATRP, Polymère répondant, Quantum dots, Superparamagnétique, Libération de médicament.

# REFERENCES

1. Li, L., Jiang, W., Luo, K., Song, H., Lan, F., Wu, Y. and Gu, Z., *Superparamagnetic iron oxide nanoparticles as MRI contrast agents for non-invasive stem cell labeling and tracking*. Theranostics, 2013. **3**(8): p. 595-615.

2. Kucheryavy, P., He, J., John, V.T., Maharjan, P., Spinu, L., Goloverda, G.Z. and Kolesnichenko, V.L., *Superparamagnetic iron oxide nanoparticles with variable size and an iron oxidation state as prospective imaging agents*. Langmuir, 2013. **29**(2): p. 710-716.

3. Ghosh Chaudhuri, R., and Paria, S., *Core/shell nanoparticles: classes, properties, synthesis mechanisms, characterization, and applications*. Chemical reviews, 2011. **112**(4): p. 2373-2433.

4. Jamal Al Dine, E., Ferjaoui, Z., Roques-Carmes, T., Schejn, A., Meftah, A., Hamieh, T., Toufaily, J., Schneider, R., Gaffet, E. and Alem, H., *Efficient synthetic access to thermo-responsive core/shell nanoparticles*. Nanotechnology, 2017.

5. Alem, H., Schejn, A., Roques-Carmes, T., Ghanbaja, J. and Schneider, R., *Thermo responsive and aqueous dispersible ZnO/PNIPAM core/shell nanoparticles*. Nanotechnology, 2015. **26**(33): p. 335605.